INVESTIGATION OF A FOCUSED-IMAGE LENS-HOLOGRAM PROJECTION SYSTEM FOR MICROLITHOGRAPHY

by

Ginetto Addiego

INVESTIGATION OF A FOCUSED-IMAGE
LENS-HOLOGRAM PROJECTION SYSTEM
FOR MICROLITHOGRAPHY

by

Ginetto Addiego

Memorandum No. UCB/ERL M90/89

5 October 1990

ELECTRONICS RESEARCH LABORATORY

College of Engineering
University of California, Berkeley
94720

INVESTIGATION OF A FOCUSED-IMAGE
LENS-HOLOGRAM PROJECTION SYSTEM
FOR MICROLITHOGRAPHY

by

Ginetto Addiego

Memorandum No. UCB/ERL M90/89

5 October 1990

ELECTRONICS RESEARCH LABORATORY

College of Engineering
University of California, Berkeley
94720

Investigation of a Focused-Image Lens-Hologram Projection System for Microlithography

by

Ginetto Addiego

ABSTRACT

A prototype focused-image holographic image projection system is studied. A simple single element bi-convex lens and a well corrected multi-element lens are employed as the imaging optics with photoresist, Polaroid's DMP-128 photopolymer, and Dupont's photopolymer as the holographic recording media. Diffraction-limited-images are achieved using both a simple lens and a multi-element lens. The system incorporating the simple lens has a theoretical resolution of 0.62 μm and achieves a resolution of 0.7 μm. The reconstructed images using the simple lens are extremely sensitive to any changes in the image reconstruction configuration.

To reduce the optical noise present in the reconstructed images, an incoherent illumination source is explored. The optical noise in the reconstructed image is significantly reduced while achieving near-diffraction-limited imaging. In addition, the general requirements for image reconstruction using an incoherent source are developed.

Two unique approaches are employed to analyze the imaging sensitivity of various reconstruction parameters to the quality of the imaging optics. The first method utilizes a simple analytic model of the imaging lens combined with an ideal model of

the hologram to ascertain the wave-front aberrations of a non-ideal lens-hologram system. Several registration errors in the reconstruction configuration are modelled including axial and lateral displacement of the hologram as well as the angular displacement of the reconstruction beam. A numerical "ray-trace" simulator is employed to analyze a specific lens-holographic system. A sensitivity analysis of several system variables such as construction beam angle, wavefront, and wavelength as well as hologram repositioning and magnification errors is presented for both lens types, the simple single bi-convex lens and the well-corrected multi-element lens. The image quality sensitivity for the simple lens was found to be very large. The multi-element lens is relatively insensitive to changes in the image construction system compared to the simple lens. Residual spherical aberration in the imaging lens has the largest influence on the sensitivity followed by coma and astigmatism.

W C Oldham

Committee Chairman

I dedicate this dissertation to my mom, Gabriella.

ACKNOWLEDGEMENTS

I would like to thank Paul Carey, Steve Holland, Francois Henley, Winston Sun, Francisco Viana, Kai-Yap Toh and the numerous others whose friendship and support over the years helped make this work possible.

I also owe many thanks to my Quantum Electronics Laboratory partners Sol Dijali and Daryoosh Vakhshoori whose over-stimulating conversations made working in a dark and dreary place palatable.

I would also like to thank the technology simulation group members William Bell, Richard Ferguson, Phillip Flanner, John Gamelin, Sherman Kwok, Keunmyung Lee, Stephen Meier, Kane Ng, Edward Scheckler, Kenny Toh, Nelson Tam, and Alexander Wong.

This work could not be completed without the expertise of the Bob Collins, Dave Erikson, Sam Higginbotham, Ben Lake, Jose Rivera, Donald Synder, John Tombaugh, and Roland Turk of the ERL Machne shop and Katalin Voros, Rosemary Spivey, Phillip Guillory, Tom Booth, Kim Chan, Marilyn Kushner, James Parrish, Robin Rudell and the rest of the staff in U.C. Berkeley Microfabrication Laboratory. I would also like to acknowledge Yvonne Dunn, Doris Simpson, Maryann Norris and the rest of the ERL staff for their expertise and assistance.

Finally, my family deserves many thanks for their encouragement and support. My brother, Joe, deserves special mention for without his vision none of this work would have been accomplished.

Investigation of a Focused-Image Lens-Hologram Projection System for Microlithography

Table of Contents

CHAPTER 1

INTRODUCTION

1.1 MOTIVATION

The semiconductor industry is continually striving to obtain faster and more complex integrated circuits (ICs). The production of these circuits requires an aggressive reduction of device geometries in both the vertical and lateral directions to achieve the desired speed and circuit function. Figure 1 illustrates the reduction in the minimum lateral feature size needed for the next several generations of Dynamic Random Access Memories (DRAMs)[1.1].

The minimum lateral feature size for the 4 Megabit DRAM is 0.8 micrometers and is predicted to be 0.35 micrometers for the 256M DRAM. In addition, the predicted image field size for the 256 Megabit DRAM is 6 cm^2, an increase in area of 600% over the 4 Megabit DRAM. Hence, from the figure, two trends are clearly established for future ICs; the lateral minimum feature size is approaching 0.2 μm and the image field size is approaching 10 cm^2.

At present, optical lithography is the primary vehicle used to define patterns for the creation of ICs. Conventional optical lithography systems such as projection steppers can delineate patterns as small as 0.8 μm in photoresist over an image field of 1 cm^2[1.2]. However, as the semiconductor industry moves to deep sub-

micrometer design rules over field sizes larger than 1 cm^2, It becomes unclear whether conventional projection optical lithography can achieve the desired performance in this regime. Current optical lithography systems cannot achieve deep sub-micrometer resolution over an image field greater than 1 cm^2[1.3].

1.2 FUTURE TRENDS FOR OPTICAL LITHOGRAPHY

The two fundamental parameters which describe the resolution of an optical system are the wavelength of illumination and the numerical aperture of the imaging system. The useful resolution of an optical system can be approximated by the following equation:

$$R = K * (\frac{\lambda}{NA})$$

1.1

where λ is the illumination wavelength, NA is the numerical aperture, and K is the photoresist technology factor. Therefore, to improve the resolution of the optical system, the illumination wavelength must be decreased or the numerical aperture must be increased or a combination of both. The photoresist technology factor is fairly constant and varies between 0.6 (research environments) and 0.8 (production environments).

Decreasing the illumination wavelength into the ultra-violet provides higher resolution but raises a number of practical difficulties for the lens designer; many of the optical glasses that might be used to color correct a lens are highly absorbent[1.1]. The use of absorbing glasses presents two major problems. First, microlithography reduction lenses contain upwards of twenty optical elements. Since each element absorbs a fraction of the illumination energy, there can be substantial loss of light. This loss of light directly impacts the throughput of the

lithography system. Second and more importantly, as each optical element absorbs a fraction of the illumination energy, their temperature increases. This rise in temperature of each optical element changes their physical size and index of refraction. This change introduces an image distortion in the field and also perturbs the magnification of the system. The change in the index of refraction of the optical elements will also directly shift the plane of best focus during operation. The end result is a degradation in the performance of the system[1.4]. Thus, the lens designer has no choice but to employ one of the few available non-absorbing optical glasses. Table 1.1 list the the available optical glasses with their corresponding operating wavelengths. All-quartz microlithography lenses have been designed[1.5-7] to circumvent these problems; however, they require narrow-band illumination and this increased coherence opens a myriad of new problems[1.8-10].

An alternative method for increasing the resolution is to increase the numerical aperture of the imaging system. However, increasing the numerical aperture of lens while maintaining or increasing the image field size increases the lens' internal complexity and physical size[1.11,12]. New reduction lenses with numerical apertures greater than 0.4 with field sizes of 20 mm consist of upwards of twenty optical elements and have an overall length of 1000 mm in length. For distortion-free, diffraction-limited performance over the entire field, each optical element in the lens must be correctly positioned to within micrometers of the specified design. In addition, each element's surface sphericity must be better than $\lambda/20$ and their corresponding thickness must also be controlled to within micrometers of specification[1.13,14]. Thus, to manufacture a large numerical aperture lens with a large image field size is extremely difficult and may be virtually impossible[1.15]. Figure 2 is a plot of current optical microlithography lenses with their corresponding numerical aperture and field size[1.16]. From the figure, it is evident that there is a

Optical Glasses	
Wavelength	Glasses
436 nm	Ordinary Glasses
365 nm	Eight Glasses
<300 nm	Fused Silica
	Magnesium Fluoride
	Calcium Fluoride
<200 nm	Lithium Fluoride
	Mirrors

Table 1.1 Optical glasses with their corresponding wavelength.

tradeoff between the numerical aperture of a lens and its field size for current production lenses. In fact, analysis of projection stepper lenses reveals that the square of the field size divided by the useful resolution has nearly a constant value of less that $10*10^{10}$ for all lenses[1.3]. That is, resolution tradeoffs image field in such a fashion to keep the number of resolvable pixels within the image field constant. This tradeoff may be due to the inevitable consideration of the size and complexity of the optics that can be fabricated with sufficient accuracy.

It is therefore understandable that researchers have been exploring new technologies that will enable the production of deep sub-micrometer patterns over a large image field. One such technology that shows great promise is optical

holography. In this dissertation, a high-resolution imaging system is investigated that uses a simple lens to focus an image of a IC mask onto a high-resolution recording material to form the basis of a hologram. Once this hologram has been recorded, it is re-illuminated with a reconstruction beam that is conjugate to the reference beam. The wave-front reconstructed from the hologram is now conjugate to the original and reverse-ray traces back through the lens cancelling the aberrations introduced on the first pass and creates an unaberrated real image of the IC mask. The key advantage of this imaging system is that only simple optical components in a simple configuration are needed. Because of the system's simplicity and adaptive nature, it is not constrained by the compromises found in conventional optical systems where for example the resolution trades off with image field size. In fact, in a focused-image holographic imaging system, in principle, there is no tradeoff between the resolution and field size[1.17].

1.3 SCOPE OF THE RESEARCH

The purpose of this dissertation is to investigate the image quality and image placement produced from a focused-image hologram and to identify key potential problems areas that must be addressed for this technology to become a viable technology for the manufacture of ICs. As a test vehicle, an experimental focused-image holographic projection imaging system is constructed to explore the image quality and placement issues. In addition, a simple analytical and a computer model of the system are developed to help pin-point and quantify critical system parameters.

This dissertation is divided into six chapters with each chapter covering a major topic. In Chapter 1, the motivation for this work is developed and the

organization of the dissertation is given. Chapter 2 briefly describes the historical account of the invention of holography and the previous attempts using holography and real-time wave-front conjugation to produce high-resolution images. Chapter 3 discusses the salient features and requirements for an off-axis focused-image holographic system to produce unaberrated real images. A description of an experimental focused-image holographic imaging system using a simple single element lens with a coherent illumination source and a complex photographic quality lens with an incoherent illumination source with their corresponding results are given in Chapter 4. In Chapter 5, a simple analytic model and a computer model of an ideal and non-ideal holographic system are developed and image quality and placement simulations for a simple and complex lens to system non-idealities are shown. Chapter 6 summarizes and concludes this work and also suggests possible future work.

1.4 REFERENCES

[1.1] M. King and D.A. Markle, Optical Lithography, SPIE, October 1988. Short Course Notes #17, SPIE's International Technical Symposium on Monitoring and Control of Plasma-Enhanced Processing of Semiconductors, OPTCON '88

[1.2] N.Ohta, T. Kojima, C. Sato, T. Ogawa, and M. Noguchi, *The Future of Projection Lenses and the New G-Line Lens for 0.7 μm Lithography.*, 922, pp. 291-299, SPIE, 1988.

[1.3] A.D. Wilson, "X-Ray Lithography: Can It Be Justified.," in *Electron-Beam, X-Ray, and Ion-Beam Techniques for Submicrometer Lithographies IV.*, vol. 537, p. 85, SPIE, 1985.

[1.4] D.A. Markle, "The Future and Potential of Optical Scanning Systems.," *Solid State Technology*, pp. 159-166, September 1984.

[1.5] T.E. Jewell, J.H. Bennewitz, G. C. Escher, V. Pol, "Effect of Laser Characteristics on the Performance of a Deep UV Projection System," *Lasers in Microlithography*, vol. 774, pp. 124-132, SPIE, 1987.

[1.6] K.F. Walsh, M.M. Dunn, D.S. Holbrook, and J. Bruning, "Performance Evaluation of a Practical 248nm Wafer Stepper," *Lasers in Microlithography*, vol. 774, pp. 155-159, SPIE, 1987.

[1.7] V. Pol, J.H. Bennewitz, G.C. Escher, M. Feldman, V.A. Firtion, T.E. Jewell, B.E. Wilcomb, and J.T. Calemens, *Excimer Laser-Based Lithography : A Deep Ultraviolet Wafer Stepper.*, 633, p. 6, SPIE, 1986.

[1.8] Lacombat, Massini, G.M. Dubroeucq, and M. Brevignon, "Laser Projection Printing.," *Solid State Technology*, pp. 115-121, August 1980.

[1.9] Y. Ozaki, K. Takamoto, and A. Yoshikawa, "Effect of Temporal and Spatial Coherence if Light Source on Patterning Characteristics in KrF Excimer Laser Lithography," *Optical/Laser Microlithography*, vol. 922, pp. 444-448, SPIE, March 1988.

[1.10] W.N. Partlo, C.A. Spence, and W.G. Oldham, "Effects of Line-Narrowing and Collimation of Excimer Radiation at 248nm," *Optical/Laser Microlithography II*, vol. 1088, pp. 448-461, SPIE, March 1989.

[1.11] E. Glatzel, "New Lenses for Microlithography.," *International Lens Conference (OSA)*, vol. 237, pp. 310-320, SPIE, 1980.

[1.12] S.G. Olson and J.H. Bruning, *Routes to Half-Micron Lithography.,* 922, pp. 300-304, SPIE, 1988.

[1.13] A.R. Phillips and M.J. Buzawa, "High Resolution Lens System for Submicron Photolithography.," *International Lens Design Conference (OSA)*, vol. 237, pp. 329-336, SPIE, 1980.

[1.14] R.E. Tibbets and J.S. Wilczynski, "Design and Fabrication of Microelectronic Lenses.," *International Lens Design Conference (OSA)*, vol. 237, pp. 321-328, SPIE, 1980.

[1.15] J.S. Wilczynski, *Manufacturing Tolerances for Diffraction Limited Optics.,* Institute of Optics, University of Rochester, 1967.

[1.16] P. Burggraaf, "Stepper Lens Options for VLSI.," *Semiconductor International,* vol. 11, no. 2, pp. 44-49, February 1988.

[1.17] A. Macovski, "Hologram Information Capacity.," *Journal of the Optical Society of America,* vol. 60, no. 1, pp. 21-29, January 1970.
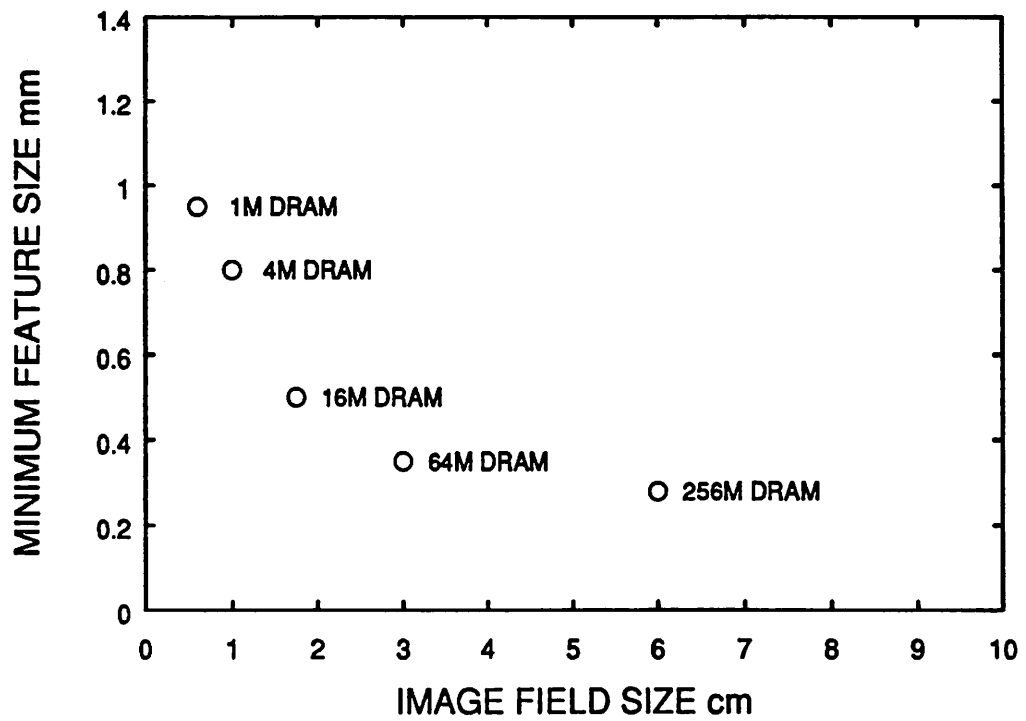
Figure 1.1 Future DRAM sizes versus their corresponding minimum feature and image field size.
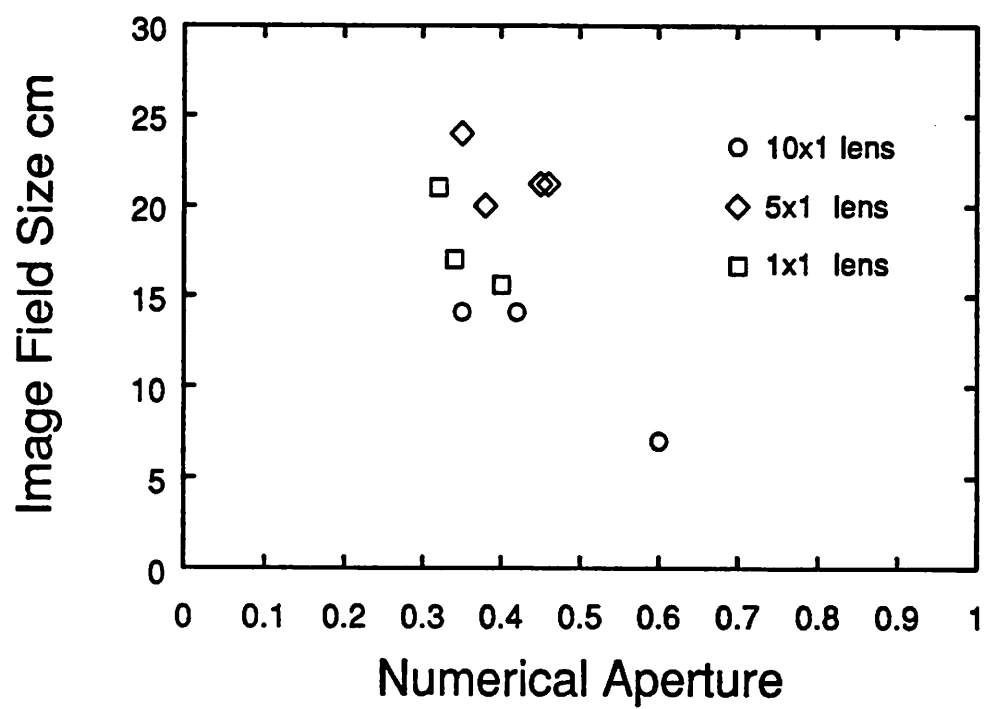
Figure 1.2 Plot of current optical microlithography lenses with their corresponding numerical apertures and field sizes.

CHAPTER 2

OVERVIEW OF HIGH-RESOLUTION HOLOGRAPHIC AND REAL-TIME WAVEFRONT CONJUGATION IMAGING

In this chapter, an overview of high-resolution holographic and real-time wave-front conjugation imaging is given to provide the reader with a reasonable background and to help put this work in context. In section 2.1, a brief historical account of the invention holography is given and in section 2.2 several high-resolution holographic imaging schemes are described. In section 2.3, a brief discussion real-time wave-front conjugation imaging using a phase-conjugate mirror is given and section 2.4 briefly discusses the advantages of focused-image lens-holograms over other coherent techniques.

2.1 HISTORICAL DEVELOPMENT OF HOLOGRAPHY

Gabor[2.1-3] first introduced the essential concept of wave-front reconstruction known more commonly as holography in 1948 as an alternative method to increase the resolution of the electron microscope. Holography is a two-step imaging process that records (photographs) the diffraction pattern of an object and then uses this recorded pattern with a suitable illumination source to construct an image of the original object. The recorded diffraction pattern normally bears little resemblance to the object, but contains most or all of the information necessary to construct the image of the object. The process requires two coherent beams of light, an object beam and a reference beam that are spatially and temporally coherent with each other to record the amplitude as well as the phase of the object wave-front. The use of a reference beam is necessitated because physical detectors are sensitive only to the intensity ($|\vec{E}\cos(\phi)|^2 = E_o{}^2$) rather that the wave amplitude ($\vec{E}\cos(\phi)$) of an object wave-front. Thus, the phase of the wave-front is not recorded in an ordinary recording process.

To record the phase and the amplitude of an object wave-front, two coherent beams, a reference and an object beam, are first combined at a plane in space where the intensity at this plane depends not only the intensities of the individual beams, but also on the phase difference between the two. Then, the intensity variations at this plane are recorded in a high-resolution recording material such as a high-resolution photographic emulsion plate. This recording is called a hologram. Illuminating the hologram with the same reference beam in same position will fully construct the image of the object even though the object is no longer present.

Gabor's[2.2] experimental holographic system for creating and viewing a holographic image is shown in figures 2.1 and 2.2. His original experiments used a monochromatic beam of light that was passed through a pin-hole to increase its

spatial coherence to insure high visibility interference patterns. The object was a clear field transparency of alpha-numeric characters. The light diffracted by the transparency and the light passing through formed the object and reference beams respectively. These two beams form an interference pattern in space directly behind the transparency. Photographic emulsion on a glass substrate sensitive to the light was inserted down-stream of the transparency to record the interference pattern. The emulsion was exposed and developed forming a hologram. The hologram was then inserted back into the original hologram recording position and illuminated with the same reference beam to construct the image of the transparency. Both real and virtual images were created on axis. This, however, led to two viewing difficulties. First, both the virtual and real images were obscured by the undiffracted portion of the reference beam used to construct the image. Second, each image obscured the other since both the real and virtual image were created on axis. Several techniques were proposed to eliminate the conjugate image but none were successful. As a result, these viewing difficulties prevented the technology from gaining wide practical acceptance.

In 1962, Leith and Upatnieks[2.4] introduced a novel arrangement to construct a hologram and to reconstruct the image of an object from a hologram eliminating the image degradation characteristic of Gabor's on-axis holograms. Figure 2.3 schematically illustrates this arrangement. This arrangement was brought about by the invention of the laser. With a laser as the constructing and illuminating source, it is no longer necessary to have both the reference beam and the object beam incident on the object from the same direction but they now can be physically separated. This allows the two images, virtual and real, and the undiffracted beam to be physically separated in space. In addition, this technique removes the requirement that the object must also be a clear field transparency. Objects of any

kind and in any configuration can be used to form the basis of a hologram. These advances set off an explosive of growth of activity and optical holography soon found a number of applications which include imaging through aberrating media[2.5], the production and correction of optical elements[2.6], and high-resolution imaging of IC masks[2.7,8].

2.2 HIGH-RESOLUTION HOLOGRAPHIC IMAGING

Leith et al.[2.9], Meier[2.10], and Armstrong[2.11] have shown that under specific circumstances, an illuminated hologram will form an unaberrated real image of an object. Whenever the conditions of image reconstruction do not exactly duplicate or exactly complement those of the hologram recording process, wave-front aberrations are present in the reconstructed image. Specifically, wave-front aberrations will be introduced into the reconstructed image unless the reconstruction is made using the same wavelength of light used to record the hologram and the reconstruction source must be placed at the same position relative to the hologram that the reference source occupied assuming an ideal recording material.

These initial theoretical findings spawned a variety of research efforts to experimentally produce diffraction limited images using holography. Two divergent experimental approaches were investigated: far-field holograms and near-field holograms.

Far-field holograms compared to near-field holograms have several rather interesting properties and requirements. Far-field holograms do not require recording materials with a large dynamic range because the light derived from the object is not spatially localized on the recording material but rather is distributed over an area due to diffraction. This distribution of information over the hologram has both advantages and disadvantages. Small imperfections on the hologram such as

scratches or dust particles will not grossly effect the quality of the reconstructed image because the information from a very small portion of the image is constructed from information over a large area on the hologram. On the other hand, any non-linearities in the hologram recording process will create anomalous images and spurious noise in the reconstructed image due to the non-linear mixing between light derived from different areas of the object[2.12]. Even though near-field holograms require a recording material with a large dynamic range, they are far less susceptible to the problems associated with material non-linearities. [2.13] In addition, images recorded from near-field holograms are far less sensitive to deviations in the illumination source size, illumination bandwidth, and to the reconstruction beam curvature compared to far-field holograms[2.14].

Far-field holograms to produce high-resolution images were investigated by Kiemle[2.8] , Beesley et al.[2.7,15], and Champagne et al.[2.16]. Using the holographic imaging system shown in figures 2.4 and 2.5, Kiemle[2.8] resolved eight micrometer spaces using a dark-field mask. In this system, a microscope objective was used to demagnify the image of the transparency which was then used to form the basis of a hologram in the far-field. The image reconstructed from the hologram was the demagnified image of the transparency located at the image plane of the microscope objective. This holographic imaging system only covered a very small field due to the small field size of the microscope objective lens. No indication was given with regards to image quality or placement.

Beesley et al[2.7]. resolved four micrometer line and spaces over a 2.5 cm diameter field using the system shown in figures 2.6 and 2.7. They observed that careful matching of the reference and reconstruction beams is necessary, and accurate alignment of the hologram plate with respect to the reconstruction beam is imperative to construct high quality images. In addition, they also observed that the

achievable resolution was dependent on the flatness of the the hologram substrate surfaces as well as the parallelism of the substrate's two surfaces.

Champagne et al[2.16]. demonstrated 456 lines/mm resolution using the holographic system shown in figures 2.8 and 2.9. They concluded that the critical factor in obtaining high resolution images with acceptable image quality and placement with a far-field hologram with a large object to hologram separation is the angular alignment of the reconstruction beam. They also concluded that the reference and reconstruction beams must be either identical or conjugates of each other. Astigmatism and coma are the primary aberrations introduced into the reconstructed image for small misalignments of the reconstruction beam. They also noted that as the object to hologram separation is decreased, the image sensitivity to the angular reconstruction beam is decreased.

In a near-field arrangement, Stetson partially resolved 600 lines/mm using an internal-reflection image hologram[2.17,18]. In this type of hologram, the hologram to object distance is only 10 - 20 μms. The reference beam is introduced to the holographic recording media through a prism and is schematically illustrated in figures 2.10 and 2.11. However, one complication noted was that the signal to noise ratio of the constructed image was only 5:1. The noise was attributed to the non-linear effects of the recording media, aliasing effects due to the geometry, and scattering from the emulsion. He also observed that gross deviations in the illuminating beam had little effect on the image quality.

Suzuki and Tsujiuchi achieved resolution of 500 lines/mm over a 50 mm field using focused-image holographic system, a derivative of near-field holography[2.19]. Figure 2.12 schematically illustrates their imaging system. They used a poor quality condenser lens to image the mask onto a photographic emulsion to form a hologram. The hologram was then illuminated with a beam of light that was

conjugate to the reference beam to create an unaberrated image of the mask at the original mask plane. The key point of this system is that the image is created at the original mask plane through reverse-ray tracing back through the original condenser lens, eliminating the aberrations introduced by the lens.

2.3 COHERENT IMAGING USING PHASE-CONJUGATE MIRRORS

Recently, conjugate-wave-front generation by degenerate four-wave mixing has been used to realize real-time high-resolution images[2.20-22]. This technique is schematically illustrated in figure 2.13[2.22]. Two counter propagating pump beams interact with a weaker object beam by means of the third order nonlinear susceptibility of the conjugate medium. The image beam propagates in the direction that is exactly opposite to the object beam and its amplitude is proportional to the complex conjugate of the amplitude of the object beam. In addition, if the wave-fronts of the two pump beams are phase conjugates of each other, the image beam wave-front will be the phase conjugate of the object beam wave-front and will propagate back towards the object source reproducing the object beam wave-front at every plane. Essentially, the image beam wave-front propagates as if the image beam wave-front was the object beam wave-front but traveling in space backwards in time (time-reversal). To add further insight to the process conjugate-wave-front generation, it can also be considered as the real-time reconstruction of the image beam wave-front by one pump beam of a volume hologram formed by the object beam wave-front and the other pump beam.

Using the apparatus schematically illustrated in figure 2.13, Levenson et al[2.22]. have demonstrated 0.75 μms lines separated by 0.5 μms spaces recorded in photoresist with an effective system numerical aperture of 0.48 that are not degraded by any speckle or optical noise. The light source for the object

illumination and pump beams was an krypton-ion laser operating at 413 nm. The numerical aperture of the system was defined by the region of the conjugator crystal illuminated by the pump beams and the spacing between the the conjugator crystal and the beam-splitter. The conjugate wave-front generator was $LiNbO_3$ crystal that had been irradiated with 0.8 Mrad of cobalt gamma rays.

There are several key advantages using this conjugate-wave-front imaging technique to realize high-resolution images. First, only simple optics in a simple configuration are needed as seen in figure 2.13. The only difficulty of this approach is securing a suitable phase conjugator at the desired wavelength (if one exists). Second, the attainable field size is only dependent on the available laser power and not on the steering or imaging optics. Third, since the phase-conjugator operates in real-time, the conjugator automatically compensates for any aberrations introduced into the object beam path as well as any mis-alignments between the object plane and image plane. However, there are several effects unique to wave-front conjugation that have the potential for affecting the image such as spatial filtering due to nonuniform generation efficiency and image distortion due to pump beam self-focusing. In photorefractive materials such as $LiNbO_3$, the conjugate wave-front generation diffraction efficiency decreases rapidly with increasing spatial frequency and thus the higher order frequency components that correspond to the detail object information are not generated with the same efficiency as the lower frequency terms and are lost, resulting in the degradation of the image. Also, when the conjugator medium acts as a lens, it becomes difficult to ensure that the counter-propagating pump beams are phase conjugates of one another. If the radii of curvature of the phase-fronts of the two pump beams differ, the change in curvature alters the effective focal length of the image projection system, breaking the the phase-conjugation symmetry between object and image wave-front. This

asymmetry has the effect of translating the the image focal plane, and thus the magnification deviates from unity. For microlithography applications, changes in magnification of 1 part 10^5 (0.1 μm overlay tolerance and 1 cm field size) produces major difficulties in overlaying patterns. Because the non-linear optical interaction that gives rise to the conjugate-wave generation also causes self-focusing phenomena of the pump beams, there is an ultimate trade-off between image brightness and image quality.

2.4 FOCUSED-IMAGE LENS-HOLOGRAM IMAGING SYSTEM

Sections 2.3 and 2.4 described several holographic methods to image high-resolution patterns.† The real-time conjugate wave-front technique at first seems very promising as a high-resolution technique, however, this method has several drawbacks. The most significant caveat is the spatial frequency response of the conjugate crystal. High spatial frequencies are not generated with the same efficiency as the lower frequencies. Secondly, there is a fundamental material problem with the conjugate crystal, the non-linear optical optical interaction that gives rise to the conjugate wave-front generation also causes the self-focusing phenomena of the pump beams limiting the attainable image quality.

Conventional holographic techniques described earlier can generally achieve a resolution of 400 lines/mm. However, the most serious problem plaguing conventional holographic far-field imaging systems is the image quality degradation due to optical noise generated from the non-linear response of the recording material and

---

† Real-time conjugate system can be regarded as a real-time holographic technique or at least as a technique analogous to holography.

wave-front aberrations from registration errors in the image reconstruction system (such as hologram repositioning errors, reconstruction beam displacements, and changes in the reconstruction wavelength).

In conventional holography, the object is located at a large distance from the recording material, thus the wave-front from a specific point on the object is recorded over the entire surface of the recording material. In this configuration, the reconstructed image is extremely sensitive to any variations in the reconstruction system and to any non-linearities in the recording material. To reduce this sensitivity, an imaging system which locates the object wave-front close to the recording material so that the wave-front from a point on the object is distributed over a small portion on the recording material is desired. Two such imaging systems that accomplish this are total internal reflection holography and focused-image holography. An internal reflection holographic system is illustrated in figures 2.10 and 2.11. This imaging system suffers from optical noise generated from the near-field scattering of light from the hologram which is introduced into the reconstructed image. In addition, additional optical noise is generated from two of the three distinct holograms that are recorded. The object wave-front interferes with the two reference wave-fronts, the incoming and reflected wave-fronts, plus the two carriers interfere with each other. Furthermore, there is an aliasing problem with the object spectrum † which potentially adds optical noise to the reconstructed image.

A focused-image lens-hologram imaging system, illustrated in figure 2.12, preserves the desire of maintaining the image of the object localized and concurrently eliminates the near-field scattering and aliasing problems. The imaging system only requires a lens with a large numerical aperture with a large imaging

---

† The aliasing problem is discussed at length in Chapter 3.

field. This imaging lens adds an additional constraint that the hologram must also be aligned to the lens or a registration error occurs degrading the final reconstructed image.

2.5 REFERENCES

[2.1] D. Gabor, "A New Microscopic Principle.," *Nature*, vol. 161, pp. 777-778, 1948.

[2.2] D. Gabor, "Microscopy by Reconstructed Wavefronts.," *Proceedings of the Royal Society A*, vol. 197, pp. 454-487, 1949.

[2.3] D. Gabor, "Microscopy by Reconstructed Wavefronts. II.," *Proceedings of the Physical Society*, vol. 64, pp. 449-469, 1951.

[2.4] E.N Leith and J. Upatnieks, "Reconstructed Wavefronts and Communication Theory.," *Journal of Optical Society of America*, vol. 52, pp. 1121-1130, 1962.

[2.5] H. Kogelnik, "Holographic Image Projection through Inhomogeneous Media.," *Bell System Technical Journal Briefs*, vol. 44, pp. 2451-2455, December 1965.

[2.6] J. Upatnieks, A. Vander Lugt, and E. Leith, "Correction of Lens Aberratons by Means of Holograms," *Applied Optics*, vol. 5, pp. 589-593, 1966.

[2.7] M. J. Beesley, H. Foster, and K.G. Hambleton, "Holographic Projection of Microcircuit Patterns.," *Electronics Letters*, vol. 4, no. 3, pp. 49-50, February 9, 1968.

[2.8] H. Kiemle, "Holographic Micro-Images for Industrial Applications.," in *The Engineering Uses of Holography*, ed. E. R. Robertson and J.M. Harvey, pp. 517-525, University Press, 1970.

[2.9] E.N. Leith and J. Upatnieks, "Microscopy by Wavefront Reconstruction.," *Journal of the Optical Society of America*, vol. 53, pp. 1295-1301, 1965.

[2.10] R.W. Meier, "Magnification and Third-Order Aberrations in Holography.," *Journal of the Optical Society of America*, vol. 55, pp. 987-992, 1965.

[2.11] J.A. Armstrong, "Fresnel Holograms: Their Imaging Properties and Aberrations.," *I.B.M. Journal of Research and Development,* vol. 9, no. 3, pp. 171-178, May 1965.

[2.12] J.W. Goodman and G.R. Knight, "Effects of Film Non-Linearities on Wavefront-Reconstruction Images of Diffuse Objects.," *Journal of the Optical Society of America,* vol. 58, pp. 1276-1283, 1968.

[2.13] I.S. Klimenko and E.G. Matinyan, "Nonlinear Recording of Focused-Image Holograms," *Soviet Journal of Quantum Electronics,* vol. 4, no. 9, p. 1176, March 9, 1975.

[2.14] G.B. Brandt, "Image Plane Holography," *Applied Optics,* vol. 8, no. 7, pp. 1421-1429, July 1969.

[2.15] M.J. Beesley, "A Potential Application of Holography to Microcircuit Manufacture.," in *The Engineering Uses of Holography,* ed. E.R. Robertson and J.M. Harvey, pp. 503-516, University Press, 1970.

[2.16] E.B. Champagne and N.G. Massey, "Resolution in Holography.," *Applied Optics,* vol. 8, no. 9, pp. 1879-1885, September 1969.

[2.17] Karl A. Stetson, "Holography with Total Internally Reflected Light.," *Applied Physics Letters,* vol. 11, no. 7, pp. 225-226, October 1, 1967.

[2.18] Karl A. Stetson, "Improved Resolution and Signal-to-Noise in Total Reflection Holograms.," *Applied Physics Letters,* vol. 12, no. 11, pp. 362-364, June 1, 1968.

[2.19] T. Suzuki and J. Tsujiuchi, "A Holographic Image Printing Technique with High Resolution.," *Optics Communication,* vol. 9, no. 4, pp. 360-363, December 1973.

[2.20] D.M. Bloom and G.C. Bjorklund, "Conjugate Wave Front Generation and Image Reconstruction by Four Wave Mixing.," *Applied Physics Letters*, vol. 31, pp. 592-54, 1977.

[2.21] M.D. Levenson, "High-Resolution Imaging by Wave-Front Conjugation.," *Optics Letters*, vol. 5, no. 5, pp. 182-184, June 1981.

[2.22] M.D. Levenson, K.M. Johnson, V.C. Hanchett, and K. Chiang, "Projection Photolithography by Wave-Front Conjugation," *Journal of the Optical Society of America*, vol. 71, pp. 737-743, 1981.
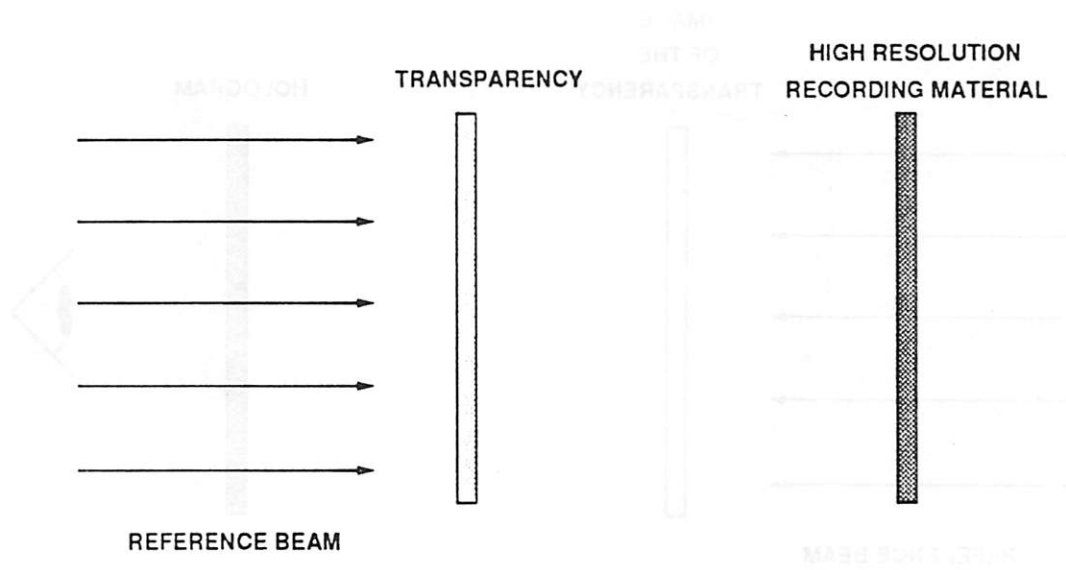
Figure 2.1 Gabor's in-line hologram forming configuration.

IMAGE
OF THE
TRANSPARENCY

HOLOGRAM

REFERENCE BEAM
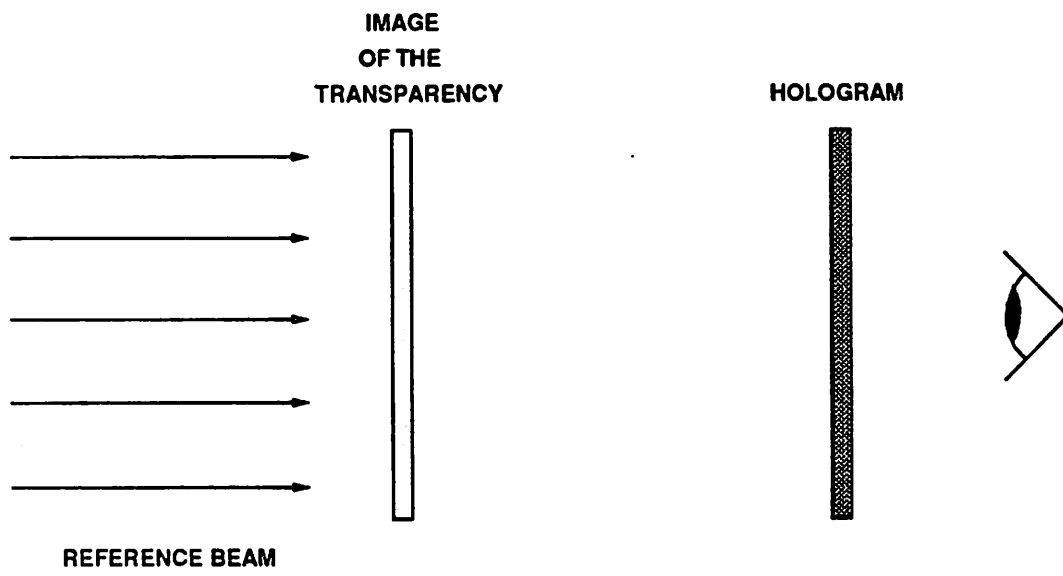
Figure 2.2 Gabor's in-line image construction configuration.

OBJECT   HOLOGRAM

COLLIMATED BEAM

PRISM
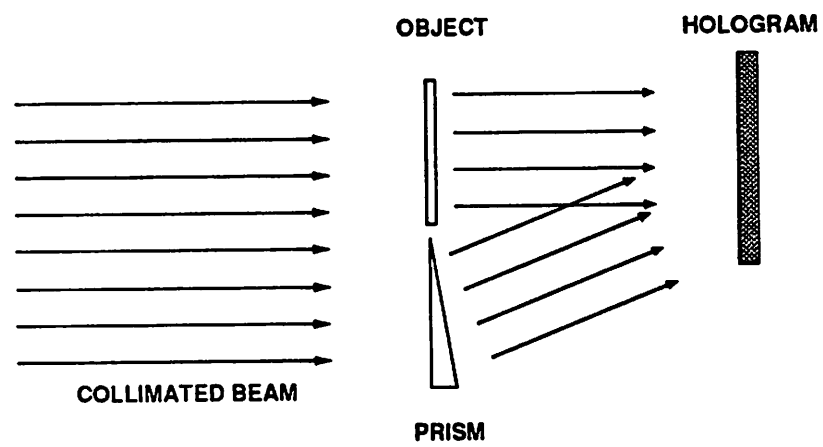
Figure 2.3   Arrangement to construct an off-axis hologram.

TRANSPARENCY

HIGH RESOLUTION
RECORDING MATERIAL

IMAGE PLANE

IMAGING
LENS

LENS

REFERENCE BEAM
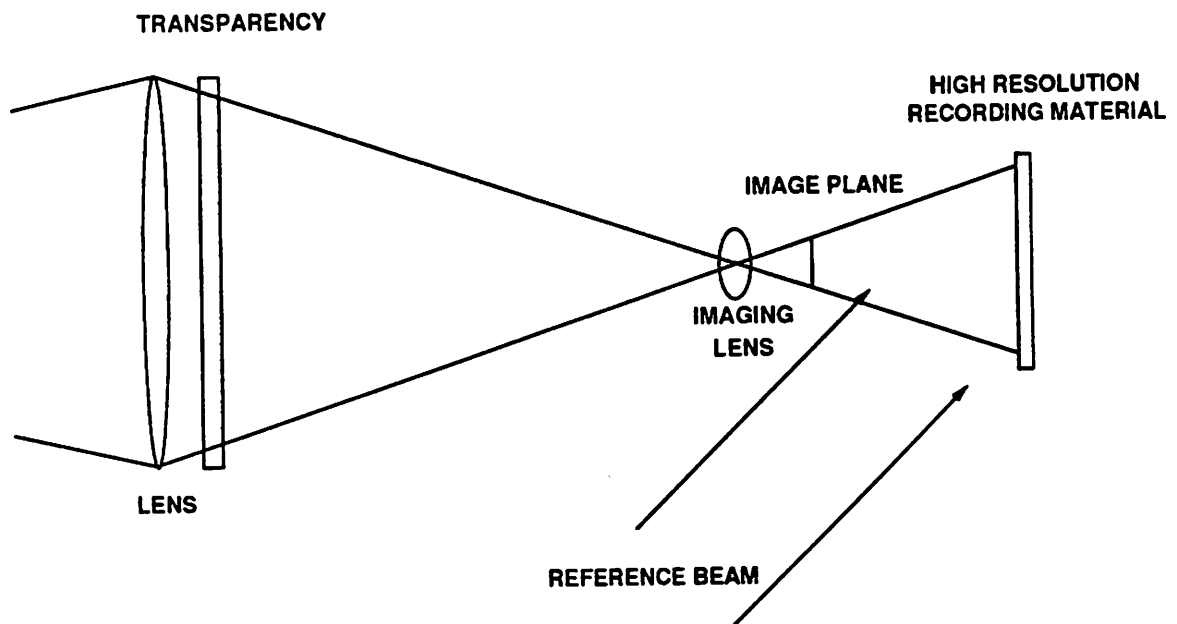
Figure 2.4   Kiemle's optical arrangement to construct a far-field hologram using a lens to demagnify the image.
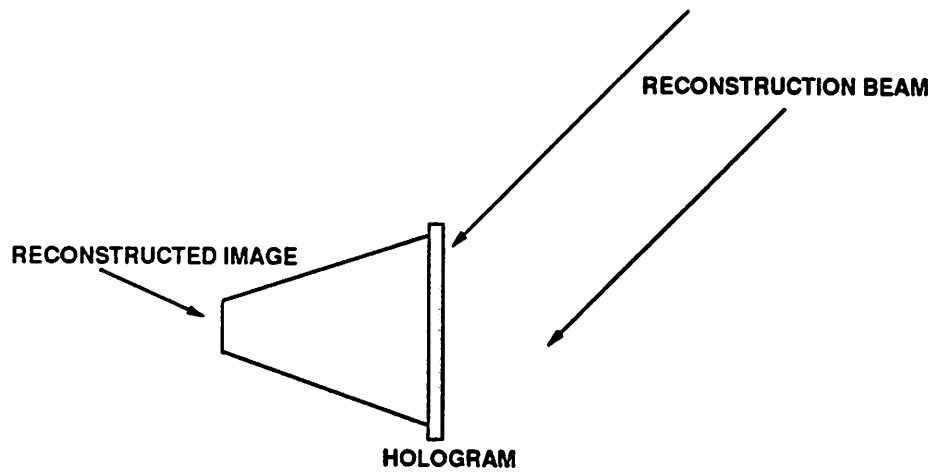
Figure 2.5 Kiemle's optical arrangement to construct a real image of the demagnified object at the len's image plane.

PARABOLIC
REFLECTOR

PIN-HOLE

MASK

LENS

DIFFUSER

HOLOGRAM

BEAM
SPLITTER

MIRROR

MIRROR

LASER BEAM
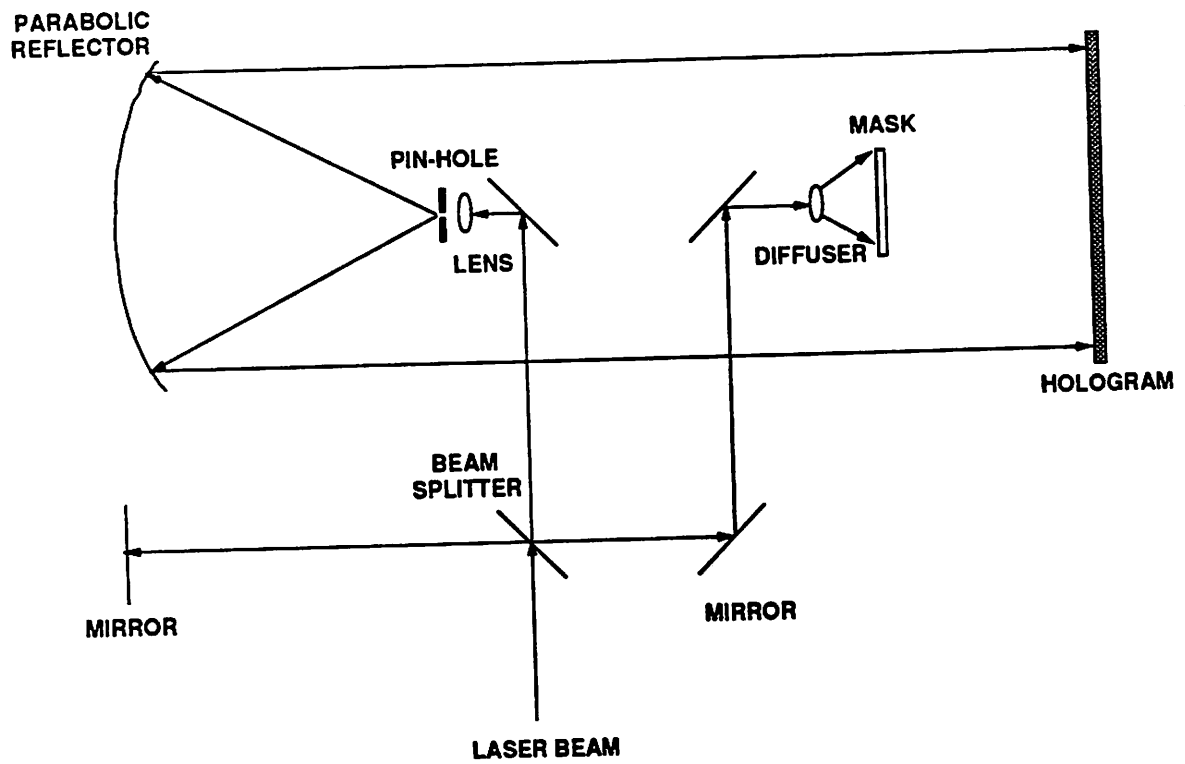
Figure 2.6 Beesley's optical arrangement to construct a far-field hologram of an object.

PARABOLIC
REFLECTOR

HOLOGRAM

RECONSTRUCTED
IMAGE

PIN-HOLE

LENS

LASER BEAM
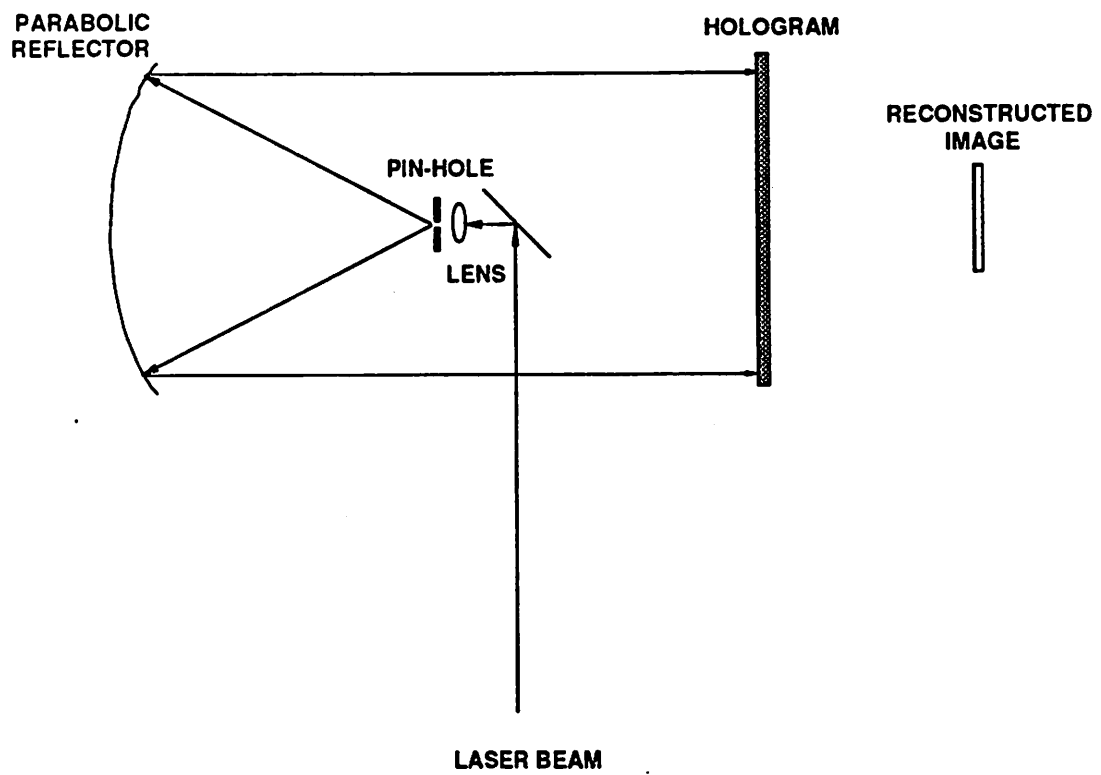
Figure 2.7   Beesley's optical arrangement to construct the real image of the object.

OBJECT

HIGH RESOLUTION
RECORDING MATERIAL

REFERENCE
SOURCE
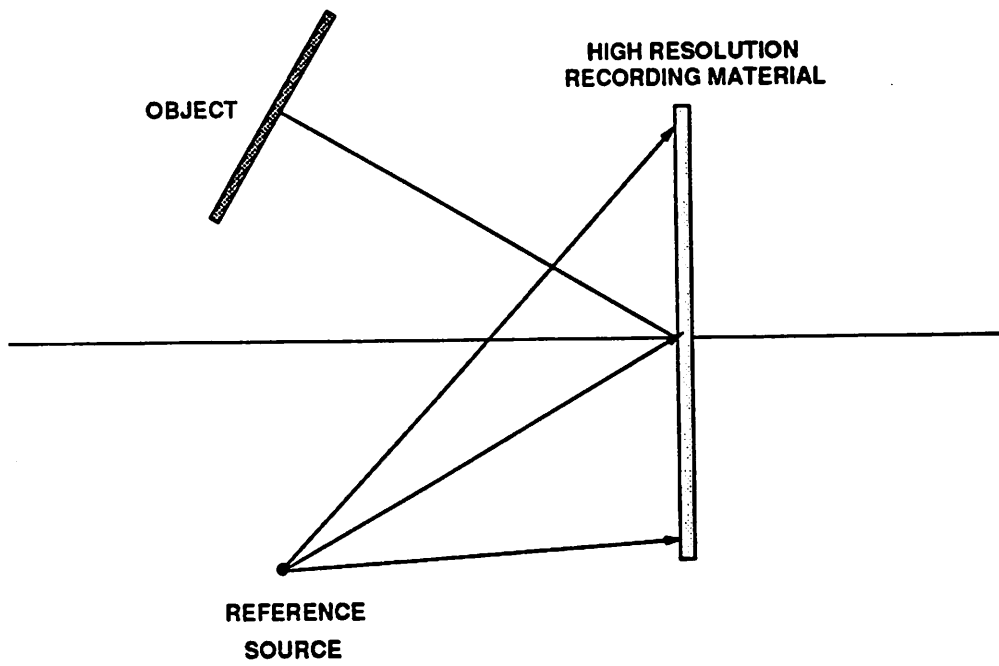
Figure 2.8 Champagne's simple optical arrangement to record a far-field holo-gram of an object.

REAL IMAGE
LOCATION

RECONSTRUCTION
SOURCE
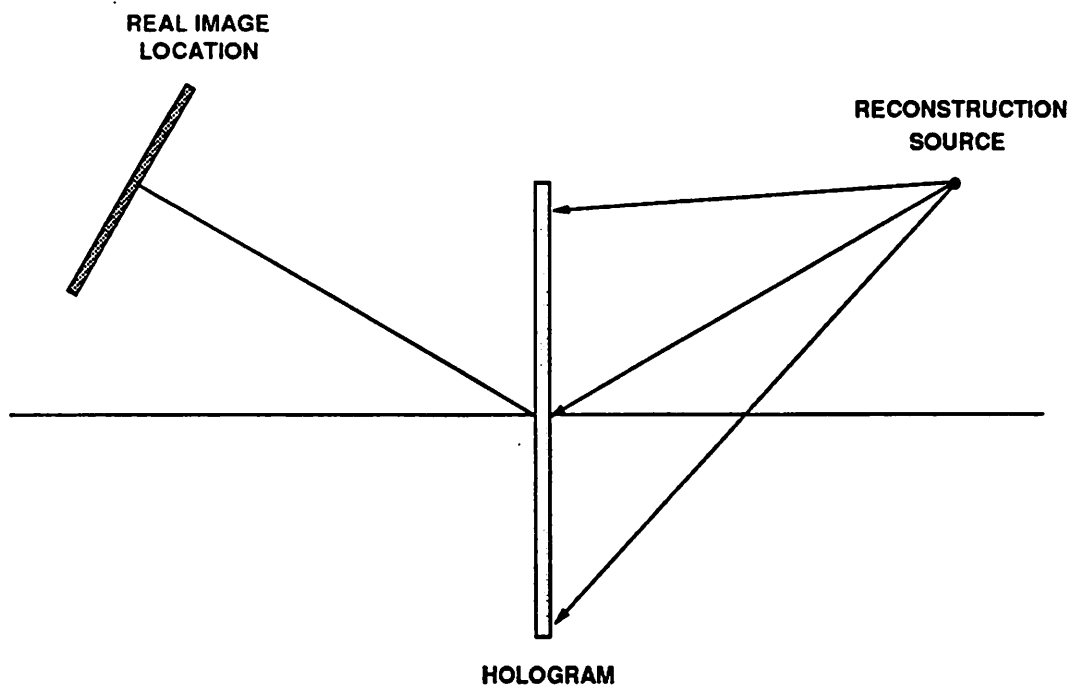
HOLOGRAM

Figure 2.9 Champagne's simple optical arrangement to construct a real image of
the object.
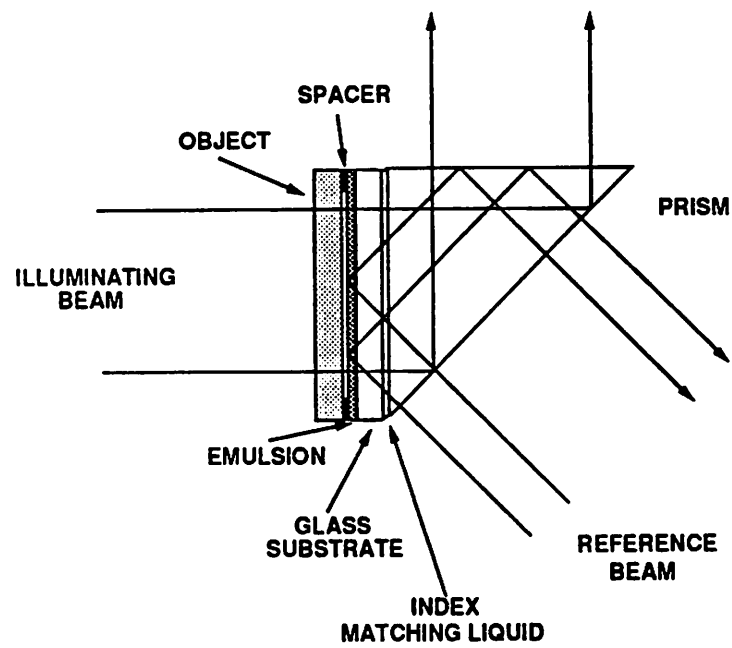
Figure 2.10 Schematic diagram to construct a total internal reflection near-field hologram.

SPACER

OBJECT
IMAGE PLANE

PRISM

RECONSTRUCTION
BEAM

HOLOGRAM

GLASS
SUBSTRATE

INDEX
MATCHING LIQUID
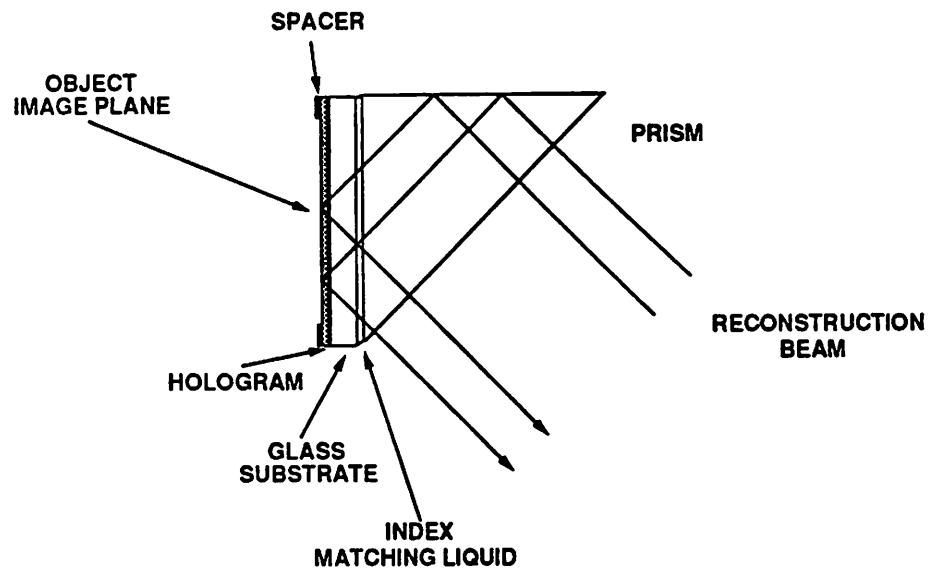
Figure 2.11 Schematic diagram to construct the image created from a total internal reflection near-field hologram.
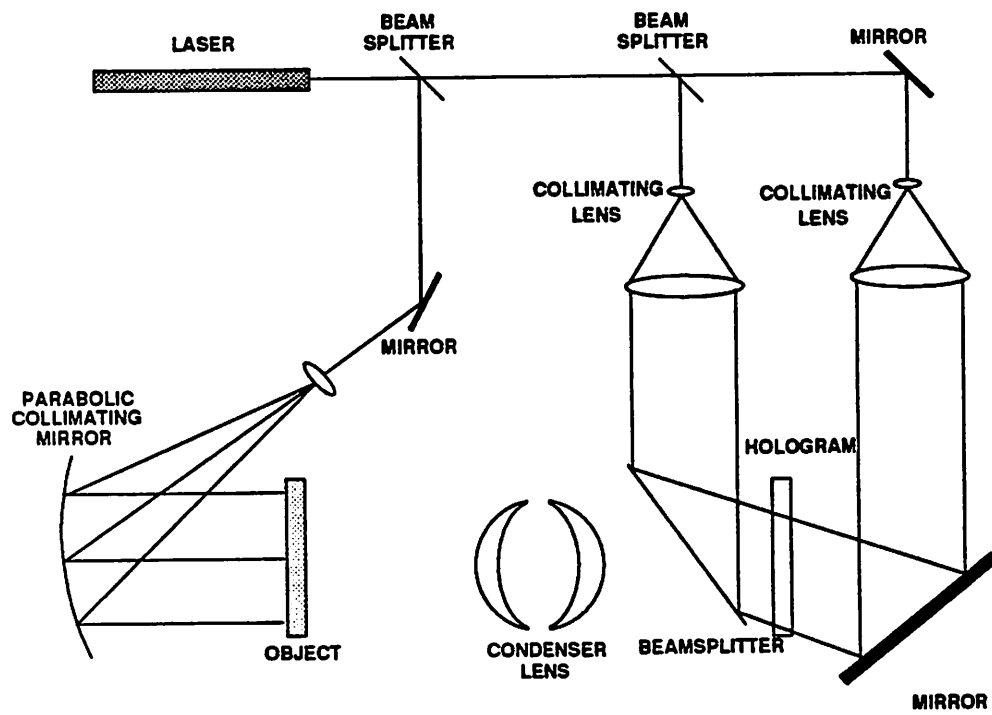
Figure 2.12 Focused-image lens-holographic imaging apparatus.
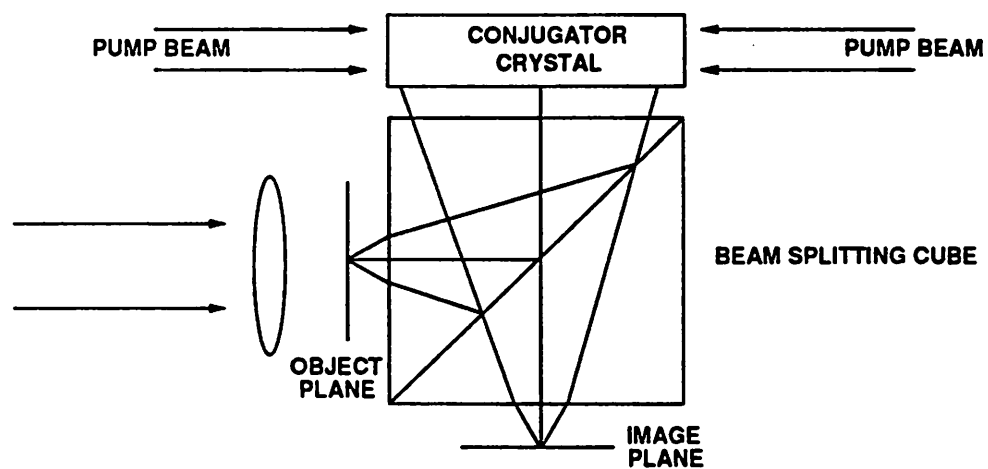
Figure 2.13 Four-wave mixing wave-front conjugation high-resolution imaging apparatus.

CHAPTER 3

THE PROPERTIES AND REQUIREMENTS

OF FOCUSED-IMAGE LENS-HOLOGRAMS

Any hologram in which the image of the object or the object itself is located near the hologram recording plane is defined as a focused-image hologram. Such holograms have several interesting and uncommon properties. In this chapter, a brief discussion is given on the salient properties and requirements of focused-image holograms. The chapter begins with a brief explanation of the holographic recording and playback process and then proceeds to describe the properties of focused-image holograms and their associated requirements for maximum image fidelity with regard to the geometry of the system, holographic recording media, and illumination source coherence.

3.1 WAVEFRONT RECONSTRUCTION PROCESS

As previously noted in Chapter 2, holographic imaging is a two-step process. The first step is to record the amplitude and phase information of an object wavefront with the use of a reference beam and the second and final step is to construct

the image of the object from the recording (hologram) with the use of a reconstruction beam.

3.1.1 RECORDING AMPLITUDE AND PHASE INFORMATION

Consider a coherent monochromatic wave with a complex amplitude travelling in space. If the distance from the source is much larger than the area of interest we can define a wave-front $\Psi = A(x,y)e^{[i\,\phi(x,y)]}$ at a particular plane in space where $A(x,y)$ is real function describing the amplitude of the wave-front and $\phi(x,y)$ describes the phase of the wave-front. Figure 3.1 schematically illustrates an off-axis holographic recording arrangement. The reference beam wave-front amplitude at the recording media plane can be written as $\Psi_{ref} = A_{ref}(x,y)e^{[i\phi_{ref}(x,y)]}$. The object beam wave-front at the recording plane can be written as $\Psi_{obj} = A_{obj}(x,y)e^{[i\phi_{obj}(x,y)]}$. The total wave-front at the recording plane is Ψ_{total} where $\Psi_{total} = \Psi_{ref} + \Psi_{obj}$. The intensity at the recording plane Γ, defined as $|\Psi_{total}|^2$, can be written as

$$\Gamma = |\Psi_{total}|^2 = |\Psi_{ref} + \Psi_{obj}|^2 = |\Psi_{ref}|^2 + |\Psi_{obj}|^2 + \Psi_{ref}\Psi_{obj}^* + \Psi_{ref}^*\Psi_{obj} \qquad 3.1$$

where Ψ^* is the complex conjugate of Ψ[3.1,2]. The first two terms of the expression only depend on the intensities of the two wave-fronts and not on their associated phases. The third and fourth terms depend on the relative phases of each of the wave-fronts as well as their associated amplitude. Thus, the amplitude and phase information of Ψ_{obj} is completely present in the total intensity at the recording plane.

It is assumed that a photographic plate has a linear mapping of intensity during exposure into amplitude transmittance after development. An additional

assumption is that the variations of exposure remain in the linear region of the exposure-transmittance regime of the recording media. Also, it is assumed that the resolution of the recording media extends to sufficiently high spatial frequencies to record all the spatial frequencies. Finally, we assume that the wave-front intensity $A(x,y)$ of the reference beam, Ψ_{ref}, is uniform across the recording surface. Thus, the transmittance of the photographic plate after exposure is

$$T_{trans} = T_{bkgd} + \beta\left\{\Psi_{ref}\Psi_{obj}^{*} + \Psi_{ref}^{*}\Psi_{obj}\right\} \qquad 3.2$$

where $T_{bkgd} = \beta\left\{\left|\Psi_{ref}\right|^{2} + \left|\Psi_{obj}\right|^{2}\right\}$ is the background transmittance level and β is the proportionality constant of the exposure-transmittance relation for the recording media[3.1].

3.1.2 RECONSTRUCTING THE IMAGE

Suppose the developed transparency (the hologram) is illuminated with a spatially and temporally coherent construction beam Ψ_{con} that propagates in the same direction as the reference beam. The light transmitted by the transparency is

$$\Psi_{trans} = \Psi_{con}T_{trans} = \Psi_{con}T_{bkgd} + \beta\left\{\Psi_{con}\Psi_{ref}\Psi_{obj}^{*} + \Psi_{con}\Psi_{ref}^{*}\Psi_{obj}\right\} . \qquad 3.3$$

If Ψ_{con} is an exact duplicate of the original reference wave-front Ψ_{ref} (i.e. $\Psi_{con} = \Psi_{ref}$), the transmitted wave-front becomes

$$\Psi_{trans} = \Psi_{ref}T_{bkgd} + \beta\left\{\Psi_{ref}^{2}\Psi_{obj}^{*} + \left|\Psi_{ref}\right|^{2}\Psi_{obj}\right\} . \qquad 3.4$$

Recalling our initial assumption that $\Psi_{ref} = e^{[i\phi_{ref}(x,y)]}$† over the exposure area and

---

† The wave-front amplitude is normalized to one.

thus $|\Psi_{ref}|^2 = 1$ over the exposure area, the last term in equation 3.4 is an exact duplicate of the original wave-front except for a simple multiplicative constant β as seen in equation 3.5.

$$\Psi_{trans} = \Psi_{ref}T_{bkgd} + \beta\left\{\Psi_{ref}^2\Psi_{obj}^* + \Psi_{obj}\right\}. \qquad 3.5$$

This step is figuratively illustrated in figure 3.2.

In a similar fashion, if Ψ_{con} is chosen as the conjugate wave-front of the reference wave-front† (i.e. $\Psi_{con} = \Psi_{ref}^*$) the third term in equation 3.3 of the constructed wave-front becomes $\beta\left\{\Psi_{obj}^*\right\}$ which is proportional to the conjugate of the original object wave-front as illustrated in figure 3.3[3.3].

Note, there are additional field components described in equation 3.3, each of which can be regarded as additional noise sources (unwanted interference). If a noiseless duplicate of Ψ_{obj} is required, some method of separating each of the various components is required.

3.1.3 IMAGING THROUGH ABERRATING MEDIA

Imaging through aberrating media (phase-distorting only) is accomplished using the conjugate wave-front generation technique[3.4]. This method consists of passing an object-beam bearing wave-front through a phase-distorting media, recording the distorted wave-front holographically, and then generating the conjugate wave-front which then passes through the phase-distorting media in the

---

† One wave-front is conjugate to another wave-front when in every plane its complex amplitude is the complex conjugate of the other and all its rays are directed anti-parallel to the others.

opposite direction. The second pass undoes the phase aberrations introduced in the first pass. Figures 3.4 and 3.5 schematically illustrates this process. The process relies on the fact that a hologram has the ability to store not only the amplitude but also the phase information of the aberrated object wave-front.

If the object wave-front impinging on the aberrating media is represented by $\Psi_{obj-aberr}$ and the amplitude and phase transmittance of the aberrating media is represented by $e^{[iW_{aberr}(x,y)]}$, the wave-front exiting the aberrating media is written as $\Psi_{obj-aberr}e^{[iW_{aberr}(x,y)]}$. This wave-front is then recorded using an unaberrated reference beam to form a hologram. This hologram when illuminated with a construction beam wave-front that is conjugate to the reference beam wave-front produces the complex conjugate of the distorted object beam wave-front, $\Psi^*_{obj-aberr-hol}$. The wave-front arriving at the phase distorting media is $\Psi^*_{obj-aberr}e^{[-iW_{aberr}(x,y)]}$. The wave-front exiting the aberrating media is

$$\Psi^*_{obj-aberr}e^{[-iW_{aberr}(x,y)]}e^{[iW_{aberr}(x,y)]} = \Psi^*_{obj-aberr} \ . \qquad 3.6$$

Thus, the wave-front exiting the aberrating media is the complex conjugate† of the wavefront that originally passed through the aberrating media.

3.2 OFF-AXIS FOCUSED-IMAGE HOLOGRAMS

Historically, off-axis holography was introduced to separate the two images, real and virtual created from illuminating a hologram, from each other and from the construction beam itself. This advance naturally lead to the creation of several different types of holograms with a wide variety of properties. In the next section,

---

† The wave-front is now travelling in the opposite direction with the opposite curvature.

we briefly discuss the features of focused-image holograms and then proceed to explore the geometrical, recording material, and illumination coherence requirements to construct a focused-image hologram.

3.2.1 PROPERTIES OF FOCUSED-IMAGE HOLOGRAMS

The main trait of a focused-image hologram is that the information about the object on the hologram is localized. Each point on the object gives rise to small region on the hologram so that the image carried by the reference wave is produced in the hologram plane or very close to it. This local nature of information reduces the stringency of the image construction requirements such as the linearity of the recording material, monochromaticity of the construction illumination, and the construction beam illumination angle and wave-front error[3.5-8].

Usually as a result of non-linear recording of an object, a noisy, diffused scattered background appears together with additional higher-order diffracted images around all the images and anomalous images appear between adjacent diffraction orders. This noise appears as a result of cross-modulation of different spatial frequencies of object waves leading to the recording of additional spatial carriers. In focused-image holograms, there is an absence of noise in the constructed image[3.7,9]. This absence of noise even though the object image may have been recorded with some non-linearity results from the storage mechanisms in this hologram since the information about each point is stored as a small area on the hologram and the effects of cross modulation between image points caused by non-linearities in the recording are limited in their spatial extents to the diameter of the hologram that constructs the image point.

If the hologram is in the exact position in the optical optical system as when it was recorded, and it is illuminated with the conjugate to the reference beam used to record it, then the real image constructed is an exact duplicate of the *original* object image. However, in any other circumstances, the constructed image may exhibit wave-front aberrations. Hologram wave-front aberrations[†] are classified in the exact manner as normal lens aberrations. The total wave-front error can be expressed as a summation of the third order aberrations and is written as

$$\Delta\Phi_3 = \frac{2\pi}{\lambda_{con}} \left[- 1/8\, \rho^4\, S \right.$$

$$+ 1/2\, \rho^3\, (C_x \cos\theta + C_y \sin\theta)$$

$$- 1/2\, \rho^2\, (A_x \cos^2\theta + A_y \sin^2\theta + 2A_x A_y \cos\theta\sin\theta)$$

$$- 1/4\, \rho^2\, F$$

$$\left. + 1/2\, \rho\, (D_x \cos\theta + D_y \sin\theta) \right]$$

3.7

where $\Delta\Phi_3$ is the total wave-front error in wavelengths, S is the coefficient for spherical aberration, C_x and C_y are the coefficients for coma, A_x and A_y are the coefficients for astigmatism, F is the coefficient for field curvature and D_x and D_y are the coefficients for distortion and ρ is the radius of the circular annulus about the center of the hologram[3.10]. These coefficients depend solely on the geometry of the optical system and the hologram construction and playback illumination wavelength[‡]. If the hologram is illuminated with the conjugate beam in the same

† Wave-front aberrations created only due to incorrect illumination of the hologram and not due to the errors in retracing back-through the imaging lens (lensless case).

‡ Assuming the hologram does not experience any magnification.

manner as it was created, all the aberration coefficients are zero, and thus the wave-front error is exactly zero[3.11]. Now, if any differences in the construction geometry or construction wavelength relative to the reference wavelength occur, the aberrations scale with the area of image point on the hologram for a constant numerical aperture[3.10-14]. Thus, as the hologram approaches that of a pure focused-image hologram, the wave-front aberrations produced by any non-idealities in the construction process approach zero.

3.2.2 SYSTEM GEOMETRY FOR FOCUSED-IMAGE HOLOGRAMS

There are several optical system configurations to construct focus-image holograms. Using a lens to form an image onto the recording material is one method to form a focused-image hologram, and special precautions must be taken to insure that the geometry of the system is consistent with the requirements for microlithography. In this section, specific restrictions on the reference beam offset angle and magnification of the image at the hologram plane are developed.

3.2.2.1 MINIMUM REFERENCE BEAM ANGLE

Consider the optical system shown in figure 3.6 which is an optical system to produce focused-image holograms. In this set-up, a reference beam which is derived from the same coherent source used to illuminate the object is used during the recording process at angle θ_{ref} to the object beam. This reference beam is a collimated beam with uniform intensity.

The complex wave amplitude due to the object at the hologram recording plane is written as

$$\Psi_{obj} = A_{obj}(x,y)e^{[i\phi(x,y)]} \qquad 3.8$$

which also includes the effects of the imaging lens. The reference beam for this specific case is written as

$$\Psi_{ref} = A_{ref}e^{(i2\pi\xi_{ref}x)} \qquad 3.9$$

where $\xi_{ref} = \sin(\theta_{ref})/\lambda$ where θ_{ref} is the offset angle.

The resultant intensity at the recording plane is written as

$$\Gamma = A_{ref}^2 + |A(x,y)|^2 + A_{ref}A_{obj}(x,y)\left[e^{[i\phi(x,y)]}e^{(-i2\pi\xi_{ref})} + e^{[-i\phi(x,y)]}e^{(i2\pi\xi_{ref})}\right] \qquad 3.10$$

which is similar to equation 3.2. If the amplitude transmittance for the recording media is linearly related to the intensity, the amplitude transmittance is

$$T_{trans} = \beta A_{ref}^2 + \beta|A(x,y)|^2 + \beta A_{ref}A_{obj}(x,y)\left[e^{[i\phi(x,y)]}e^{(-i2\pi\xi_{ref})} + e^{[-i\phi(x,y)]}e^{(i2\pi\xi_{ref})}\right] \qquad 3.11$$

Using the conjugate wave-front, $\Psi_{con} = \Psi_{ref}^* = A_{ref}e^{(-i2\psi\xi_{ref}x)}$, as the illumination beam, the complex amplitude of the transmitted wave-front from the hologram is

$$\Psi_{con-obj} = \beta A_{ref}^2 e^{(-2i\pi\xi_{ref}x)} + \beta|A_{obj}(x,y)|^2 e^{(-2i\pi\xi_{ref}x)} + \qquad 3.12$$

$$\beta A_{ref}A_{obj}(x,y)\left[e^{[i\phi(x,y)]}e^{(-i4\pi\xi_{ref})} + e^{[-i\phi(x,y)]}\right].$$

The first term in equation 3.12 is the attenuated reference beam which is a plane wave transmitted through the hologram. This beam is surrounded by a "halo" due to the second term which is spatially varying. Similarly, the fourth term is identical to the original object wave except for a proportionality constant and generates a real image of the object at an angle θ_{ref} with the directly transmitted beam. The third term gives rise to the virtual image plus an exponential factor which indicates

that the virtual is formed at an angle $2\theta_{ref}$ with the reference beam.

Even though two images are constructed with this arrangement†, they are angularly separated from the directly transmitted beam, the halo, and each other and if the offset angle θ_{ref} is made large enough, i.e. no overlap will occur.

The minimum offset angle θ_{ref} required to ensure that each of the images are observed without any interference from the twin images as well as from the directly transmitted beam and the halo is determined to a great extent by the spatial frequency of the object wave-front at the hologram recording plane.

Expressing the object, reference, and construction wave-fronts in terms of their Fourier transforms in spatial frequency domain at the hologram plane we can re-write equation 3.12 as the following manner

$$\Psi_{con-obj}(\xi,\zeta) = \beta\, A_{ref}^2 \delta(-\xi_{ref}) + \beta \left[\Psi_{obj}(\xi,\zeta) \ominus \Psi_{obj}^*(\xi,\zeta)\right] \ominus \delta(-\xi_{ref}) + \qquad 3.13$$

$$\beta A_{ref}\Psi_{obj}(\xi-2\xi_{ref},\zeta) + \beta A_{ref}\Psi_{obj}^*(\xi,\zeta)$$

where $\Psi(\xi,\zeta)$ is the Fourier Transform of $\Psi(x,y)$, $\delta(\xi)$ is the Dirac delta function, and $\ominus$ is the convolution operator[3.15].

As seen from figure 3.7 which shows these spectra schematically, the fourth term is the object beam spectrum multiplied by a constant and centered at the origin of the spatial frequency plane. The first term corresponds to the carrier frequency and is located at ($-\xi_{ref}$, 0). The second term is centered on this δ function and is the auto-correlation of $\Psi(\xi,\zeta)$ which has twice the frequency extent of the object wave-front spectrum. The third term is similar to the last term but is displaced to a center frequency of $(-2\xi_{ref},0)$. Thus, the twin images will not overlap

---

† Assuming a thin absorptive hologram.

the first two terms if the offset angle of the reference beam is chosen such that its spatial frequency is

$$\xi_{ref} \geq 3\xi_{obj} \qquad 3.14$$

where ξ_{ref} is the largest frequency in the spatial frequency spectrum of the object. Translating to angles, this requires that the reference beam angle must be at least three times the angular spectrum of the object.

3.2.2.2 MAGNIFICATION AT THE IMAGE PLANE

From the previous section, the minimum construction beam angle, $\theta_{ref-min}$, required to insure that the constructed image can be observed without any interference from its twin image as well as from the directly transmitted beam and the surrounding halo of scattered light can be written in the following manner from equation 3.14 as

$$\theta_{ref-min} = \sin^{-1} (3 * NA_{holo}) \qquad 3.15$$

where $\theta_{ref-min}$ is the minimum construction angle and NA_{holo} is the numerical aperture of the optical system as seen from the hologram plane. Specifically, the use of a lens operating at a fixed magnification between the object and image plane to focus the image of the object onto the holographic recording material permits the use of a larger numerical aperture at the object plane. The numerical aperture as seen by the high-resolution recording material is

$$NA_{holo} = \frac{NA_{obj}}{M_{mag}} \qquad 3.16$$

where NA_{holo} is the numerical aperture at the hologram recording plane NA_{obj} is the numerical aperture at the object plane, and M_{mag} magnification of the object at the hologram plane. Now, re-formatting the $\theta_{ref-min}$ using equation 3.12 we obtain

$$\theta_{ref-min} = \sin^{-1} \left(\frac{3 * NA_{obj}}{M_{mag}} \right).$$ 3.17

Also, the maximum spatial frequency which is necessary to be recorded is dependent on the numerical aperture at the object as well as the reference offset angle and the dependence is

$$\theta_{sfm} = \sin^{-1} \left(\frac{4 * NA_{obj}}{M_{mag}} \right).$$ 3.18

The physical size of the hologram is also dependent of the system magnification and can be written as

$$Holo_{size} = M_{mag}^2 l_{ifs}$$ 3.19

where l_{ims} is the image field size. From equations 3.17, 3.18, and 3.19 several tradeoffs are formed. As the magnification at the hologram plane is increased, the hologram size becomes prohibitively large because the total power needed to expose the holographic recording material increases as the square of the magnification. In addition, as the physical size of the recording material substrate is increased, it becomes awkward to physically handle. Thus, for practical image field sizes of 20-30mm diameter, a magnification of 4~5 is attractive in terms of balancing the hologram size against spatial frequency and energy requirements.

3.2.3 HOLOGRAPHIC RECORDING MATERIAL REQUIREMENTS

The formation of any hologram involves the exposure of light-sensitive materials to the holographic interference fringes resulting from the object and reference beam. The physical changes in the recording material after exposure must affect the construction beam to form an image. This means that the hologram alters either the amplitude of phase of this beam. In addition, the information carrying structure can be either two or three dimensional. In all, there are four basic types of holograms: the thick (volume) and thin versions of amplitude and phase holograms. In this section, the general characteristics of holographic recording media are discussed along with their associated requirements for microlithography. In the 3.2.3.1, the minimum spatial frequency of the recording material is defined. In the next section, the diffraction efficiency of various hologram types is discussed and finally, a brief discussion of the noise sources from holographic recording media is presented.

3.2.3.1 MINIMUM SPATIAL FREQUENCY RESPONSE

As noted from section 3.2.2.1, the maximum spatial frequency needed to be recorded for an off-axis focused image hologram for a faithful construction of the image is

$$\xi_{max} = 4 \, \xi_{object-lens-max} \qquad 3.20$$

where $\xi_{object-lens-max}$ is the maximum spatial frequency the lens passes. Thus, to form an undistorted image of the object the recording media must have the ability to record the ξ_{max} with no change in visibility compared to the lower spatial frequencies.

3.2.3.2 DIFFRACTION EFFICIENCY OF HOLOGRAMS

The relative success of a lithography method will depend on requirements for device performance, cost, and volume. From a volume viewpoint, the throughput of a lithography system is an important factor for establishing its viability. A key throughput parameter is the intensity at the image plane. To prevent the exposure time at the image plane from being the limiting factor for throughput, the hologram should possess the largest diffraction efficiency possible. Since there are several possible types of holograms, a brief discussion concerning their diffraction efficiency is presented.

Any hologram in which the thickness of the hologram recording material is small compared with the average spacing of the interference fringes can be classified as a "thin"† hologram and can be characterized by the following equation

$$T(x,y) = |t(x,y)| e^{[i\Phi(x,y)]}$$ 3.21

where $|t(x,y)|$ is the amplitude variation and $e^{[i\Phi(x,y)]}$ is the phase variation over the hologram. In an amplitude hologram, the phase variation is constant and the transmittance of the hologram varies. To calculate the maximum diffraction efficiency, we can consider a grating formed by two collimated plane waves. Assuming that the amplitude transmittance is linearly related to the intensity of the interference pattern, the amplitude transmittance of the grating can be written as

$$T(x) = |t(x)| = t_0 + t_1 \cos(\xi x)$$ 3.22

___

† The distinction between "thin" and "thick" gratings may be described in terms of the factor Q[3.16] given by

$$Q = 2\pi\lambda d/n_0 L^2 \cos(\theta)$$

where λ is the free-space wavelength if the incident plane wave, d is the thickness of the grating, n_0 is the average index, L is the grating period and θ is the angle of incidence inside the recording media. For Q less that 1, the grating is in thin regime and for Q > 10, the grating is in thick regime.

where t_0 is the average transmittance of the grating, t_1 is the transmittance amplitude of the spatial grating, and $\xi = 2\pi/\Lambda$ where Λ is the fringe spacing.

From equation 3.22, the diffracted beam amplitude is maximum when the transmittance has the following values

$$T(x) = |t(x)| = 1/2 + 1/2 \cos(\xi x) \qquad 3.23$$

which can be also written as

$$T(x) = |t(x)| = 1/2 + 1/4 \ e^{(i\xi x)} + 1/4 \ e^{(-i\xi x)}. \qquad 3.24$$

The diffracted electric field amplitude is directly proportional to the the transmittance and the intensity is proportional to the square of the electric field amplitude. Thus, the maximum theoretical diffraction efficiency† in the first order is $(1/4)^2 = 6.25\%$.

For a loss-less phase-grating where the transmittance can be written as

$$T(x,y) = e^{[i\Phi(x)]}, \qquad 3.25$$

and the phase shift is linearly proportional to the intensity in the interference pattern such that

$$\Phi(x) = \Phi_0 + \Phi_1 \cos(\xi x). \qquad 3.26$$

Thus, the transmittance of the hologram can be written as

$$T(x) = e^{[i\Phi_0]} e^{[i\Phi_1 \cos\xi x]}. \qquad 3.27$$

This can be expanded into a Fourier series using Bessel function expansion to give

$$T(x) = e^{[i\Phi_0]} \sum i^n J_n(\Phi_1) e^{[in\xi x]} \qquad 3.28$$

When the hologram is illuminated, $J_0(\Phi_1)$ is the undiffracted wave and the term

---

† Diffraction efficiency is defined as the ratio of power diffracted into the first order to the power in the illumination beam.

proportional to $J_1(\phi_1)$ is the grating order which diffracts to form the image. The other orders represent sinusoidal gratings of multiple spatial frequencies. The phase grating diffracts an infinite number of orders and the maximum diffracted efficiency in the first order $(J_1^2(\Phi_1))$ is 33%.

Comparing the properties of "thin" phase-only holograms to those of "thin" absorptive holograms, phase-only holograms can diffract much more light into the first order, but they also generate higher order diffractions which do not contribute to the constructed image. The higher order terms add optical noise to the image.

In the real world, holographic recording materials are not usually linear over the full range of exposure to make the transmittance vary between 0-1. Thus, the maximum diffraction efficiency cannot be achieved if it is also necessary to construct a wave-front proportional to the original wave-front.

Volume absorption holograms construct with maximum efficiency only if the constructing wavelength is incident from a direction that satisfies the Bragg condition. A volume amplitude transmission type hologram reaches a peak efficiency of 3.7%. In addition[3.17], it requires a precise selection of the thickness-absorption coefficient product because the efficiency drops after exceeding a particular value of this parameter.

Volume phase holograms, just as volume amplitude holograms, construct with maximum efficiency only if the constructing wavelength is incident from a direction that satisfies the Bragg condition. It also requires a precise selection of the thickness-index change product because the efficiency drops after exceeding a particular value of this parameter[3.17].

Comparing the properties of "volume" phase-only holograms to those of "volume" absorptive holograms, phase-only holograms can diffract much more light

into the first order. Plus, volume phase holograms on the whole diffract light only into the first order. They do not generate higher order diffractions terms as do "thin" phase holograms. Thus, no additional light is introduced into the image.

3.2.3.3 HOLOGRAM RECORDING MEDIA NOISE

Optical noise emanating from the hologram is unwanted light either diffracted or scattered in the same direction as the constructing image. This noise can be attributed to the following:

1) Random scattering of the object and reference beam during the construction of the hologram

2) Random scattering of the constructed object beam and construction beam due to the granularity of the holographic recording material after development

3) Inhomogeneities and surface deformations of the holographic recording material before and after development.

4) Non-linear recording and playback of the object wave-front

Optical noise due to source 1 can be eliminated with careful handling and preparation of the system optics. Source 2 is a fundamental property of the recording material and cannot be altered. Sources 3 and 4 are controllable to a certain extent. Source 3 can be eliminated by using holographic recording materials do not change their physical shape after exposure and development such as photopolymers[3.18]. Increasing the reference to object beam ratio can decrease the non-linearity in the recording of a hologram but only at the expense of the playback diffraction efficiency. Intrinsic non-linearity is a fundamental response which is present in almost all phase holograms and again can be reduced by increasing the

reference to object beam ratio. These non-linearities cause several noise effects in the images produced from holograms (such as harmonic and intermodulation distortion noise).

The origins of intermodulation noise can be determined by including higher order terms to the exposure-transmittance relationship. Consider the interference of an object wave-front Ψ_{obj} and reference wave-front Ψ_{ref} to form an amplitude hologram for simplicity. If the amplitude transmittance is linearly related to the intensity of the interference pattern, the amplitude transmittance of the grating can be written as

$$T_{trans} = \beta \left\{ \Psi_{ref}\Psi_{ref}^{*} + \Psi_{obj}\Psi_{obj}^{*} + \Psi_{ref}\Psi_{obj}^{*} + \Psi_{ref}^{*}\Psi_{obj} \right\} \qquad 3.29$$

where β is the proportionality constant of the exposure-transmittance relation for the recording media. Now assume that the amplitude transmittance is not linearly related to the intensity of the interference pattern but can be described using a polynomial series. The amplitude transmittance can be written as

$$T_{trans} = \beta_1\Gamma + \beta_2\Gamma^2 + \beta_3\Gamma^3 \ldots \ldots \qquad 3.30$$

where β_1, β_2, and β_3 are the polynomial expansion coefficients for the recording material and Γ is the intensity. Equation can be expanded similarly to equation 3.2 to

$$T_{trans} = \beta_1 \left\{ \Psi_{ref}\Psi_{ref}^{*} + \Psi_{obj}\Psi_{obj}^{*} + \Psi_{ref}\Psi_{obj}^{*} + \Psi_{ref}^{*}\Psi_{obj} \right\} + \qquad 3.31$$

$$\beta_2 \left\{ (\Psi_{obj}\Psi_{obj}^{*})^2 + (\Psi_{ref}\Psi_{ref}^{*})^2 + 4\Psi_{obj}\Psi_{obj}^{*}\Psi_{ref}\Psi_{ref}^{*} + \right.$$

$$2\Psi_{obj}\Psi_{ref}(\Psi_{obj}^{*})^2 + \Psi_{obj}^{*}\Psi_{ref}^{*}\Psi_{obj}^{2} + 2\Psi_{obj}^{*}\Psi_{ref}^{*}\Psi_{ref}^{2} +$$

$$2\Psi_{obj}\Psi_{ref}(\Psi_{ref}^{*})^{2} + \Psi_{obj}^{2}(\Psi_{ref}^{*})^{2} + \Psi_{ref}^{2}(\Psi_{obj}^{*})^{2} \Bigg\} .$$

If, for example the higher orders greater than two are neglected, then when the hologram is illuminated by a reference wave-front that is assumed to be a plane wave-front with unit amplitude that is conjugate to the reference wave, the complex amplitude of the transmitted wave-front is

$$\Psi_{obj-con} = \beta_{1}\Bigg\{ \Psi_{ref}^{*} + \Psi_{obj}\Psi_{obj}^{*}\Psi_{ref}^{*} + \Psi_{obj}^{*} + (\Psi_{ref}^{*})^{2}\Psi_{obj} \Bigg\} + \qquad\qquad 3.32$$

$$\beta_{2}\Bigg\{ (\Psi_{obj}\Psi_{obj}^{*})^{2}\Psi_{ref}^{*} + \Psi_{ref}^{*} + 4\Psi_{obj}\Psi_{obj}^{*}\Psi_{ref}^{*} +$$

$$2\Psi_{obj}(\Psi_{obj}^{*})^{2} + \Psi_{obj}^{*}\Psi_{obj}^{2}(\Psi_{ref}^{*})^{2} + 2\Psi_{obj}^{*} +$$

$$2\Psi_{obj}(\Psi_{ref}^{*})^{2} + \Psi_{obj}^{2}(\Psi_{ref}^{*})^{3} + (\Psi_{obj}^{*})^{2}\Psi_{ref} \Bigg\} .$$

The immediate result of the non-linearity is the production of additional diffracted light in the first and second diffracted orders.

The first three terms in the second order expansion represent wave-fronts that appear on the same axis as the construction beam. The last two terms describe wave-fronts that appear as second order diffracted wave-fronts. Note that not only is the offset-angle is doubled, but also the phase of the wave-fronts is doubled. For example, the $\Psi_{obj}^{2}(\Psi_{ref}^{*})^{3}$ term appears at twice the angle as the linear $\Psi_{obj}\Psi_{ref}^{*}$ and it has its amplitude distribution squared along with its phase variation doubled.

The sixth and seventh terms represent wave-fronts propagating at the same off-set angle as the first order wave-front and they produces noise in the first order

images only if Ψ_{ref} does not have a uniform amplitude.

The fourth and fifth terms always add noise to the first order images. The degree to which these terms degrade the image depends on the ratio of β_2 / β_1. Further expansion of the higher order terms will also show that they too contribute noise terms to the first order images.

The analysis presented is valid for thin absorption holograms exhibiting material non-linearities. A similar analysis can be applied to thin phase holograms. Thin phase holograms suffer from intrinsic non-linearity as seen from equation 3.28. Thus, both thin amplitude and phase holograms can generate significant noise in the constructed image. The non-linearity can be reduced by increasing the intensity ratio between the reference beam and the object beam for both amplitude and phase holograms, but only at the expense of decreasing image intensity[3.3].

Volume amplitude and phase holograms do not fall under this analysis. Volume holograms construct images only if the construction alignment satisfies the Bragg relations[3.17]. Intermodulation noise is suppressed in volume holograms because the non-linearity produces diffracted components which do not satisfy the Bragg relations. The components of the hologram transmittance propagating away from the Bragg angle are attenuated by the angular selectivity of the recording media. Thus, with sufficiently thick media, a noise free image should be obtainable for any diffraction efficiency and object to reference beam ratio[3.19,20].

3.2.4 RECORDING AND ILLUMINATION SOURCE REQUIREMENTS

The spatial and temporal coherence requirements of the illumination beams for focused-image holograms differ in many respects from the more common far-field holograms both in recording the hologram and reconstructing the image of the

object. These requirements can be estimated by modelling the imaging lens as an ideal lens with a non-zero separation between the lens' image plane and the hologram construction plane. The model provides a first order approach to discern the tradeoff between the image quality and the source size and bandwidth. A more accurate model is presented in Chapter 5.

In this section, we will discuss the temporal coherence requirements of the illumination for recording and playback of the object image as well as the spatial coherence requirements of the source. Also, a brief discussion on polarization state of the reference beam and object wave-front is presented.

3.2.4.1A TEMPORAL COHERENCE FOR RECORDING A HOLOGRAM

The minimum temporal coherence for maximum fringe visibility needed to form a focused-image hologram can be directly related to the hologram formation geometry. Consider the interference of two plane waves as shown in figure 3.8. The object beam is perpendicular to the hologram and the reference beam is at a angle θ_{ref} with it. For the worst case scenario, setting the reference wave-front ray and the object wave-front ray paths equal for the reference wave-front ray at the edge of the hologram in which case the object to reference beam path distance difference is

$$l = h \sin(\theta_{ref}) \qquad 3.33$$

where h is the length of the hologram and θ_{ref} is the offset angle. Thus, for a plane wave-front as the object beam, the temporal coherence length must be greater than $h \sin(\theta_{ref})$.

Now consider the added path length due to imaging lens. For an ideal lens which images the object plane onto the hologram recording plane, no extra path length is added†. However, if the lens introduces wave-front aberrations or is not used to focus the image onto the recording plane, path length differences will occur. These differences tend to be very small compared to the size of the hologram and are rarely significant.

3.2.4.1B TEMPORAL COHERENCE FOR RECONSTRUCTING THE IMAGE

To obtain the highest achievable resolution in the constructed image from a focused-image hologram, the illumination must be temporally coherent over the image point spread area‡ (IPSA) of the imaging lens at the hologram construction plane. This requirement limits the bandwidth of the illumination.

For an off-axis focused-image hologram with an ideal imaging lens, the temporal coherence length must be larger than than the diameter of the IPSA. Thus, the illumination bandwidth, $\Delta\lambda$, must satisfy the following condition :

$$\Delta\lambda < \frac{\lambda^2}{2 \cdot D_{IPSA}}$$

3.34

where D_{IPSA} is the effective diameter of the image point spread area and λ is the nominal illumination wavelength[3.3].

---

† For an ideal lens, each point in the object plane is the same optical distance to its corresponding image point no matter which path the imaging forming light ray travels.

‡ IPSA is the size of the image point in the image plane for a pin-hole in the object plane.

The temporal coherence is further restricted because the illumination bandwidth also determines the achievable angular image resolution. For an off-axis focused-image hologram created with a dispersion free imaging lens, the geometric traverse image blur resulting from a finite bandwidth, $\Delta\lambda$ from $\frac{\Delta\lambda}{2} + \lambda - \frac{\Delta\lambda}{2}$ is

$$\Delta B_t = \frac{D_{IP-H}}{M_{mag}} \cdot \Delta\lambda \cdot \frac{d\theta_r}{d\lambda} \qquad 3.35$$

where D_{IP-H} is the separation distance between the lens' image plane and the holo-gram construction plane and $\frac{d\theta_r}{d\lambda}$ is the angular the dispersion of the holo-gram[3.21]. The angular dispersion of the hologram assuming the hologram is a simple grating can be written as

$$\frac{d\theta_r}{d\lambda} = \frac{\tan(\theta_r)}{\lambda_{cons}} \qquad 3.36$$

where λ_{cons} is the hologram construction wavelength[3.22].

The diameter of the IPSA is related to the separation distance between the lens' image plane and the hologram construction plane in the following manner:

$$D_{IPSA} = 2 \cdot NA_{holo} \cdot D_{IP-H} \qquad 3.37$$

where D_{IP-H} is the separation distance between the lens' image plane and the holo-gram construction plane.

Thus, the geometric traverse image blur, ΔB_t, due to a finite illumination bandwidth is

$$\Delta B_t = \frac{D_{IPSA}}{2 \cdot M_{mag} \, NA_{Holo}} \cdot \tan(\theta_r) \cdot \frac{\Delta\lambda}{\lambda_{cons}} \qquad 3.38$$

The geometric longitudinal blur, ΔB_l, due to finite illumination bandwidth is[3.21]

$$\Delta B_l = \frac{D_{IPSA}}{2 * M_{mag}^2 \, NA_{holo}} * \frac{\Delta \lambda}{\lambda_{cons}}. \qquad 3.39$$

If the maximum geometric traverse blur and geometric longitudinal blur values are equal to the nominal construction wavelength λ, equations 3.38 and 3.39 are transformed into the following

$$\Delta \lambda < \frac{\lambda^2}{2^* D_{IPSA}} \frac{4 \, M_{mag} \, NA_{holo}}{\tan(\theta_r)} \qquad 3.40$$

$$\Delta \lambda < \frac{\lambda^2}{2^* D_{IPSA}} \, 4 \, M_{mag}^2 \, NA_{holo} \qquad 3.41$$

Comparing equation 3.34 with equations 3.40 and 3.41 indicates that the coherence length restriction is determined by the requirement to be temporally coherent over the lens' IPSA and not by the either the traverse or longitudinal geometric blur requirement. In addition, equation 3.34 also indicates that the coherence length required is inversely proportional to the to the lens' IPSA.

3.2.4.2A SPATIAL COHERENCE FOR RECORDING A HOLOGRAM

The minimum spatial coherence for fringe visibility needed to form a focused-image hologram is dependent on the recording geometry. Assuming that the reference and object beams originated from the same source and that the temporal coherence source length is much larger than the path differences to the recording

media, interference fringes are produced if both beams are spatially coherent† with each other. The limiting case occurs at the edge of the lens' image field at the hologram recording plane. Using the von Cittert-Zernicke theorem, we can estimate the effective source size such that the illumination is spatially coherent between the reference wave-front and object wavefront at the hologram plane. Assuming a complex degree of spatial coherence value of $1/\sqrt{2}$, the effective source radius must satisfy the following condition:

$$r_{source} < \frac{\lambda * f_{cl}}{2 * (M_{mag}-1)D_{IPSA}}$$

3.42

where f_{cl} is the focal length of the lens used to collimate the reference beam[3.3]. However, the angular resolution of the image is limited by the angular resolution of the reference and construction wave-fronts. In fact, the constructed image can be represented as the weighted cross correlation of the reference and construction sources convolved with the object wave-front[3.23]. Assuming the construction source is not the limiting factor, the geometric image blur, ΔB_r, due to a finite reference beam source size can be written as[3.13]

$$\Delta B_r = 2 * \frac{r_{source}}{f_{cl}} * \frac{D_{IP-H}}{M_{mag}}$$

3.43

This equation can be written to eliminate D_{IP-H} using equation 3.37 and becomes

$$\Delta B_r = \frac{r_{source}}{f_{cl}} * \frac{D_{IPSA}}{M_{mag} NA_{holo}}$$

3.44

---

† Wave-fronts from two different areas on a beam interfere.

3.2.4.2B SPATIAL COHERENCE FOR RECONSTRUCTING THE IMAGE

To obtain the highest achievable resolution in the constructed image from a focused-image hologram, the illumination must be temporally and spatially coherent over the image point spread area (IPSA) of the imaging lens at the hologram construction plane. The spatial coherence requirement limits the effective source size.

Using the von Cittert-Zernicke theorem, we can estimate the maximum effective source size such that the illumination is spatially coherent over the lens' IPSA. Assuming a complex degree of spatial coherence value of $1/\sqrt{2}$, the effective source radius must satisfy the following condition:

$$r_{source} < \frac{\lambda \cdot f_{cl}}{2 \cdot D_{IPSA}}$$

3.45

where f_{cl} is the focal length of the lens used to collimate the re-construction illumination beam[3.13].

In addition to the effective source size requirements necessary to form a image, the spatial coherence is further restricted because the effective illumination source size also determines the achievable angular image resolution†.

Assuming the reference beam source is not the limiting factor, the geometric traverse image blur, ΔB_r, due to a finite source size can be written as[3.21]

$$\Delta B_r = 2 \cdot \frac{r_{source}}{f_{cl}} \cdot \frac{D_{IP-H}}{M_{mag}}$$

3.46

† As noted in the previous section, the angular resolution is limited by the angular resolution of the reference and construction wave-fronts. The constructed image can be represented as the weighted cross correlation of the reference and construction sources convolved with the object wave-front[3.23].

This equation can be written to eliminate D_{IP-H} using equation 3.37 and becomes

$$\Delta B_r = \frac{r_{source}}{f_{cl}} \cdot \frac{D_{IPSA}}{M_{mag} \, NA_{holo}}$$

<div align="right">3.47</div>

3.2.4.3 POLARIZATION EFFECTS

The maximum visibility of the interference fringes which form the basis of a hologram is obtained when the angle between the two interfering electric field vectors is zero. This condition is completely satisfied for two plane waves regardless of the angle between them when their electric field vectors polarized in the directions perpendicular to the plane formed by their propagation vectors. However, trans-illuminating a mask containing features on the order of the illumination wavelength will significantly change the polarization of the original illumination beam due to diffraction which results in a significant loss of visibility in the fringe formation.

Figure 3.9 schematically illustrates the polarization asymmetries for a focused-image holographic optical system. In this figure, the electric field vector of the illumination beam as well as the reference beam are polarized such that their polarization vectors are perpendicular to the plane which is parallel to the table top. As the object beam diffracts due to the features on the mask, the polarization of the electric field vectors are modified. In the X-Y plane, the diffracted light propagating in the along the "Y" axis is polarized with its electric field vector perpendicular to the table top. However, as figure 3.10 and 3.11 illustrates, the electric field vectors are not perpendicular to X-Z plane resulting in a loss of fringe visibility. The diffracted light propagating along the "X" axis is no longer polarized perpendicular

to the table top, but is at finite angle. This change in polarization results in a degradation in fringe visibility for information contained at at large diffracted angles. The interference fringe visibility is directly proportional to the cosine of the angle between the between the direction of polarization of the reference and object beams[3.3]. If the diffraction efficiency of the hologram is linear with the grating modulation, the maximum angle between the the direction of polarization of the reference and object beams is ten degrees for a variation of the grating modulation of less than 2%.

In order to alleviate the polarization problems, the the numerical aperture as seen from the hologram can be reduced due to the image magnification at the hologram plane. In addition, the reference beam can be brought in with a offset angle such that $\theta_y = \theta_x = \theta_{ref}$ where θ_y and θ_x are the angle the reference beam makes with the optic axis respectively. This offset angle now distributes the polarization error equally between the diffracted light in both the "X" and "Y" directions.

3.5 REFERENCES

[3.1] D. Gabor, "Microscopy by Reconstructed Wavefronts.," *Proceedings of the Royal Society A*, vol. 197, pp. 454-487, 1949.

[3.2] D. Gabor, "Microscopy by Reconstructed Wavefronts. II.," *Proceedings of the Physical Society*, vol. 64, pp. 449-469, 1951.

[3.3] R.J. Collier, C.B. Burckhardt, L.H. Lin, *Optical Holography*, Academic Press, New York, 1072.

[3.4] H. Kogelnik, "Holographic Image Projection through Inhomogeneous Media.," *Bell System Technical Journal Briefs*, vol. 44, pp. 2451-2455, December 1965.

[3.5] Karl A. Stetson, "Holography with Total Internally Reflected Light.," *Applied Physics Letters*, vol. 11, no. 7, pp. 225-226, October 1, 1967.

[3.6] Karl A. Stetson, "Improved Resolution and Signal-to-Noise in Total Reflection Holograms.," *Applied Physics Letters*, vol. 12, no. 11, pp. 362-364, June 1, 1968.

[3.7] G.B. Brandt, "Image Plane Holography," *Applied Optics*, vol. 8, no. 7, pp. 1421-1429, July 1969.

[3.8] L. Rosen, "Focused-Image Holography With Extended Sources," *Applied Physics Letters*, vol. 9, pp. 337-339, 1966.

[3.9] I.S. Klimenko and E.G. Matinyan, "Nonlinear Recording of Focused-Image Holograms," *Soviet Journal of Quantum Electronics*, vol. 4, no. 9, p. 1176, March 9, 1975.

[3.10] R.W. Meier, "Magnification and Third-Order Aberrations in Holography.," *Journal of the Optical Society of America*, vol. 55, pp. 987-992, 1965.

[3.11] J.A. Armstrong, "Fresnel Holograms: Their Imaging Properties and Aberrations.," *I.B.M. Journal of Research and Development*, vol. 9, no. 3, pp. 171-178, May 1965.

[3.12] J.N. Latta, "Computer-Based Analysis if Hologram Imagery and Aberrations. I. Hologram Types and Their Nonchromatic Aberrations.," *Applied Optics*, vol. 10, no. 3, pp. 599-608, March 1971.

[3.13] E.B. Champagne and N.G. Massey, "Resolution in Holography.," *Applied Optics*, vol. 8, no. 9, pp. 1879-1885, September 1969.

[3.14] J.N. Latta, "Computer-Based Analysis of Hologram Imagery and Aberrations. II: Aberrations introduced by a wavelength shift.," *Applied Optics*, vol. 10, no. 3, pp. 609-618, March 1971.

[3.15] J.W. Goodman, *Introduction to Fourier Optics.*, McGraw-Hill, San Francisco, 1968.

[3.16] R. Magnusson and T.K. Gaylord, "Diffraction Regimes of Transmission Gratings," *Journal of Optical Society of America*, vol. 68, no. 6, pp. 809-814, June 1978.

[3.17] H. Kogelnik, "Coupled Wave Theory For Thick Hologram Gratings," *The Bell System Technical Journal*, vol. 48, no. 9, pp. 2909-2947, American Telephone and Telegraph Company, November 1969.

[3.18] R.T. Ingwall and H.L. Fielding, "Hologram Recording with a New Photopolymer System.," *Optical Engineering*, vol. 24, no. 5, September/October 1985.

[3.19] J. Upatnieks and C Leonard, "Efficiency and Image Contrast of Dielectric Holograms," *Journal of the Optical Society of America*, vol. 60, no. 3, pp. 297-305, March 1970.

[3.20] P. Hariharan, "Intermodulation Noise In Amplitude Holograms: The Effect Of Hologram Thickness," *Optica Atca*, vol. 26, no. 2, pp. 211-215, 1979.

[3.21] Hariharan, *Optical Holography.*, Cambridge University Press, Cambridge, 1984.

[3.22] M.C. Hutley, *Diffraction Gratings*, Academic Press, London, 1982.

[3.23] J.T. Winthrop and C.R. Worthington, "X-Ray Microscopy By Successive Fourier Transformation," *Physics Letters*, vol. 15, no. 2, pp. 124-126, March 15, 1965.
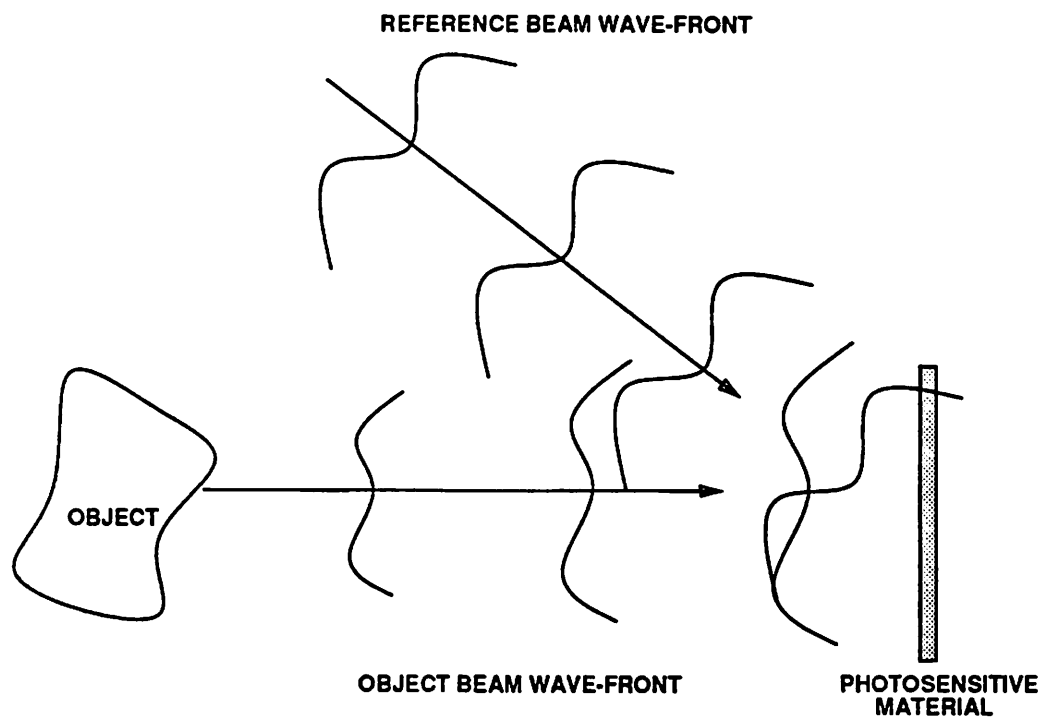
REFERENCE BEAM WAVE-FRONT

OBJECT

OBJECT BEAM WAVE-FRONT

PHOTOSENSITIVE
MATERIAL

Figure 3.1   An off-axis hologram recording arrangement.
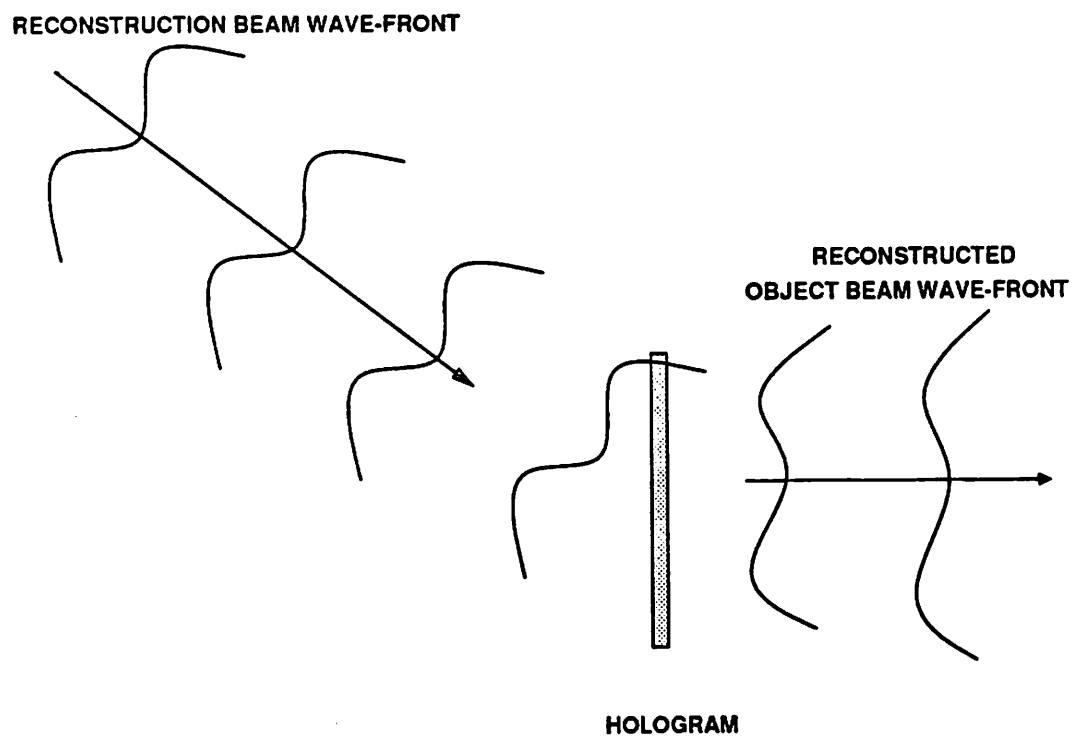
Figure 3.2   Reconstructing the virtual image recorded on a hologram.

RECONSTRUCTED
OBJECT BEAM WAVE-FRONT

HOLOGRAM
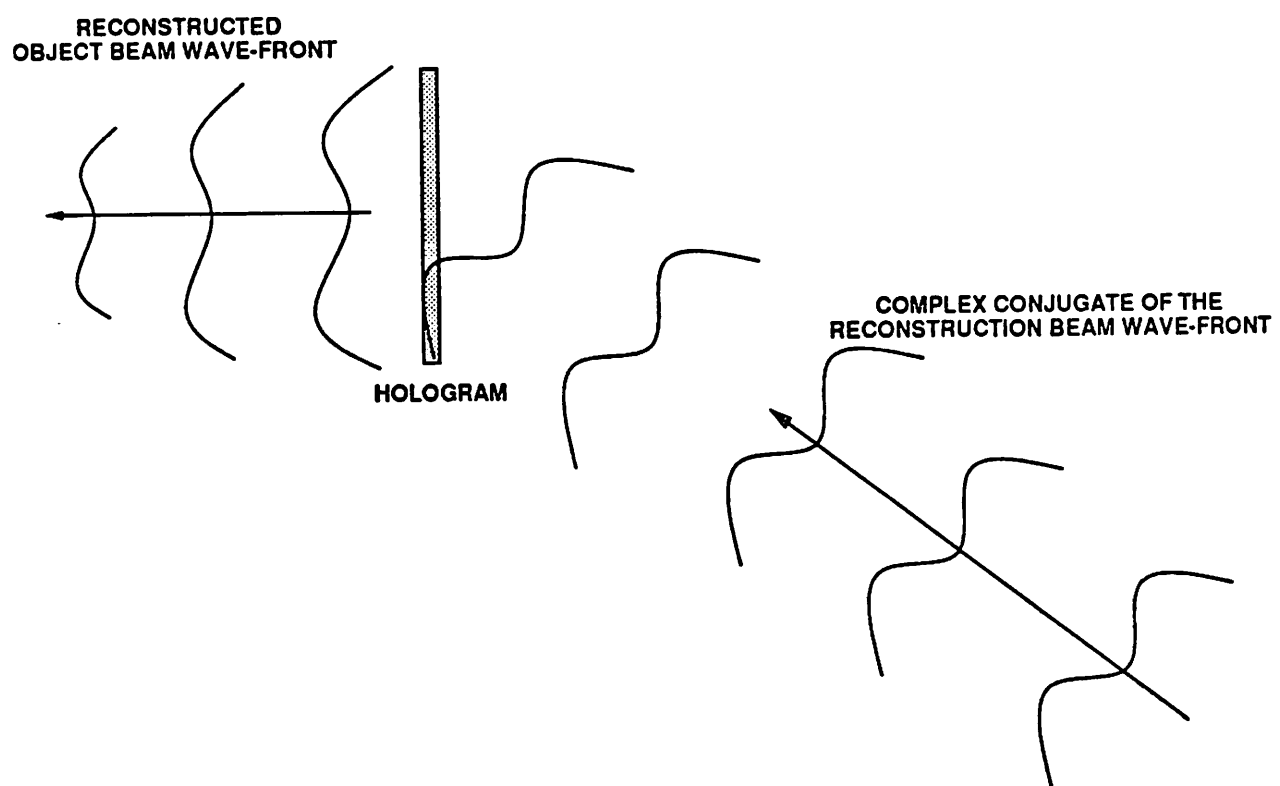
COMPLEX CONJUGATE OF THE
RECONSTRUCTION BEAM WAVE-FRONT

Figure 3.3 Reconstructing the conjugate (real) image with a construction wave-front that is conjugate to the construction wave-front.
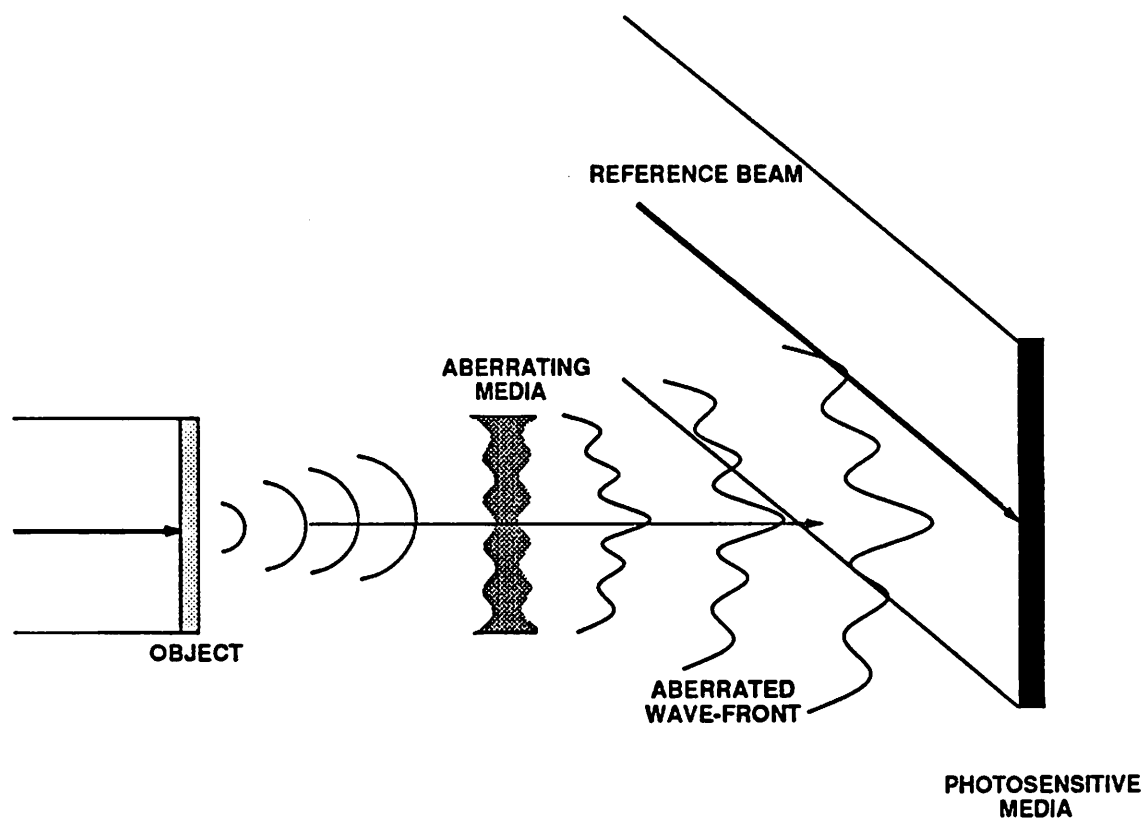
Figure 3.4   Holographically recording an aberrated object beam.

HOLOGRAM

ABERRATING MEDIA

RECONSTRUCTION BEAM

IMAGE OF OBJECT

ABERRATED WAVEFRONT

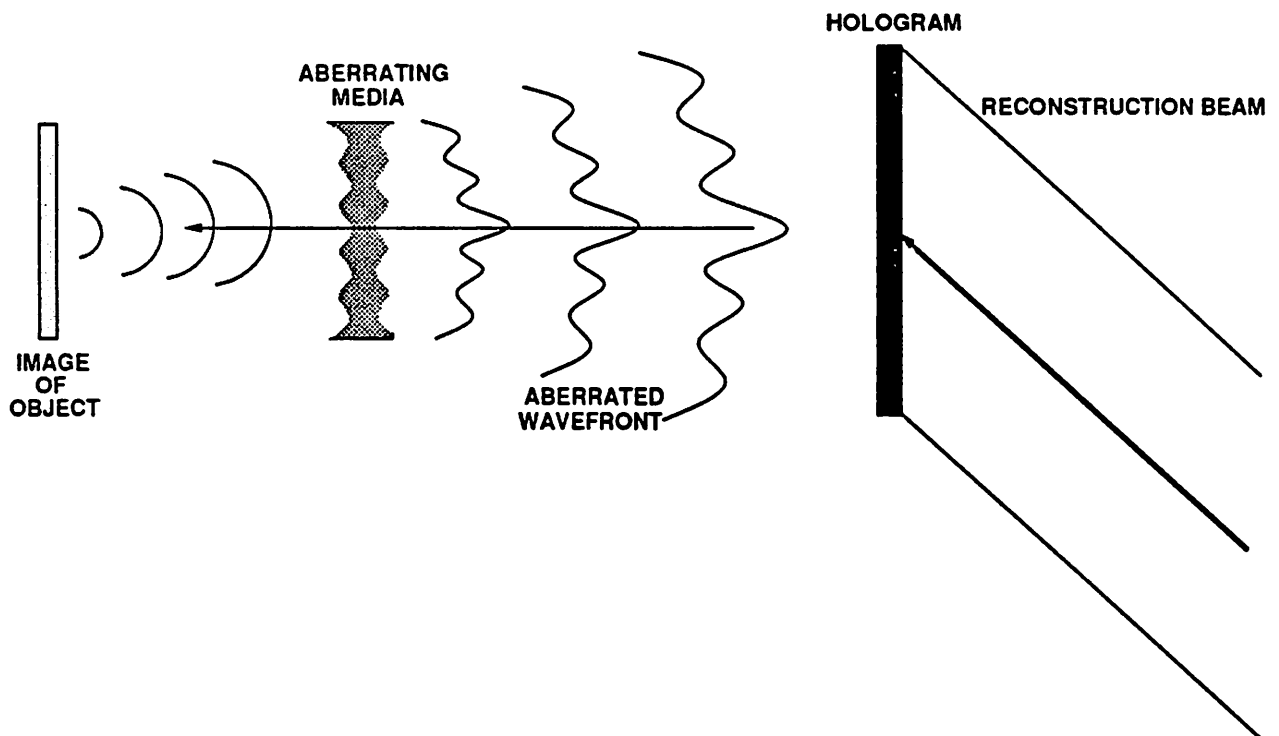**Figure 3.5**   Reconstructing the unaberrated image of the object.
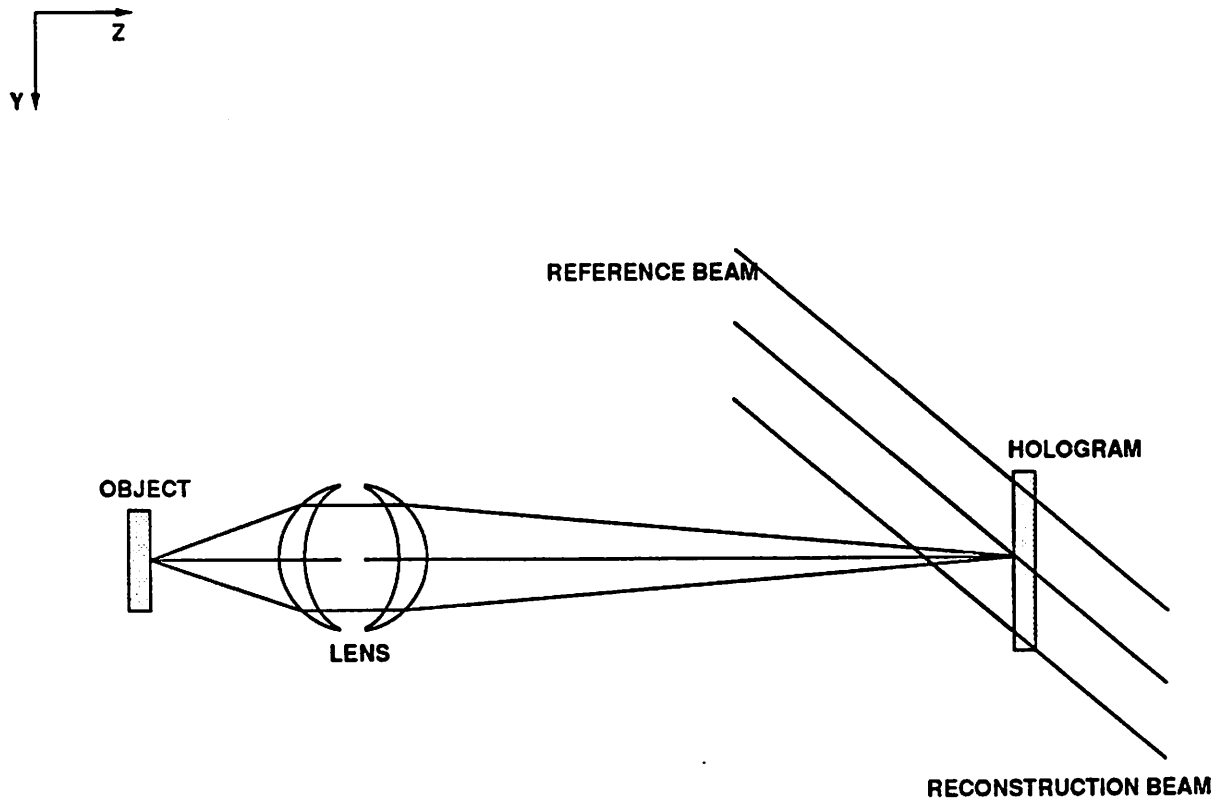
Figure 3.6 Holographic focused-image arrangement.
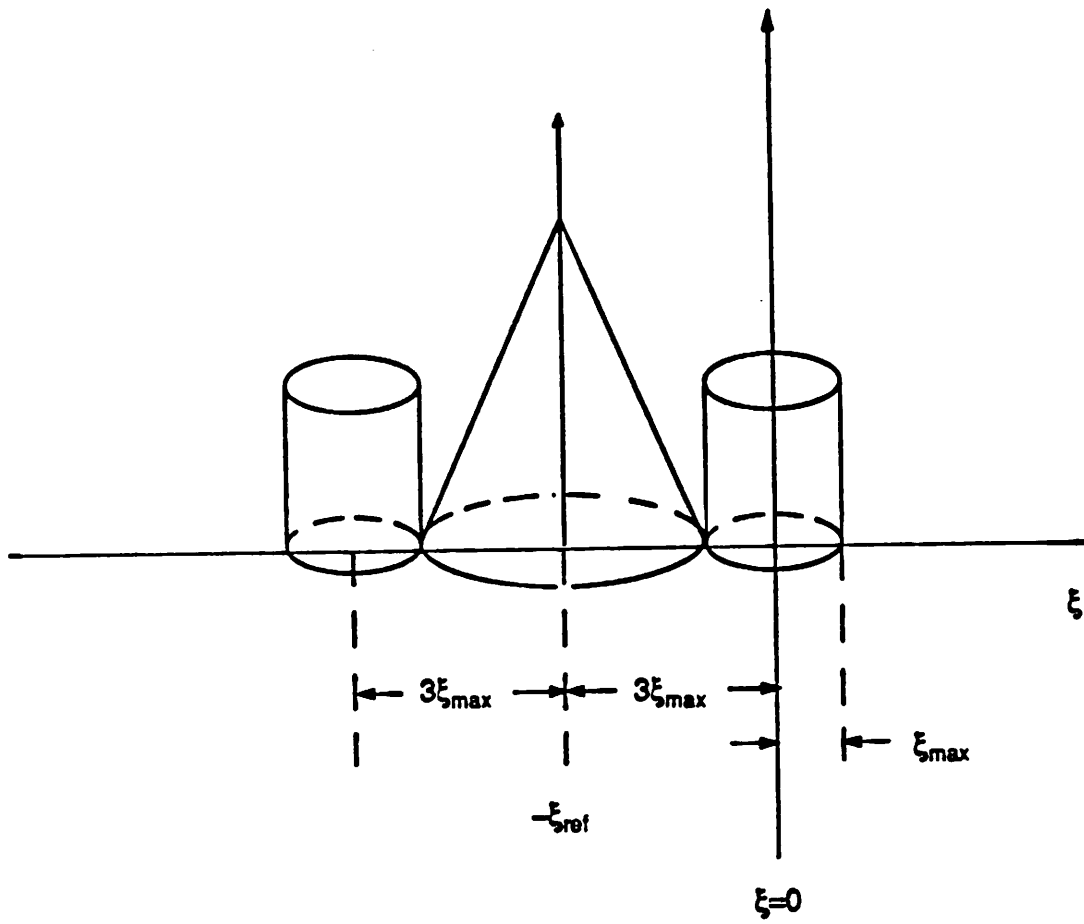
Figure 3.7   Spectral content of an illuminated off-axis hologram.
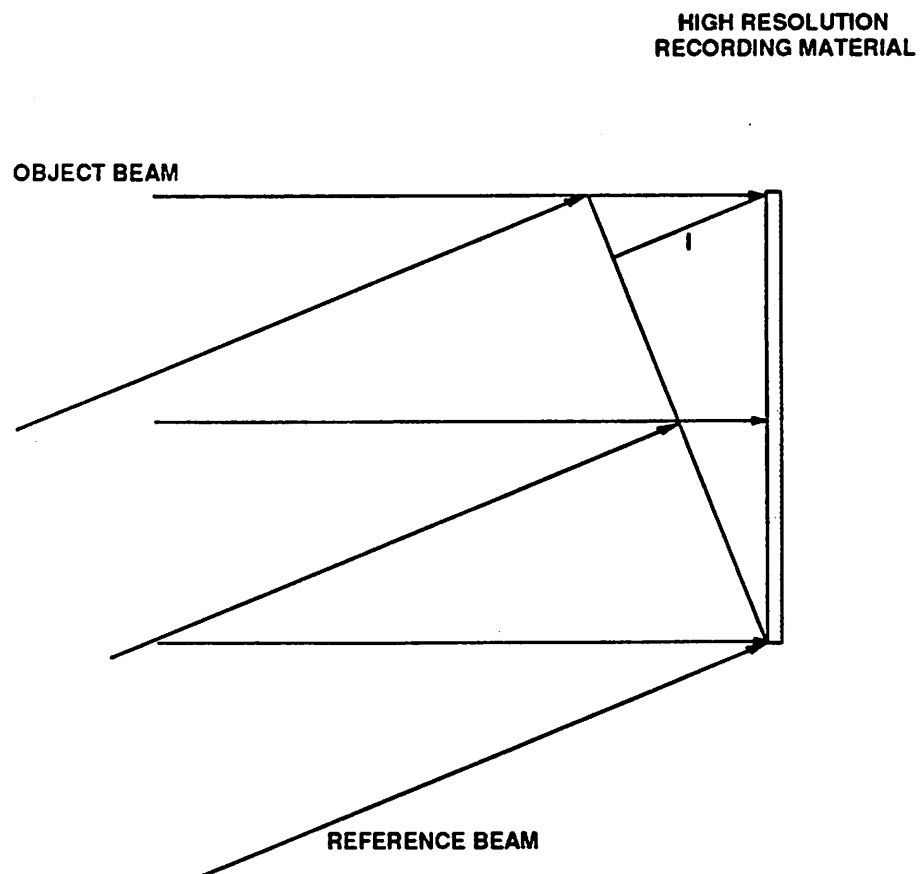
Figure 3.8   Minimum path difference I at the hologram plane for an off-axis reference wave.
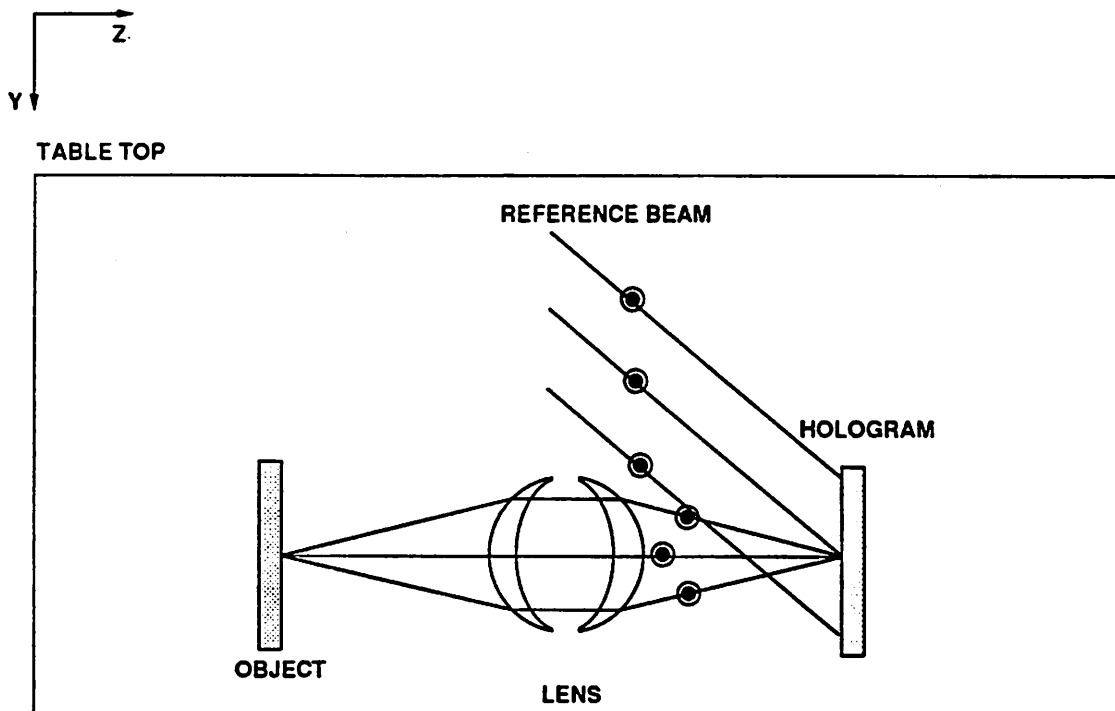
Figure 3.9 Polarization of the object and reference beams at the center of the field viewed perpendicular to the table top.
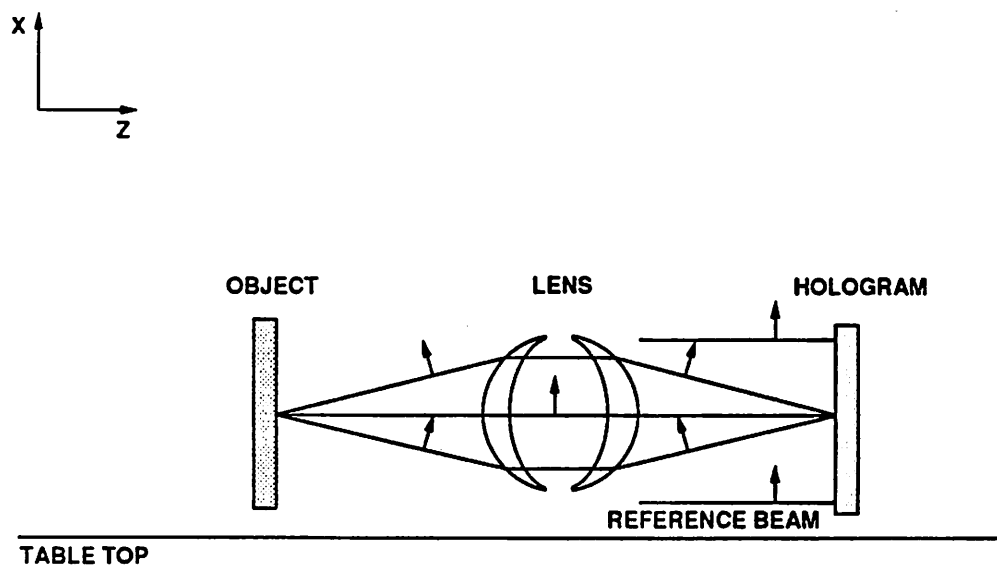
Figure 3.10 Polarization of the object and reference beams at the center of the field viewed parallel to the table top.
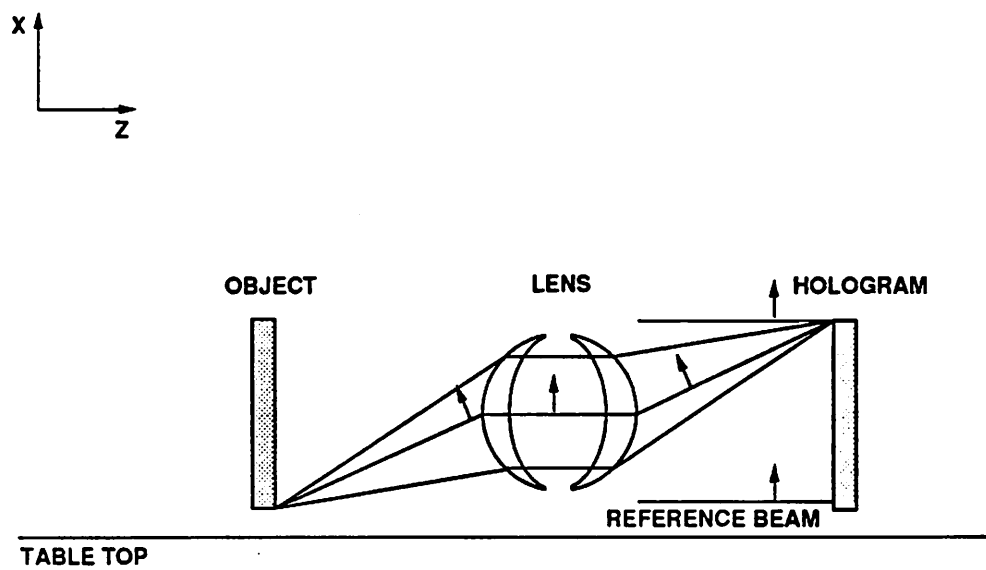
Figure 3.11 Polarization of the object and reference beams at the edge of the field viewed parallel to the table top.

CHAPTER 4

IMAGES RECONSTRUCTED FROM COHERENT

AND INCOHERENT ILLUMINATION BEAMS

In this chapter, experimental results from a focused-image projection holographic imaging system are described. The first section in this chapter describes the general optical and geometrical configuration of the holographic imaging system. The next section, 4.2, discusses the results using a simple single element imaging lens together with a HeCd laser as the hologram recording and image reconstruction illumination source and with optical photoresist as the holographic recording media. Section 4.3 describes the imaging results using an Argon Ion laser as the hologram recording and image reconstruction illumination source operating at 488nm, a single element imaging lens and Polaroid DMP-128 photopolymer[4.1] as the holographic recording media. Section 4.4 describes the imaging results using a well corrected 35mm photographic camera objective as the imaging optics together with an Argon Ion laser operating at 488 nm as the hologram recording and image reconstruction illumination source and Dupont photopolymer[4.2] as the holographic recording media. In addition, results using a spatially

and temporally filtered Hg arc lamp as the image reconstruction source instead of an Argon Ion laser will be described.

4.1 DESCRIPTION OF THE HOLOGRAPHIC IMAGING SYSTEM

The holographic imaging system for both recording a hologram of a mask and reconstructing the image of the mask is shown in figure 4.1 and 4.2 respectively.† The illumination source for recording the hologram is a single line laser with a coherence length of greater than 1 cm. In addition, the beam emanating from the laser is polarized perpendicular to the top surface of the optical table. Downstream from the laser is a beam steering device consisting of two mirrors that raises the laser beam to a working height of four inches and then directs the beam into a variable attenuating beam-splitter. This device divides the laser beam into two separate but coherent beams. Both beams now emanating from the beam-splitter are polarized with their electric field vectors perpendicular to the surface of the optical table. The beams are then directed into spatial-filters and collimating units to filter and expand the beams. In these units, the beams are first focused with a 60x microscope objective to a diffraction limited spot, then filtered with a 5 μm pin-hole and collimated with a 160mm focal length lens corrected for infinite image to object ratio. The resulting output beam is 50 mm in diameter.

To form the hologram, the object illumination beam is focused by a condenser lens to trans-illuminate the object mask by imaging the source into the entrance pupil of the imaging lens. The imaging lens collects the transmitted and diffracted light and focuses it at the lens' rear image plane with a magnification − 5. The

---

† A detailed roster of the equipment is listed in Appendix A.

hologram is formed at this plane using a high resolution recording material. The recording material is exposed simultaneously to both the focused image and the second collimated beam which is commonly referred to as the reference beam. The reference beam is directed to the hologram recording plane by a removable mirror M3 and a fixed mirror M4. Both mirrors, M3 and M4, are four inches in diameter and flat to $\lambda/2$† with a surface quality figure of 10-5. The reference beam intersects the optical axis formed by the imaging optics at forty-five degrees. After the holographic recording material is exposed, it is physically removed from the set-up, chemically developed and then returned to its original position in the system.

Once the hologram is returned to its original position, reconstruction of the image is possible. Figure 4.2 illustrates the configuration changes needed in the optical arrangement. To form the image, the hologram is illuminated by a beam conjugate to the original reference beam (another collimated beam propagating in a direction that is opposite to the original reference beam). This beam is reflected from mirror M5 after removing mirror M3 from the beam path. The wave-front emanating from the illuminated hologram is now "conjugate" to the original wave-front produced by the lens, that is the light rays diffracted from the hologram now exactly reverse ray traces the original light rays resulting in a real unaberrated image at the original mask plane.

In the formation of the hologram, a variable attenuating beam-splitter controls the relative intensity of the reference and object illumination beams.‡ The optical

---

† The wavelength, λ, referred to is 632.8 nm.

‡ This is accomplished by converting the incoming vertically polarized laser beam to a circularly polarized beam using a quarter wave-plate. It is then converted to linearly polarized light of any direction by rotating the quarter-wave plate. The beam is then divided by a beam-splitting Glan-Thompson prism into one vertically polarized beam and one horizontally polarized beam, the distribution of energy in the two beams being determined by the direction of polarization of the incoming beam to the prism. The horizontally polarized beam is then finally transformed into one with a vertical polarization by a half-wave plate, so at the hologram, the two beams are vertically

path distances between the object beam and reference beam beginning at the variable attenuator beam-splitter and ending at the hologram recording plane must be kept to a minimum while also keeping the overall set-up as compact as possible. The path differences between the reference and object beam need to be much less than the temporal coherence length of the illumination source to insure that the two beams interfere strongly. In addition, the overall beam path lengths should be minimized to reduced the sensitivity of the interference fringes to movement due to changes in the local air pressure, acoustic variations, temperature gradients, and air flow.

The holographic recording materials were coated on several different glass substrates. The first substrates were three inch square in size and were previously used as chrome mask blanks. To utilize these mask blanks, they were first stripped of any residual photoresist and then chemically etched of the remaining chrome. Several of the mask blanks were rejected because of the lack of parallelism between the front and rear surfaces while several others were rejected because of large surface undulations and the lack of material homogeneity. The second set of substrates were constructed of lime glass with no specifications on the parallelism or surface quality figure of the substrate's surfaces. The third substrates were two and a quarter inches square fused-silica glass plates with each surface flat to λ† over the entire surface with a surface quality figure of 60-40 or better. The parallelism of the front and rear surfaces is better than 1 arc-minute.

The glass substrates did not have an anti-reflection coating on their front surface to match the the index of refraction of the holographic recording material to

polarized.

† The wavelength, λ, referred to is 632.8 nm.

prevent any modulation of the intensity inside the recording material volume. More importantly, the rear surface of the substrate did not have an anti-reflection coating or an anti-halation coating. However, an anti-halation technique can be realized by using a neutral density filter with a index matching fluid. The neutral density filter is attached to the substrate using capillary action of the matching index fluid. Xylene is used as the fluid matching liquid since its index of refraction† is very close to that of the glass substrates and is relatively available.

The reference and reconstruction beam collimating unit was setup using two different methods and both of these methods achieved similar results. The first method is an auto-collimation technique. The output beam from the collimating unit is reflected back into itself using a plane mirror located at a distance from the collimating unit. The resulting output light exiting from the rear of the spatial-filter collimating unit is monitored using a pellicle as a beam-splitter. The collimating lens is then moved axially until the output light observed reflected from the pellicle is maximized. The second method involves using a shearing interferometer[4.3, 4]. This unit is introduced into the collimated beam at a forty-five degree angle and generates two beams, one reflected from the front surface as well as another reflected from the back surface. The two beams interfere and produce interference fringes. The degree of collimation is dependent of the pitch of these fringes. The smaller the modulation pitch, the higher the degree of collimation. The collimation achieved was close to the theoretical limit of λ/D where D is the diameter of the beam. Thus, the minimum angular divergence for the reference beam is 2 arc-seconds (1 wave at 488nm).

---

† The nominal index of refraction of xylene at 488 nm is 1.5.

A key alignment technique is the procedure used to setup the optical path for reference wave conjugate. This method uses several pin-holes inserted at various points in the reference and reconstruction beam paths. Figure 4.3 illustrates the locations of each of these pin-holes. Pin-hole A reduces the collimated 50mm diameter beam to a 1mm diameter beam. With mirror M3 removed, pin-holes G and F are aligned to pin-hole A. With mirrors M3 and M4 in place, pin-holes B through E are aligned to the reference beam. Mirror M5 is adjusted until the reference beam propagates through pin-holes F and G unscathed. Once this is accomplished, mirror M3 is removed and the beam location at pin-hole B is verified. If the beam does not pass through the pin-hole unscathed, mirror M5 is adjusted and mirror M3 is replaced and the beam location at pin-hole G is verified. This scheme is iterated until removal of mirror M3 produces no change in beam location at pin-holes G and B. The overall path length of the of the beam from mirror M3 is two meters with a detectable error of a quarter of a millimeter, thus, the conjugate beam has a maximum angular displacement error of approximately 25 arc-seconds.

4.2 IMAGES RECONSTRUCTED USING SURFACE RELIEF HOLOGRAMS

A material well-suited for recording thin-surface relief holograms is photoresist. Photoresists are light-sensitive materials which form surface relief patterns upon exposure with actinic radiation followed by chemical development. In positive type photoresist, the exposed areas become soluble and dissolve away during the development process.

Photoresist holograms are made by exposing the photoresist which is coated on a glass substrate to the holographic fringe pattern and then immersing it into a development solution. Since the solubility of photoresist is dependent of the local

exposure, a fringe pattern consisting of intensity variations is recorded as a variation in photoresist thickness. These surface variations modulate the phase† of the reconstruction (conjugate) beam to form the desired image.

Positive photoresists have the following advantages over photographic emulsions as a holographic recording media:

1) the resolution capability of photoresists is dependent on molecular dimensions unlike grain emulsions where the dimensions of the developed grains are on the order of the exposing wavelength,

2) all gelatin based materials such as photographic emulsions experience dimensional changes in the presence of water which form the development solution basis, but photoresist experiences very little dimensional change after development,

3) spinning techniques pioneered in the microlithography industry for coating photoresist onto a silicon wafer enable optical flats to be easily coated (holograms on optically flat substrates are essential for high-resolution images[4.5]).

However, the major disadvantage of using photoresists as a holographic recording media is that they introduce optical noise into the reconstructed image through two types of non-linearity : intrinsic and material. Because the transmittance function of a thin-phase hologram is a non-linear function of the recorded intensity, thin phase holograms are inherently non-linear as discussed in Chapter 3. The material non-linearity is caused because the surface relief depth is a non-linear function of the exposure energy.

---

† Surface relief holograms have similar properties to that of thin-phase holograms.

In order to assess both the resolution of the optical imaging system and the performance of photoresist as a holographic recording material, several holograms of an integrated circuit (IC) mask were recorded using the optical apparatus described in section 4.1† with a simple single element symmetrical bi-convex lens as the imaging optic. The illumination source was a HeCd laser operating at a wavelength of 441 nm with a 3 GHz bandwidth and a total power of 40 mw. AZ1350J optical photoresist was coated on a used mask blank using the same coating techniques used to coat photoresist on silicon wafers. The photoresist was exposed with an average dose of 50 mj/cm^2 and then developed in diluted 5:1 AZ303 developer for 30 seconds. The intensity ratio between the reference and object beam was 10.

The IC mask was a bright-field mask containing several features which vary in line-widths from 10 μms to 100 μms. The reconstructed images from the holograms exhibited significant amounts of optical noise. In fact, the features were difficult to identify; they were overwhelmed with optical noise. The optical noise was attributed to several sources: the IC mask, the imaging lens, the hologram substrate, and the hologram itself. It was hypothesized that the largest noise source was the hologram itself because it not only diffracted significant intensity into the "+1" diffraction order, but also into all the other higher orders. This effect suggests that there was considerable intrinsic non-linearity as well as material non-linearity. This non-linearity can be reduced by increasing the intensity ratio between the reference beam and the object beam, but only at the expense of decreasing image intensity. In addition, careful material characterization is also necessary to insure

---

† The optical system configuration for recording a hologram in photoresist is slightly different than that described in section 4.1 to accommodate the small temporal coherence of the HeCd laser.

that exposure and development characteristics are linear with diffraction efficiency[4.6]. An alternative solution is to use a volume recording media rather than a surface relief media for the hologram. With a volume hologram, the Bragg condition is satisfied for the original signal frequencies only and not for the intermodulation frequencies which will eliminate the optical noise due to intrinsic as well as material non-linearity[4.7,8].

4.3 IMAGES RECONSTRUCTED USING VOLUME HOLOGRAMS

Silver-halide photographic emulsions are the most commonly used holographic recording material used today. They have relatively high sensitivity, high resolving power, and are easily attainable. However, the developed emulsions have a tendency to scatter light, shrink non-uniformly after development, and are extremely sensitive to processing conditions.

The optical properties of dichromated gelatin (DCG) holograms are nearly ideal. A properly recorded DCG hologram absorbs and scatters very little light. In addition, volume DCG holograms can approach the theoretical diffraction efficiency of 100%. However, DCG recording media records two holograms, one on the surface and the other in the volume. The surface modulation introduces optical noise into the reconstructed image due to the inherent non-linear response of surface relief holograms. In addition, reliable and reproducible DCG holograms require elaborate preparation, exposure, and processing. The environmental sensitivity of the resulting hologram requires careful handling and hermetic sealing. Also, its very short shelf-life requires users to formulate and coat their own DCG films for immediate use.

Several new photopolymer holographic recording material systems have been recently introduced that have significant advantages over both photographic emulsions and DCG. Photopolymers have near ideal holographic recording properties. They have high diffraction efficiency, rapid self development (in-place development), no wet processing, no grating shrinkage, temperature and moisture stability, high sensitivity and resolution, low exposure threshold, and long shelf-life. The Polaroid Corporation has introduced a new photopolymer recording system, DMP-128[4.1], for volume phase recording that is relatively sensitive (5 mj/cm^2 at 488nm for full exposure) and has a high signal to noise ratio figure. The only drawback is that the material requires a simple wet development step. E.I. Dupont De Nemour Corporation has also introduced a new photopolymer system which is just as sensitive as DMP-128 and requires no chemical processing[4.2] (self developing process).

Section 4.3.1 describes the imaging results using a simple bi-convex imaging lens and Polaroid DMP-128 photopolymer as the holographic material. Section 4.3.2 describes the experimental results using a Nikkor 35mm f/1.2 photographic camera lens as the imaging optics, the Dupont photopolymer as the recording material, and an Argon Ion laser and Hg arc lamp as the reconstruction source.

4.3.1 IMAGES CONSTRUCTED WITH A SIMPLE LENS

Focused-image holograms were recorded using dark-field as well as bright-field IC mask as the object and Polaroid DMP-128 photopolymer as the holographic recording material. The imaging lens was a single element symmetrical bi-convex spherical lens with a focal length of 38.1mm and a diameter of 50.8mm operating at magnification − 5. The hologram was formed in the paraxial image plane of the

lens.† The object-space numerical aperture (NA) is .4 . After the photopolymer was exposed, it was physically removed from the setup and was chemically developed. The hologram was then returned to its original position in the set-up. No special alignment was used other than careful hand positioning of the hologram. In fact, mirror M5 was adjusted to reduce the wave-front aberrations present in the reconstructed image. Thus, no quantitative measure of the registration error is available.

Figure 4.4 is a photo-micrograph‡ of a reconstructed aerial image. The mask was a dark-field mask possessing the following line widths:

Line width μm	Lines/mm
1.5	333
1.2	417
1.1	455
1.0	500
0.9	555
0.8	625
0.7	715

The resolution observed in the reconstructed image is at least 715 lines/mm. The maximum theoretical resolution of the holographic system is 0.61 μm (815 lines/mm) which is the theoretical resolution for a fully coherent imaging system $\frac{\lambda}{2NA}$. As discussed in Chapter 3, the angular resolution of the reconstructed image can also be limited by the angular resolution of the of the reference and reconstruction illumination wave-fronts. The reconstructed image can be represented as the weighted cross correlation of the reference and reconstruction sources convolved with the object wave-front. Using equation 3.44 and assuming the diameter of the point spread function of the lens is ten centimeters† in diameter,

---

† The paraxial image plane was found by locating the plane where the image of the object image was the sharpest at the center of the field.

‡ The photo-micrographs were taken using an ordinary 40X Canon microscope objective with a 10X eyepiece focusing the image onto Polaroid type 35 instant film.

† The diameter of the point spread function is calculated in Chapter 5.

the maximum resolution attainable is 1.56 µms. However, this is a very simplistic model. A much more accurate model is presented in Chapter 5, and using the results from Chapter 5, the maximum angular divergence of the illumination beams must be less .04 wavelengths from figure 5.12. However, the minimum achievable angular divergence is 1.0 wavelength. In addition, maximum angular displacement of the reference and construction beam must be less than 0.3 arc-seconds from figure 5.11. The maximum angular displacement from the collimating unit is r_s/f_{cl} where r_s is the radius of the source and f_{cl} is the focal length of the collimating lens. For this particular system, the maximum angular displacement is 3.2 arc-seconds. Thus, the maximum attainable resolution is limited not by the theoretical limit of the lens but by the size of the effective illumination source.

In figure 4.4, the dark-field areas in the reconstructed image are clear of any significant random optical noise (speckle). The reconstructed image also exhibits pattern-dependent fringes in the field areas. Theses fringes are produced because of non-idealities in the reconstruction setup which introduce wave-front aberrations into the image.‡ The possible non-idealities include repositioning errors of the hologram, errors in the reconstruction beam, and the angular divergence and angular displacement due to the finite illumination source size. Also noting in figure 4.4, there is a general decrease in the intensity level of the image as the line-width decreases.‡‡ This can be attributed to two reasons: the effective size of the reference as well as the reconstruction source and the large spot size of the lens in combination with a physically small hologram. From the preceding paragraph, the

‡ The wave-front aberrations in the reconstructed image produce pattern dependent fringes. The larger the wave-front aberrations, the more pattern dependent fringes occur in the reconstructed image.

‡‡ The spatial frequency response of the photopolymer is greater than 6000 lines/mm.

effective size of the reference and reconstruction source introduces aberrations into the image of the smaller line-widths (less 1 μms) and thus, decreases the contrast of these images. The diameter of the spot size of the lens in this configuration is ten centimeters while the hologram diameter is less than five centimeters. Thus, much of the energy at the higher spatial frequencies is lost.

The reconstructed images of the smaller line-widths were found to be extremely sensitive to the hologram reconstruction position and reconstruction beam parameters. Small deviations of the hologram from its original recording position quickly deteriorated the image. Displacements on the order of a micrometer and angular displacements of arc-seconds in the reconstruction system degraded the the smallest features in the image. Figure 4.5 is a photo-micrograph of a reconstructed image of various size contact holes (1.0 μm to 1.5 μm) with the hologram correctly positioned (as correctly as possible). The reconstructed image of all the contact holes are clearly resolved. Figure 4.6 is is a photo-micrograph of the same contact holes but with the imaging lens vertically displaced approximately 25 μm from the location where the hologram was originally recorded. The images of the contact holes are all deformed and all show signs of having comatic aberrations. The image of the one micrometer contact holes are completely absent. A laterally displaced lens will introduce coma into the the reconstructed image.

Figure 4.7 is a photo-micrograph of an aerial image reconstructed from a hologram recorded using a bright-field mask. The field areas in the reconstructed image are littered with random optical noise (speckle). However, the large masked (dark) patterns are fairly clear of any optical noise. The image also exhibits pattern-dependent fringes, in both the pattern areas and the field area. The sources of the fringes are due to various non-idealities in the system. A major contribution of the random optical noise is the microscope system used to view and

photograph the aerial image (This can be verified by moving either the microscope or the hologram and observing the motion of the optical noise). Further discussion of the sources of noise is presented in section 4.3.4.

4.3.2 IMAGES CONSTRUCTED WITH A MULTI-ELEMENT LENS

As noted in the previous section, the reconstructed image is extremely sensitive to non-idealities of the optical reconstruction system such as the hologram reconstruction position and reconstruction beam wave-front errors. Replacing the single element lens with a well-corrected (but not diffraction-limited) multi-element lens will reduce the sensitivity†[4.9] to system non-idealities. In addition, using the Dupont photopolymer as the holographic recording material eliminates any hologram repositioning errors because the material is self-developing.‡

Using an ordinary NIKKOR 50mm/f1.2 multi-element photographic lens as the imaging optic at a magnification ~ 5, several focused-image holograms of a bright-field mask as the object were recorded. The object space numerical aperture of this configuration is .33 and the theoretical resolution of the imaging system is 0.82 μm (610 l/mm) $\frac{\lambda}{2NA}$. The hologram was formed in the paraxial image plane‡‡ using the Dupont photopolymer[4.2] as the high resolution recording material. The photopolymer was exposed simultaneously to both the focused image and a

---

† It will be shown in Chapter 5 that in fact that the less aberrated the lens is, the less sensitive the reconstructed image is to non-idealities of the of the image constructing system.

‡ Once the photopolymer has been exposed with the object and reference beam, a flood-exposure with a UV source completes the development process. There is no need to physically handle the hologram after exposure and thus, no repositioning errors are introduced.

‡‡ The paraxial image plane is found by locating the plane where the image of the object is sharpest at the center of the field.

reference beam. After the exposure, the photopolymer was flood exposed with a uniform UV source to complete the recording process.

Figure 4.8 is a photo-micrograph† of a re-constructed aerial image of the bright-field mask. The mask is a bright field mask possessing the following line and space combinations: 1.0 μm line and space, 1.0 μm line and 2.0 μm space, 1.5 μm line and 1.5 μm space, 1.5 μm line and 3.0 μm space, 2.0 μm line and 2.0 μm space. The resolution is observed to be 1.0 μm, the smallest feature on the original mask. The lines and spaces are all well-defined. No decrease in the contrast is observed at the smaller line-widths. This suggest that the limiting resolution of the system is due to the finite aperture of the lens and not the effective illumination source size as was the case for the simple lens. Displacements of the hologram of several micrometers (10-20 μm) in the axial and lateral directions did not have a pronounced effect on the images. In addition, angular displacements (10-20 arc-seconds) and angular divergence of the reconstruction beam did not have a significant effect on the image. The reconstructed images are much more insensitive to any changes in the reconstruction configuration compared to the reconstructed images in the system using the simple lens. A general conclusion from these results indicate that the closer the lens presents a spherical wave-front, the less sensitive the reconstructed image is to non-idealities of the system.

In figure 4.8, the field areas are dotted with random optical noise (speckle). However, the image does not exhibit any pattern-dependent fringes, in both the pattern areas and the field area. The lack of pattern dependent fringes in the reconstructed image suggests that there are no detectable wave-front aberrations

† The reconstructed image photo-micrographs were taken using an ordinary 40X canon microscope objective with a 10X eyepiece focusing the image on Polaroid type 35 medium contrast instant film.

introduced into the reconstructed image. Moving the microscope viewing system moves the location of the image, but does not move the location and amount of optical noise. This suggests that the major contribution of the noise is the microscope system used to view and photograph the aerial image.

4.3.3 OPTICAL NOISE SOURCES

As discussed in Chapter 3, there are a number of possible optical noise sources in this imaging system. Figures 4.7 and 4.8 show that for this specific experimental system, there is a significant amount of optical noise present in the reconstructed images that are observed through the microscope viewing system. Several simple experiments were performed to help identify the major sources of optical noise. The first experiment was to assess the amount of noise introduced by the viewing optics, a simple 40X Canon microscope objective with a Melles Griot 10X wide-field eye piece. A mask containing a bright-field as well as a dark-field areas was illuminated with a spatially filtered coherent illumination beam and observed through the microscope viewing system. The image of the mask was speckled with optical noise both in the dark areas as well as in the clear areas. When the microscope was displaced laterally from its position, the image of the mask moved in the viewing field but the speckle did not. For very large dark areas, the amount of optical noise observed in those areas using the microscope viewing system was very small. As soon as the viewing system captured any amount of direct illumination, a sharp increase of optical noise was observed. These observations strongly suggest that the microscope viewing system introduces a significant portion of the optical noise present in the observed reconstructed image.

In the reconstructed images, the optical noise level in the dark areas was higher than expected if all the noise was generated from the microscope viewing system itself. Thus, a second experiment was performed. A 25 x 25 μm^2 clear aperture opening in a dark-field mask was procured. The mask was inserted into the holographic imaging system which used the Nikkor multi-element lens as the imaging optic. The mask was illuminated with a spatially filtered coherent illumination beam. The resulting image at the hologram recording plane was then investigated. The areas surrounding the clear aperture were speckled with optical noise even though the viewing field of the microscope was not imaging the clear aperture. This result suggests three possible optical noise sources. First, the imaging lens introduces noise throughout its image field due to surface reflections and scattering from the lens' barrel and the element surfaces. The two other possible noise sources are reflections from the front lens element which then are reflected to the mask and then back from the mask into the lens and the illumination energy emerging directly through the chrome plating. The last two sources were dismissed because when black construction paper was introduced between the lens and the mask except for a very small opening for the clear aperture, no reduction of optical noise was seen in the dark field areas at the hologram recording plane. Thus, the largest source of optical noise in the forward imaging path is due to the imaging lens itself, an ordinary Nikkor 35mm photographic cameras lens. For this particular lens, its surfaces and anti-reflection coatings are optimized for a broad spectrum of wavelengths and not for a single coherent beam. In fact, the anti-reflection coatings used on this camera lens can scatter much more light than for an uncoated lens[4.10].

The third experiment was developed to pin-point the role of the photopolymer and glass substrate as optical noise sources. A glass substrate as well as un-

exposed and exposed† photopolymer were illuminated with the reconstruction beam in the hologram recording plane and their scattering centers imaged with the Nikkor lens and observed through the microscope viewing system at the original mask plane. An insignificant amount optical noise was observed. This result suggests that the glass substrates and the unexposed and blanket exposed photopolymer generate very little optical noise.

Finally, a hologram was recorded using the image of the small aperture as the object. Then, the image was reconstructed and observed through the micro-scope viewing system. The optical noise observed in the dark areas had much more optical noise in the reconstructed image than just imaging the aperture at the hologram recording plane. This increase is attributable to both the photopolymer and the imaging lens. The photopolymer, after recording an image, scatters more light compared to the unexposed and blanket exposure. The noise source may be scattering from random surface relief on the photopolymer film or from relatively smooth random errors in the recorded fringe positions and amplitudes. [4.11, 12] The imaging lens in this system produces twice the amount of optical noise than a lens in a conventional single pass imaging system. The hologram records not only the wave-front to reconstruct the image of the aperture, but also the scattered field from the lens' elements. On reconstruction, the reconstructed wave-front that forms the image of the aperture is again scattered by the imaging lens as the wave-front traverses through lens. This scattered field is imaged at the original mask plane as well as the previously recorded scattered field. Thus, the imaging lens introduces a significant amount of optical noise into the reconstructed image. In addition, this effect may also limits the type of imaging lens which can be used.

† Blanket exposure using a single beam.

Lenses with large positive and negative powers tend to reflect much more illumination than lenses with small positive powers. For example, the main attribute of a Petzval lens is the fact that the constituent element members of the lens are all positive. As a result, the refractive power is distributed among the all the members, and each has a power less than the total lens. This is contrasted to other types of lenses like the Double Gauss and the Cooke Triplet where excessive power is introduced and is then balanced by a lesser amount of negative power to yield the residual power of the lens.

4.4 IMAGES RECONSTRUCTED WITH AN INCOHERENT SOURCE

In the previous section, diffraction-limited imaging was demonstrated. However, as expected in any fully coherent imaging system, random optical noise was present in the reconstructed image. This optical noise in a focused-image lens-hologram system arises primarily from two sources: the optical train and the hologram itself. Optical train noise originates from surface reflections from the member element lenses, scattering from the barrel, baffles, element surfaces, and from particulates on the lens. In fact, from section 4.3.3, it was found that the imaging lens contributed a significant amount of optical noise in the reconstructed image. Hologram noise originates from material non-linearities and intrinsic non-linearities as well as from scattering centers in the hologram material volume and on the surface of the hologram.

Illuminating the hologram with a spectrally-broad source with its wavelength centered about the hologram's reconstruction wavelength, decreases the coherence length of the illumination beam which can reduce the optical train noise† in the

---

† The temporal coherence length should be less than the thickness of the optical elements.

reconstructed image while still achieving diffraction-limited performance. The illumination bandwidth must be sufficiently broad to insure no coherent interaction of the scattered light, but sufficiently narrow to insure coherent interaction of the diffracted light from the hologram that forms the image.

Figure 4.9 illustrates the changes needed in the optical arrangement to reconstruct the image using an incoherent source. The hologram is illuminated by a beam of light from a spectrally and spatially filtered Hg arc lamp that is conjugate to the original reconstruction beam. The reconstruction beam is reflected from mirror M5 after removing mirror M3 from the beam path.

The light generated from the Hg arc lamp is collected with a condenser lens and spatially filtered with a 100 μm diameter pin-hole. The light exiting the pin-hole is then collimated with an 80mm focal length lens corrected for infinite image to object ratio. The collimated light is then directed through a narrow-band interference filter with a center wavelength of 488 nm and with a FWHM bandwidth of 10 nm. The pin-hole size and filter bandwidth were selected solely on energy transfer considerations. Smaller diameter pin-holes and narrower interference filters were investigated, but the collimated light beam produced had insufficient amount of energy to produce a discernible reconstructed image.

Several focused-image holograms were recorded using a NIKKOR 50mm/f1.2 multi-element photographic lens as the imaging lens at a magnification – 5 and with Dupont photopolymer as the holographic recording material. Extreme care was taken to insure that the image of the mask was in the plane of best focus at the hologram recording plane. The focused-image holograms were recorded using a bright-field mask possessing an array of line widths spanning from 1.0 μm to 10.0 μm. Figure 4.10 is a photo-micrograph† of the reconstructed aerial image of the

† The photo-micrographs were taken using an Bausch and Lomb microscope camera with a Polaroid instant (667) film.

bright-field mask using coherent illumination. The bright as well as the dark areas in the reconstructed image are clearly speckled with optical noise. Figure 4.11 is a photo-micrograph† of the reconstructed aerial image of the identical bright-field mask but reconstructed with a beam of filtered light from a Hg arc lamp. The optical noise in the field areas is substantially reduced, however, there is a small decrease in the observed resolution. The possible reasons for this decrease are that the effective source size is too large, the temporal coherence if the reconstruction beam is too small, and the lens' lateral and longitudinal chromatic aberrations are much too large to produce a diffraction-limited images.

From section 3.2.4, the effective source size must satisfy the spatial coherence and angular blur requirements for diffraction-limited imaging. The effective source size must satisfy equation 3.45 which is $r_{source} < \lambda^* f_{col} / 2^* D_{IPSA}$. For this particular configuration, assuming a D_{IPSA} of 25 μm, the effective source size must be less than 80 μm. Since the actual source size is 100 μm, this should not limit the achievable resolution. The governing equation for the maximum angular displacement can be found in section 4.3.1, where the angular displacement of the reconstruction beam with a effective source size of 100 μm collimated with a lens having a focal length of 80 mm is r_s/f_{col} which is 125 arc-seconds. From the results of Chapter 5, an angular displacement of 125 arc-seconds should not be the limiting factor for achieving the desired resolution for a well corrected-lens. The minimum temporal coherence to reconstruct the hologram is given by equation 3.34 in Chapter 3 and must satisfy the the following relationship $\lambda^2/\Delta\lambda > 2^* D_{IPSA}$. The temporal coherence of the illumination beam is $\lambda^2/\Delta\lambda$ which is 23.5 μm. Assuming a D_{IPSA} of 25 μm, the the temporal coherence requirement is not satisfied by a factor of 2 approximately. Thus, the temporal coherence length of the filtered illumination beam may be too small to construct a diffracted-limited image. The lens'

chromatic aberrations are unknown, however extrapolating using the results from microlithography lenses where most lenses are corrected for a bandwidth of less that 10 nm, the image should also be degraded by the chromatic aberrations in the imaging lens.

The reconstructed image also exhibits low-level periodic and non-periodic modulation. The periodic modulation is recorded in the hologram due to the interferometric effect between the reference beam and the glass substrate employed to support the hologram recording material. This modulation is generated during the recording of the hologram and is present in the reconstructed image. In this specific recording, no anti-halation technique was used to eliminate the reflection from the rear surface of the substrate. Any optical noise during the hologram recording process is also recorded. Thus, this noise is reconstructed even when using a incoherent source to reconstruct the image.

4.5 SUMMARY

In this chapter, the imaging results from a prototype focused-image holographic projection system have been presented. Diffraction-limited images were reconstructed from holograms recorded using a simple single element lens and a well corrected multi-element lens. In addition, the images reconstructed using the simple lens were found to be much more sensitive to any changes in the image reconstruction configuration compared to the well-corrected the multi-element lens. As expected in a fully coherent system, random optical noise was present in the reconstructed images. To reduce the amount of optical noise in the images, a reconstruction beam derived from a spatially and temporally filtered Hg arc lamp was employed. With this reconstruction beam, a considerable reduction of optical

noise in the reconstructed image was achieved while achieving near diffraction-limited imaging.

4.5 REFERENCES

[4.1] R.T. Ingwall and H.L. Fielding, "Hologram Recording with a New Photopolymer System.," *Optical Engineering*, vol. 24, no. 5, September/October 1985.

[4.2] B. M. Monroe, W. K. Smothers, R. R. Krebs, and D. J. Mickish, "Holographic Photopolymers.," *SPSE Abstracts*, p. 131, Wilmington, 1987.

[4.3] Manfred W. Grindel, "Testing Collimation Using Shearing Interferometry," *Surface Characterization and Testing*, vol. 680, SPIE, 1986.

[4.4] M.V.R.K. Murty, "The Use Of A Single Plane Parallel Plate As A Lateral Shearing Interferometer With A Visible Gas Laser Source," *Applied Optics*, vol. 3, no. 4, pp. 531-534, April 1964.

[4.5] M. J. Beesley, H. Foster, and K.G. Hambleton, "Holographic Projection of Microcircuit Patterns.," *Electronics Letters*, vol. 4, no. 3, pp. 49-50, February 9, 1968.

[4.6] R.J. Collier, C.B. Burckhardt, L.H. Lin, *Optical Holography*, Academic Press, New York, 1072.

[4.7] J. Upatnieks and C Leonard, "Efficiency and Image Contrast of Dielectric Holograms," *Journal of the Optical Society of America*, vol. 60, no. 3, pp. 297-305, March 1970.

[4.8] P. Hariharan, "Intermodulation Noise In Amplitude Holograms: The Effect Of Hologram Thickness," *Optica Atca*, vol. 26, no. 2, pp. 211-215, 1979.

[4.9] B.J. Lin and S.A. Collins,Jr., "Holographic Imaging and Aberrations Due to an Incorrectly Repositioned Hologram in a System with Lenses Having Aberrations.," *Journal of the Optical Society of America*, vol. 63, no. 5, pp. 537-547, May 1973.

[4.10] Ken Walsh. Private Communication

[4.11] J.A. Jenney, "Holographic Recording with Photopolymers," *Journal of the Optical Society of America*, vol. 60, no. 9, pp. 1155-1161, September 1970.

[4.12] J.A. Jenney, "Nonlinearities of Photopolymer Holographic Recording Materials," *Applied Optics*, vol. 11, no. 6, p. 1371, June 1972.

LASER

M1

M3

BEAM
SPLITTER

LENS

M2

MASK

HOLOGRAM

M4

SPATIAL FILTER
COLLIMATORS
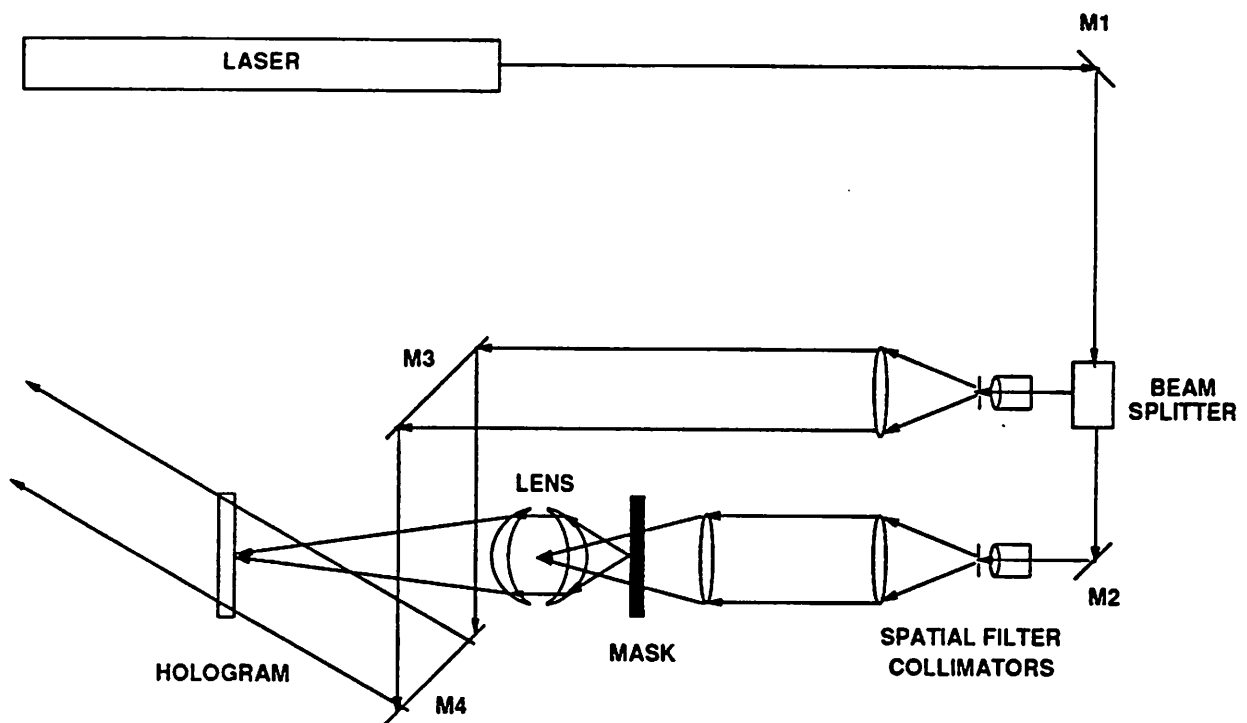
Figure 4.1 Schematic diagram of the apparatus to record the hologram.

M1

LASER

M5

LENS

IMAGE

M2

SPATIAL FILTER
COLLIMATORS

HOLOGRAM

M4
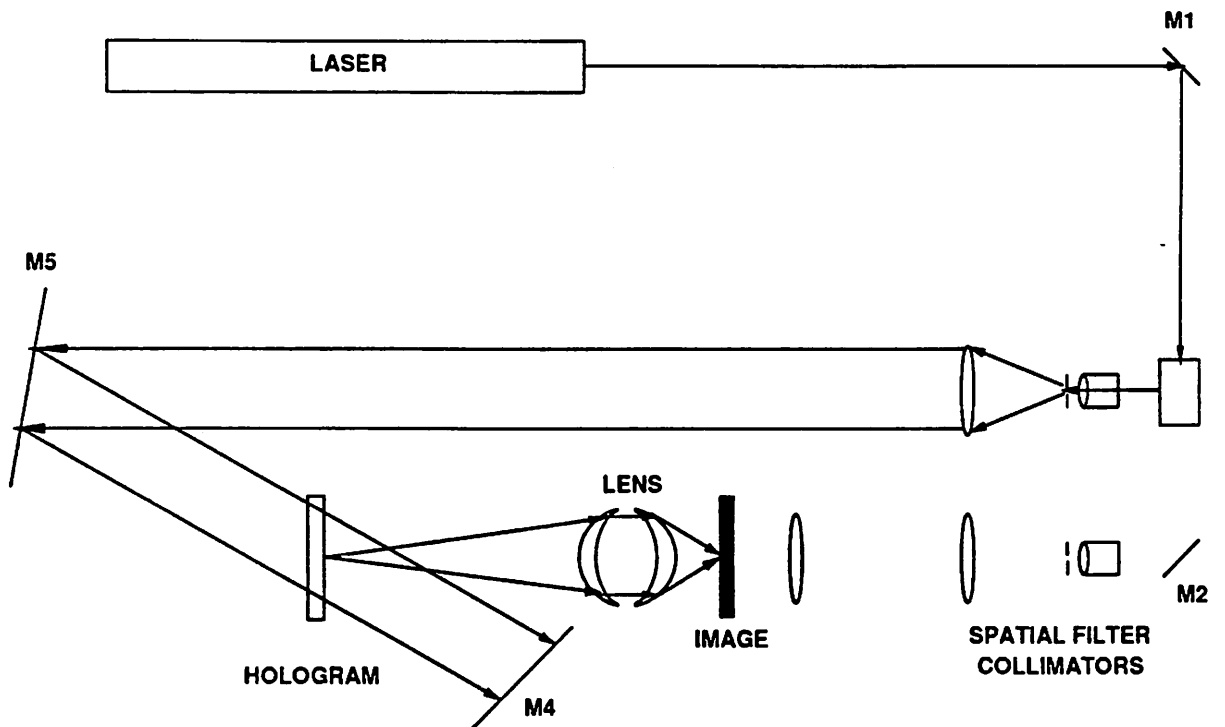
Figure 4.2 Schematic diagram of the apparatus to reconstruct the image from the hologram.
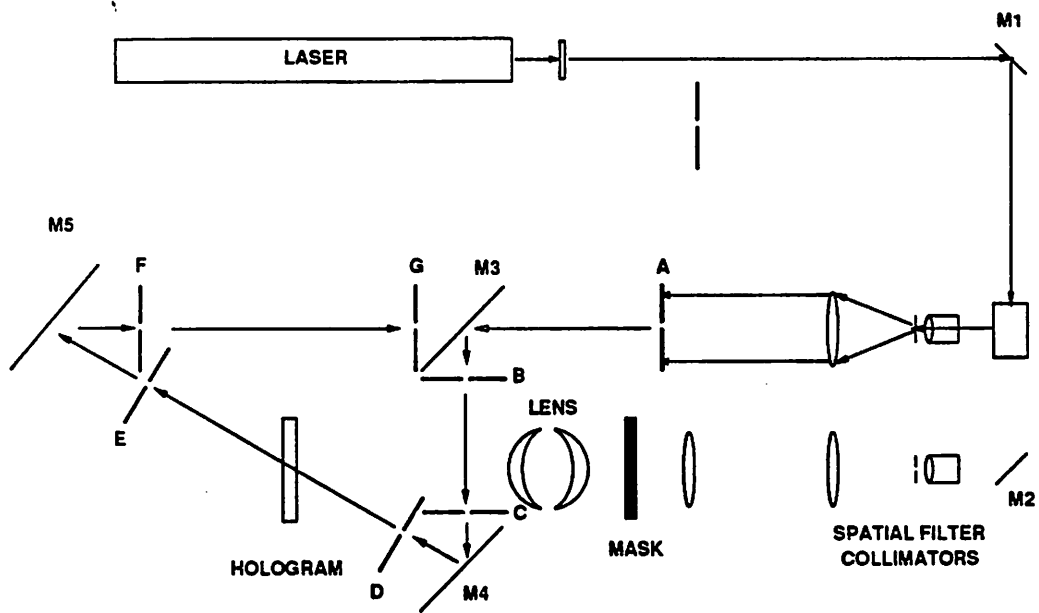
Figure 4.3   Schematic diagram of the location of the pin-holes to align the reference beam to the reconstruction beam.
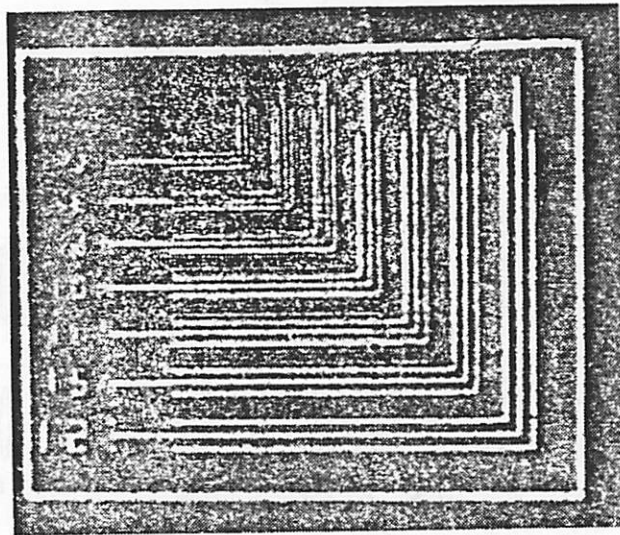
Figure 4.4   A photo-micrograph of a reconstructed aerial image of various equal
line and space widths (0.7 μm to 1.5 μm).
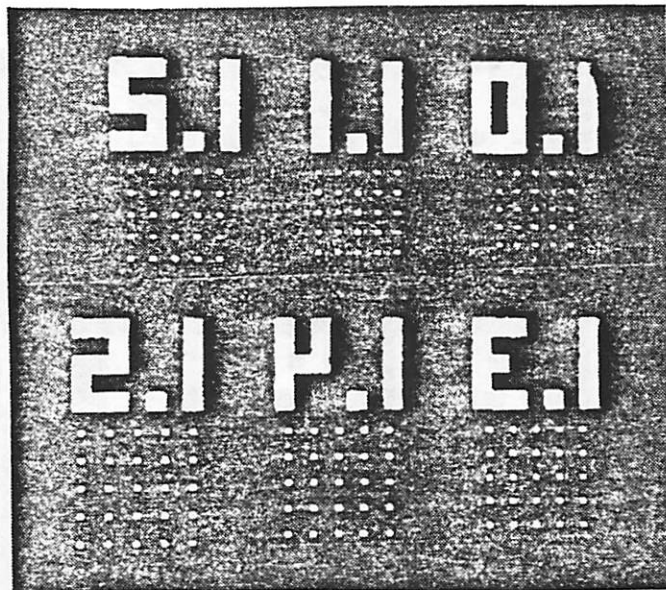
Figure 4.5 A photo-micrograph of a reconstructed aerial image of various contact holes (1.0 μm to 1.5 μm) with hologram correctly repositioned.
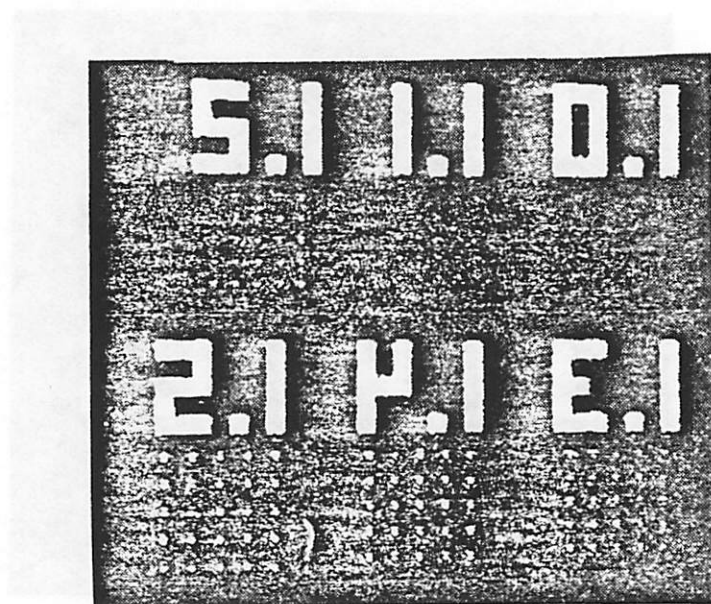
Figure 4.6 A photo-micrograph of a reconstructed aerial image of various contact holes with the imaging lens displaced 25 µms from the hologram recording position.
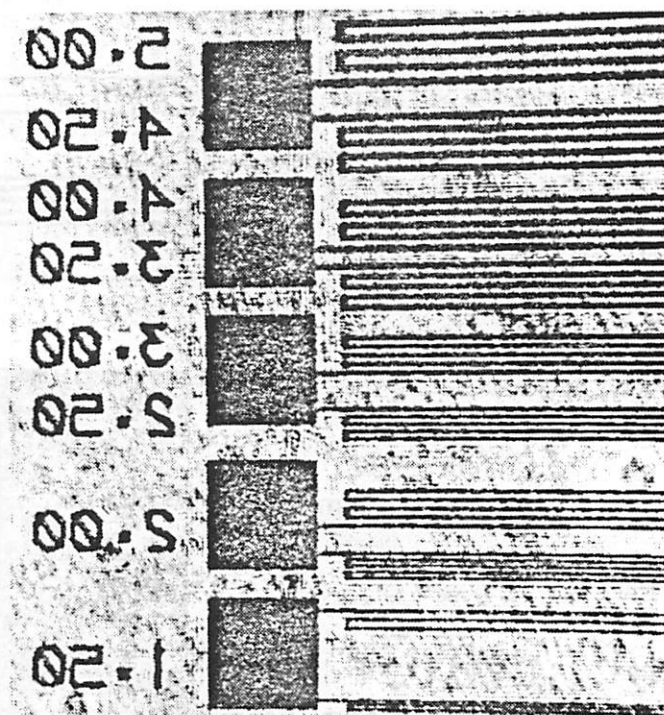
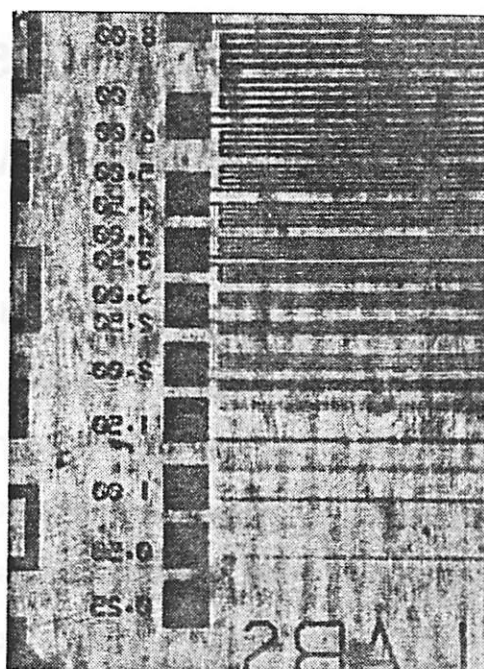**Figure 4.7**   A photo-micrograph of a reconstructed aerial image of various line and space widths (1.5 μm to 5μm) using a bright-field mask.

1.0μm line 1.0μm space

1.0μm line 1.5μm space

1.5μm line 1.5μm space

1.5μm line 1.5μm space

2.0μm line 2.0μm space

(a)

1.0μm line 1.0μm space

1.0μm line 1.5μm space

1.5μm line 1.5μm space

(b)
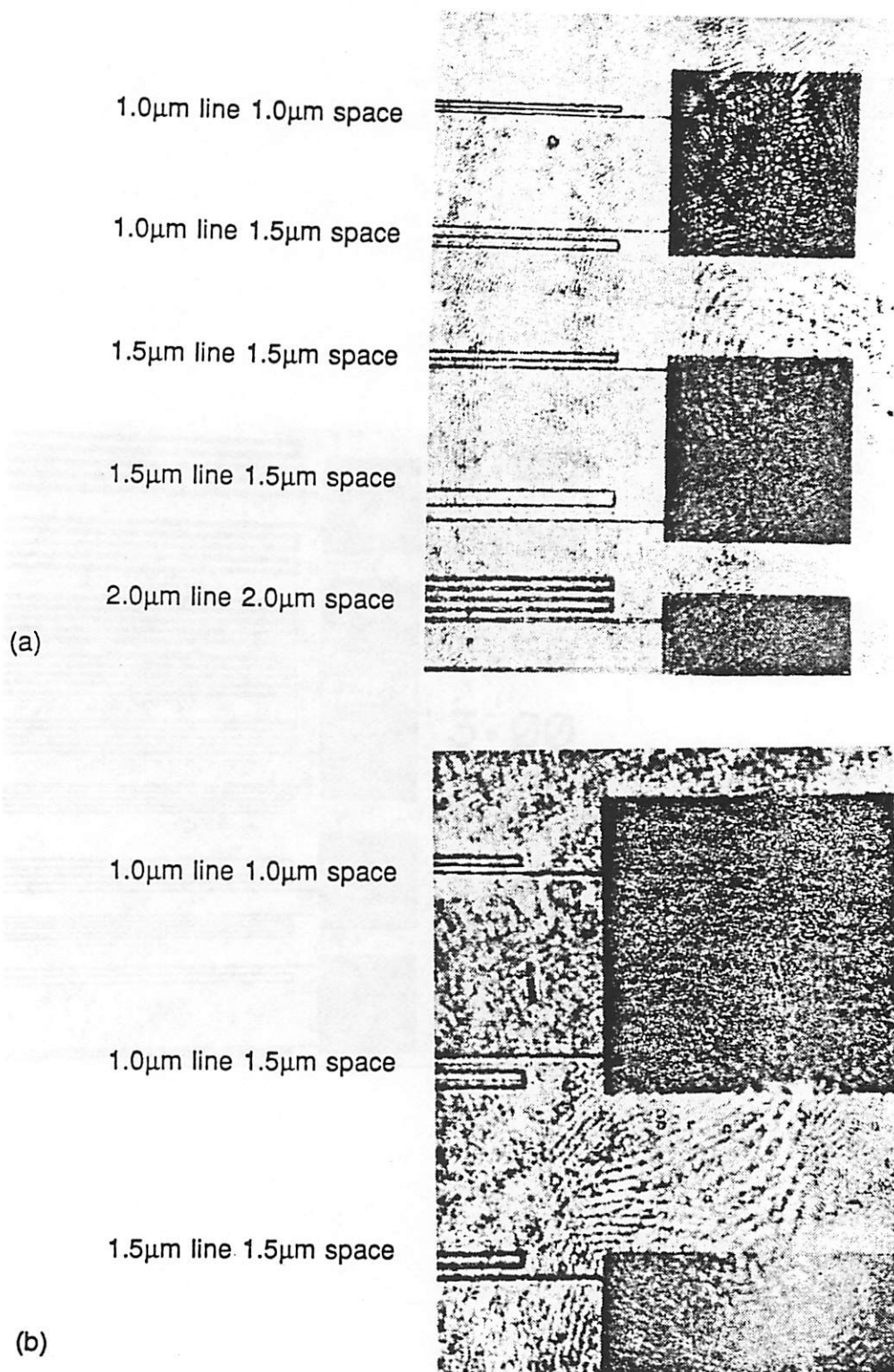
Figure 4.8 A photo-micrograph of a reconstructed aerial image of various line and space widths (1.0 μm to 3 μm) using a bright-field mask at a magnification of (a) 400x and (b) 600x.
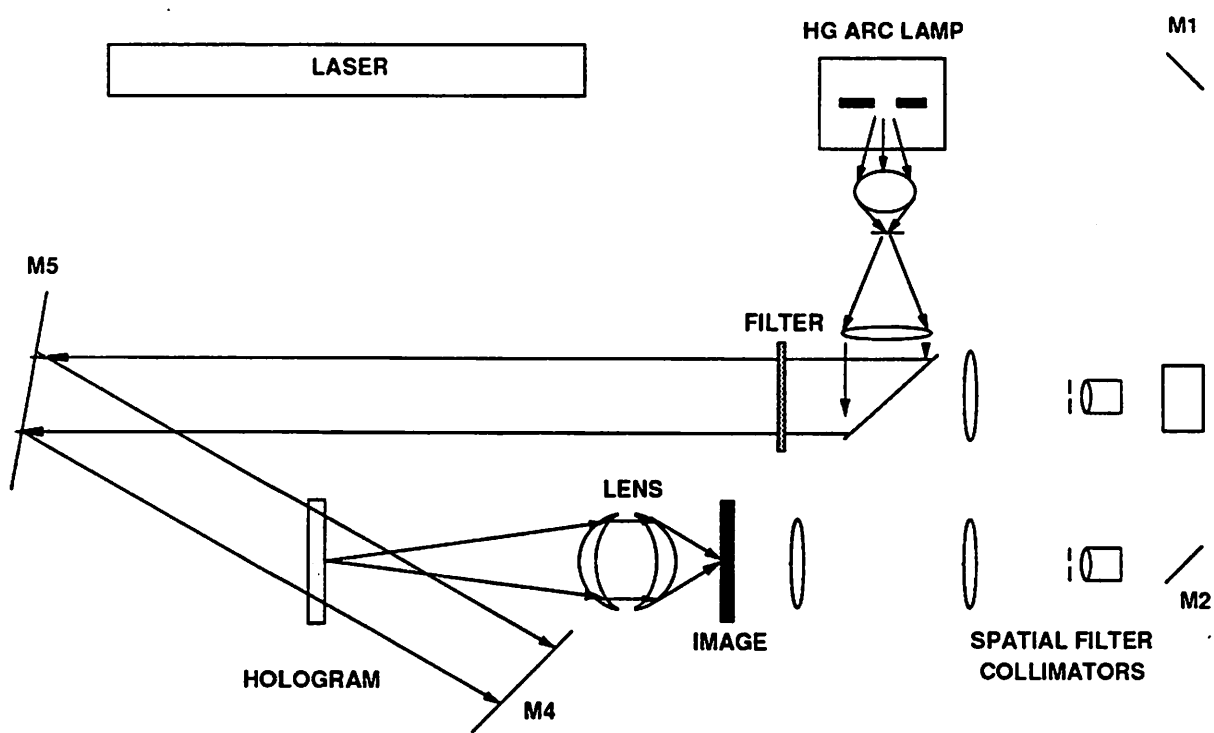
Figure 4.9 Schematic diagram of the apparatus to reconstruct the image from the hologram using a Hg arc lamp.
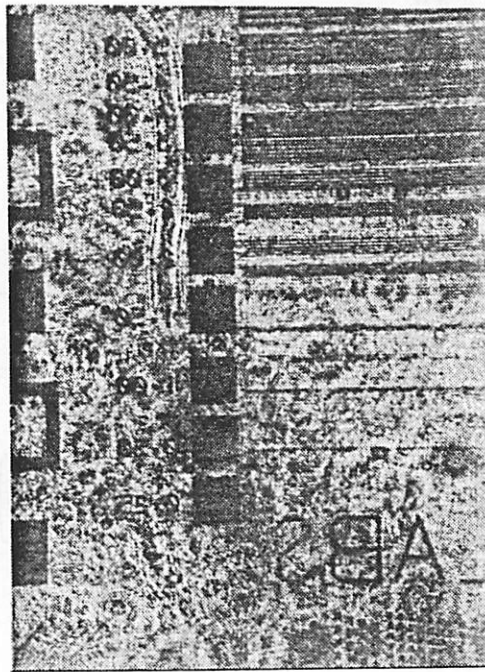
Figure 4.10 A photo-micrograph of a reconstructed aerial image of various line and space widths (1.0 μm to 10.0 μm) using coherent illumination.

Figure 4.11 A photo-micrograph of a reconstructed aerial image of various line and space widths (1.0 μm to 10.0 μm) using incoherent source.

CHAPTER 5

ABERRATIONS

OF A LENS-HOLOGRAM SYSTEM

The imaging lens plays a vital role in a focused-image lens-hologram imaging system. The main purpose of this lens is to capture the maximum amount of information diffracted from the illuminated object and then focus this information onto a small area on a high resolution recording material to form an image-hologram. If the hologram is ideal and is in the exact position as in the set-up in which it was recorded, and the reconstruction beam is the exact conjugate to the reference beam, the real image produced is an exact duplicate of the original object and no wave-front aberrations are present. However, in any other circumstances, the reconstructed image exhibits wave-front aberrations. As revealed in Chapter 4, the attributes of the imaging lens have a large impact on the quality of the reconstructed images in a real system. In particular, a "better" imaging lens results in lesser image degradation resulting from system errors such as mis-registration of the hologram, mis-alignment or imperfect conjugation of the reference beam. Identifying the impact of these system non-idealities is essential for establishing limits and specifications for the system optics, and apparatus configuration geometry, and

hologram material properties.

5.1 Analysis Approach

Meier[5.1] and Leith[5.2] have analytically analyzed the aberrations of lens-less holograms assuming ideal recording and reconstruction conditions have been violated. Both Meier and Leith used a point source on the optical axis as the object wave-front source and represented the spherical reference and reconstruction beams by off-axis point sources. All of the wave-fronts from the point sources were treated as paraxial wave-fronts with respect to the object beam's optical axis. The wave-fronts used were either planar or spherical and hence, the analysis is limited to only the lensless case. In addition, the paraxial representation of the reference and reconstruction wave-fronts with respect to the object beam optical axis limits the analysis to the cases where the reference beam is at angle of less that ten degrees[5.3] with respect to the the object beam axis.

Champagne[5.3] removed the paraxial restriction by representing the wave-fronts about their individual axis. The reference wave-front is treated as paraxial to the axis joining the reference point source and the center of the hologram. Similarly, the image reconstruction wave-front is paraxial to the axis joining the reconstruction point source and the center of the hologram. This analysis is still limited to the lensless holographic cases only.

To include lenses in the optical system, the wave-fronts must be treated as aberrated wave-fronts, as all real lenses have aberrations. In the lensless case, the effect of reconstructing an image with an incorrectly repositioned hologram can be modelled by a system with a correctly positioned hologram with a corresponding

displaced image reconstruction source. With lenses, preserving the relative position of the image reconstruction beam to the hologram does not preserve the relative position of the object beam to the hologram. Thus, the hologram *repositioning* errors can not be absorbed in the relocation of the image reconstructing beam.

Lin[5.4] analyzed a lens-hologram system with a collimated but aberrated reference beam, an identical reconstruction beam, an aberrated object beam, and an incorrectly positioned hologram originally aligned to the object axis. The analysis is a generalization of the Meier and Leith approach which utilizes wave-front matching techniques to solve for the image wave-front aberrations in a closed form.

The resultant wave-front aberrations of the analyzed system are in fourth order polynomials of the object position and image ray slope[5.5]. The coefficients are functions of the reference wave-front beam angle, reference and reconstruction lens' Gaussian image and Seidel aberration coefficients, reference and reconstruction beam pin-hole positions, object lens' Gaussian image and Seidel aberration coefficients, object lens to hologram distance, and rotational and translational variables related to the hologram repositioning errors. However, the analysis is not applicable to the very important case† where the object lens images the object point onto the hologram. Two critical assumptions are violated in this particular case. First, the expansion of the object wave-front after being aberrated by the object lens and directed to the holographic recording material requires the following conditions to be satisfied

$$Z_{og(o)} > X_{og(o)} \qquad\qquad 5.1$$

_____

† We will demonstrate in fact that the system sensitivities to non-idealities such as hologram positioning errors are minimized when the hologram is at the object conjugate.

$$Z_{og(o)} > Y_{og(o)} \qquad\qquad 5.2$$

and

$$Z_{H(o)} - Z_{og(o)} > X_{H(o)} - X_{og(o)} \qquad\qquad 5.3$$

$$Z_{H(o)} - Z_{og(o)} > Y_{H(o)} - Y_{og(o)} \qquad\qquad 5.4$$

where $(X_{H(o)}, Y_{H(o)}, Z_{H(o)})$ is the point on the hologram where the wave-front expansion is matched and $(X_{og(o)}, Y_{og(o)}, Z_{og(o)})$ is the Gaussian conjugate object point. As the Gaussian conjugate image approaches the hologram plane, equations 5.1 through 5.4 are no longer satisfied and thus, the requirements for the wave-front expansion are violated.

Secondly, the Seidel lens aberration coefficients are usually defined with respect to the object or image plane and the exit pupil plane of a lens. The wave-front deviation is correct only when referring to the reference sphere at the exit pupil for a given set of Seidel aberration coefficients. In Lin's[5.4] analysis, the Seidel aberration coefficients for the object lens used to express the wave-front deviations are reference at the hologram plane instead of the exit pupil plane of the object lens. The Seidel aberration coefficients must be converted with respect to the object or image plane and the hologram plane which corresponds to the exit pupil. Aberrated wave-fronts have similar shapes at various different planes and they can be converted to other planes by using a simple linear extrapolation[5.4,5]. However, the extrapolation does not hold for planes in the vicinity of the image plane. Following the analysis by Nijboer[5.6] for computing the Seidel aberration coefficients for a lens, the approximate relations between the wave aberration function and ray aberrations are

$$\frac{\partial W(x,y)}{\partial x} = -\frac{\Delta X}{R} \qquad\qquad 5.5$$

$$\frac{\partial W(x,y)}{\partial y} = -\frac{\Delta Y}{R} \qquad\qquad 5.6$$

where W(x,y) is the wave-front aberration function, R is the radius of the reference sphere, and ΔX, ΔY are the components of the ray aberration. The approximation is only valid as long as R >> W and R >> X. As the conjugate image point approaches the hologram plane, these basic assumptions are violated, and the Seidel aberration coefficients cannot be extrapolated in the vicinity of the image plane of a lens.

Several ray tracing studies[5.7] of hologram aberrations have been completed for mostly lensless holographic cases. Abramowitz[5.8] has completed an analysis that treats an aberrated image through an objective of an aberration-free holographic system, so that the aberrations are solely due to the objective element. The analysis assumes ideal image and recording and reconstruction. In such a holographic system, the aberrations are those of the object lens if the image is evaluated at the image position of the object lens. If the image is evaluated at the original object position, there are no aberrations at all (due to reverse ray tracing)[5.9]. Thus, the present analyses deal with both non-perfect optics and the violation of ideal image reconstruction conditions in order to completely identify and quantify the aberrations in a real system. A first order modelling approach of the system is developed to quickly identify and estimate the key aberrations of the imaging lens that are the dominate factors affecting the sensitivity.

5.2 ANALYTIC MODEL

The main purpose of this section is to help elucidate several of the system sensitivities with regard to the quality of the imaging optics. As discussed in the previous section, Lin[5.4] analytically solved for the third order aberration coefficients for the wave-front aberration function for various perturbations of the reconstruction configuration parameters for a lens-hologram imaging system. However, as was discussed in the previous section, the solution is valid only with the hologram plane at a distance from the lens' image plane. In addition, an intuitive understanding of the behavior of the aberrations coefficients with the quality of the imaging lens is difficult to attain because of the large number of variables and expansion terms as well as the complex dependencies in each of the expansion terms. In this analysis, a much simpler approach is taken to provide insight to the complex behavior of the wave-front aberrations generated for small alterations in the reconstruction system configuration parameters. Although the analysis does not include the aberrations produced by the hologram, it nevertheless provides insight into the complex interaction of the hologram and lens.

The wave-front aberrations of a lens-hologram system for small perturbations of the reconstruction configuration are computed simply as the difference of two wave-fronts which are defined using the third order Siedel coefficients of the imaging lens. The first wave-front is the wave-front recorded by the hologram which is described by the wave-front aberration function of the imaging lens at a particular field point for a specific axial plane. The second wave-front is described by the wave-front aberration function computed for the disturbed system; in particular the field point is modified because the hologram is displaced and the exit-pupil location is displaced because the principle ray is displaced. The aberrations introduced into the reconstructed image are then the difference between these two wave-fronts.

The functional expression for the aberration wave-front for any point in the image field of a lens is written as[5.10]

$$W(x_p, y_p, h) = F\ (x_p^2 + y_p^2) +$$

<div align="right">5.7</div>

$$\frac{1}{8}\ S\ (x_p^2 + y_p^2)^2 +$$

$$\frac{1}{2}\ C\ y_p(x_p^2 + y_p^2)\ \frac{h}{h_o} +$$

$$\frac{1}{4}\ A\ (x_p^2 + 3y_p^2)\ \frac{h^2}{h_o^2} +$$

$$\frac{1}{4}\ P\ (x_p^2 + y_p^2)\ \frac{h^2}{h_o^2} +$$

$$\frac{1}{2}\ D\ y_p\ \frac{h^3}{h_o^3}$$

where $W(s_p, y_p, h)$ is the wave-front deviation from a perfect sphere, x_p and y_p are the normalized exit pupil coordinates, h is the specific field point of interest in the image field, and F† is the coefficient for a constant focus error over the entire field, S is the coefficient for spherical aberration, C is the coefficient for coma, A is the coefficient for astigmatism, P is the coefficient for Petzval curvature, and D is the coefficient for distortion. The wave-front aberration function can be written in a much more compact form by not including the pupil dependencies explicitly and is

$$W_h = F +\ S + C\frac{h}{h_o} + A\frac{h^2}{h_o^2} + P\frac{h^2}{h_o^2} + D\frac{h^3}{h_o^3}.$$

<div align="right">5.8</div>

Consider what occurs when the hologram is displaced laterally from its original construction position and then illuminated at this new position. At the original

---

† A shift of amount $2F/NA^2$[5.6] occurs along the principle ray.

recording position, the hologram has recorded the aberrated wave-front for a specific point in a particular object plane. Now laterally displacing the hologram and illuminating it, the wave-front generated by the hologram is transmitted back-through the lens through a different zone than when it was created. The new wave-front aberration function describing this wave-front is the old wave-front aberration function except displaced by a lateral displacement distance d in the field coordinates. In addition, the effective exit-pupil must also be displaced to that position that yields the same principle ray angle as before the displacement of the hologram.

The wave-front aberration function for a displacement d from a field point h is

$$W_{h+d} = F + S + C\frac{(h+d)}{h_o} + A\frac{(h+d)^2}{h_o^2} + P\frac{(h+d)^2}{h_o^2} + D\frac{(h+d)^3}{h_o^3}. \qquad 5.9$$

For diffraction-limited performance, only very small displacements are possible without completely degrading the reconstructed image. Thus, only the terms that have first order dependence on the displacement length d are included. The wave-front aberration function is then approximated to

$$W_{h+d} = F + S + C\frac{(h+d)}{h_o} + A\frac{(h^2+2dh)}{h_o^2} + P\frac{(h^2+2dh)}{h_o^2} + D\frac{(h^3+3dh^2)}{h_o^3}. \qquad 5.10$$

For this new position, the exit-pupil needs to displaced such that the position for which the exiting ray angle from the exit pupil is the same as when the hologram was recorded. Figure 5.1 illustrates a hologram that has undergone pure lateral displacement and then illuminated. Although it is possible to move the exit-pupil and recalculate the aberrations for this new wave-front, there is a simple method for determining the affect of moving a pupil using the current Siedel coefficients of the wave-front. If the exit-pupil is shifted laterally some distance, the

new principle ray from an object of height h_o crosses the plane of the old exit pupil at a height y' and if the axial ray in the plane of the pupil is y, the ratio of the two ray heights $Q = y'/y$ is the only parameter needed to compute the aberrations of the new system from those of the old. Using the pupil-shift dependencies equations derived in Appendix B, the additional terms to the wave-front aberration function are written as

$$\Delta W_{s-s} > \Delta F^{\bullet} = 0$$

$$\Delta S^{\bullet} = 0$$

$$\Delta C^{\bullet} = QS$$

$$\Delta A^{\bullet} = 2QC\frac{h+d}{h_o} + Q^2 S$$

$$\Delta P^{\bullet} = 0$$

$$\Delta D^{\bullet} = Q(P + 3A)(h + \frac{d)^2}{h_o^2} + 3Q^2 C\frac{h+d}{h_o} + QF + Q^3 S$$

The total wave-front aberration is $W_{tot} = W_{h+d} - W_h + \Delta W_{s-s}$ which can be written as

$$W_{tot} = \frac{1}{2}C^{\bullet} + \frac{1}{4}A^{\bullet} + \frac{1}{4}P^{\bullet} + \frac{1}{2}D^{\bullet} \qquad 5.11$$

where the coefficients are defined as

$$C^{\bullet} = \left[C\frac{d}{h_o} + QS\right] y_p(x_p^2 + y_p^2)$$

$$A^{\bullet} = \left[2A\frac{dh}{h_o^2} + 2QC\frac{h+d}{h_o}\right](x_p^2 + 3y_p^2)$$

$$P^{\bullet} = \left[2P\frac{dh}{h_o^2}\right](x_p^2 + y_p^2)$$

$$D^* = \left[3D\frac{dh^2}{h_o^3} + Q(P + 3A)(h\frac{+d)^2}{h_o^2} + QF\right]y_b$$

From these results, several general conditions for the imaging optics for optimum image reconstruction fidelity and placement for lateral displacements of the hologram can be concluded. The larger the deviation of the lens' image wave-front from a spherical wave-front the more sensitive the reconstructed image is to the hologram lateral displacement error. From a third order analysis, only coma and astigmatism are introduced, spherical aberration is not. However, residual spherical aberration in the lens configuration directly introduces a constant amount of coma over the entire image field into the reconstructed image for lateral displacements errors in the hologram. All the aberration coefficients increase as the image field is traversed. This leads to larger sensitivity to lateral displacement errors at the edge of the field than at the center of the field. The distortion of the image increases linearly with the displacement error d and increases as the square of the image field with constant value related to the residual astigmatism and Petzval curvature coefficient. It is also worth noting that if the hologram recording plane is located not at the paraxial plane, but a distance downstream, only a constant amount of distortion is introduced into the reconstructed image, no other aberration is introduced.

Now, consider what occurs when the reconstruction beam is angularly displaced and then is used to reconstruct the image. First, assume that the hologram produces no wave-front aberrations in this configuration even though the reconstruction geometry is not the conjugate of the recording configuration. At the original hologram recording position, the hologram has recorded the aberrated wavefront for a specific object plane with a particular exit pupil configuration. Now reconstructing the original wave-front with an angularly displaced reconstruction beam shifts the effective exit-pupil location because the angular displacement of the

reconstruction beam adds a constant angular displacement to the entire recon-structed wave-front. This is illustrated in figure 5.2. Thus, the exit pupil needs to be laterally shifted such that the position for which the exiting principle ray angle from the exit pupil will be the same as when the hologram was recorded. The wave-front aberration function due to a change in the exit-pupil is similar to that for the case of lateral displacement. Using the pupil-shift dependencies equations, the additional terms to the aberration function are written as

$$\Delta W_{s-s} > \Delta F^* = 0$$

$$\Delta S^* = 0$$

$$\Delta C^* = QS$$

$$\Delta A^* = 2QC\frac{h}{h_o} + Q^2 S$$

$$\Delta P^* = 0$$

$$\Delta D^* = Q(P + 3A)\frac{h^2}{h_o^2} + 3Q^2 C\frac{h}{h^o} + QF + Q^3 S$$

Terms in higher powers of Q are included here because fairly large Q's are obtained for very small angular displacements due to the lever arm action. The fac-tor Q is found by finding the respective intersection of the new principle ray from the hologram with the exit pupil plane.

Modelling the hologram as a simple diffraction grating, the exit beam direction is governed by the grating equation

$$\frac{\lambda}{a} = \sin(\alpha) + \sin(\beta) \qquad\qquad 5.12$$

where λ is the reconstruction wavelength, a is the grating pitch, α and β are the

incident and exit beam angles respectively. Thus, with a constant grating pitch and wavelength, a small change in incident beam angle is converted to a small change in exit angle. The displaced principle ray is written as $\Delta\theta^*L$ where $\Delta\theta$ is the angular displacement of the reconstruction beam and L is the distance from the hologram recording plane to the exit pupil. Thus, the factor $Q = \Delta\theta^*L / R_{ep}$ where R_{ep} is the radius of the exit pupil.

The total wave-front aberration is $W_{tot} = \Delta W_{s-s}$ which can be written as

$$W_{tot} = \frac{1}{2}C^* + \frac{1}{4}A^* + \frac{1}{2}D^* \qquad 5.13$$

where the coefficients are defined as

$$C^* = \left[QS \right] y_p(x_p^2 + y_p^2)$$

$$A^* = \left[2QC\frac{h}{h^o} + Q^2S \right](x_p^2 + 3y_p^2)$$

$$D^* = \left[Q(P + 3A)\frac{h^2}{h_o^2} + 3Q^2C\frac{h}{h^o} + QF + Q^3S \right]y_b$$

If the reconstruction illumination is altered compared to the hologram record-ing illumination wavelength, the reconstructed wave-front is angularly displaced by a constant amount and the effect to the reconstructed wave-front is very similar to the result to that of an angular displacement of the reconstruction beam. Assuming that the hologram produces no aberrations, the total wave-front aberration function is $W_{tot} = \Delta W_{s-s}$ which can be written as

$$W_{tot} = \frac{1}{2}C^* + \frac{1}{4}A^* + \frac{1}{2}D^* \qquad 5.14$$

where the coefficients are defined as

$$C^* = \left[QS \right] y_p(x_p^2 + y_p^2)$$

$$A^{\cdot} = \left[2QC\frac{h}{h^o} + Q^2S \right](x_p^2 + 3y_p^2)$$

$$D^{\cdot} = \left[Q(P + 3A)\frac{h^2}{h_o^2} + 3Q^2C\frac{h}{h^o} + QF + Q^3S \right]y_b$$

Again, the full set of terms are included because fairly large Q's are obtained for very small shifts in the reconstruction wavelength.

Modelling the hologram as a simple diffraction grating, the exit beam direction is governed by the grating equation 5.12. Using equation 5.12 and fixing the incident beam direction, the change in the exit beam angle β with a change in the incident wavelength is

$$\Delta\theta = \frac{\partial\beta}{\partial\lambda} = \frac{1}{a\cos(\beta)} . \qquad\qquad 5.15$$

Thus, for small deviations of the reconstruction wavelength from the recording wavelength, the reconstructed wave-front is angularly displaced by constant amount. The displaced principle ray intersection at the exit pupil is found as $\Delta\theta^*L$ where $\Delta\theta$ is the angular displacement of the reconstruction wave-front and L is the distance from the hologram recording plane to the exit pupil plane. Again, the factor $Q = \Delta\theta^*L / R_{ep}$ where R_{ep} is the radius of the exit pupil.

From these results, several general conditions for the imaging optics for optimum image reconstruction fidelity and placement for shifts in the wavelength and angular displacements of the reconstruction beam can be established. As was concluded from the lateral displacement of the hologram, the larger the deviation of the lens' wave-front image from a spherical wave-front, the more sensitive the reconstruction image is to the hologram lateral displacement error. From an image quality stand point, only coma and astigmatism are introduced, spherical aberration is not. The coma introduced is constant over the entire field while astigmatism has

both an amount that is constant as well as one that varies over the field. Furthermore, no curvature of the image field is introduced. The distortion of the image increases with displacement d and is related to the astigmatism, Petzval curvature, and coma coefficient. There is also a fixed distortion depending on the residual spherical aberration and fixed focus error coefficient. It is also interesting to note that just as with the lateral displacement of the hologram, if the hologram recording plane is located not at the paraxial plane, but a distance downstream, a constant distortion is introduced. In addition, the factor Q increases proportional to the distance between the exit-pupil and the hologram recording plane (not the lens' image plane).

Finally, we consider what occurs when the hologram is displaced axially along the optical axis and then is illuminated to reconstruct the image. For this registration error, the hologram does not introduced any aberrations into the image because the hologram geometry is constant with the reconstruction source. The hologram records the location of the exit pupil and and displacing the hologram axially also displaces its associated exit pupil. Since the the wave-front error is the difference between the old wave-front function and the modified wave-front function at the exit-pupil plane, the two wave-fronts must be subtracted at the identical exit pupil plane location. Thus, the aberration wave-front function defined for the reconstruction wave-front at its new exit pupil location must be now redefined so that it coincides with the old exit pupil location. Figure 5.3 illustrates this effect.

Usually, the Siedel coefficients are defined with respect to the object and exit-pupil plane of the lens and the wave-front deviation is only correct when referenced to the reference sphere at that plane. However, aberrated wave-fronts have similar shapes at other planes† Thus, using a conversion formula[5.4] to align the

---

† Except for planes near the image plane as discussed in the previous section.

reconstructed exit pupil to the old exit pupil generates the following modifications to the wave-front aberrations of the reconstructed image. The wave-front aberration function is

$$W_{eq} = F^* + \frac{1}{8}S^* + \frac{1}{2}C^* + \frac{1}{4}A^* \quad \frac{1}{4}P^* + \frac{1}{2}D^*$$ 5.16

where the coefficients are defined as

$$F^* = FK^2$$

$$S^* = SK^4$$

$$C^* = 4SK^3L + CK^3$$

$$A^* = 4SK^2L^2 + 2CK^2L + AK^2$$

$$P^* = 2SK^2L^2 + CK^2L + PK^2$$

$$D^* = 4SKL^3 + 3CKL^2 + 2AKL + 2PKL + 2FKL + D$$

where K is $\dfrac{Z_p}{Z_p - \Delta D}$ and L is $-\dfrac{\Delta D}{Z_p - \Delta D}$. Also, Z_p is the exit pupil reference sphere length and ΔD is the axial displacement error of the hologram†.

Since the image plane is displaced axially along the optic axis, the new object plane for best focus is also displaced by an amount $\Delta D/M^2$ where M is the magnification of the system. This axial displacement alters the wave-front aberration function because this displacement alters conjugate positions. Following the analysis by Wynne[5.11] on aberrations produced by conjugate changes, the following adjustments to the Siedel coefficients are required:

$$\Delta W_{cc} > \Delta S = \gamma \left[4C + H\overline{\Delta}(\Pi) \right]$$

---

† ΔD is positive going away from the lens.

$$\Delta C = \gamma \left[2A + PH^2 + H\overline{\Delta}(\mu\underline{\pi}) \right]$$

$$\Delta A = \gamma \left[2D + H\overline{\Delta}(\mu)^2 \right]$$

$$\Delta D = \gamma S$$

where γ is $\dfrac{NA_{obj} \, \Delta D}{M^2 \, FH_{obj}}$, H is $NA_{obj}{}^* FH_{obj}$ the Smith-Helmhotz invariant, P is the Petzval sum, μ is the object space field angle, $\underline{\pi}$ is the image space field angle, FH_{obj} is the object field height, and $\overline{\Delta}$ denotes the change on refraction.

In addition, there is a field dependent pupil-shift which also must be addressed. Using the pupil-shift equations derived in Appendix B, the additions to the Siedel coefficients are written as

$$\Delta W_{s-s} > \Delta F^* = 0$$

$$\Delta S^* = 0$$

$$\Delta C^* = QS$$

$$\Delta A^* = 2QC\frac{h}{h_o} + Q^2 S$$

$$\Delta P^* = 0$$

$$\Delta D^* = Q(P + 3A)\frac{h^2}{h_o^2} + 3Q^2 C\frac{h}{h^o} + QF + Q^3 S$$

where Q is $\dfrac{\Delta D \, FH_{im}}{Z_p \, R_{ep}}$ a function of the image field height and the radius of the exit pupil.

However, the added aberrations due to a change of conjugate and shift in the exit pupil as a function of the field height are negligible for systems requiring very

precise accuracy of the magnification. For example, a maximum displacement of 0.1mm with an exit pupil aperture of 10mm and an exit pupil reference sphere length of 200mm produces a Q of .001. With a Q of .001, the additional aberrations are insignificant for aberrations coefficients less than 100 wavelengths. In addition, the added contributions from the change in conjugate position are also insignificant. A 0.1mm displacement produces γ of .0002, thus, the aberrations from a conjugate change can also be ignored.

Thus, the total wave-front error is written as

$$W_{tot} = W_{con} - W_{eqv} \qquad\qquad 5.17$$

which is

$$W_{tot} = F(1 - K^2)\,(x_p^2 + y_p^2) + \qquad\qquad 5.18$$

$$\frac{1}{8}S(1 - K^4)\,(x_p^2 + y_p^2)^2 +$$

$$\frac{1}{2}\left[4SK^3L + C(1 - K^3)\right]y_p(x_p^2 + y_p^2)\,\frac{h}{h_o} +$$

$$\frac{1}{4}\left[4SK^2L^2 + 2CK^2L + A(1 - K^2)\right](x_p^2 + 3y_p^2)\,\frac{h^2}{h_o^2} +$$

$$\frac{1}{4}\left[2SK^2L^2 + CK^2L + P(1 - K^2)\right](x_p^2 + y_p^2)\,\frac{h^2}{h_o^2} +$$

$$\frac{1}{2}\left[4SKL^3 + 3CKL^2 + 2AKL + 2PKL + 2FKL\right]y_p\,\frac{h^3}{h_o^3}$$

From these results, several general conditions for the imaging optics for optimum image reconstruction fidelity and placement for axial displacements of the hologram can be concluded. Again, the larger the deviation of the lens' image wave-front from a spherical wave-front the more sensitive the reconstructed image is to the hologram axial displacement error. From an image quality standpoint,

spherical aberration, coma, and astigmatism are introduced. Coma and astigmatism term also rely on the the residual Spherical aberration. All aberration coefficients increase as the image field is traversed. This increase leads to larger sensitivity to lateral displacement errors at the edge of the field than at the center of the field. The distortion of the image increases linearly with the displacement error related to the residual astigmatism and Petzval curvature coefficient. It is also worth noting that if the hologram recording plane is located not at the paraxial plane, but a distance downstream, distortion is introduced into the reconstructed image.

The results of this analysis can be applied to other registration errors. For example, a tilt of the hologram about the optical axis can be modelled as a angular displacement of the reconstruction beam with a corresponding axial and lateral displacement of the hologram. Also, for magnification of the hologram, the model would be an displacement due to grating pitch with a field displacement. The divergence of the reference and reconstruction beam can not be included in this simple analysis because the hologram introduces many more aberrations than the other registration errors into the image, and thus a more complete analysis technique is required. However, it may be modelled very simply as a field dependent angular displacement for small spot sizes.

A comparison of the the results derived from this analytic model to the results from the numerical ray-tracing analysis described in the next section for an imaging system using a simple single element lens is discussed in section 5.5 of this chapter.

5.3 RAY-TRACING THROUGH A LENS-HOLOGRAM FOCUSED-IMAGE SYSTEM

Ray-tracing is a analysis technique that tracks the path of a ray from surface to surface for specific optical systems. It is computationally intensive and applicable only to a specific system, but provides a solution of arbitrary precision if the interaction of the ray with each optical element is known.

Evaluation of the image quality and placement of a lens-holographic optical system requires that the wave-front aberration function of the particular optical configuration to be computed. The following is a block description of the procedure:

1). Define the optical configuration (function of the lens properties, ideal location, and positioning error)

2). Trace light rays through optical system† to the hologram plane then back-through the optical system and record their intersection at the original object plane.

3). Using the traverse ray aberrations, calculate the wave-front aberration function to fourth order accuracy.

4). Compute whatever performance parameters are desired (such as the Strehl Intensity Ratio and image location) from the wave-front aberration function.

The next section, 5.3.1 describes the the optical configurations analyzed. Section 5.3.2 describes the ray modelling of the hologram. Section 5.3.3 discusses the wave-front aberration function for an aberrated holographic system and section 5.3.4 discusses the image quality merit measure used to evaluate the optical performance of the holographic system.

---

† Detailed ray tracing procedures for normal optics can be found in MIL-HDBK-141 (1962)

5.3.1 OPTICAL CONFIGURATION

The schematic diagram in figure 5.4 illustrates the recording geometry for the ray-tracing analysis. The object point is located at $P_o(x_o,y_o,z_o)$. The imaging lens is located downstream of the object point source and the hologram is located downstream of the imaging lens in the X-Y plane centered on the optical axis. A transmission hologram is made from two point sources P_o and P_r shown in figure 5.4. The reference beam source is located at $P_r(x_r,y_r,z_r)$ which is in the same z-axis space as the object point. The reference beam is a diverging beam propagating in an index of refraction n_o. The object beam source, P_o, is also a diverging beam propagating in an index of refraction n_o. The imaging lens captures the light rays emanating from the object source and then directs them to the hologram. The hologram has dimensions X_H and Y_H with a holographic recording material thickness D with an initial index of refraction of n_{H-B} before exposure and development. The recording wavelength is λ_R.

The image reconstructing geometry is illustrated in figure 5.5. The image reconstruction beam point source is located to the right of the hologram in an index of refraction of n_o. The image reconstruction beam is also a diverging beam. The reconstructed real image is shown as P_I and is in an index of refraction of n_o. The image reconstruction wavelength is λ_c, which can be different than the the reference wavelength. Also, several rather important changes in the hologram have taken place. The average hologram index of refraction after exposing and development is now n_{H-A}. In addition, the hologram has been linearly and angular displaced from its original construction location and the hologram may have undergone a magnification change, a reduction or magnification of the hologram dimension by a factor M which corresponds to M_x, M_y, and M_z in their corresponding x, y, and z

directions. The scaling factors allow the hologram dimensions to change between exposure and image reconstruction phase to account for fringe spacing in their respective direction independently.

5.3.2 RAY MODELLING OF A HOLOGRAM

A hologram can be described as a record whose optical modulation function corresponds to the intensity pattern between two light beams, reference and object beams. The implicit assumption in this ray-tracing analysis is the interference pattern formed by the two beams is a infinite plane grating.

Illustrated in figure 5.6 are the object and reference rays, $\vec{O}$ and $\vec{R}$, with the direction cosines $\alpha_o, \beta_o, \gamma_o$ and $\alpha_R, \beta_R, \gamma_R$ respectively. The vector form of these rays can be written as

$$\vec{O} = \alpha_o \hat{x} + \beta_o \hat{y} + \gamma_o \hat{z} \qquad 5.19$$

$$\vec{R} = \alpha_R \hat{x} + \beta_R \hat{y} + \gamma_R \hat{z} \qquad 5.20$$

where $\hat{x}, \hat{y},$ and $\hat{z}$ are unit vectors in the x, y, and z direction. The grating plane created by the object and reference beam is shown in figure 5.6. To determine the equation of this plane, it is necessary to compute the direction cosines of the vector normal to the plane. Two vectors are need to needed to define the grating plane. The first vector locates the plane that lies in the direction that bisects the object and reference rays which is

$$\vec{A} = \frac{\vec{O} + \vec{R}}{2}. \qquad 5.21$$

The second vector, $\vec{P}$ is the cross product of the object and reference rays.

$$\vec{P} = \vec{O} \times \vec{R} \qquad 5.22$$

Both vectors, $\vec{A}$ and $\vec{P}$ are illustrated in figure 5.6. The vector $\vec{P}$ defines the plane of incidence for the two vectors. The grating vector is perpendicular to this vector. Thus, the vector perpendicular to both $\vec{A}$ and $\vec{P}$, $\vec{N}$ is the cross product of the two vectors.

$$\vec{N} = \vec{A} \times \vec{P}$$ 5.23

Also illustrated in figure 5.6 is the grating vector $\vec{N}$. The length of this vector, $\|N\|$ is $\frac{2\pi}{\Lambda}$ where Λ is the distance between the grating planes. From Smith[5.12], the respective grating plane distances along each of the axis are

$$d_x = \lambda_r/(\alpha_o - \alpha_r)$$ 5.24

$$d_y = \lambda_r/(\beta_o - \beta_r)$$

$$d_z = \lambda_r/(\gamma_o - \gamma_r)$$

where λ_r is the reference and object wavelength. The distance between the grating plane, Λ can be found by applying equation 5.24 into 5.21.

$$\Lambda = \frac{d_x}{\alpha_N}$$ 5.25

or if $\alpha_N = 0$ then Λ can be found from the other two components. The grating properties have been found before exposure and development, the next step is to examine the image reconstruction properties of the resultant grating after the hologram has been processed.

In the image reconstruction process, the image reconstruction beam interferes with the hologram and is diffracted. Any change in hologram physical properties will change the diffraction properties of the hologram. Now assume the holographic recording material after exposure and development has the dimensions $M_x \cdot x_H$, $M_y \cdot y_H$, $M_z \cdot z_H$ which is a scaled version of the original recording†. Two

---

† In reality, M_x, M_y = 1 because the recording material is coated onto a substrate.

important changes have occurred to the hologram properties: the direction of the grating vector and its magnitude. Figure 5.7 illustrates the changes that occur for $M_z = .5$.

To determine the new grating vector direction and magnitude, the new component grating plane distances are found. The new distances are

$$d_{x_a} = M_x * d_x$$

$$d_{y_a} = M_y * d_y \hspace{6cm} 5.26$$

$$d_{z_a} = M_z * d_z$$

where d_{x_a}, y_a, z_a are the new component grating distances. The new grating vector magnitude , Λ_a, can be written using equation 5.25 and 5.26 as

$$d_{x_a} * \alpha_a = \Lambda_a = M_x * d_x * \alpha_a$$

$$d_{y_a} * \beta_a = \Lambda_a = M_y * d_y * \beta_a \hspace{4cm} 5.27$$

$$d_{z_a} * \gamma_a = \Lambda_a = M_z * d_z * \gamma_a$$

where α_a, β_a, and γ_a are the direction cosines of the grating vector.

The next vector to compute is the direction cosines of the new grating vector. Given a vector $\vec{V} = (X, Y, Z)$ with direction cosines (α, β, γ), the new vector will have coordinates $\vec{V}_a = (M_x x, M_y y, M_z z)$ with directions cosines ($\alpha_a, \beta_a, \gamma_a$) . The direction cosines (α, β, γ) are transformed into the new direction cosines with the following transformation:

$$\alpha_a = \frac{1}{\sqrt{1 + \frac{1}{(M_x \alpha)^2}[(M_y \beta)^2 + (M_z \gamma)^2]}} \hspace{3cm} 5.28$$

$$\beta_a = \frac{\beta M_y}{M_x \alpha} \alpha_0$$

$$\gamma_a = \frac{\gamma M_z}{M_x \alpha} \alpha_o$$

for $\alpha \neq 0$. If $\alpha = 0$ and $\beta \neq 0$ then the following transformations should be exercised:

$$\beta_a = \frac{1}{\sqrt{1 + \frac{1}{(M_y \beta)^2} [(M_x \alpha)^2 + (M_z \gamma)^2]}} \qquad \qquad 5.29$$

$$\alpha_a = \frac{\alpha M_x}{M_y \beta} \beta_o$$

$$\gamma_a = \frac{\gamma M_z}{M_y \beta} \beta_o$$

If $\alpha = 0$ and $\beta = 0$, then the last transformation must be used.

$$\gamma_a = \frac{1}{\sqrt{1 + \frac{1}{(M_z \gamma)^2} [(M_x \alpha)^2 + (M_y \beta)^2]}} \qquad \qquad 5.30$$

$$\alpha_a = \frac{\alpha M_x}{M_z \gamma} \gamma_o$$

$$\beta_a = \frac{\beta M_y}{M_z \gamma} \gamma_o$$

To determine the equation of the grating plane, equations 5.28-5.30 must be applied to to the vectors defined in equations 5.22 and 5.23. The vector normal to the grating plane is then given by 5.11 using the modified vectors $\vec{P}_o$ and $\vec{A}_o$.

Now assume that reconstruction beam impinges on the hologram with direction cosines α_c, β_c, and γ_c. The hologram diffracts this beam producing an image ray with direction cosines of[5.12]

$$\alpha_i = \alpha_c \pm (\lambda_c/d_{x_o}) \qquad\qquad 5.31$$

$$\beta_i = \beta_c \pm (\lambda_c/d_{y_o}) \qquad\qquad 5.32$$

$$\gamma_i = \pm\, \text{sign}(\gamma_c)\sqrt{1.0 - \alpha_i^2 - \beta_i^2} \qquad\qquad 5.33$$

where α_c and β_c are the $\hat{x}$ and $\hat{y}$ direction cosines for the recording beam and λ_c is the recording wavelength. If the hologram is considered to be a generalized diffraction grating, the image ray produced is considered the +1 order ray, since the image ray leaves the hologram with the same tilt in the same direction with regard to the reconstructing ray as had the original object ray with regard to the reference ray. Thus, the positive sign in equation 5.31-5.33 is used to compute the direction cosines of the image ray. The direction cosines for the image ray are only correct for the specific geometry such that the hologram is illuminated with a reconstruction beam which is conjugate to the reference beam direction.

Summarizing, the object and reference rays generate a series of grating planes within the holographic recording media. The recording media volume can be scaled by multiplicative factors M_x, M_y, and M_z. Then, by applying the correct vector transformations to the vectors describing the grating, a new set of vectors characterizing the the grating can be computed. The grating diffraction process generates an image-beam ray that is described as a function of the grating parameters and incoming beam-direction-cosines.

5.3.3 THIRD ORDER ABERRATIONS FOR A HOLOGRAM

The wave-front reconstruction process produces aberrations in the recon-structed image when ever the condition of image reconstruction does not accurately duplicate or complement those of the hologram producing process. These aberrations can be described by a wave-front aberration function that is a fourth order polynomial function of the pupil coordinates and coordinates of the image point. The traverse ray aberrations are computed through numerical ray-tracing and are functionally related to the wave-front aberration function. The functional dependence is

$$\Delta x_i = \frac{1}{NA_x} \frac{\partial w(x_p, y_p)}{\partial x_p} \qquad \qquad 5.34$$

$$\Delta y_i = \frac{1}{NA_y} \frac{\partial w(x_p, y_p)}{\partial y_p} \qquad \qquad 5.35$$

where Δx_i and Δy_i are the traverse ray aberrations, NA_x and NA_y are the numerical aperture of the imaging system from their corresponding axes as seen from the imaging plane, and $W(x_p, y_p)$ is the wave-front aberration function expanded in rec-tangular coordinates with normalized pupil coordinates as variables.

The wave-front aberration function for an off-axis hologram is quite different than that for a centered lens system. Because the reference beam and reconstruc-tion beam are at an off-axis angle with respect to the optical axis of the system, there are no planes of symmetry for a holographic system; the wave-front aberra-tion function must contain all possible combinations of the exit pupil and image coordinates.

The wave-front aberration function can be separated into a series expres-sion[5.5]

$$W_{(T)} = W_{(0)} + W_{(1)} + W_{(2)} + W_{(3)} + W_{(4)} \qquad 5.36$$

where $W_{(n)}$ is of degree n in (x_o, y_o, p, q). The term $W_{(0)}$[5.5] is a constant and can be set to zero with no of loss generality.

The $W_{(1)}$ term is:

$$W_{(1)} = A_1p + A_2q. \qquad 5.37$$

A_1 and A_2 represent lateral shifts in the image location in the p and q directions.

The $W_{(2)}$ term is:

$$W_{(2)} = B_1p^2 + B_2x_op + B_3y_oq + B_4q^2 + B_5pq + B_6x_oq + B_7y_op. \qquad 5.38$$

B_2 and B_3 are magnifications in the x and y directions respectively. The terms B_6 and B_7 represent distortions. A point is imaged as a point, but extended objects and their images are not similar since the distance of the image point from the axis is not proportional to the distance of the object point from the axis.

The $W_{(3)}$ term is:

$$W_{(3)} = C_1p^3 + C_2p^2q + C_3pq^2 + C_4q^3 + C_5x_op^2 + C_6y_op^2 + \qquad 5.39$$

$$C_7x_o^2p + C_8y_o^2p + C_9x_oy_op + C_{10}x_oq^2 + C_{11}y_oq^2 +$$

$$C_{12}x_o^2q + C_{13}y_o^2q + C_{14}x_oy_opq + C_{15}x_opq + C_{16}y_opq.$$

The coefficients C_7, C_8, C_9, C_{12}, and C_{13} represent distortion terms.

The third order aberrations have their wave-front expansion $W_{(4)}$:

$$W_{(4)} = D_1p^4 + D_2p^3q^1 + D_3p^2q^2 + D_4pq^3 + D_5q^4 + \qquad 5.40$$

$$D_6x_op^3 + D_7x_opq^2 + D_8x_opq^2 + D_9x_oq^3 + D_{10}y_op^3 + D_{11}y_op^2q +$$

$$D_{12}y_opq^2 + D_{13}y_oq^3 + D_{14}x_o^2p^2 + D_{15}x_o^2q^2 + D_{16}x_o^2pq + D_{17}y_o^2q^2 +$$

$$D_{18}y_o^2p^2 + D_{19}y_o^2pq + D_{20}x_oy_op^2 + D_{21}x_oy_oq^2 + D_{22}x_oy_opq +$$

$$D_{23}x_o^3p + D_{24}x_o^3p + D_{25}y_o^3p + D_{26}y_o^3q + D_{27}x_o^2y_op + D_{28}x_o^2y_oq+$$

$$D_{29}x_oy_o^2q+ D_{30}x_oy_o^2p.$$

The coefficients D_{23}, D_{24}, D_{25}, D_{26}, D_{27}, D_{28}, D_{29}, and D_{30} are distortion terms.

The aberration coefficients can be collapsed into various orders and re-written as functions of only p and q†, which can be represented as coordinates of the exit pupil. This allows the determination of the wave-front aberration function at a unique field position. From a computational and data storage viewpoint, this is much more advantageous because many rays are required for a ray-tracing analysis to compute the coefficients of the wave-front aberration function over the entire image field rather than for a single field point.

The collapsed wave-front is :

$$W_{(T)} = Ap + Bq + Cpq + Ep^2 + Fq^2 + Gp^2q + Hpq^2 + Ip^3 + Jq^3 + \qquad 5.41$$

$$D_1p^4 + D_2p^3q^1 + D_3p^2q^2 + D_4pq^3 + D_5q^4$$

where the coefficients can be derived from equations 5.37-5.40. The coefficients A and B represent lateral image shifts in the p and q directions. The terms C, E, and F are defocusing coefficients (function of square of the pupil coordinates) with E and F in the p and q directions. The coefficient C expresses a focusing error for a tilted wave-front. G, H, I, and J are non-symmetric third order terms expressing comatic aberrations.

The coefficients of the collapsed wave-front aberration function can be computed with relationships expressed in equation 5.35 and 5.36. A simple linear regression algorithm produces the correct coefficients given appropriate number

---

† The derivation is listed in Appendix C

and location of rays are chosen[5.13].

5.3.4 IMAGE ASSESSMENT

There are several image quality criteria used today; these are the Rayleigh quarter-wave criterion[5.6] which is the requirement that the peak to peak wave-front aberration is less than a quarter of a wave at the edge of the exit pupil, the spot size criterion[5.14, 15] which measures the radius of the traverse ray aberrations, the the Optical Transfer Function[5.16] (OTF) which describes the image quality in terms of the Fourier Transform of the point spread function, and the Strehl Intensity Ratio [5.17] which compares the maximum value of the point spread function of an aberrated system to that of an aberration free system.

The Raleigh criterion is a tolerance applicable to optical systems which have almost perfect correction except for a very specific aberration.† The criterion relies on the fact that if the wave-front at the exit pupil deviates from a reference sphere centered on the ideal image point by less than a quarter wavelength, then the effect on the Airy image pattern is small. However, the type of aberration present in an optical system has a strong influence on the magnitude of the wave-front aberration that will affect the Airy image pattern.

The spot diagram is a plot of ray intersection points in the image plane. The size of the spot is a faithful representation of the image point spread function, however, the wave nature of light is completely ignored. Thus, it is not commonly used for evaluating near-diffraction-limited optical systems.

---

† Criterion was originally used by Sir Raleigh [5.6] for the the special case of spherical aberration.

The optical transfer function is today the major basis for establishing an optical system quality criterion[5.18]. However, the use of the OTF is time consuming process due to the necessity of evaluating the OTF at different frequences and azimuth directions.

The Strehl Intensity Ratio is physically meaningful for small aberrations. Marchel[5.6] related the Strehl Intensity Ratio of small aberrations to the variance of the wave-front aberration function. The variance of the wave-front is easily related to the wave-front aberration coefficients. If the wave-front aberration function is expanded in Zernike[5.19] polynomials, the corresponding coefficients can be directly related to the Strehl Intensity Ratio[5.6]. The utility of the Strehl Intensity Ratio is in its ability to consider the significance of an arbitrary combination of aberrations. However, the criterion is only useful for small aberrations (such that the Strehl Intensity Ratio is greater than $\approx .8$).

The Strehl Intensity Ratio criterion has the best applicability for near-diffraction-limited optical systems where good performance at spatial frequencies up to the cut off frequency is of interest and for gaining insight into system tolerances for maximum performance. In addition, the Strehl Intensity Ratio bears a direct relationship to the process latitude available to control the line-width of small features in an image recording medium. For features on the order of $\frac{\lambda}{NA}$, the Strehl Intensity Ratio accurately reflects the peak image intensity. In this sense, the Strehl Intensity Ratio is directly related to the final pattern definition in the image recording media[5.18].

The Strehl Intensity Ratio for small aberrations is simply related to the wave-front aberration function. The Strehl Intensity Ratio is

$$SR = 1 - \frac{4\pi^2}{\lambda^2}\left[\frac{\iint W^2 ds}{S} - \left[\frac{\iint W ds}{S} \right]^2 \right]$$

5.42

where λ is the image forming wavelength, W is the wave-front aberration function which is evaluated over the exit pupil of area S of the optical system[5.6].

Expressing the variance† in equation 5.42 of the collapsed wave-front aberration in equation 5.41 the following expression is obtained:

$$\text{Variance} = \frac{A^2}{4} + \frac{B^2}{4} + \frac{C^2}{24} + \hspace{4cm} 5.43$$

$$\frac{AI}{4} + \frac{BJ}{4} + \frac{GB}{12} + \frac{AH}{12} +$$

$$\frac{E^2}{8} + \frac{F^2}{8} + \frac{EF}{12} +$$

$$\frac{5}{64}\left[I^2 + 2ED_1\right] + \frac{5}{64}\left[J^2 + 2FD_5\right] +$$

$$\frac{1}{64}\left[G^2 + 2CD_2 + 2ED_3 + 2FD_1 + 2HJ\right] +$$

$$\frac{1}{64}\left[H^2 + 2CD_4 + 2ED_5 + 2FD_3 + 2GH\right] +$$

$$\frac{7}{128}\left[D_1^2 + D_5^2\right] + \frac{3}{640}\left[D_3^2 + 2D_5D_1 + 2D_2D_4\right] +$$

$$\frac{1}{128}\left[D_2^2 + D_4^2 + 2D_1D_3 + 2D_3D_5\right] - \left[\frac{E+F}{4} + \frac{D_1+D_5}{8} + \frac{D_3}{24}\right]^2$$

where the coefficients have been defined previously.

---

† The variance of the wave-front aberration function is $\left[\dfrac{\iint W^2 ds}{S} - \left(\dfrac{\iint W ds}{S}\right)^2\right]$.

5.4 ABERRATIONS OF A NON-IDEAL LENS-HOLOGRAM

In this section, simulation results of the optical performance are presented for the simple holographic optical imaging system using the single element lens described in Chapter 4 as well as for a similar system which uses a well-corrected imaging lens. The holographic optical imaging system is schematically illustrated in figure 5.4. The reference source is an off-axis point source. The object point in the analysis is also modelled as a point source. The imaging lens is located axially along the optic axis such that the object plane is imaged with a magnification M. The hologram is positioned in the paraxial image plane of the object and is assumed to be perpendicular to the optical axis during the recording, The holographic recording material is assumed to produce a local grating with a constant grating amplitude.

In reconstruction mode, the reconstruction point source is nominally located conjugate to the reference point source. Figure 5.5 illustrates the reconstruction geometry. The optical performance of the system is evaluated at the original object plane except when the hologram is axially displaced in which case it is evaluated at the plane of best focus. The results are presented using the Strehl Intensity Ratio for image quality and image distortion plots for image placement. The analysis identifies key system sensitivities and establishes allowable variations in the the image reconstruction wavelength, and hologram location, reconstruction point location.

5.4.1 IMAGING PERFORMANCE OF THE SIMPLE LENS

Table 5.1 enumerates the lens specifications and the relevant geometry of the

the system.

Single Element Lens and System Specifications		
Object Plane Location	0	mm
First Surface Location	40	mm
Radius of Front Surface	34.44	mm
Thickness	28.36	mm
Radius of Back Surface	-34.44	mm
Entrance Pupil	40	mm
Index of refraction	1.5	
Magnification	3.6	
Reference Beam Curvature	0.0	mm^{-1}
Construction Beam Curvature	0.0	mm^{-1}
Construction Beam Angle	45	degrees
Hologram Location	242	mm
Hologram Material Thickness	.025	mm
Hologram Material Index of Refraction	1.5	

Table 5.1 Single Element Lens and System Specifications

The hologram is located at the paraxial image plane. The performance for numerical apertures of the imaging system in object space up to .4 is examined. Figure 5.8 illustrates the traverse ray aberrations also commonly known as spot diagrams for the lens at the center of its field in this configuration.† Also included in this figure is the optical path difference (OPD) graph.‡ The lens displays fourth, sixth, and eighth order spherical aberration at the center of its field. From the spot diagram,

---

† The imaging performance of such a simple lens is so poor that the Strehl Ratio is not useful; hence the use of the spot diagram.

‡ The optical path difference is a measure of the distance each ray travels compared to that of the principle ray.

the object point rays are not concentrated in small area, but are distributed over a wide area in the image plane. As discussed in Chapter 3, the size of the spot diagram dictates the image reconstruction illumination beam temporal coherence requirements. From equation 3.34, the illumination beam bandwidth must be less than

$$\Delta\lambda \approx \frac{\lambda_{cons}^2}{2 D_{spot}}$$ 5.44

where λ_{cons} is the image reconstruction wavelength and D_{spot} is the diameter of the traverse ray aberration spot. The illumination bandwidth for λ_{cons} = 488 nm is $\approx$ 2.3 pm for NA .4.

Figure 5.9 and 5.10 display the spot diagrams and OPD graphs for the identical lens in the same configuration but operating with a numerical aperture of .2 and .1 respectively. The spot diagrams and corresponding OPD graphs show a large reduction in spherical aberration. With the large decrease in the spot sizes, the temporal coherence requirement is significantly reduced and is 29 pm for NA .2 and 230 pm for NA .1.

5.4.2 IMAGING PERFORMANCE OF THE LENS-HOLOGRAM SYSTEM

An ideal holographic lens-hologram imaging system would use the simplest possible imaging lens[5.20], and would display no aberrations because of reverse ray tracing. In fact, the Strehl Intensity Ratio would be unity. However, a real system has a variety of imperfections as noted earlier. Figures 5.11 through 5.17 illustrates the degradation of the image quality for the three operating numerical apertures, .1 .2 and .4, as various system parameters are altered one at a time. In figure 5.11, the Strehl Intensity Ratio is plotted versus the lateral displacement of

the hologram from its original recording position for the three numerical apertures. The image quality of the system operating with NA of .4 is extremely sensitive to any lateral displacement in the hologram. As expected, the lateral displacement sensitivity is reduced as the operating NA is reduced because the effective lens quality (spherical aberration is reduced) is increased. Figure 5.12 displays the Strehl Ratio versus axial displacement of the hologram from its original recording position with refocussing. The NA .4 system is extremely sensitive to repositioning errors of the hologram. As anticipated, the system operating with NA .2 or NA .1 is less sensitive. The degradation of the image quality for hologram displacements laterally and axially are strong functions of the of the residual spherical aberration of the lens.† Thus, a lens corrected for spherical aberration will decrease the sensitivity of the image quality to lateral or axial displacements of the hologram from its original recording position.

Any differences in the image reconstruction wavelength, reconstruction beam angle, or reconstruction beam wave-front curvature also degrades the image quality, because the changes create wave-front aberrations from the hologram which are then coupled with the lens' aberrations to introduce wave-front errors into the image wave-front. Figure 5.13 displays the Strehl Ratio versus a change in the image reconstruction wavelength from the reference wavelength. It is assumed that the index of refraction of the lens remains constant. Again, the wave-front error increases with NA, because of the coupling noted above. Figure 5.14 illustrates the Strehl Ratio with the image reconstruction angle displaced from the its conjugate position. The NA .4 system is again found to be extremely sensitive to any angular

---

† The reconstruction beam is conjugate to the reference beam for hologram displacements in the lateral and axial directions. Thus, the hologram is under ideal illumination conditions for changes in the hologram position.

displacement. The NA .2 and .1 show less sensitivity. Figure 5.15 displays the Strehl Ratio against the image reconstruction beam wave-front error measured in wavelengths. The sensitivities to the wave-front error in the reconstruction beam are similar. For example, at NA = .4, a SR of .97 requires the reconstruction beam curvature to be less than .01 of a wavelength flat over the hologram at 488nm. The other two NA's show an improvement greater than two orders of magnitude in reduced sensitivity.

If the hologram undergoes a small change in its physical dimensions (such as a small lateral linear growth due to a rise in ambient temperature assuming the holographic material is coated on glass substrate), the resulting reconstructed image will be aberrated. Figure 5.16 illustrates the Strehl Ratio for equal magnifications in the "X" and "Y" directions. The NA = .4 system again is extremely sensitive to any magnifications. The NA = .2 and .1 show much less sensitivity.

The formation of any hologram involves the exposure of light-sensitive materials to the object and reference beam. The exposure alters the index of refraction of the recording material. This change in the index from recording the hologram to reconstructing the image violates the assumption that the reconstruction process is perfectly conjugate to the recording process. Figure 5.17 illustrates the Strehl Ratio for changes in the average index of refraction of the hologram. The NA = .4 system is found to be very sensitive to any changes in the hologram index of refraction. The NA = .2 and .1 are much less sensitive. The typical change in index of refraction of a hologram is much less than 0.1, and thus, for the low NA systems, it not a crucial parameter.

Sensitivity graphs of the traverse ray spot diameters at the different numerical apertures versus each of the reconstruction parameters for Strehl Intensity Ratio of .8 are shown in figure 5.18. From the graphs, there is a one to one correlation

between the traverse ray spot diameter at the center of the field and the lateral displacement of the hologram, the angular displacement of the reconstruction beam, angular deviation of the reconstruction beam, and the magnification of the hologram grating. This suggest a one to one correspondence between the amount of residual spherical aberration in the imaging lens and these reconstruction parameters to achieve a Strehl Intensity Ratio of .8. The sensitivity graphs of axial displacement of the hologram and divergence of the reconstruction beam show a dependence greater than a one to one correspondence on traverse ray spot diameter. This suggest a non-linear process between the traverse ray spot diameter and these two parameters.

The lens operating at NA .1 satisfies the goal of localizing the object image to effectively exploit the properties[5.21] of focused image holograms. Figure 5.19 through 5.21 illustrate the spot diagrams and OPD graphs at the center of the field and also at half the field height and at the edge of the field for the lens operating at NA .1. As the image field is traversed, the lens' ability to focus the image point is severely degraded as seen in the the associated spot diagrams. Figures 5.22 through 5.27 illustrates the Strehl intensity Ratio versus several system parameters that are altered. The Strehl Intensity Ratio degrades as the image field is traversed. The image fidelity sensitivity is dominated by the lens aberrations at the edge of the field.

The sensitivity graphs of the traverse ray spot diameters across the field versus several reconstruction parameters for Strehl Intensity Ratio of .8 are shown in figure 5.28. The lateral displacement of the hologram, the angular displacement of the reconstruction beam, the deviation of the reconstruction wavelength, and the magnification of the hologram grating show a smaller sensitivity as the spot size increases as the field is traversed than the axial displacement of the hologram and

the divergence of the reconstruction beam.

Microlithography applications not only require image fidelity to be perfect, but they also have very stringent image placement requirements. For a typical microlithography imaging system, image placement must be better than .05 μm through the entire image field[5.22]. Figures 5.29 through 5.31 displays the distortion through the image field for changes in image reconstruction wavelength, reconstruction beam wave-front, and reconstruction beam angle. The image distortion† is the largest for wavelength and angular displacement change. The distortion plots for angular displacement and deviation in the reconstruction wavelength have similar shapes. This suggest that the distortion from these two parameters have similar functional dependencies. The distortion plot for divergence of the reconstruction beam show zero distortion at the center of the field as expected and a large increase at the edge of the field. This due to the reconstruction beam's effective illumination angle has been displaced with respect to the edge of the field. Even though the Strehl Intensity Ratio is greater than .95 over the entire field for these alterations, the image distortion is much too large for a practical system.

5.4.3 ABERRATIONS USING A MULTI-ELEMENT LENS

In the previous section, the sensitivity of the holographic imaging system utilizing a single element lens was studied. Results from reducing the operating numerical aperture suggest that a well corrected lens may be less sensitive to any system non-idealities than for a simple, uncorrected lens. Definite conclusions could not be ascertained because as the lens' numerical aperture is decreased, the

---

† Distortion is defined to be the original object point location minus the imaged point location.

effective numerical aperture seen at the hologram plane is also decreased. The aberrations of a hologram are functions of its effective numerical aperture[5.23, 24] and thus, as the lens aberrations are decreased by reducing its effective numerical aperture, the hologram's ability to distort the wave-front is also similarly reduced. Using a well corrected lens with a large NA increases the numerical aperture seen by the hologram but does not increase the lens' effective spot size at the hologram plane.

The system performance with a model well-corrected lens is examined. A diagram of the optical elements is shown in figure 5.32[5.25] and the specifications are listed in table 5.2. The lens is a simple four-element lens corrected for use at infinite conjugate and a field of view of 6 degrees. This lens was chosen because the design was in the public domain and the lens has the typical performance of an ordinary 4 element lens (such as used in photography). The hologram is located at the paraxial image plane and the numerical aperture of the imaging system in object space is .2 with an image magnification of 3.6. Figures 5.32 through 5.34 illustrate the spot diagrams and OPD graphs of the lens at the center, half field height, and at the edge of the field. The lens has a spot diameter of 60 μms at the center of the field and increases as the image field is traversed to approximately 2.5 mm. Figures 5.36 through 5.41 display the Strehl Ratio with various system parameters altered. As expected, the image quality sensitivity increases as the field is traversed because the lens' aberrations increase with the field.

The image distortion with changes in the illumination beam wavelength at $\Delta\lambda$ = 10 pm and 50 pm is shown in figure 5.42. The distortion is less 0.02 μms over the field for $\Delta\lambda$ = .01 nm which corresponds to a Strehl Ratio of .95 over the entire image field. Increasing the wavelength deviation $\Delta\lambda$ to .05 nm reduces the field in half to attain a Strehl Ratio of .95. Comparing the two graphs, the distortion

Lens and System Specifications		
Object Plane Location	0	mm
Lens Magnification Factor	40	
First Surface Location	33	mm
Radius of Front Surface	-.538534	mm
Index of refraction	1.62	
Thickness	.2941	mm
Radius of Next Surface	.96835	mm
Thickness	.0696	
Radius of Next Surface	.430533	mm
Index of refraction	1.649	
Thickness	.25	mm
Radius of Next Surface	-1.1314649	mm
Thickness	.0568	mm
Radius of Next Surface	8.41326	mm
Index of Refraction	1.62	
Thickness	.1900	mm
Radius of Next Surface	.6568792	mm
Thickness	.0144	mm
Radius of Next Surface	-1.516898	mm
Index of Refraction	1.62	
Thickness	.25	mm
Radius of Next Surface	11.239744	mm
Entrance Pupil	-.025	mm
Magnification	3.6	
Reference Beam Curvature	0.0	mm^{-1}
Construction Beam Curvature	0.0	mm^{-1}
Construction Beam Angle	45	degrees
Hologram Location	231.1	mm
Hologram Material Thickness	.025	mm
Hologram Material Index of Refraction	1.5	

Table 5.2 Multi-Element Lens and System Specifications

increases linearly with the change in wavelength, but is well below 0.1 μms. Figures 5.42 and 5.43 illustrate the distortion with changes in the angular position and wave-front curvature of the illumination beam.

5.4.4 COMPARISON OF A SINGLE ELEMENT LENS WITH A MULTI-ELEMENT LENS

The spot diagrams for the single element lens operating with an NA of .1 and the multi-element lens with operating with NA of .2 are comparable. The aberrations that dominate each lens are different but the maximum path differences displayed in their OPD graphs are very similar when used in the lens-hologram imaging system. The degradation behavior of the Strehl Intensity Ratio for both the lateral and axial displacements are very similar (although the well corrected lens shows much faster degradation at the edge of the field). The other variations which are dependent on the both the hologram and lens show only slight differences even though the numerical aperture seen by the hologram is much larger for the system with the well-corrected lens. The sensitivity with the image field follows the same trend as for the sensitivity to lateral and axial displacements. This suggests that lens quality is the dominant factor and not the aberrations introduced by the hologram which influence the image fidelity sensitivity at this level of lens correction.

5.4.5 SENSITIVITY AT A PLANE OTHER THAN THE IMAGE PLANE

Figures 5.45 through 5.47 illustrate the spot diagrams and OPD graphs for the multi-element lens at the center, half, and edge of the field at a plane 50 mm downstream from the paraxial image plane. The spot diameters have all

dramatically increased, however, if the hologram is placed here its effective numerical aperture is the same as at the ideal conjugate plane. Figures 5.48 through 5.53 illustrate the image quality degradation for alterations in the various system parameters. As expected, the image fidelity sensitivity to both lateral and axial displacement of the hologram show very little difference in sensitivity compared to those with the hologram recorded in the paraxial image plane. This result is in agreement with the analytic model presented in section 5.2. Alterations in the reconstruction wavelength, angular displacement, and wave-front curvature of the illumination beam exhibit greater sensitivity compared to those with the hologram recorded in the image plane. Again, this result is in agreement with the analytic model presented in section 5.2. The divergence of the reconstruction wave-front at the the center and half field position show much greater sensitivity than those with the hologram recorded in the paraxial image plane.

Figures 5.54 through 5.56 displays the distortion over the image field for changes in reconstruction wavelength, angular displacement, and wave-front curvature of the illumination beam. The graphs all exhibit a large increase in the image distortion. There is a constant distortion added through out the field for both the angular displacement of the reconstruction beam and for deviation of the reconstruction wavelength. These results can be predicted from the analytic model.

5.5 COMPARISON OF THE ANALYTIC MODEL AND THE RAY-TRACE MODEL

The results from the ray-tracing analysis of the simple lens at the center of its field at various numerical apertures suggest that there is a one to one relationship between the amount of residual spherical aberration and the registration tolerance to achieve a Strehl Intensity Ratio of 0.8 for the lateral displacement of the

hologram, an angular displacement of the reconstruction beam, and a deviation in the reconstruction wavelength. From the analytic model, only coma is introduced for these registration errors and the amount introduced is proportional to the residual spherical aberration. For example, a lateral displacement introduces coma proportional to the lateral displacement multiplied by the residual spherical aberration. The angular displacement of the reconstruction beam and deviation in the reconstruction wavelength have similar relationships to the lateral displacement; they are all modelled by displacing the exit-pupil. The coma introduced for these errors is proportional to the amount of residual spherical aberration and distance between the exit-pupil plane and the hologram recording plane. Thus, there is a general correlation between the two analysis.

To assess the accuracy and limits of the analytic model and to corroborate the numerical model, a quantitative comparison with the results from the numerical tray-tracing simulations is made with the analytic results. The registration error tolerances from the numerical ray-tracing are computed for the simple lens† described in section 5.4.1 to achieve a Strehl Intensity Ratio equal to 0.8. These tolerances are then inserted into the wave-front aberration model from the analytic model to compute the equivalent Strehl Intensity Ratio. Table 5.3A and table 5.3B summarize the results from a lateral displacement of the hologram. For the low NA system, good agreement between the approaches is observed. The large NA system shows a small discrepancy due to the higher order aberrations which are not included in the analytic model. They also show good agreement across the field. Table 5.4A and table 5.4B summarize the results for an angular displacement of the

---

† The third-order wave-front aberration function coefficients for the simple lens are S=-40, C=35, A=-60, and P=-20 waves for the NA = .1 system.

Lateral Displacement of the Hologram		
System	Lateral displacement in mm to produce SR=.8 (Simulation)	Analytic SR
.4	.00029	.88
.2	.0055	.82
.1	.05	.8

Table 5.3A Comparison of lateral displacement tolerances.

Lateral Displacement of the Hologram For NA=.1		
Field Position	Lateral displacement in mm to produce SR=.8 (Simulation)	Analytic SR
Center	.05	.8
Half	.04	.805
Edge	.022	.84

Table 5.3B Comparison of lateral displacement tolerances across the field.

reconstruction beam.

Angular Displacement of the Reconstruction Beam		
System	Angular displacement in arcsecs to produce SR=.8 (Simulation)	Analytic SR
.4	.35	.86
.2	7.5	.73
.1	80	.6

Table 5.4A Comparison of angular displacement tolerances.

For the low NA system, the sensitivity computed from the analytic model is worse than from the numerical ray-trace results. This is due to the coupling of the aberrations produced from the hologram with the aberrations produced by the displacement of the exit-pupil. However, for the large NA system, the aberrations resulting from the displacement of the exit-pupil-front is the dominant factor. This effect is also observed as the field is traversed. Table 5.5A and 5.5B summarize the results

Angular Displacement of the Reconstruction Beam For NA = .1		
Field Position	Angular displacement in arcsecs to produce SR=.8 (Simulation)	Analytic SR
Center	80	.6
Half	55	.73
Edge	25	.89

Table 5.4B Comparison of angular displacement tolerances across the field.

for an axial displacement of the hologram.

Axial Displacement of the Hologram		
Field Position	Axial displacement in mm to produce SR=.8 (Simulation)	Analytic SR
.4	.0009	.98
.2	.95	.88
.1	2.1	.82

Table 5.5A Comparison of axial displacement tolerances.

Axial Displacement of the Hologram For NA = .1		
Field Position	Axial displacement in mm to produce SR=.8 (Simulation)	Analytic SR
Center	2.1	.82
Half	.70	.79
Edge	.3	.82

Table 5.5B Comparison of axial displacement tolerances across the field.

There is discrepancy in the large NA systems due to the aberrations from a conjugate change which are described in section 5.2. The low NA systems show good agreement. The field dependence also shows good agreement as long as the aberrations due to a change in the field are included since the axial displacement is rather large. For most lithography applications, the axial displacement is much smaller.

5.6 SUMMARY

In this chapter, two methods to identify and quantify the aberrations introduced through the complex interaction between the imaging lens and the hologram into the imaging system have been developed. The first method is based on a simple model of the lens interacting with an ideal hologram. The second method applies a ray-tracing methodology to evaluate the wave-front aberrations produced by a non-ideal lens-hologram system. The analytic model provides insight into which attributes of the imaging lens are the dominant factors affecting the sensitivity of the reconstruction system even though the third order aberrations of the hologram are not included. The ray-tracing simulation results provide important quantitative results into as well as the behavior of the image quality with the hologram aberrations included.

The larger the the deviation of the lens' image wave-front from a spherical wave-front the more sensitive the reconstructed image is to the errors in the reconstruction configuration. Residual spherical aberration is the most significant aberration and should be reduced at the expense of the other aberrations. Coma and astigmatism are the next important aberrations that should be reduced. The hologram recording plane should lie in the conjugate plane. If the recording plane must lie out of the conjugate plane, the plane should be towards the imaging lens reducing the the lever arm action. The change in average index of refraction is not of a major concern for well corrected imaging optics.

5.7 REFERENCES

[5.1] R.W. Meier, "Magnification and Third-Order Aberrations in Holography.," *Journal of the Optical Society of America*, vol. 55, pp. 987-992, 1965.

[5.2] E.N. Leith and J. Upatnieks, "Microscopy by Wavefront Reconstruction.," *Journal of the Optical Society of America*, vol. 53, pp. 1295-1301, 1965.

[5.3] E.B. Champagne and N.G. Massey, "Resolution in Holography.," *Applied Optics*, vol. 8, no. 9, pp. 1879-1885, September 1969.

[5.4] B.J. Lin and S.A. Collins,Jr., "Holographic Imaging and Aberrations Due to an Incorrectly Repositioned Hologram in a System with Lenses Having Aberrations.," *Journal of the Optical Society of America*, vol. 63, no. 5, pp. 537-547, May 1973.

[5.5] R.K. Luneburg, in *Mathematical Theory of Optics*, University of California Press, Berkeley, 1964.

[5.6] M. Born and E. Wolf, in *Principles of Optics*, Pergamon Press, New York, 1984.

[5.7] C.W. Helstrom, "Image Luminance and Ray Tracing in Holography," *Journal of the Optical Society of America*, vol. 56, no. 4, pp. 433-441, April 1966.

[5.8] I.A. Abramowitz, "Evaluation of Hologram Imaging by Ray Tracing," *Applied Optics*, vol. 8, no. 2, pp. 403-410, February 1969.

[5.9] H. Kogelnik, "Holographic Image Projection through Inhomogeneous Media.," *Bell System Technical Journal Briefs*, vol. 44, pp. 2451-2455, December 1965.

[5.10] H.H. Hopkins, in *Wave Theory of Aberrations*, Clarendon Press, London, 1950.

[5.11] C.G. Wynne, "Primary Aberrations and Conjugate Change," *Proceedings of the Physical Society of London*, vol. 65B, pp. 429-437, 1952.

[5.12] Howard Smith, in *Principles of Holography*, Wiley, New York, 1975.

[5.13] W.T. Welford, in *Aberrations of Optical Systems*, Adam Hilger Ltd, Bristol, 1986.

[5.14] M. Herzberger, "Light Distribution in the Optical Image," *Journal of the Optical Society of America*, vol. 37, no. 6, pp. 485-493, June 1947.

[5.15] M. Herzberger, "Analysis of Spot Diagrams," *Journal of the Optical Society of America*, vol. 47, no. 7, pp. 584-594, July 1957.

[5.16] William B. Wetherell, in *Applied Optics and Optical Engineering*, ed. Robert R. Shannon and James C. Wyant, vol. 8, Academic Press, New York, 1980.

[5.17] H.H. Hopkins, "The Aberration Permissable in Optical Systems," *Proceedings of the Royal Society of London*, vol. 75-B, pp. 449-470, 1957.

[5.18] N Bobroff, P. Fadi, A. Rosenbluth, and D.S. Goodman, "Bench Evaluation of Lithographic Lenses from Measurements of the Point Spread Function," in *Optical/Laser Microlithography (1988)*, ed. Burn Lin, vol. 922, pp. 376-386, SPIE, March 1988.

[5.19] F. Zernike, *Physica*, vol. 1, p. 689, 1934.

[5.20] G. Addiego and W.G. Oldham, "High-Resolution Imaging Using Focused-Image Holography with Wave-Front Conjugation.," *Optical/Laser Microlithography*, vol. 922, pp. 18-25, SPIE, March 2-4, 1988.

[5.21] G.B. Brandt, "Image Plane Holography," *Applied Optics*, vol. 8, no. 7, pp. 1421-1429, July 1969.

[5.22] Burn J. Lin, "The Paths to Subhalf-Micrometer Optical Lithography," in *Optical/Laser Microlithography (1988)*, ed. Burn J. Lin, vol. 922, pp. 256-269, SPIE, March 1988.

[5.23] J.N. Latta, "Computer-Based Analysis if Hologram Imagery and Aberrations. I. Hologram Types and Their Nonchromatic Aberrations.," *Applied Optics*, vol. 10, no. 3, pp. 599-608, March 1971.

[5.24] J.N. Latta, "Computer-Based Analysis of Hologram Imagery and Aberrations. II: Aberrations introduced by a wavelength shift.," *Applied Optics*, vol. 10, no. 3, pp. 609-618, March 1971.

[5.25] Berlyn Brixner, "The Symposium Lens Improved," *Applied Optics*, vol. 2, no. 12, p. 1331, December 1963.

NEW WAVE-FRONT

NEW IMAGE POINT

Y'

OLD IMAGE POINT

EXIT PUPIL

(a) OLD WAVE-FRONT

WAVE-FRONT
FOR
AN OFF-AXIS POINT

EXIT PUPIL

IMAGE POINT

(b)

NEW EXIT PUPIL

IMAGE POINT

OLD EXIT PUPIL

(c)
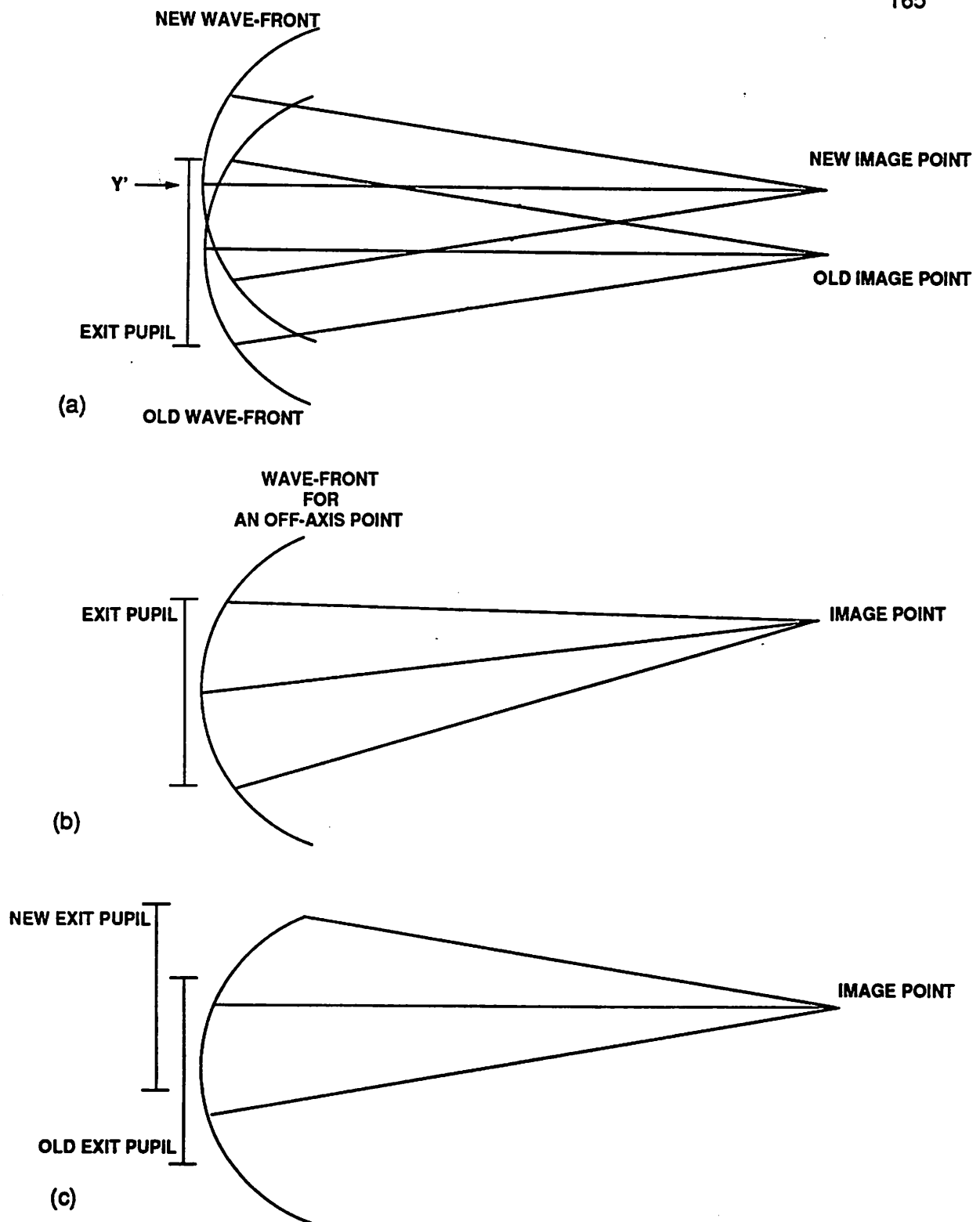
Figure 5.1   Pure lateral displacement of an image point is shown in (a) with the corresponding tilt in the wave-front describing the new field point (b) and finally a shift in the exit pupil (c).
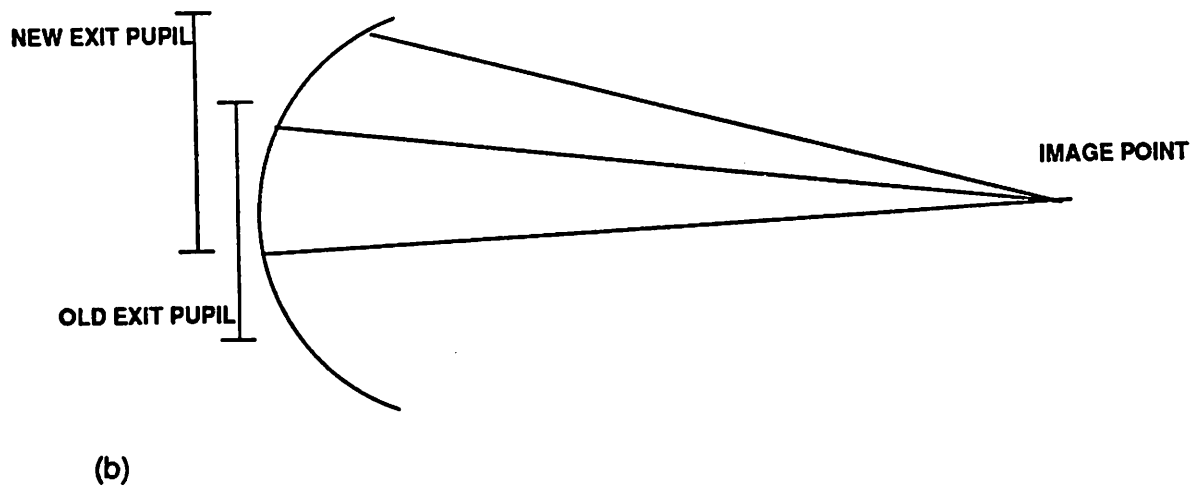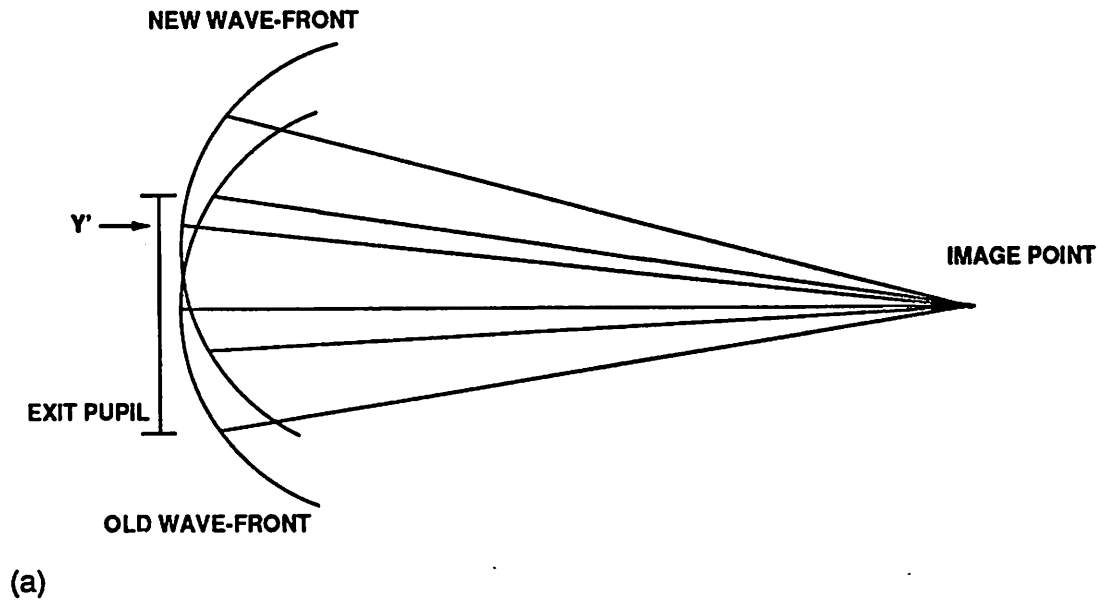
Figure 5.2 Angular displacement of the reconstructed wave-front (a) and the corresponding displacement of the exit-pupil (b).

EXIT PUPIL

NEW IMAGE POINT

OLD IMAGE POINT

OLD WAVE-FRONT

(a)

EXIT PUPIL
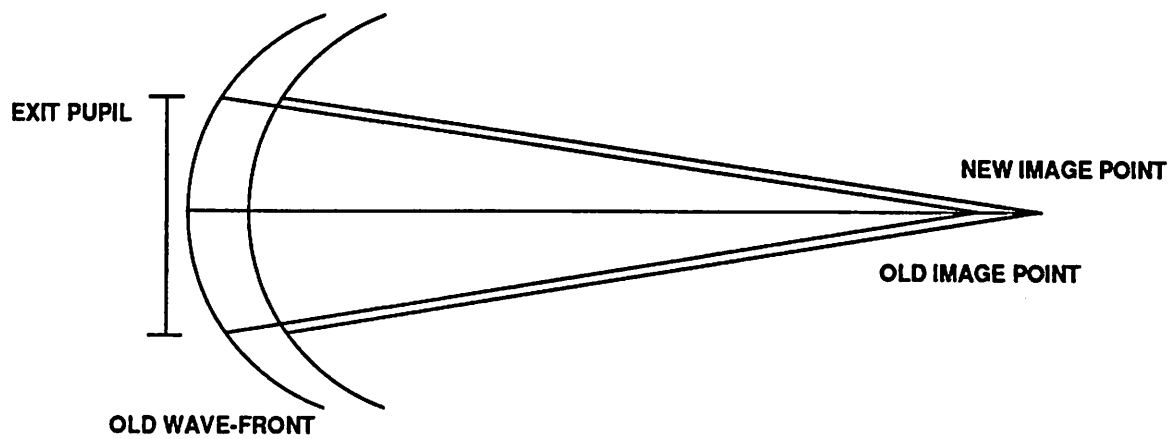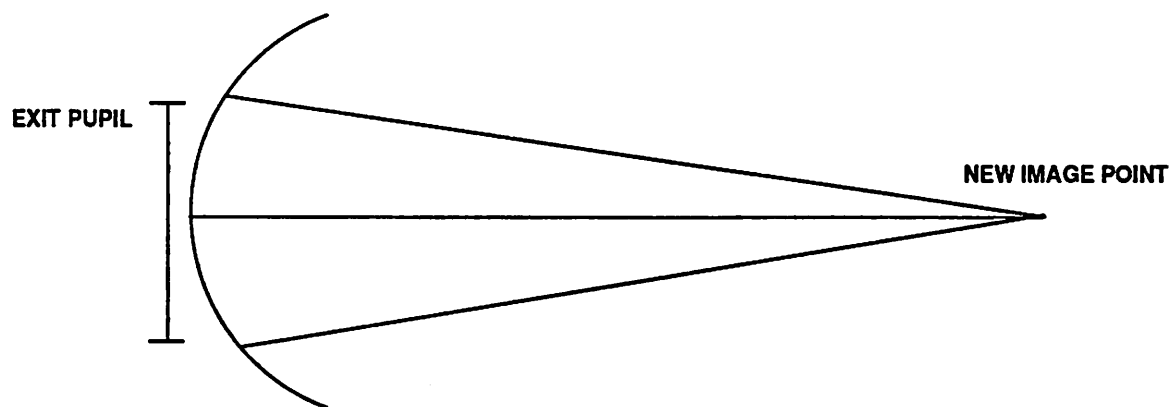
NEW IMAGE POINT

(b)

Figure 5.3   Axial displacement of the image point (a) and the corresponding axial movement of the exit-pupil (b).
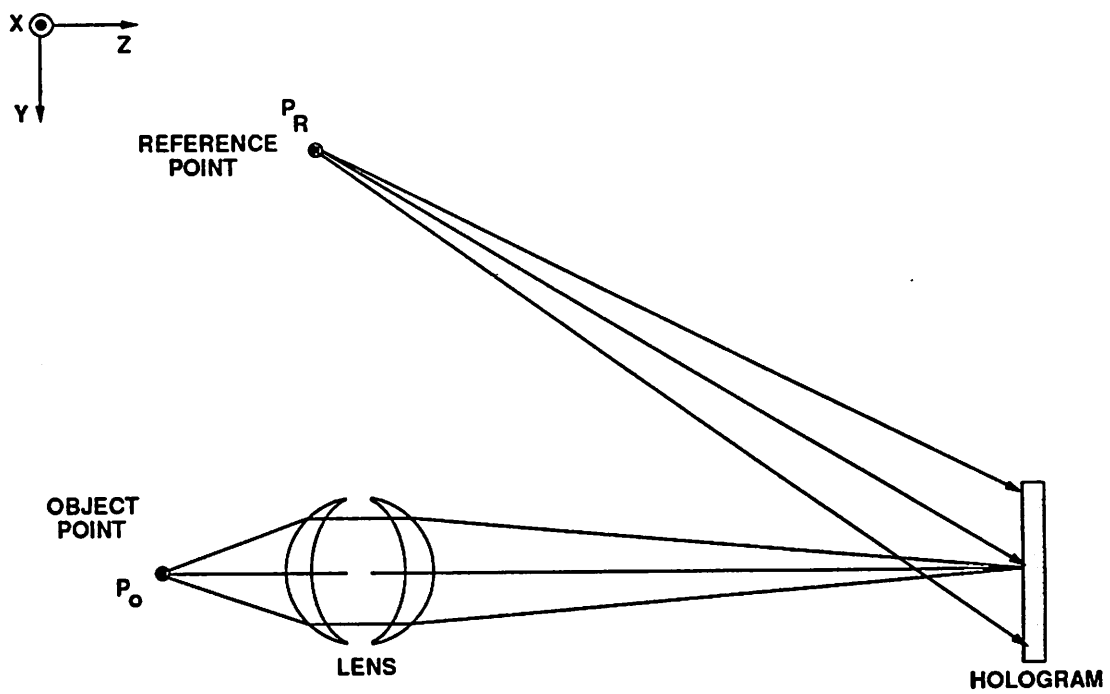
Figure 5.4 Schematic illustration of the hologram recording configuration for the ray-trace analysis.
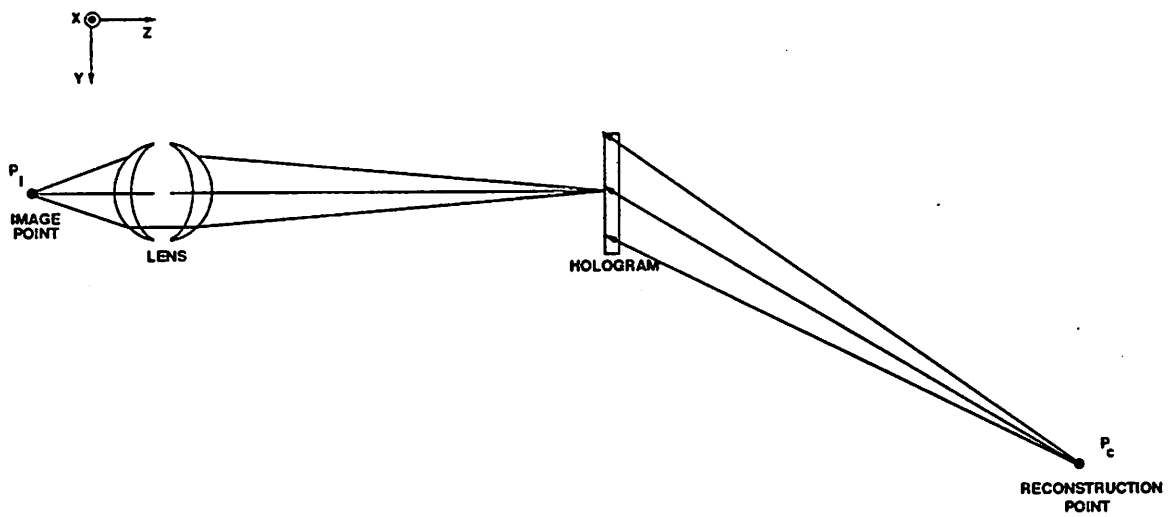
Figure 5.5 Schematic illustration of the image reconstruction configuration for the ray-trace analysis.
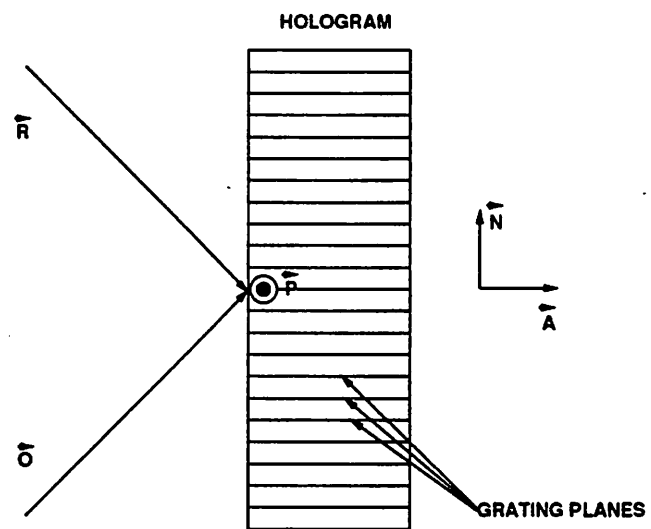
Figure 5.6   Diagram of the direction vectors that define the grating.

HOLOGRAM BEFORE MAGNIFICATION

$M_z = .5$

$\tilde{x}$

$\tilde{z}$

NEW GRATING PLANES

OLD GRATING PLANES

HOLOGRAM AFTER MAGNIFICATION
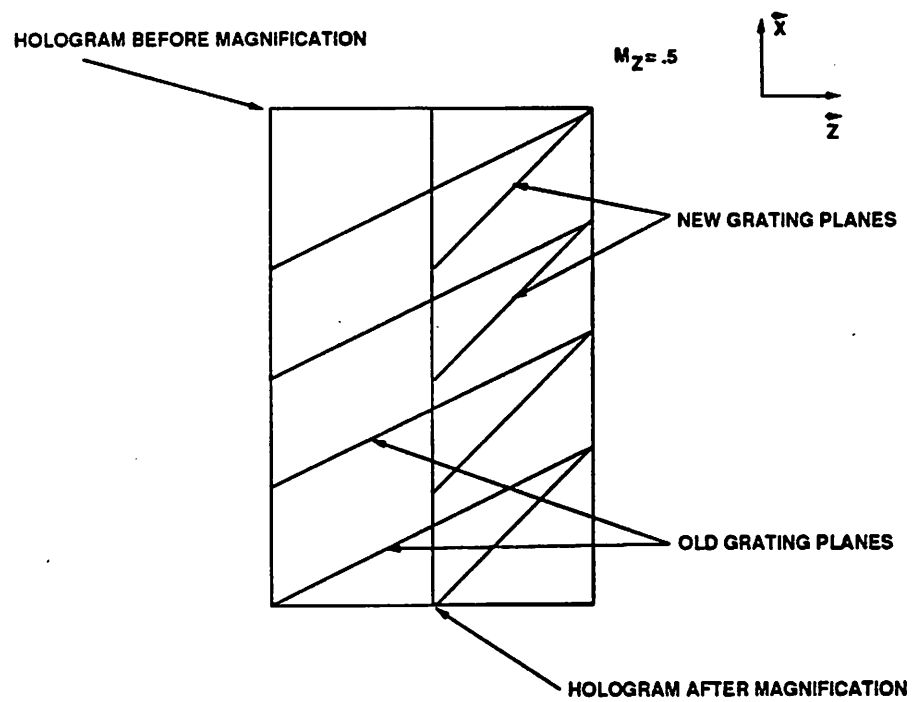
Figure 5.7   Illustration of the grating transformation for M_z = .5 scaling in the Z direction.

Spot Diagram at the Center of the Field NA = .4

Optical Path Difference at the Center of Field NA = .4
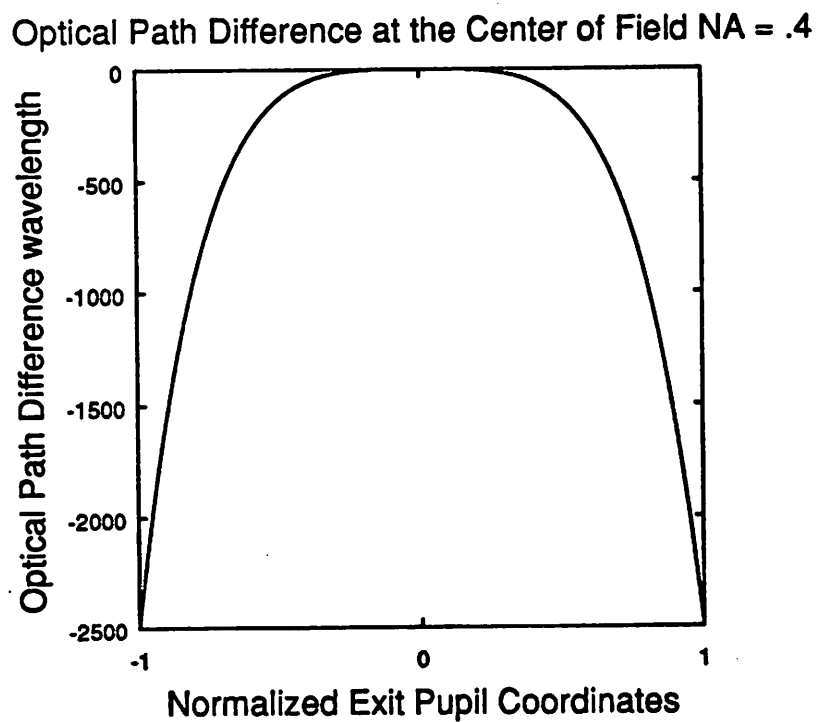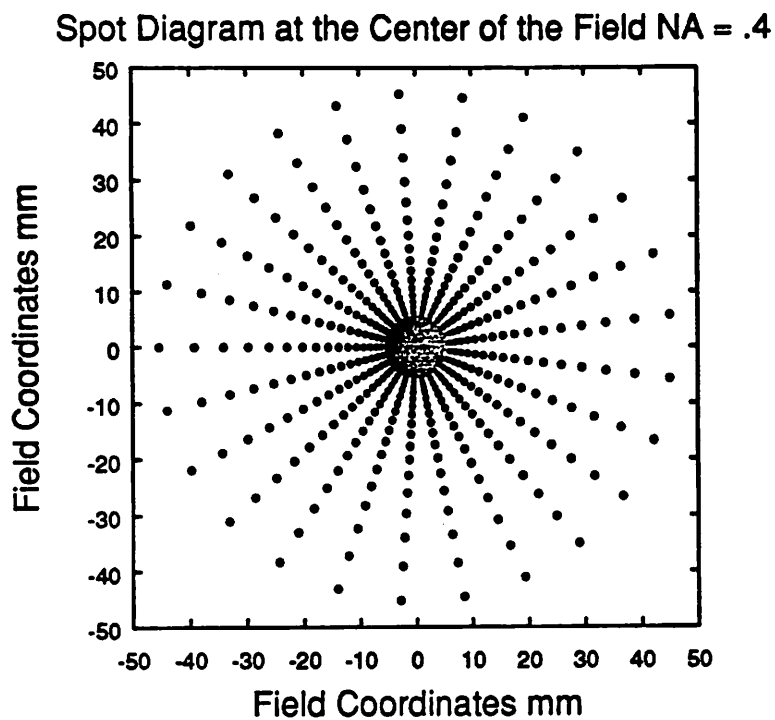
Figure 5.8   Spot Diagram and OPD graph for a single element lens operating with

an NA of .4 at the center of its image field.

Spot Diagram at the Center of the Field NA = .2

Field Coordinates mm

Field Coordinates mm

Optical Path Difference at the Center of Field NA = .2

Optical Path Difference wavelength

Normalized Exit Pupil Coordinates
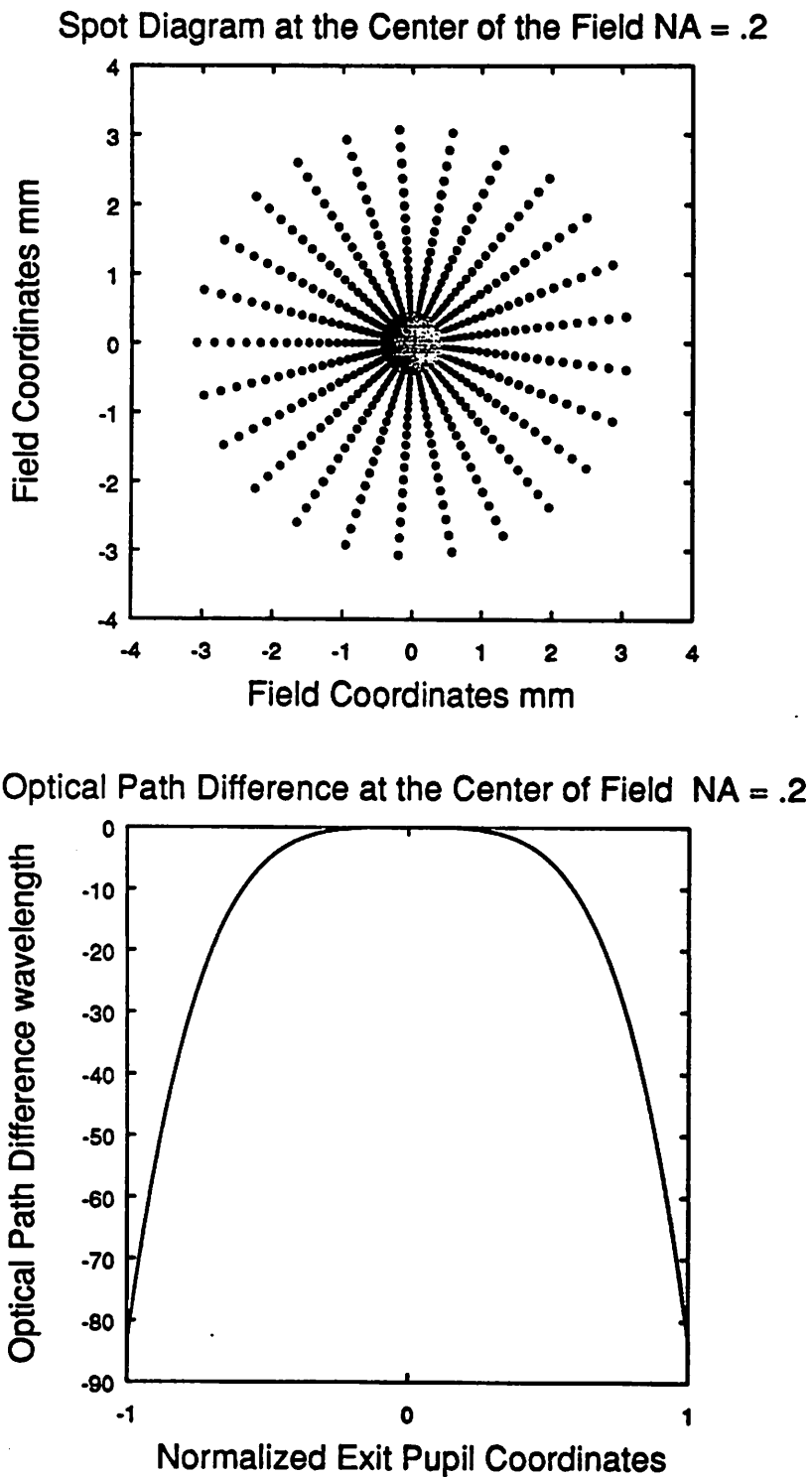
Figure 5.9   Spot Diagram and OPD graph for a single element lens operating with

an NA of .2 at the center of its image field.

Spot Diagram at the Center of the Field NA = .1
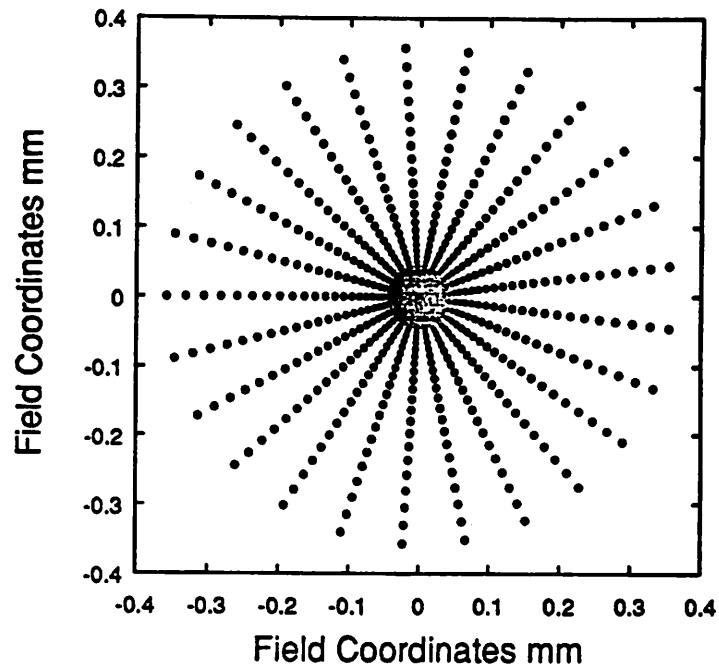
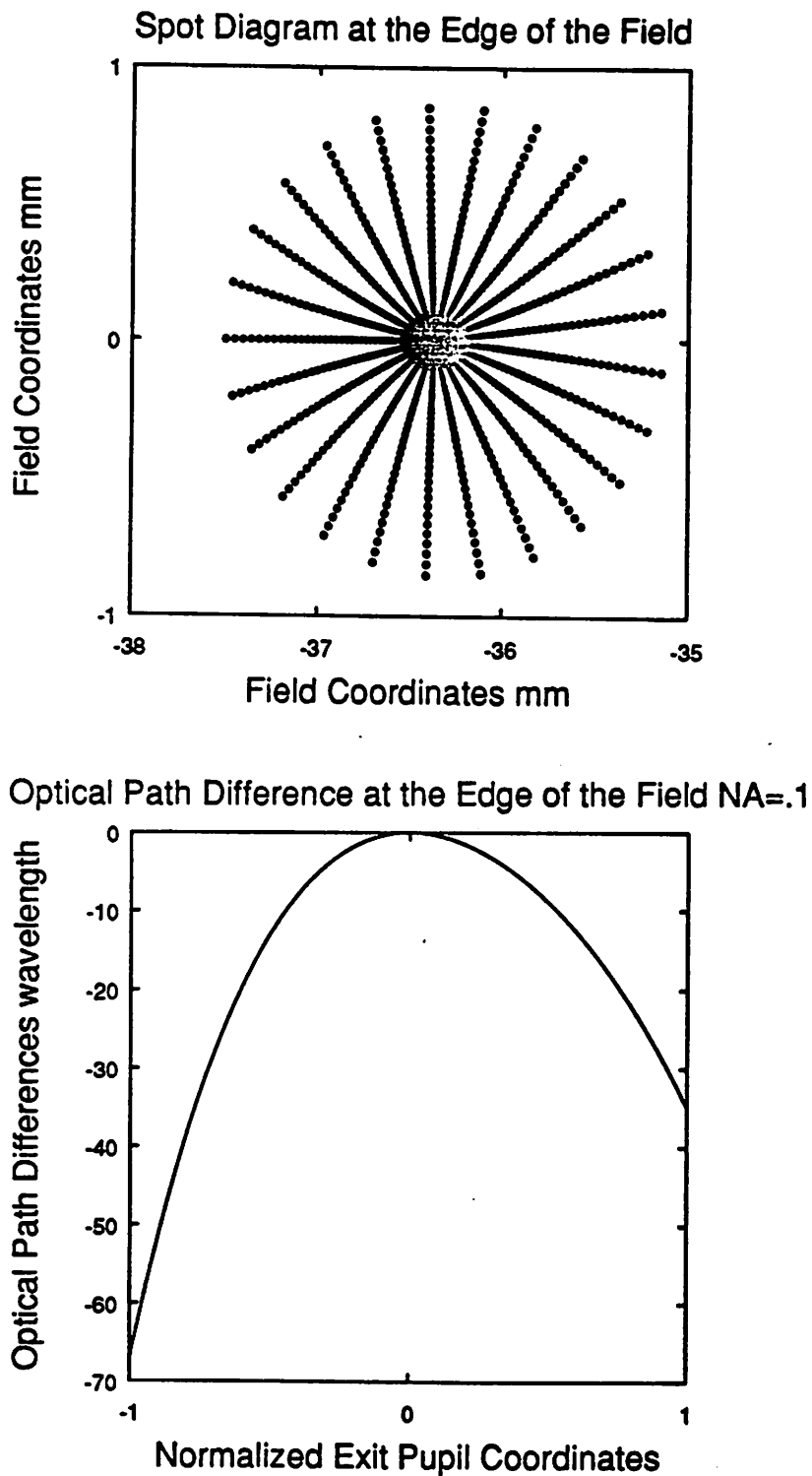## Optical Path Difference at the Center of Field NA = .1
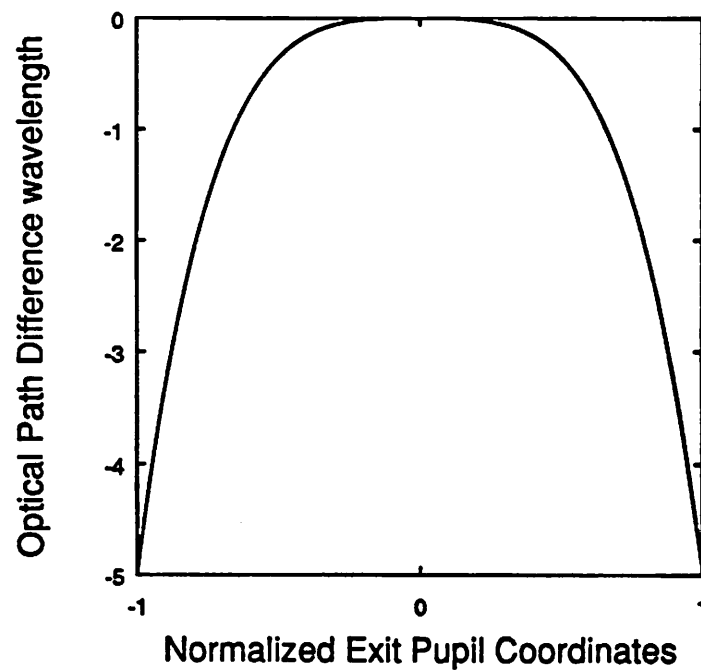
Figure 5.10 Spot Diagram and OPD graph for a single element lens operating with

an NA of .1 at the center of its image field.

Strehl Intensity vs Lateral Displacement of Hologram NA=.4

(a)

Strehl Intensity vs Lateral Displacement of Hologram NA = .2

(b)

Strehl Intensity vs Lateral Displacement of Hologram NA=.1

(c)
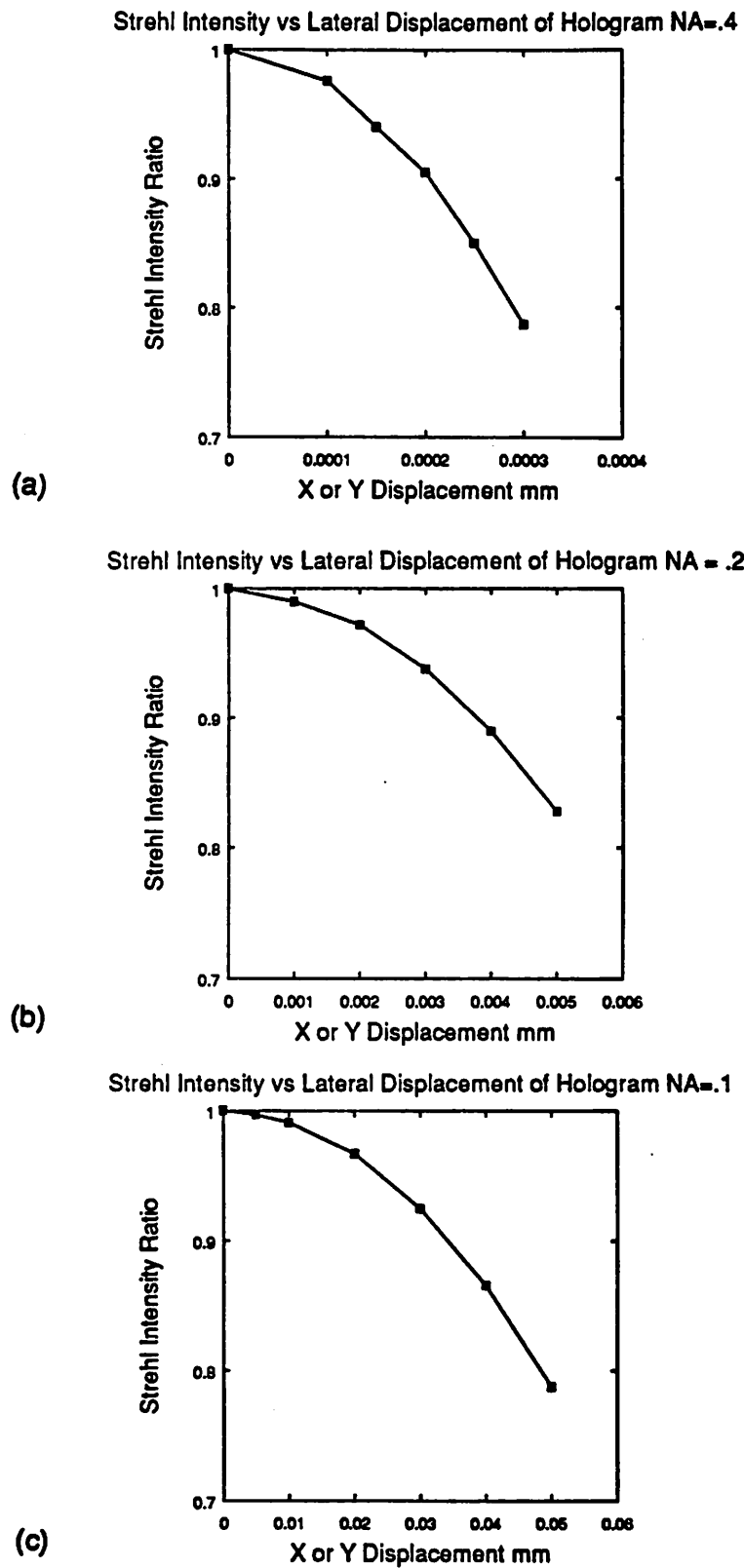
Figure 5.11 Strehl Intensity Ratio for lateral displacement of the hologram for (a) NA = .4, (b) NA = .2, (c) NA = .1.

Strehl Intensity vs Hologram Axial Displacement NA=.4

(a)

Strehl Intensity Ratio

Axial Displacement mm

Strehl Intensity vs Lateral Displacement of Hologram NA=.1

(b)

Strehl Intensity Ratio

Axial Displacement mm

Strehl Intensity vs Hologram Axial Displacement NA=.2

(c)

Strehl Intensity Ratio

Axial Displacement mm
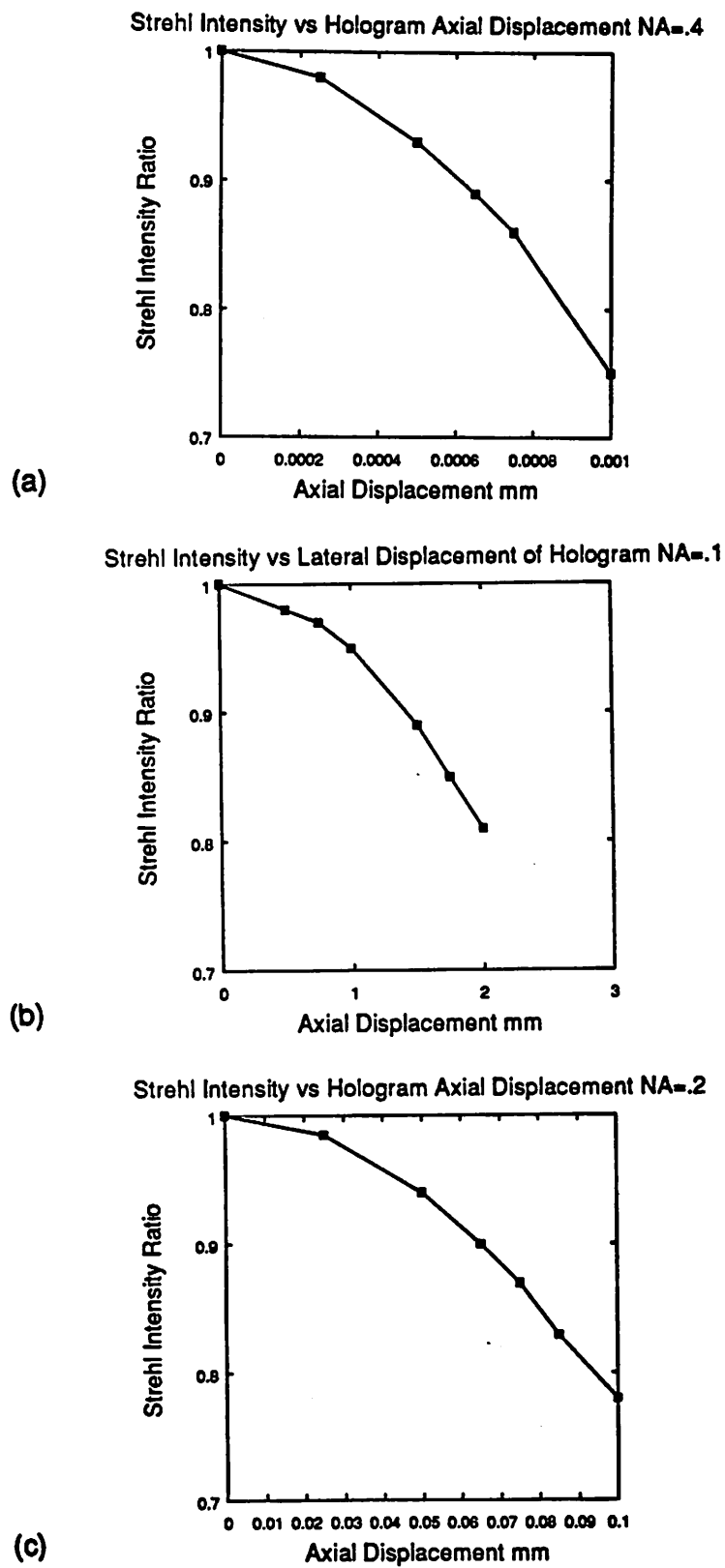
Figure 5.12 Strehl Intensity Ratio for axial displacement of the hologram for (a) NA = .4, (b) NA = .2, (c) NA = .1.

Strehl Intensity vs Change in Reconstruction Wavelength NA=.4

(a)

Strehl Intensity vs Change in Reconstruction Wavelength NA=.2

(b)

Strehl Intensity vs Change in Reconstruction Wavelength NA=.1

(c)
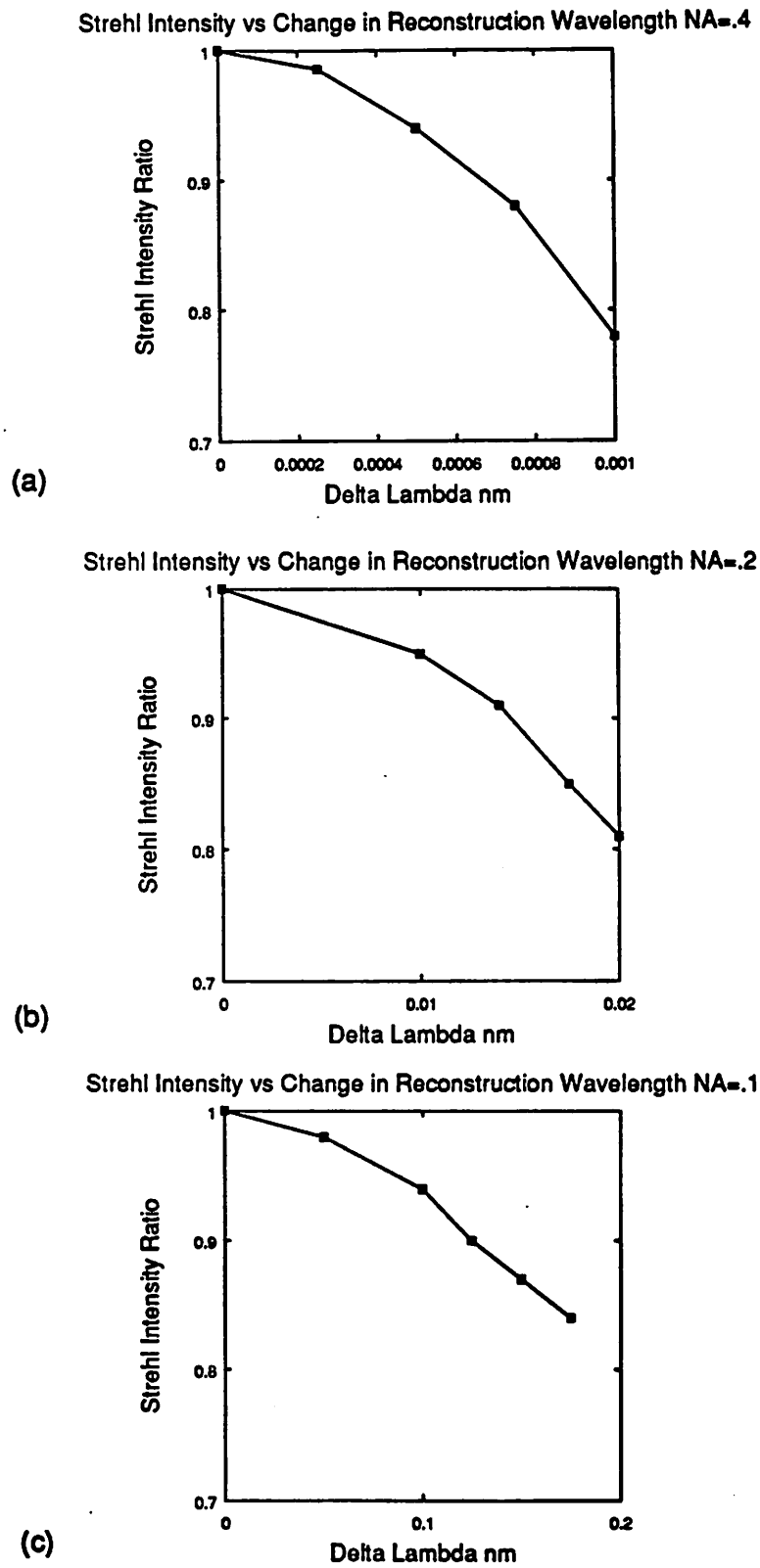
Figure 5.13 Strehl Intensity Ratio for change in illumination wavelength for (a) NA = .4, (b) NA = .2, (c) NA = .1.

Strehl Intensity vs Reconstruction Beam Angular Displacement NA=.4

(a)
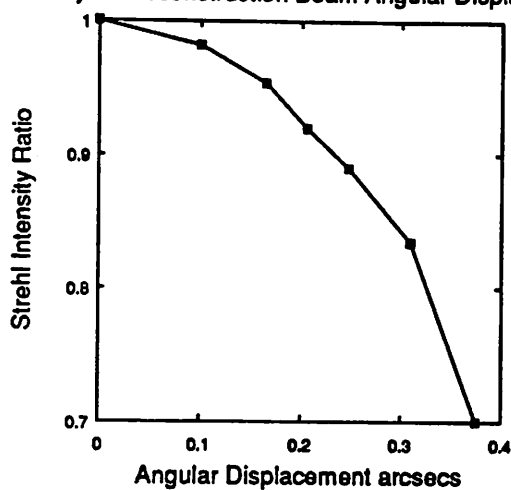
Strehl Intensity vs Reconstruction Beam Angular Displacement NA=.2

(b)
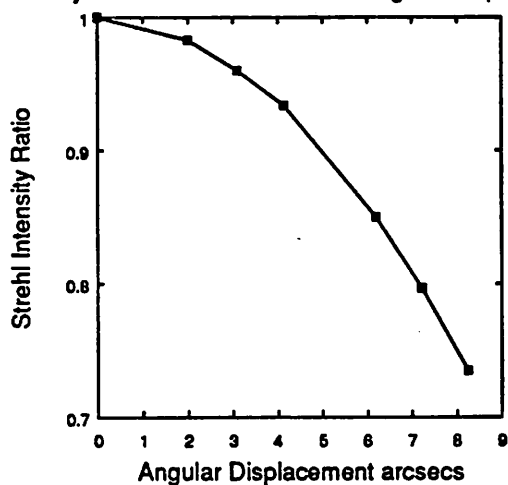
Strehl Intensity vs Reconstruction Beam Angular Displacement NA = .1
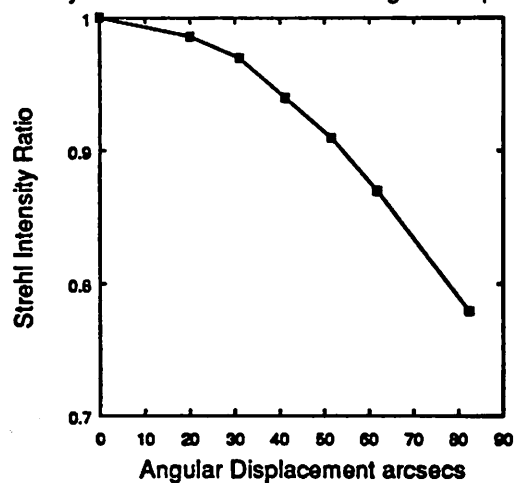
(c)

Figure 5.14 Strehl Intensity Ratio for angular displacement of the illumination beam

for (a) NA = .4, (b) NA = .2, (c) NA = .1.

Strehl Intensity vs Divergence of Reconstruction Beam NA=.4

(a)
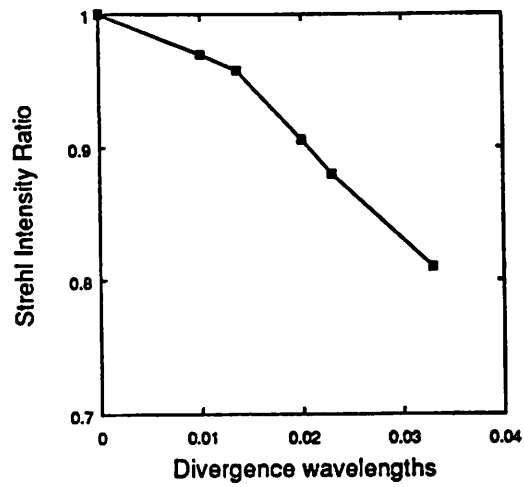
Strehl Intensity vs Divergence of Reconstruction Beam NA=.2

(b)
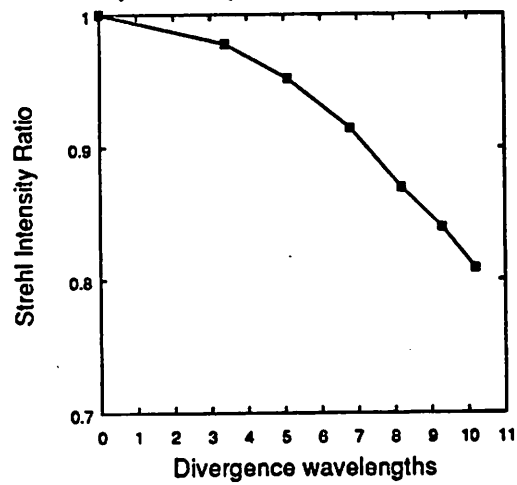
Strehl Intensity vs Divergence of Reconstruction Beam NA=.1
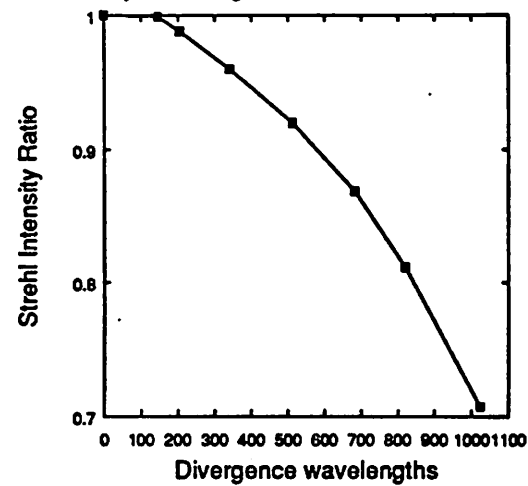
(c)

Figure 5.15 Strehl Intensity Ratio for divergence of the illumination beam wavefront for (a) NA = .4, (b) NA = .2, (c) NA = .1.

Strehl Intensity vs Change in Magnification NA=.4

(a)

Strehl Intensity Ratio

Parts per Million

Strehl Intensity vs Change in Magnification NA=.2

(b)

Strehl Intensity Ratio

Parts per Million

Strehl Intensity vs Change in Magnification NA=.1

(c)

Strehl Intensity Ratio

Parts per Million
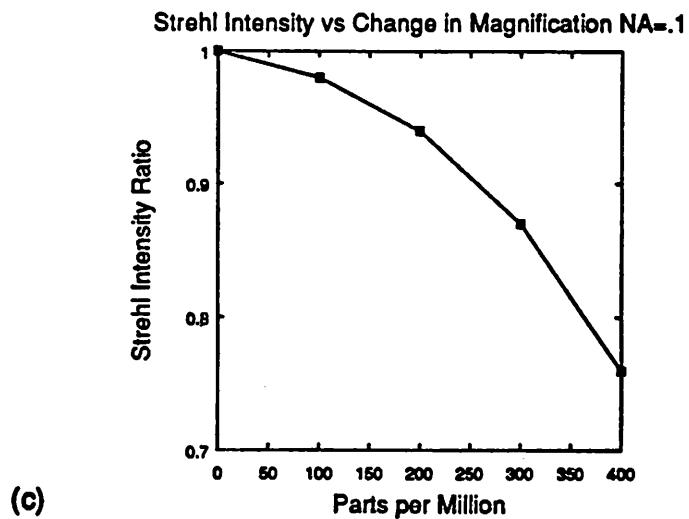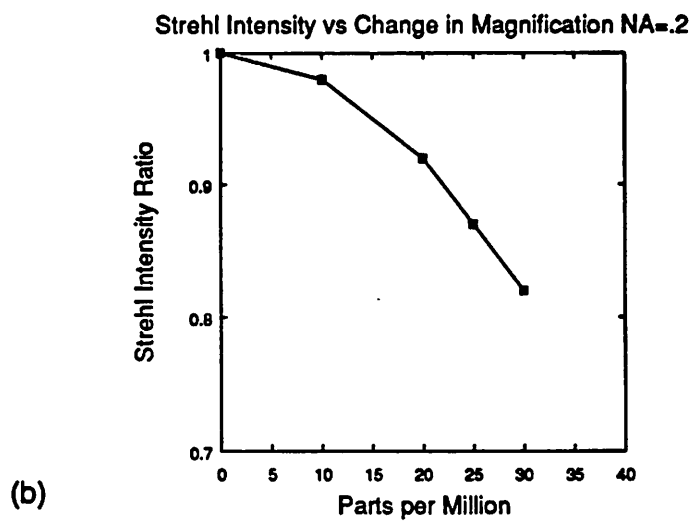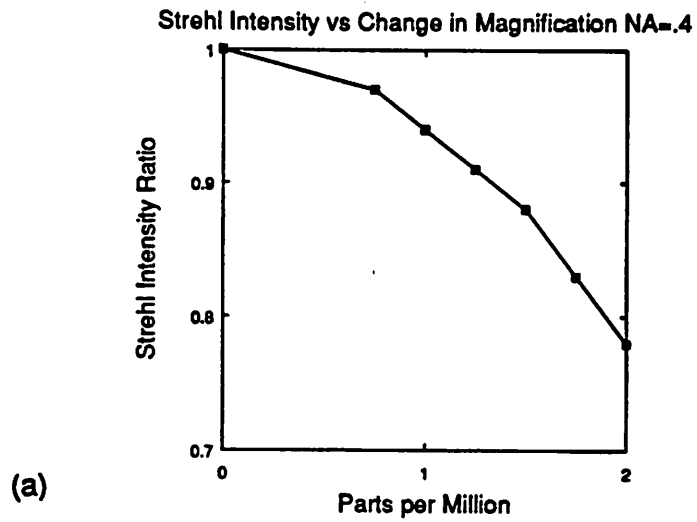
Figure 5.16 Strehl Intensity Ratio for changes magnification of the hologram for (a) NA = .4, (b) NA = .2, (c) NA = .1.

Strehl Intensity vs Change in the Index of Refraction NA=.4

(a)
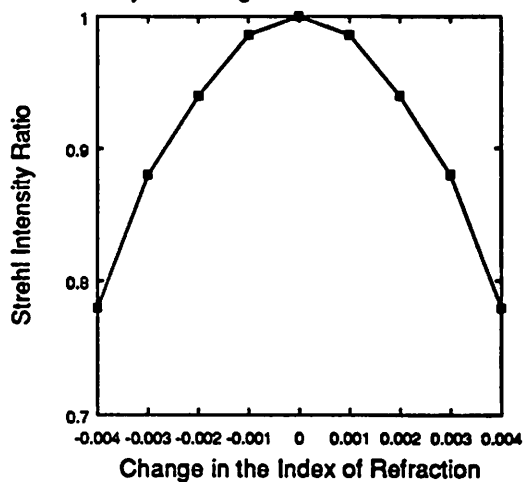
Strehl Intensity vs Change in the Index of Refraction NA=.2

(b)
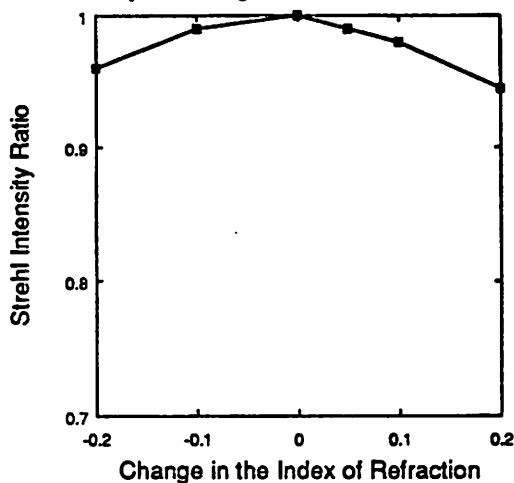
Strehl Intensity vs Change in the Index of Refraction NA=.1
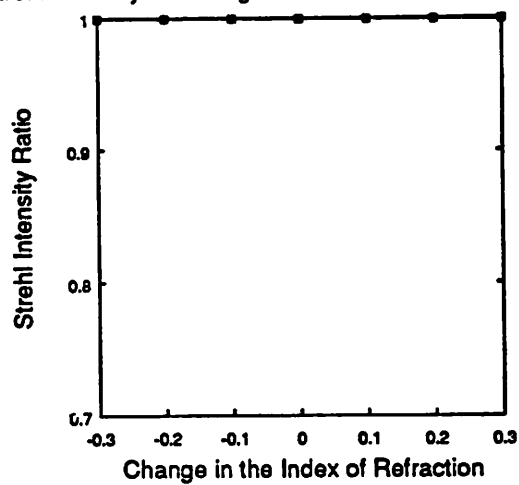
(c)

Figure 5.17 Strehl Intensity Ratio for the change in the hologram average index of refraction for (a) NA = .4, (b) NA = .2, (c) NA = .1.

Lateral Displacement vs Spot Size SR=.8

Angular Displacement vs Spot Size SR=.8

Axial Displacement vs Spot Size SR=.8

Divergence of Reconstruction Beam vs Spot Size SR=.8

Wavelength Deviation vs Spot Size SR=.8

Magnification vs Spot Size SR=.8
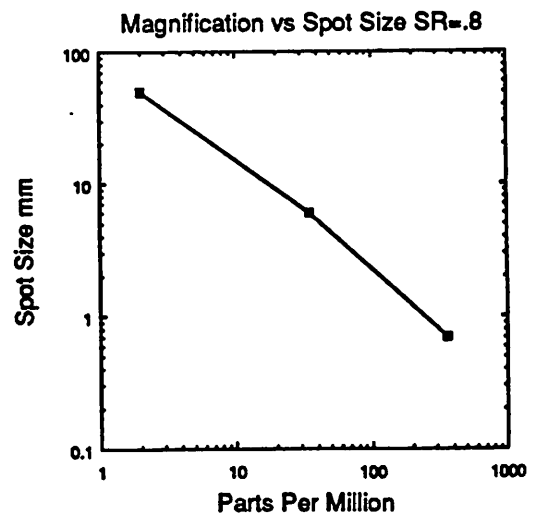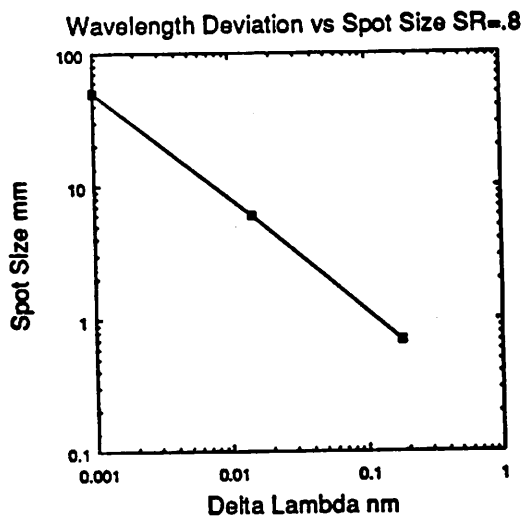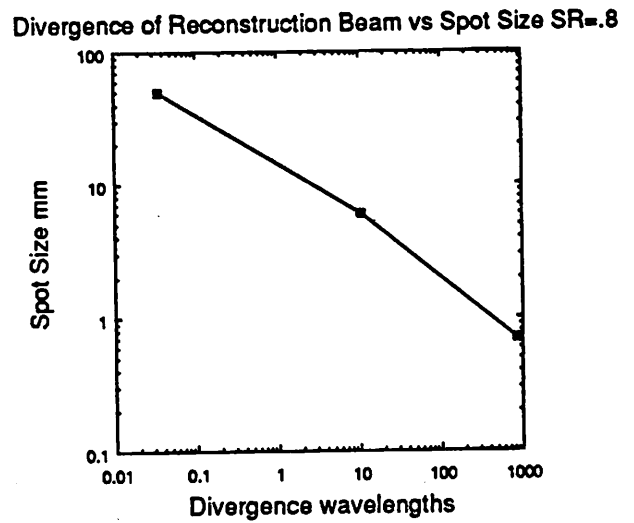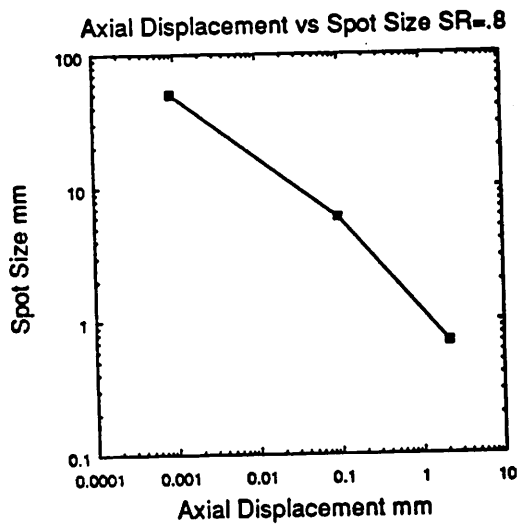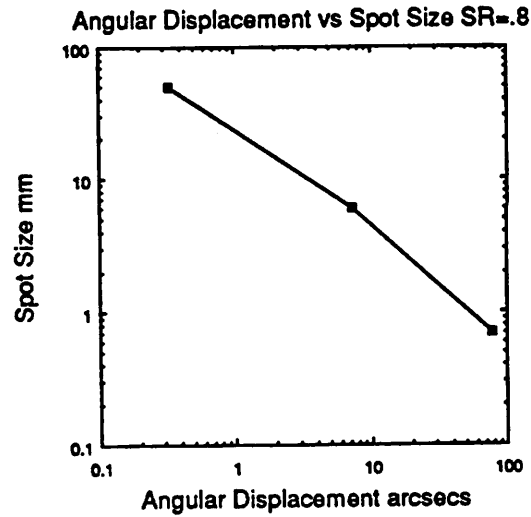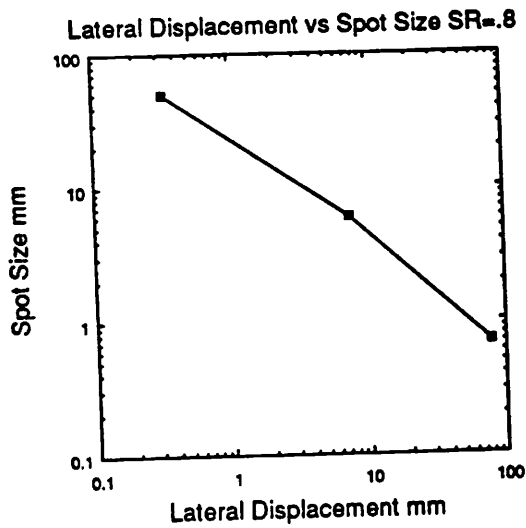
Figure 5.18 Sensitivity graphs of the traverse ray spot diameter versus several reconstruction system parameters.

Spot Diagram at the Center of the Field
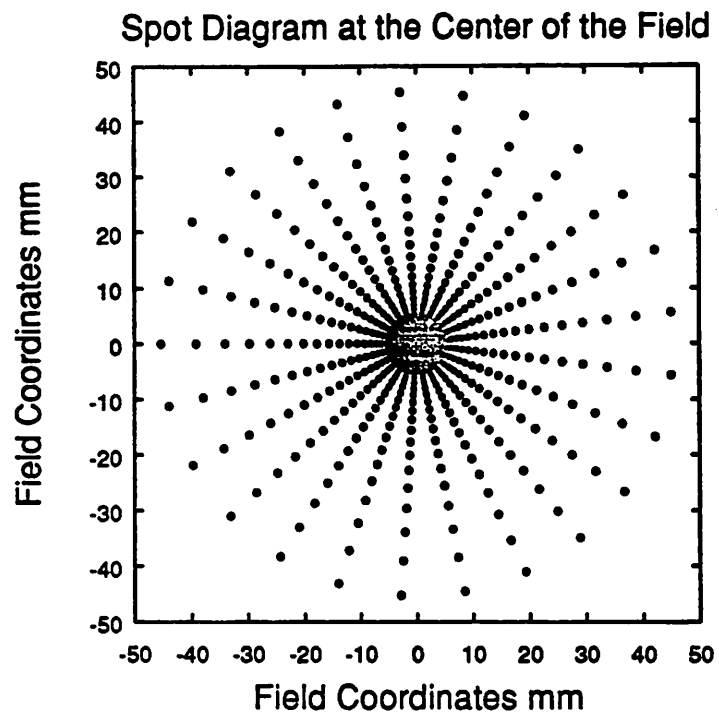
Optical Path Difference at the Center of Field NA = .1
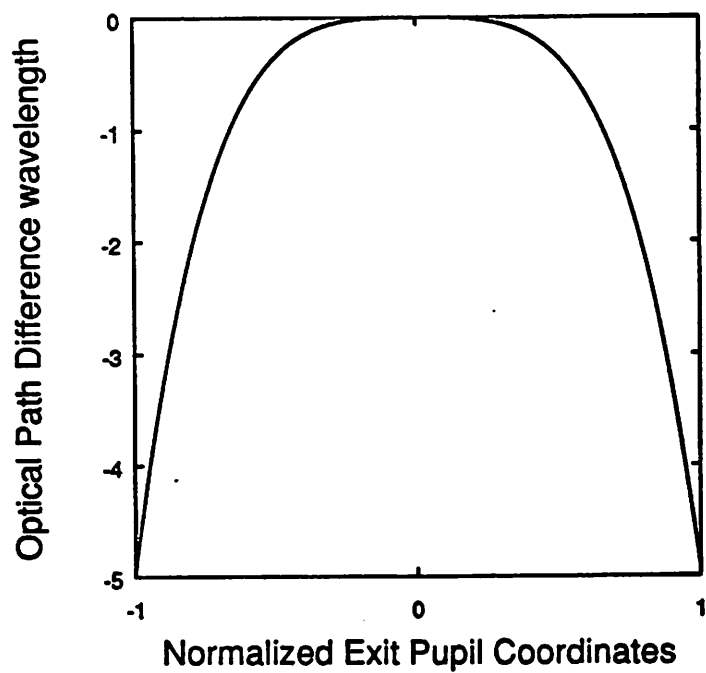
Figure 5.19 Spot Diagram and OPD graph for a single element lens operating with an NA of .1 at the center of its image field.

Spot Diagram at Half the Field

Optical Path Difference at the Half Field NA=.1
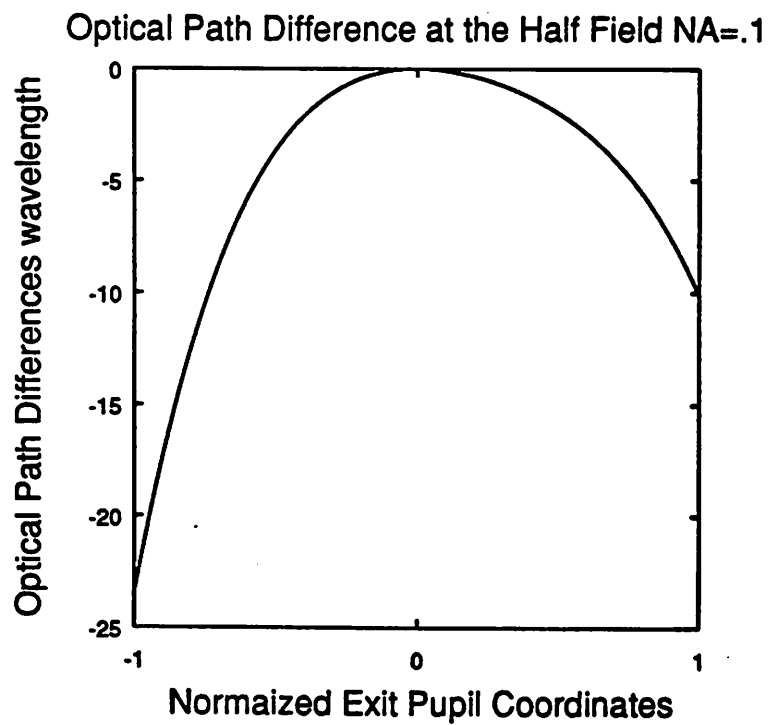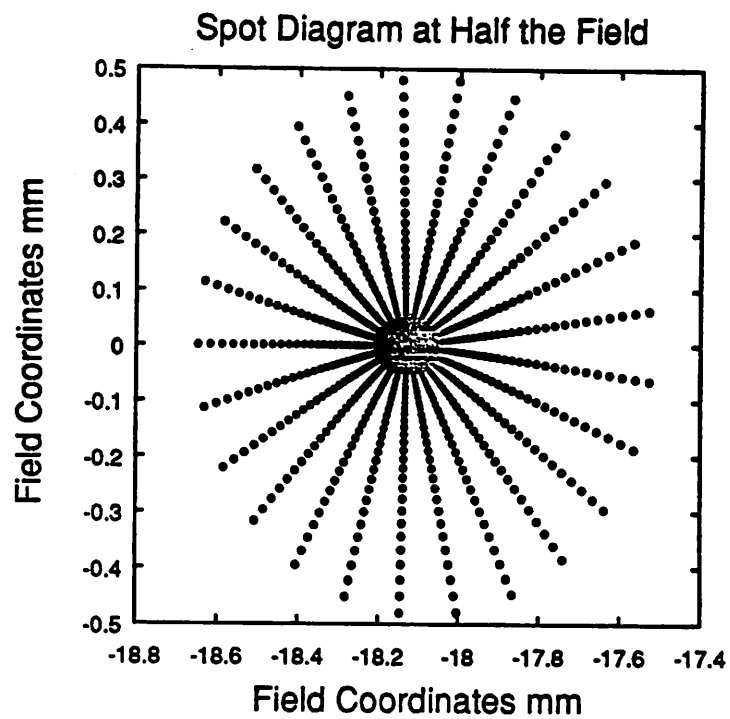
Figure 5.20 Spot Diagram and OPD graph for a single element lens operating with an NA of .1 at the half of its image field height.

Spot Diagram at the Edge of the Field

Optical Path Difference at the Edge of the Field NA=.1

Figure 5.21 Spot Diagram and OPD graph for a single element lens operating with an NA of .1 at the edge of its image field.

Strehl Intensity vs Lateral Displacement of Hologram NA=.1
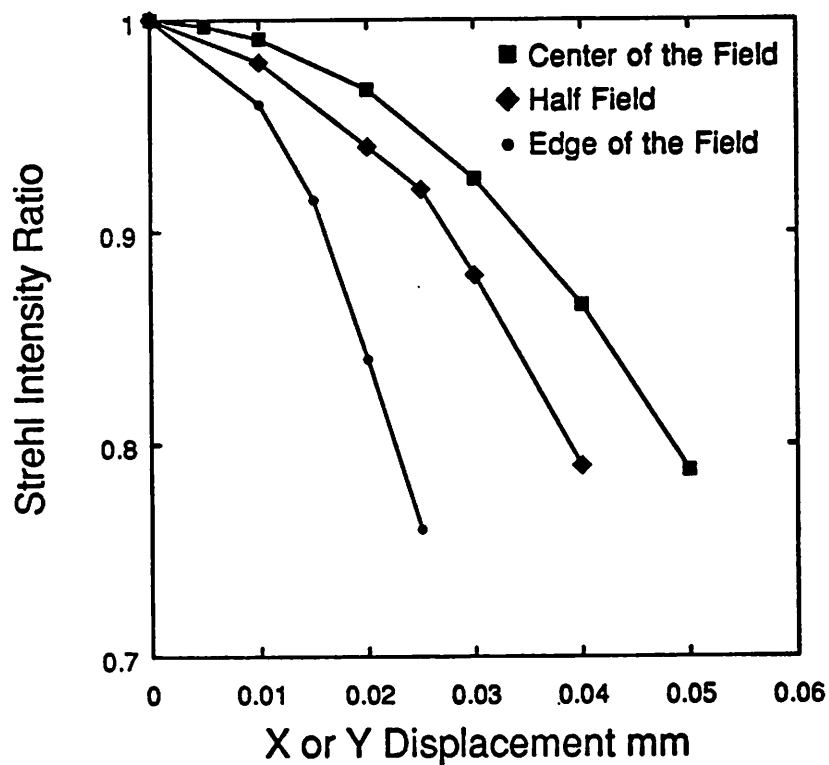
Figure 5.22 Strehl Intensity Ratio for lateral displacement of the hologram at the center, half height, and edge of the field for NA of .1.

Strehl Intensity vs Hologram Axial Displacement NA=.1
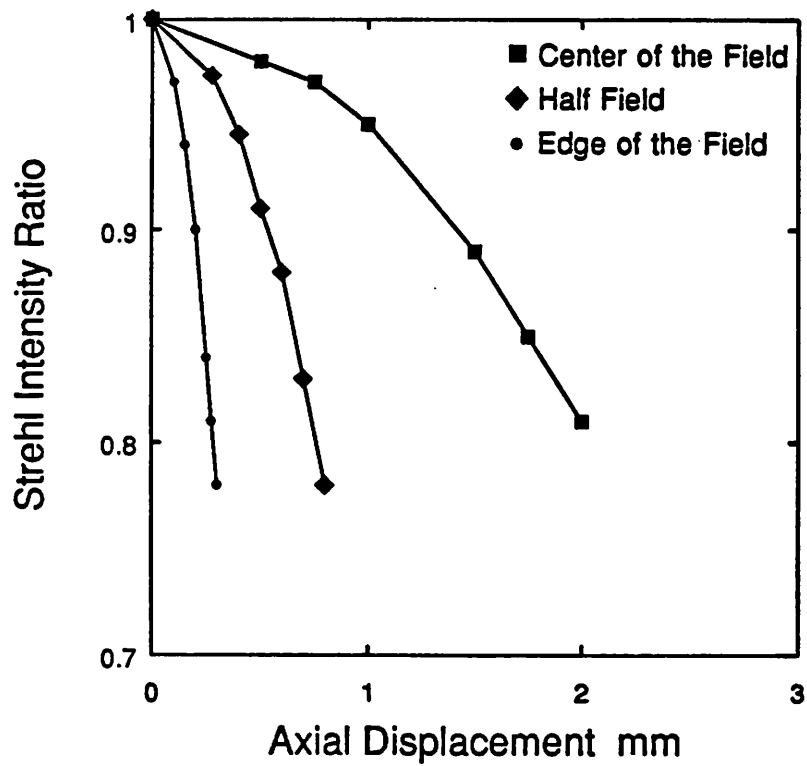
Figure 5.23 Strehl Intensity Ratio for axial displacement of the hologram at the center, half height, and edge of the field for NA of .1.

Strehl Intensity vs Change in Reconstruction Wavelength NA=.1
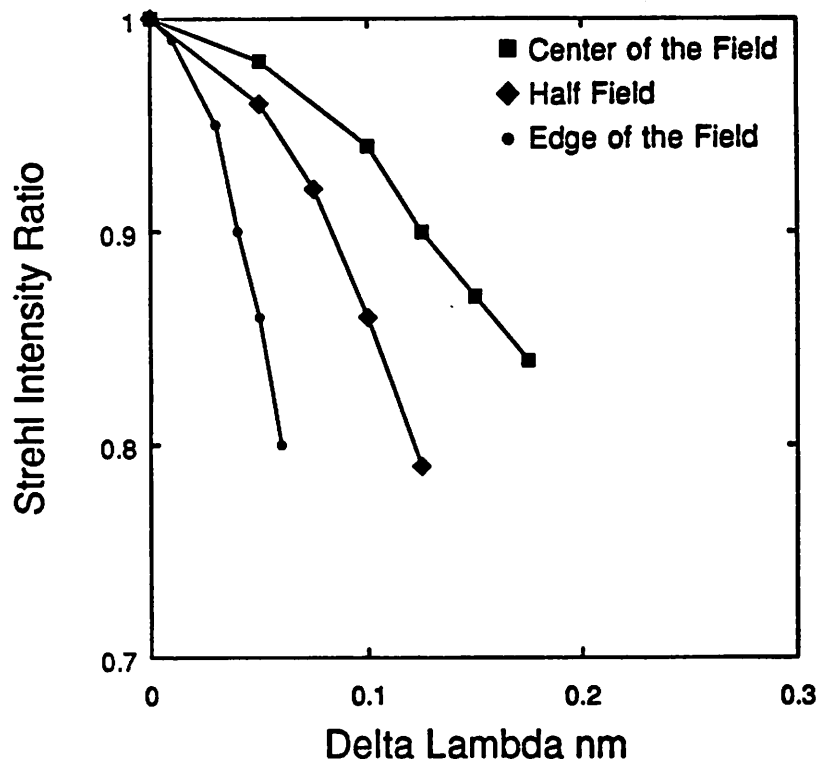
Figure 5.24 Strehl Intensity Ratio for a change of illumination wavelength at the center, half height, and edge of the field for NA of .1.

Strehl Intensity vs Reconstruction Beam Angular Displacement NA = .1
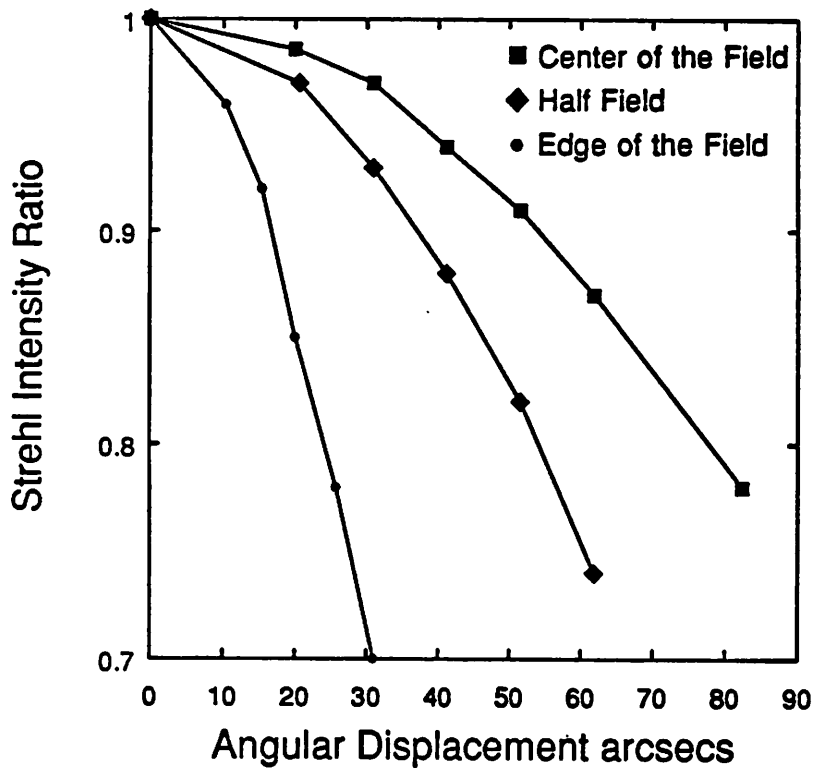
Figure 5.25 Strehl Intensity Ratio for angular displacement of the illumination beam at the center, half height, and edge of the field for NA of .1.

Strehl Intensity vs Divergence of Reconstruction Beam NA=.1
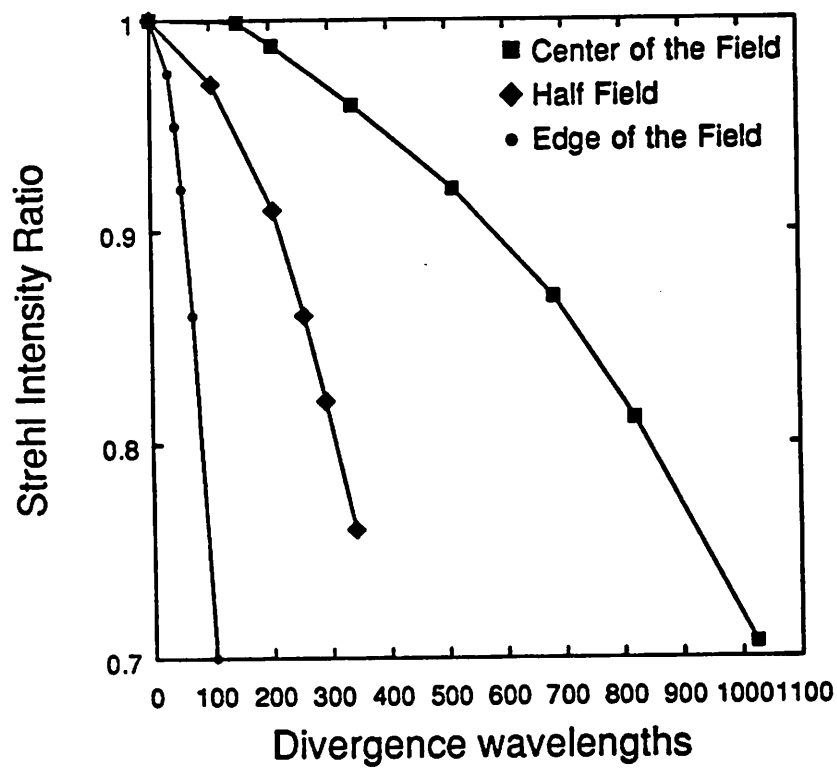
Figure 5.26 Strehl Intensity Ratio for divergence of the illumination wave-front at the center, half height, and edge of the field for NA of .1.

Strehl Intensity vs Change in Magnification NA=.1
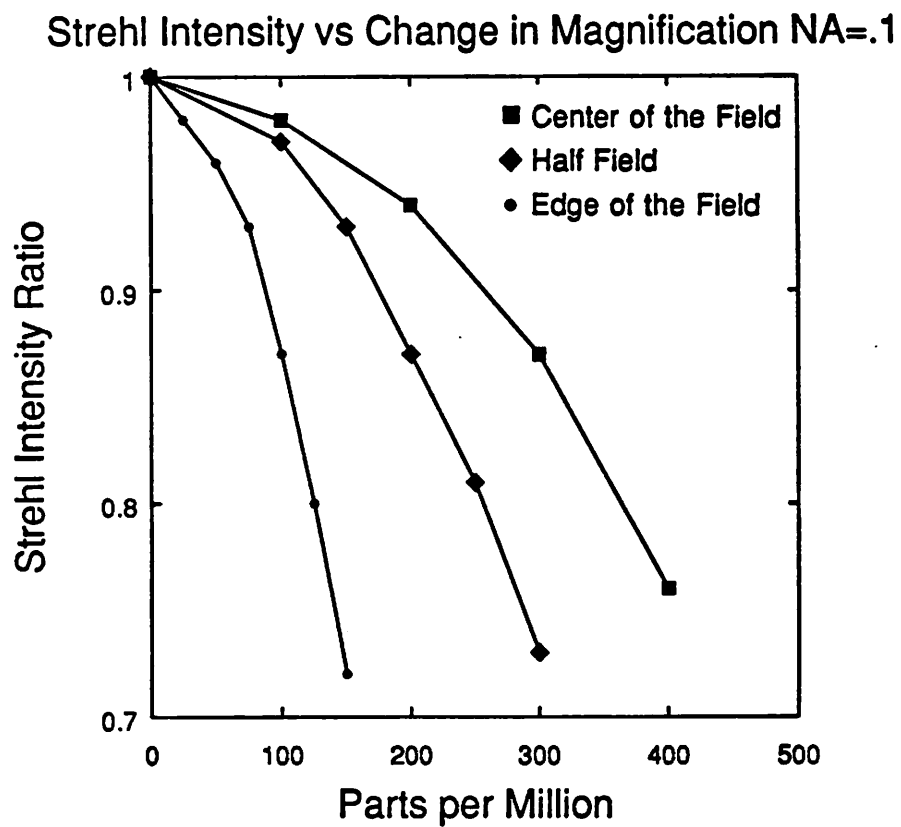
Figure 5.27 Strehl Intensity Ratio for changes magnification of the hologram at the center, half height, and the edge of the field for NA of .1.

Lateral Displacement vs Spot Size SR=.8

Angular Displacement vs Spot Size SR=.8

Axial Displacement vs Spot Size SR=.8

Divergence of Reconstruction Beam vs Spot Size SR=.8

Wavelength Deviation vs Spot Size SR=.8

Magnification vs Spot Size SR=.8
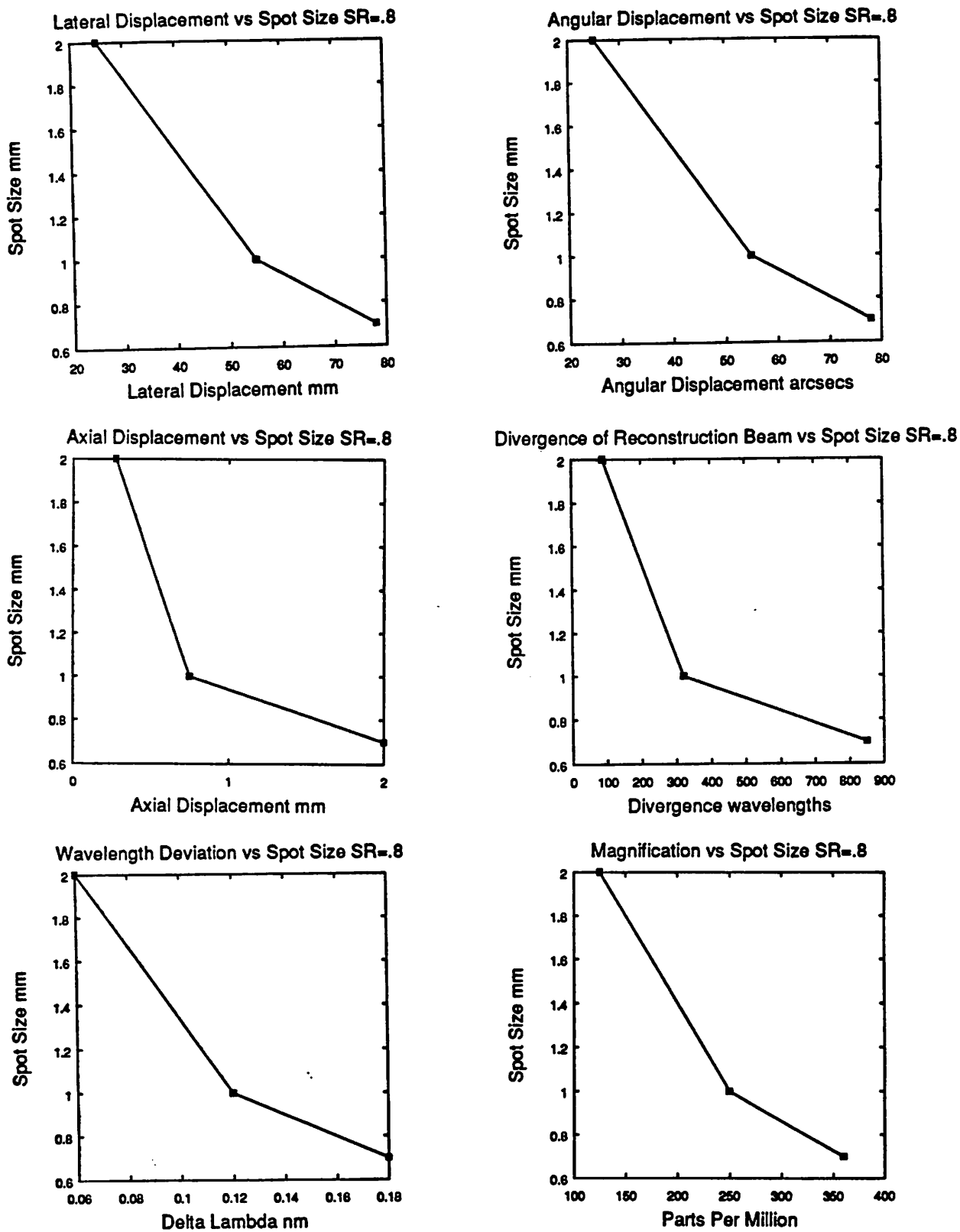
Figure 5.28 Sensitivity graphs of the traverse ray spot diameter across the field versus several reconstruction system parameters.
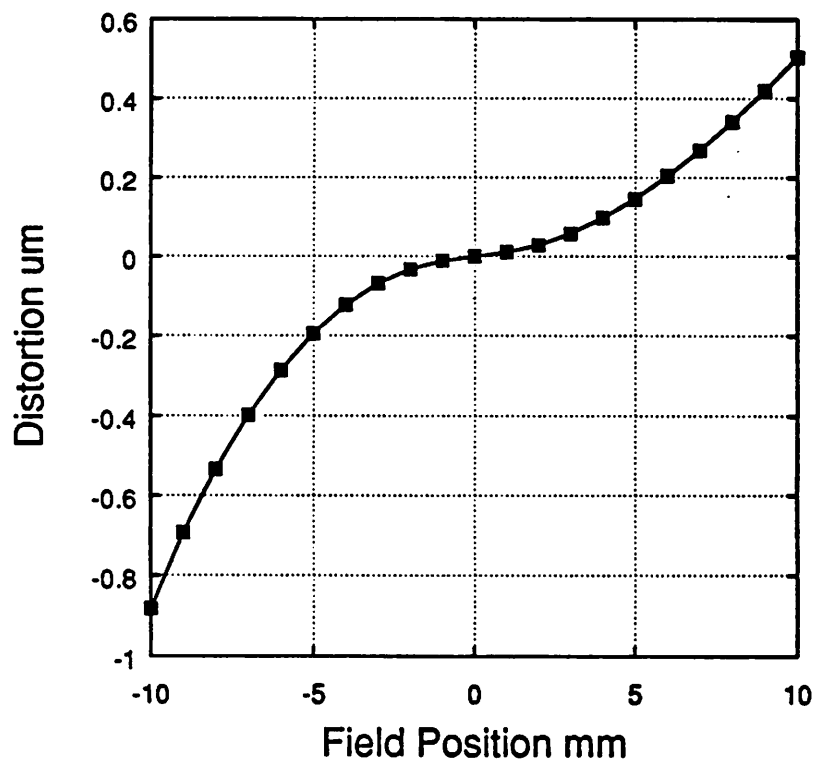
Figure 5.29 Image distortion across the image field for change in illumination wavelength of .05 nm.
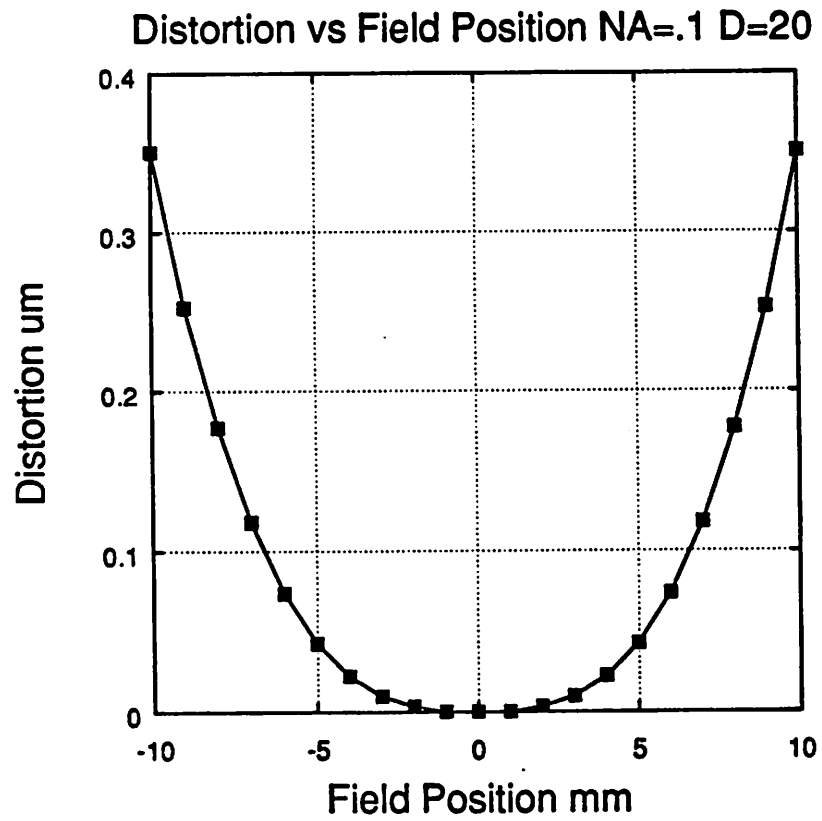
Figure 5.30 Image distortion across the image field for a angular displacement of the illumination beam of 20 arcsecs.

Distortion vs Field Position NA=.1 AD=20
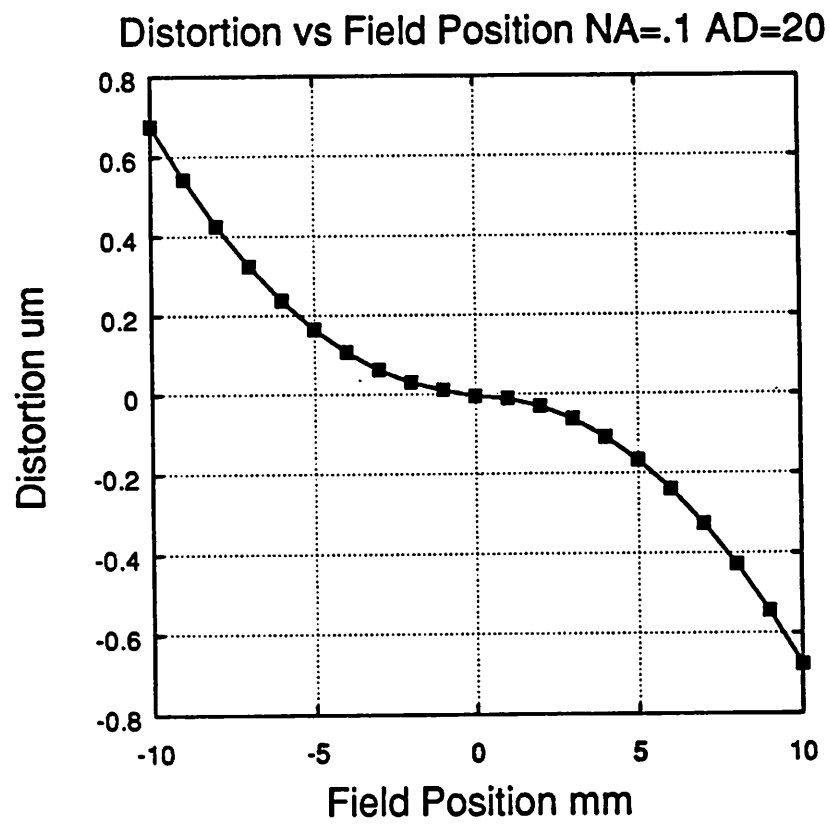
Figure 5.31 Image distortion across the image field for divergence of the illumination beam of 20 wavelengths.
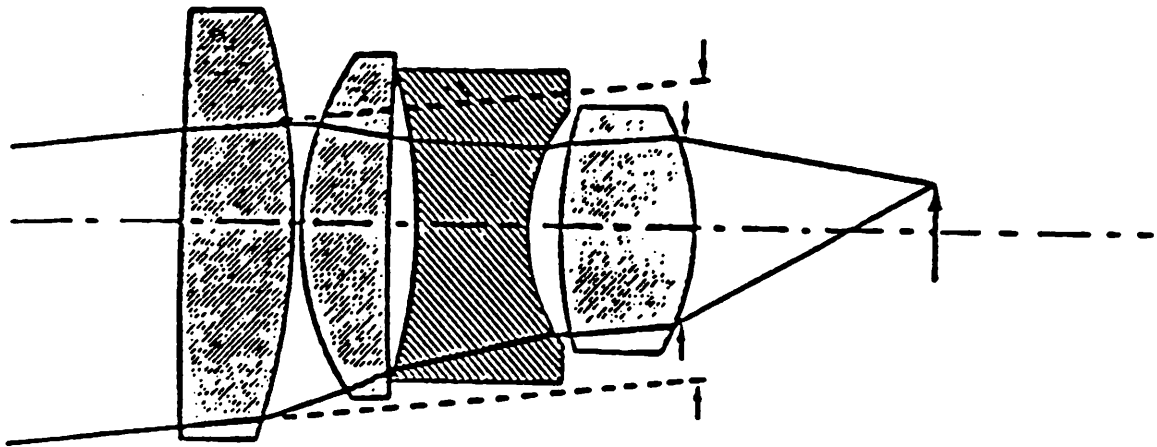
Figure 5.32 Schematic illustration of the components of the well-corrected multi-element lens.

Spot Diagram at the Center of the Field

Optical Path Difference at the Center of the Field
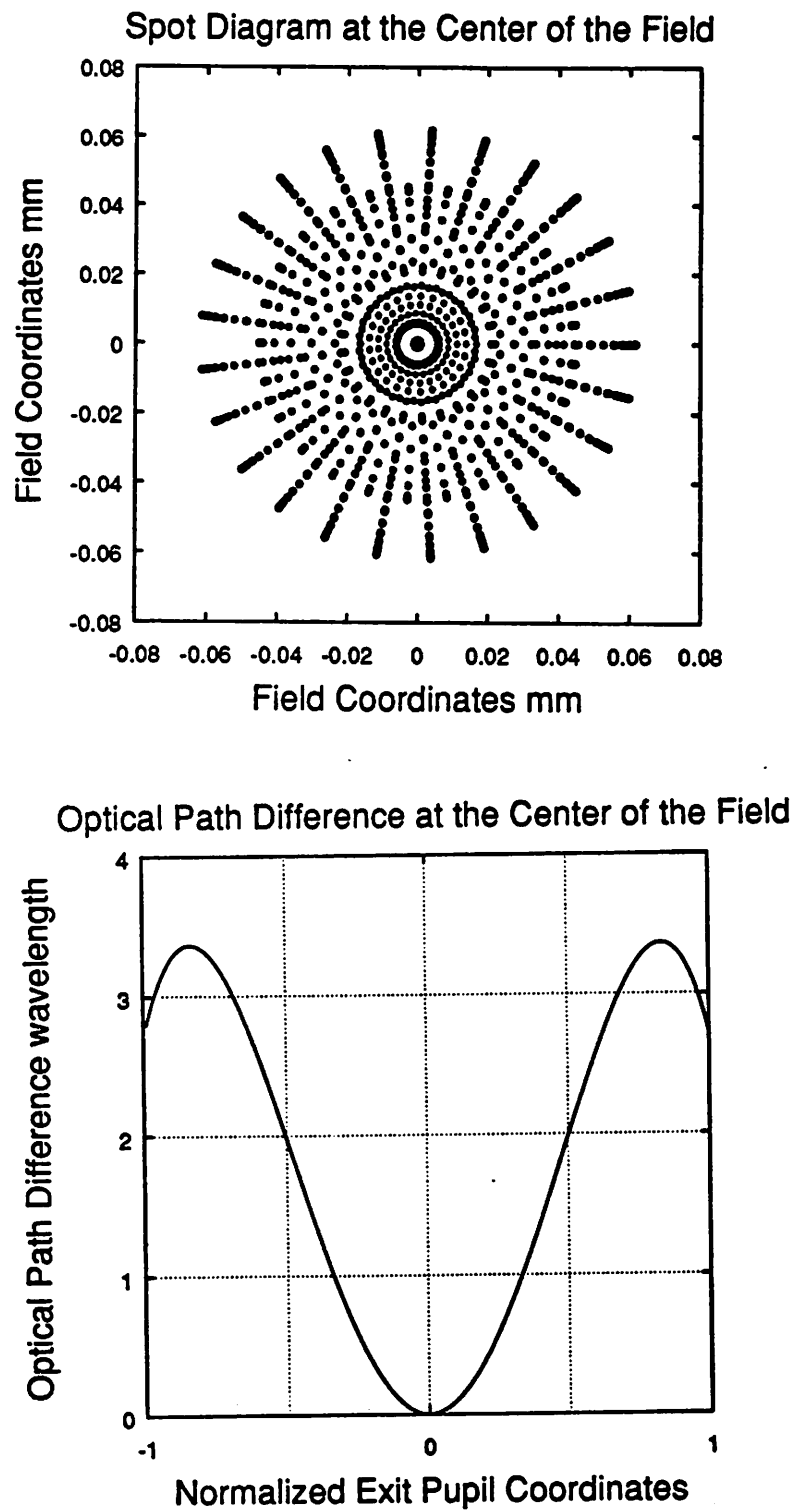
Figure 5.33 Spot Diagram and OPD graph for a well-corrected multi-element lens operating with an NA of .2 at the center of its image field.
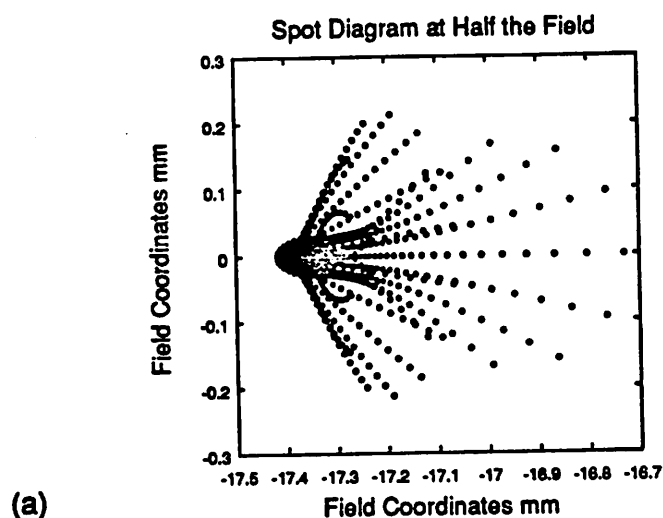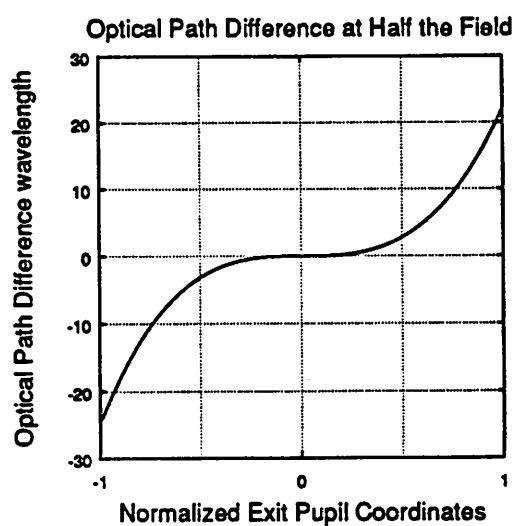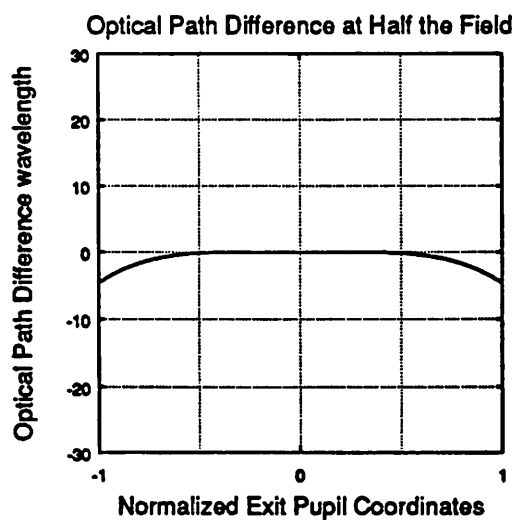
Figure 5.34 Spot Diagram (a), Tangential (b), and Sagittal (c) OPD graph for a well corrected multi-element lens operating with an NA of .2 at the half height of its image field.

Spot Diagram at the Edge of the Field

(a)

Optical Path Difference at the Edge of Field

(b)

Optical Path Difference at the Edge of Field

(c)
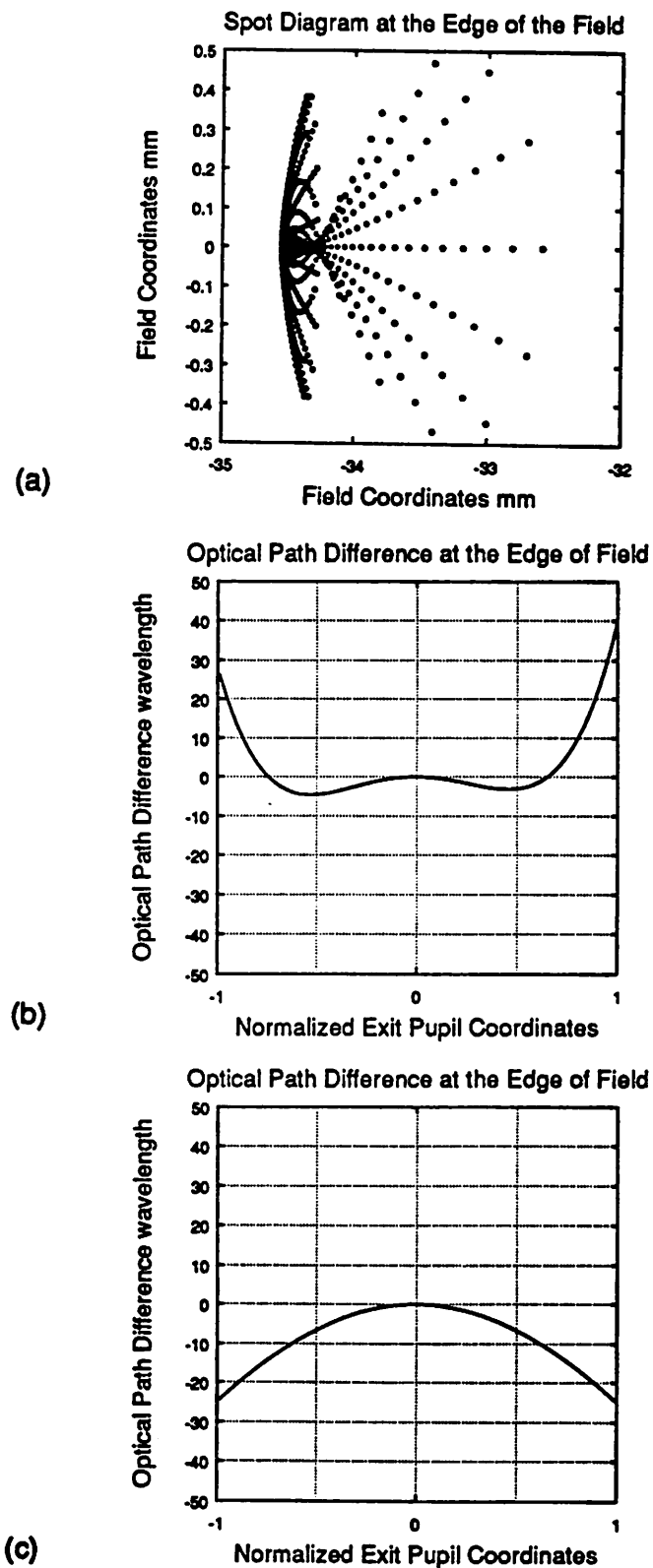
Figure 5.35 Spot Diagram (a), Tangential (b), and Sagittal (c) OPD graph for a well corrected multi-element lens operating with an NA of .2 at the edge of its image field.

Strehl Intensity vs Lateral Displacement of Hologram
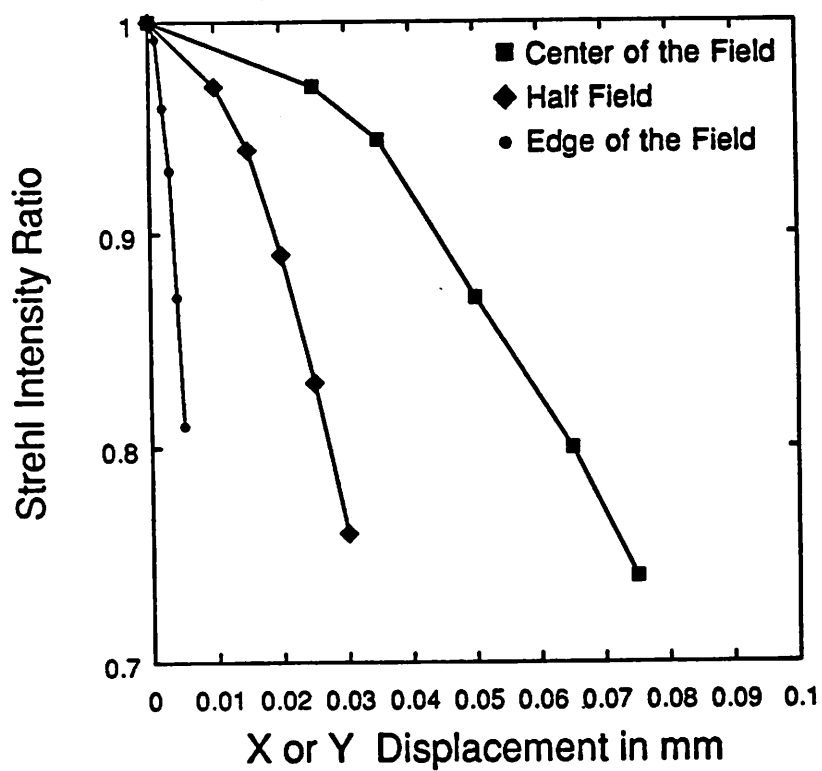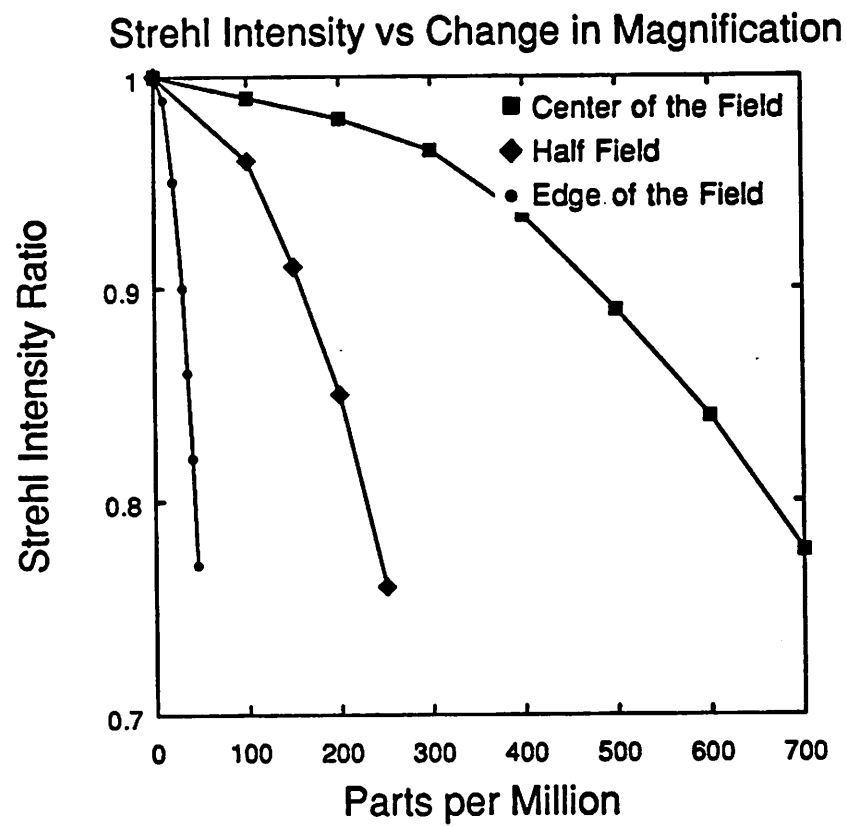

Figure 5.36 Strehl Intensity Ratio for lateral displacement of the hologram at the center, half height, and edge of the field for multi-element lens at NA of .2.

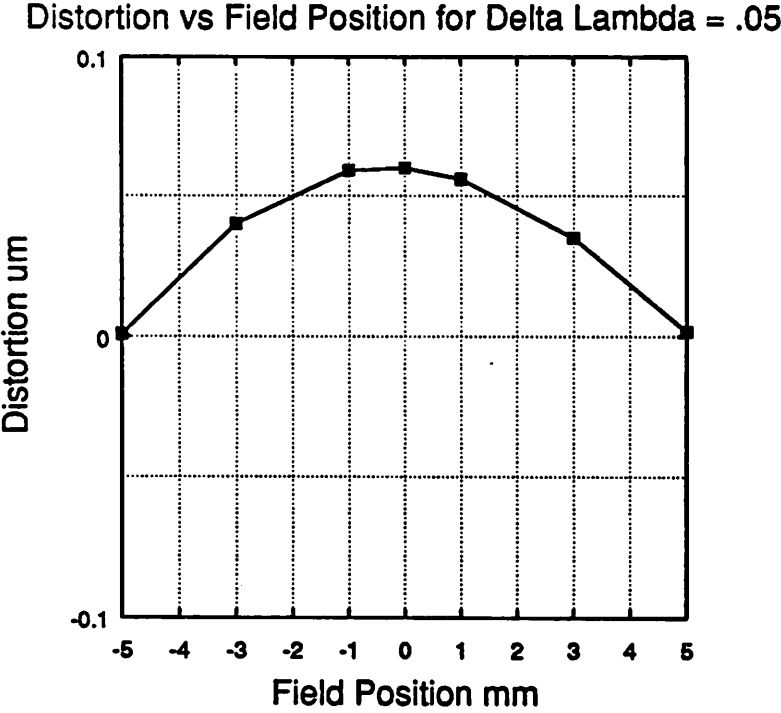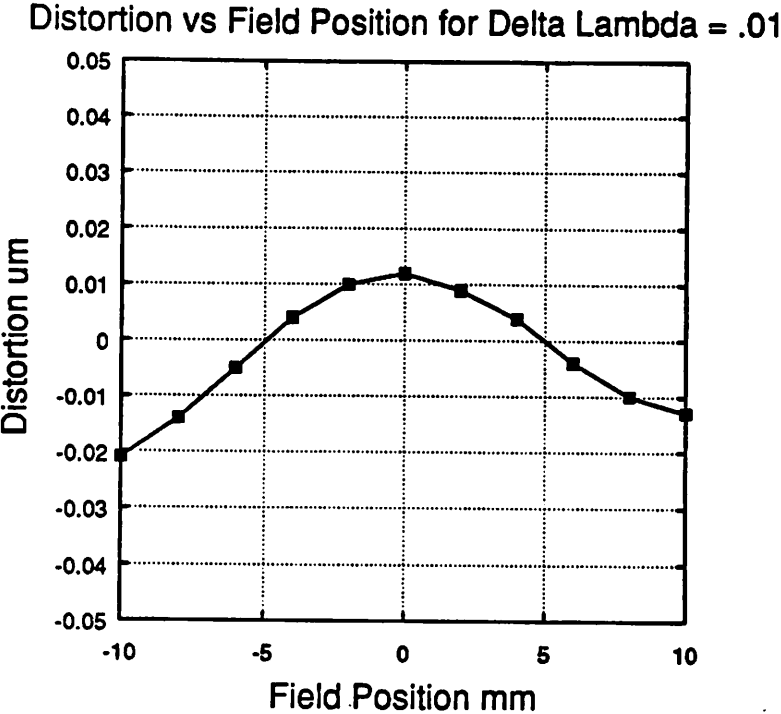## Strehl Intensity vs Hologram Axial Displacement
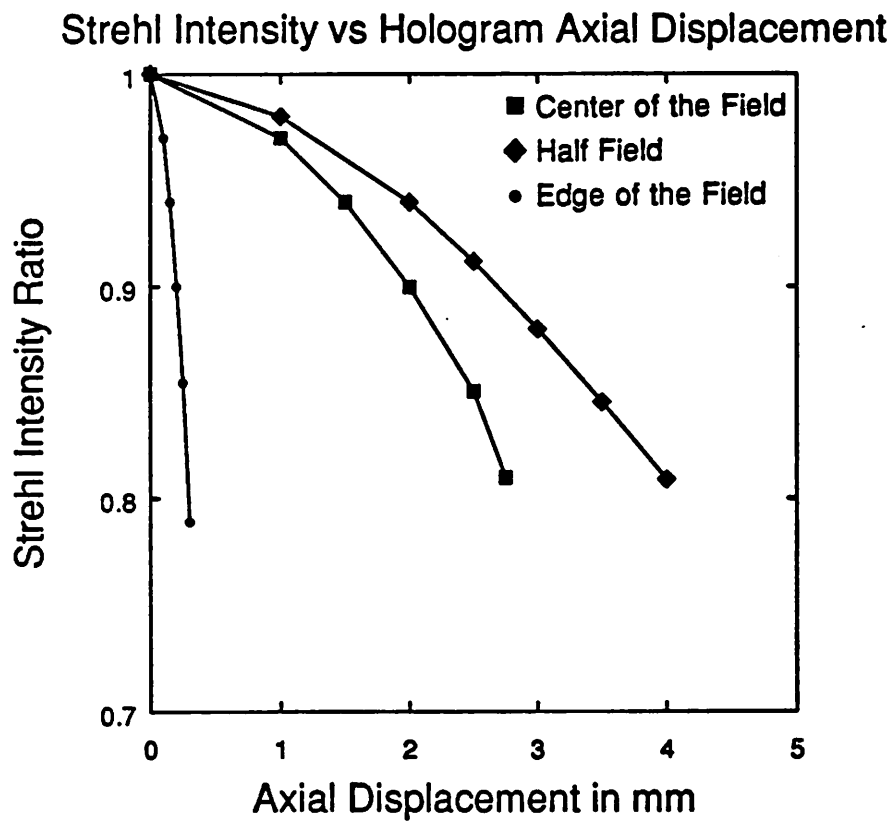
Figure 5.37 Strehl Intensity Ratio for axial displacement of the hologram at the center, half height, and edge of the field for multi-element lens at NA of .2.

Strehl Intensity vs Change in Reconstruction Wavelength
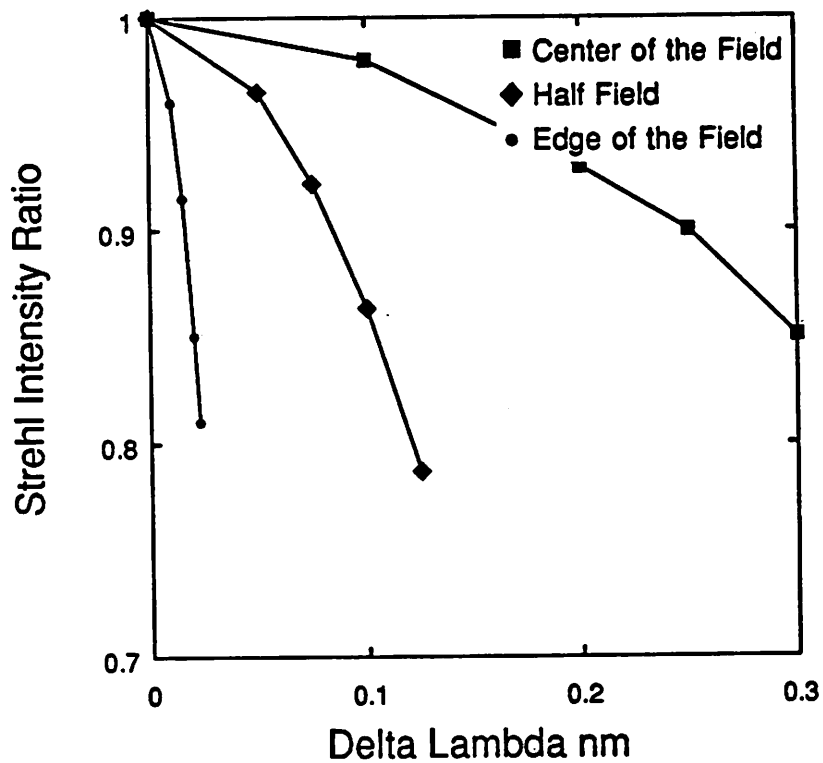
Figure 5.38 Strehl Intensity Ratio for change of illumination wavelength at the center, half height, and edge of the field for multi-element lens at NA of .2.

Strehl Intensity vs Reconstruction Beam Angular Displacement
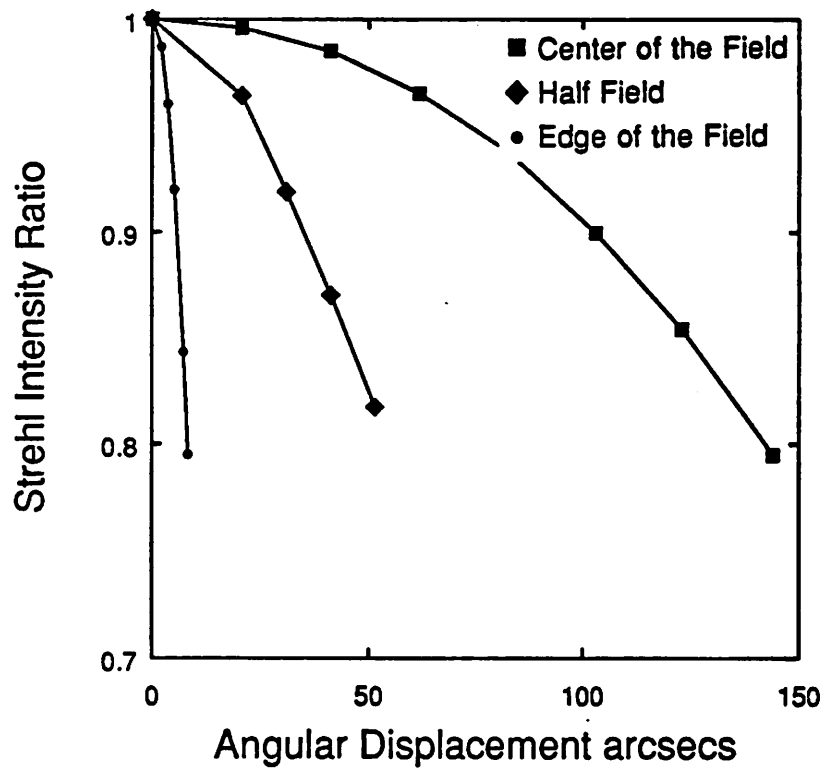
Figure 5.39 Strehl Intensity Ratio for angular displacement of the illumination beam at the center, half height, and edge of the field for multi-element lens at NA of .2.

Strehl Intensity vs Divergence of Reconstruction Beam

Strehl Intensity Ratio (y-axis)

Divergence wavelengths (x-axis)

Legend:
- ■ Center of the Field
- ◆ Half Field
- ● Edge of the Field
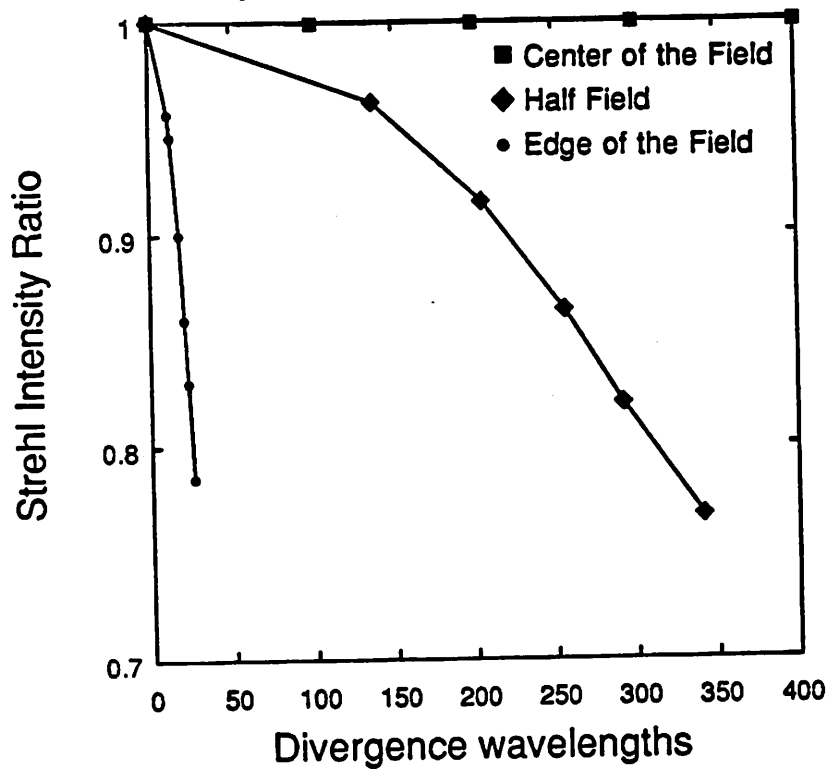
Figure 5.40 Strehl Intensity Ratio for divergence of the illumination wave-front at the center, half height, and edge of the field for multi-element lens at NA of .2.

Strehl Intensity vs Change in Magnification

Figure 5.41 Strehl Intensity Ratio for changes magnification of the hologram at the center, half height, and the edge of the field for the multi-element lens at NA of .2.

Distortion vs Field Position for Delta Lambda = .01

Distortion vs Field Position for Delta Lambda = .05

Figure 5.42 Distortion across the image field for change in the illumination wavelength of (a) .01 and (b) .05 nm.

Distortion vs Field Position for AD = 3.6

Distortion vs Field Position for AD = 20.6
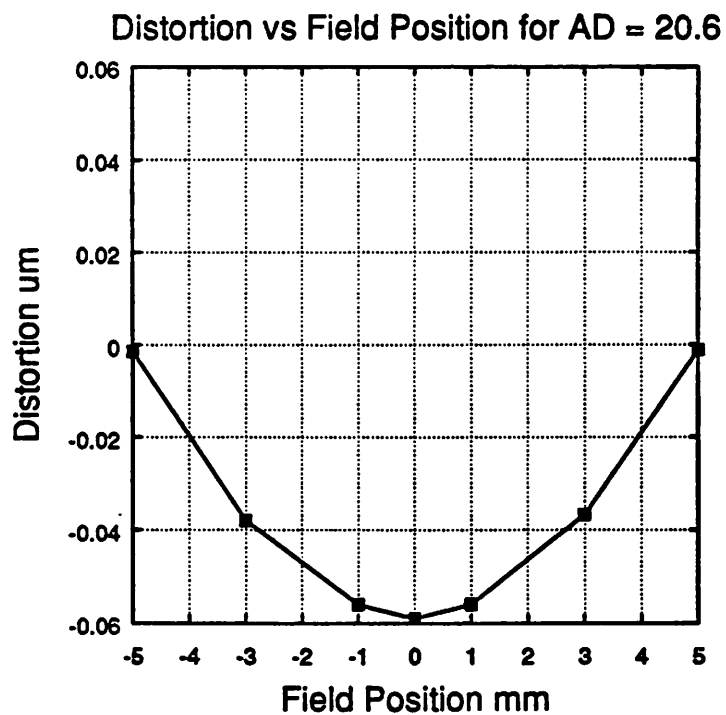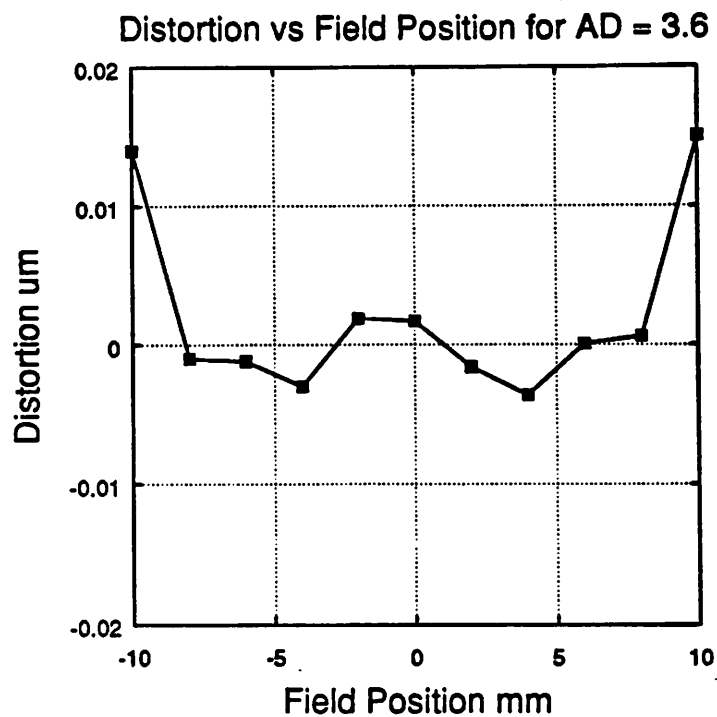
Figure 5.43 Distortion across the image field for angular displacement of the illumination beam of (a) 3.6 and (b) 20.6 arcsecs.

Distortion vs Field Position for D=11.3

Distortion vs Field Position for D=137
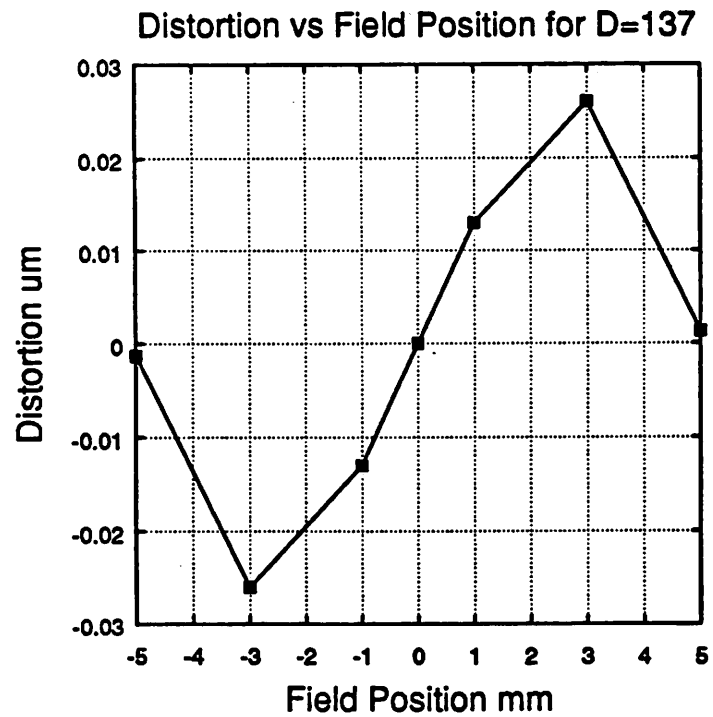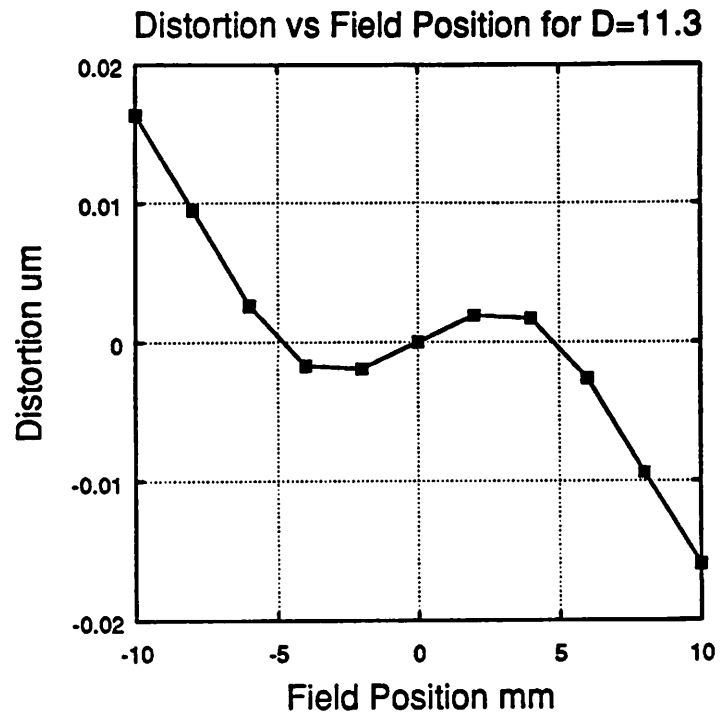
Figure 5.44 Distortion across the image field for divergence in the illumination beam wave-front of (a) 11.3 and (b) 137 wavelengths.

Spot Diagram at the Center of the Field

Optical Path Difference at the Center of the Field
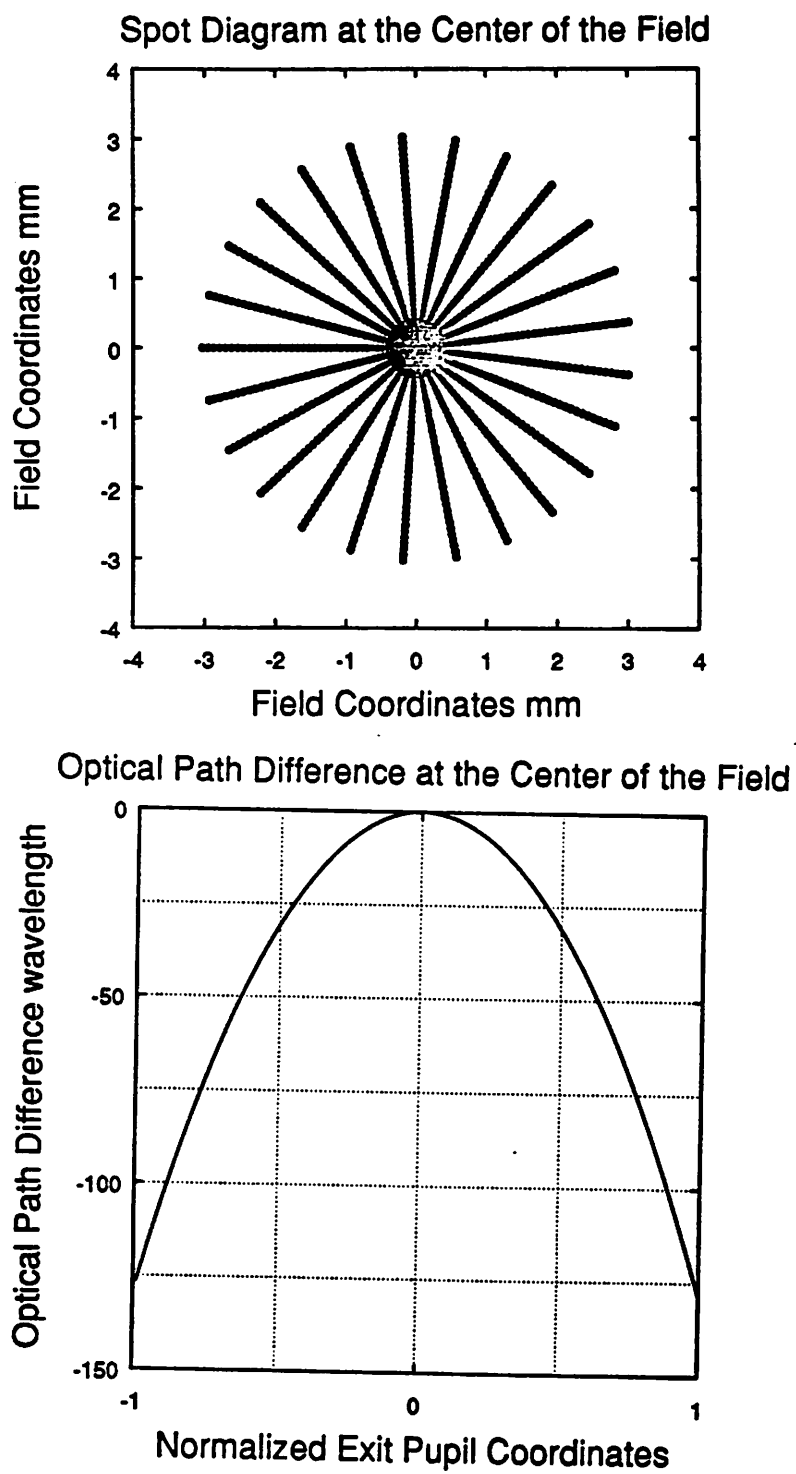
Figure 5.45 Spot Diagram and OPD graph for a well-corrected multi-element lens operating with an NA of .2 at the center of its image field.

Spot Diagram at Half the Field

(a)

Optical Path Difference at Half the Field

(b)

Optical Path Difference at Half the Field

(c)
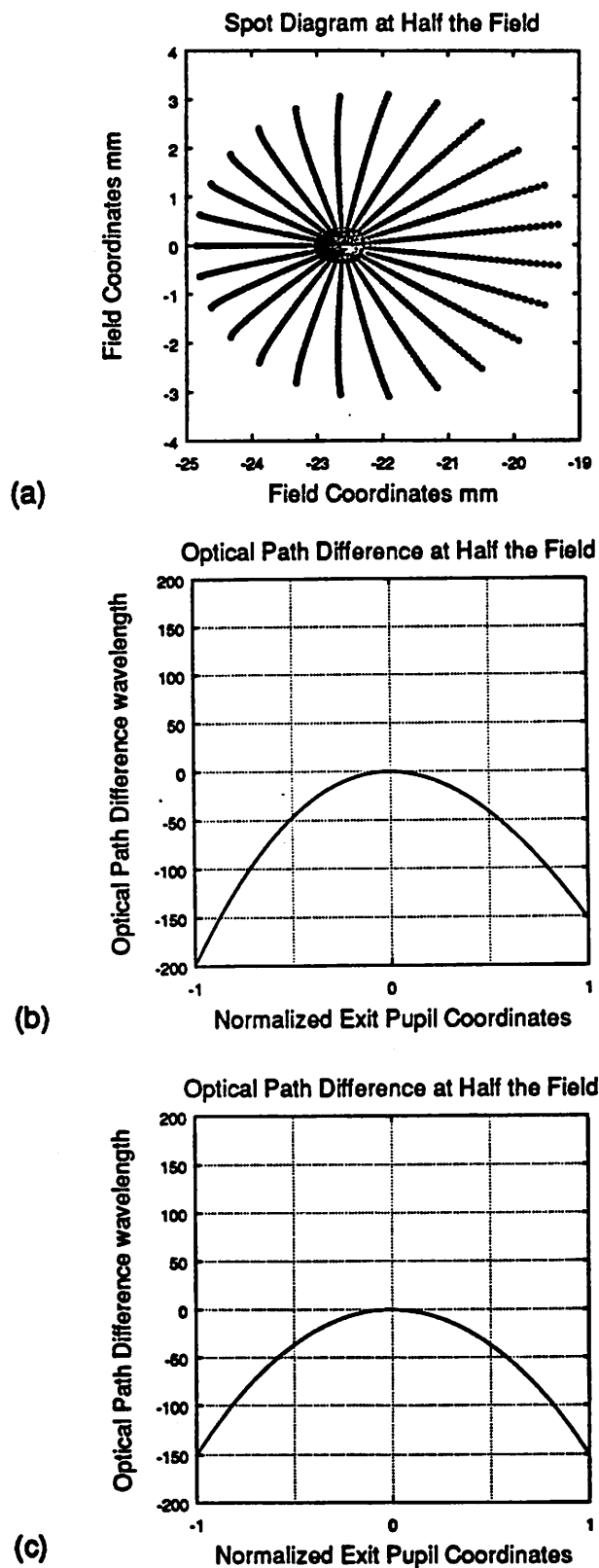
Figure 5.46 Spot Diagram (a), Tangential (b), and Sagittal (c) OPD graph for a well corrected multi-element lens operating with an NA of .2 at the half height of its image field.
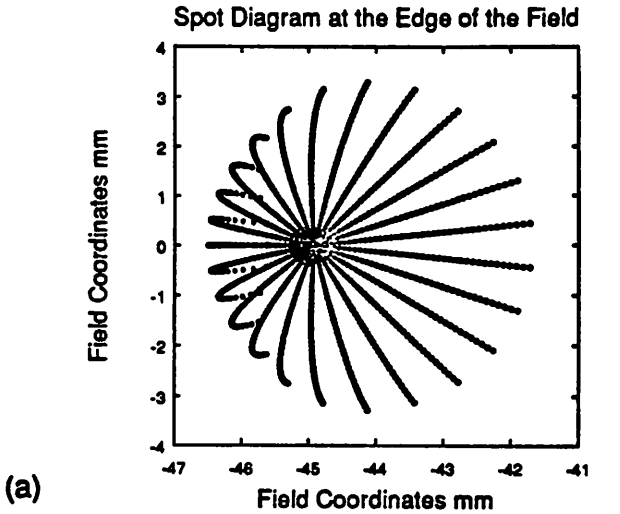
Spot Diagram at the Edge of the Field

(a)

Field Coordinates mm

Optical Path Difference at the Edge of Field

(b)

Normalized Exit Pupil Coordinates

Optical Path Difference at the Edge of Field

(c)

Normalized Exit Pupil Coordinates
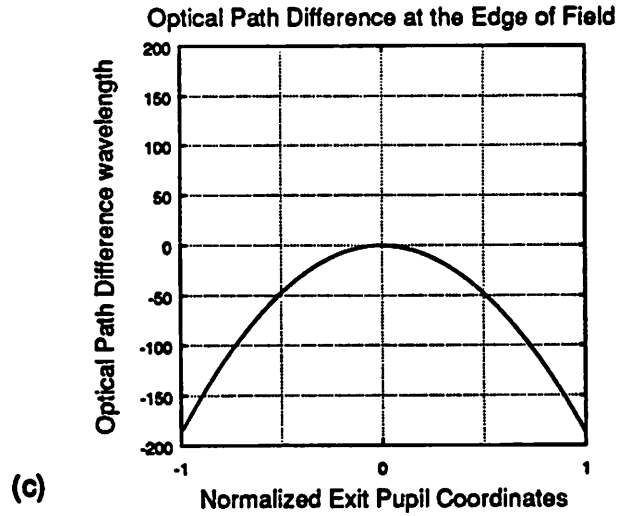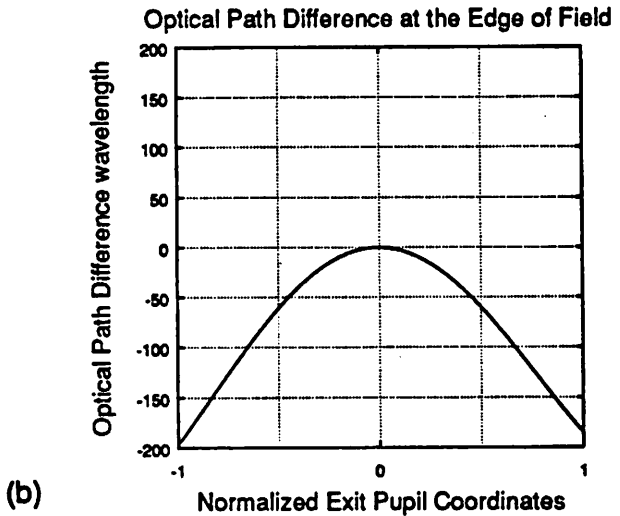
Figure 5.47 Spot Diagram (a), Tangential (b), and Sagittal (c) OPD graph for a well corrected multi-element lens operating with an NA of .2 at the edge of its image field.
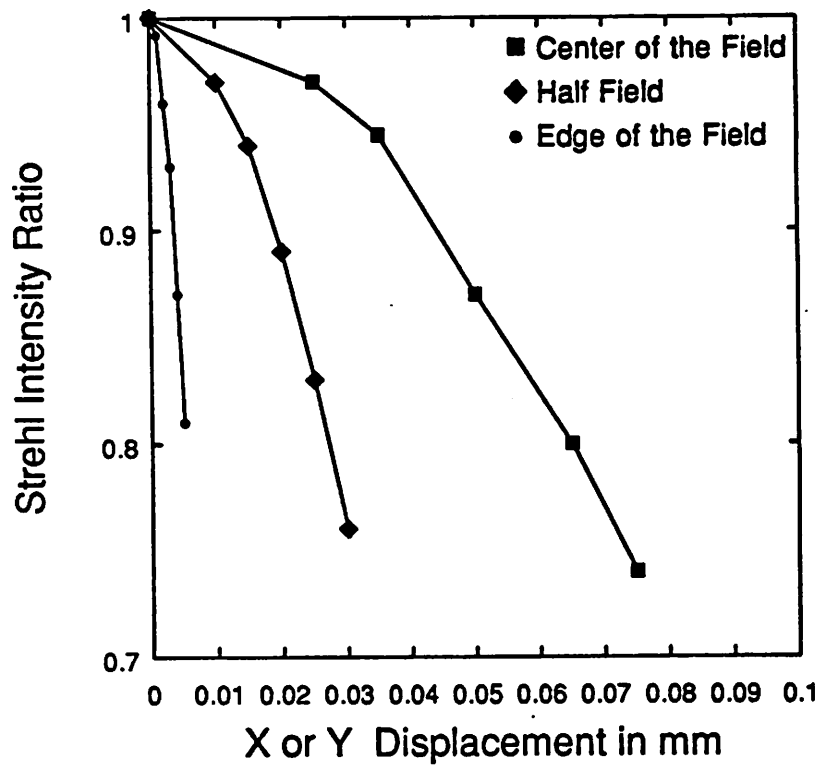
Strehl Intensity vs Lateral Displacement of Hologram

Figure 5.48 Strehl Intensity Ratio for lateral displacement of the hologram at the center, half height, and edge of the field for multi-element lens at NA of .2.
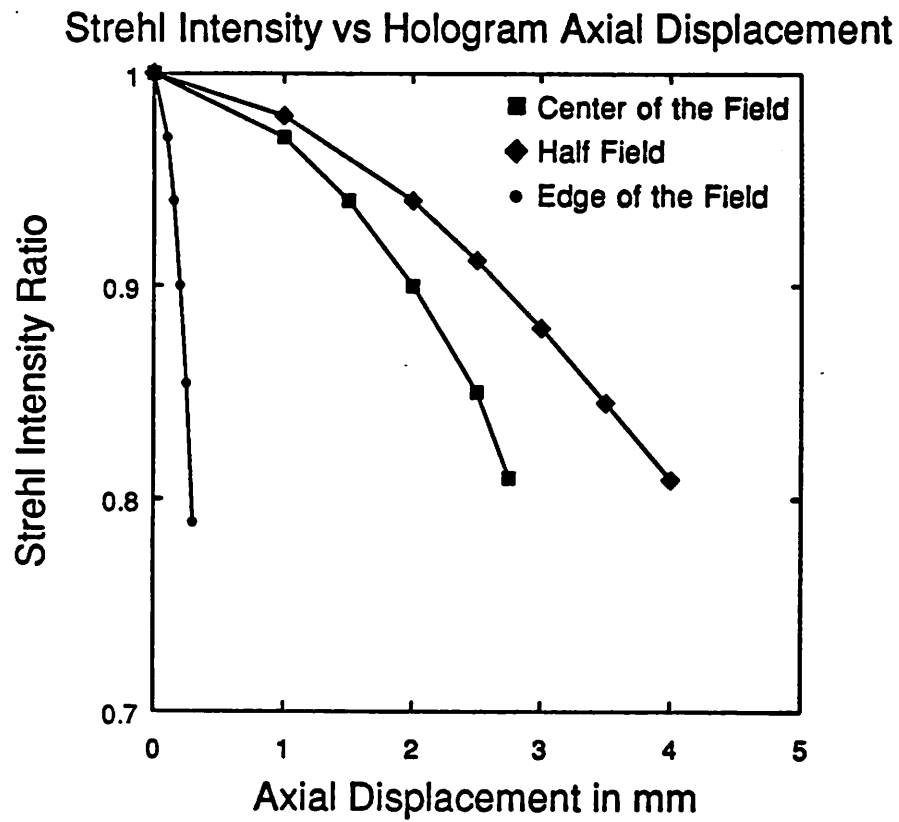
Strehl Intensity vs Hologram Axial Displacement

Figure 5.49 Strehl Intensity Ratio for axial displacement of the hologram at the center, half height, and edge of the field for multi-element lens at NA of .2.

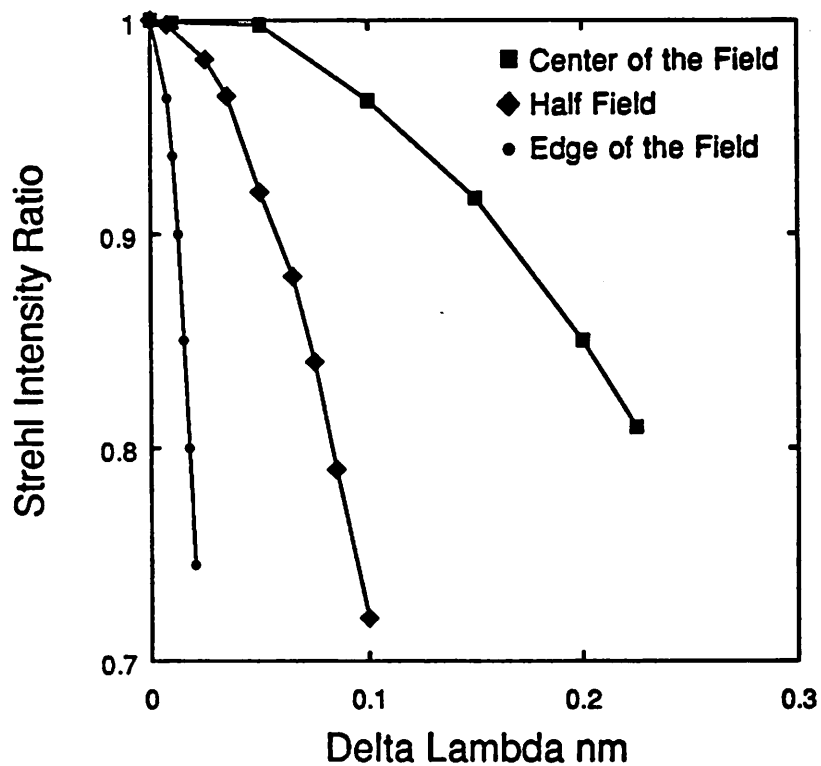## Strehl Intensity vs Change in Reconstruction Wavelength

Figure 5.50 Strehl Intensity Ratio for change of illumination wavelength at the center, half height, and edge of the field for multi-element lens at NA of .2.

Strehl Intensity vs Reconstruction Beam Angular Displacement
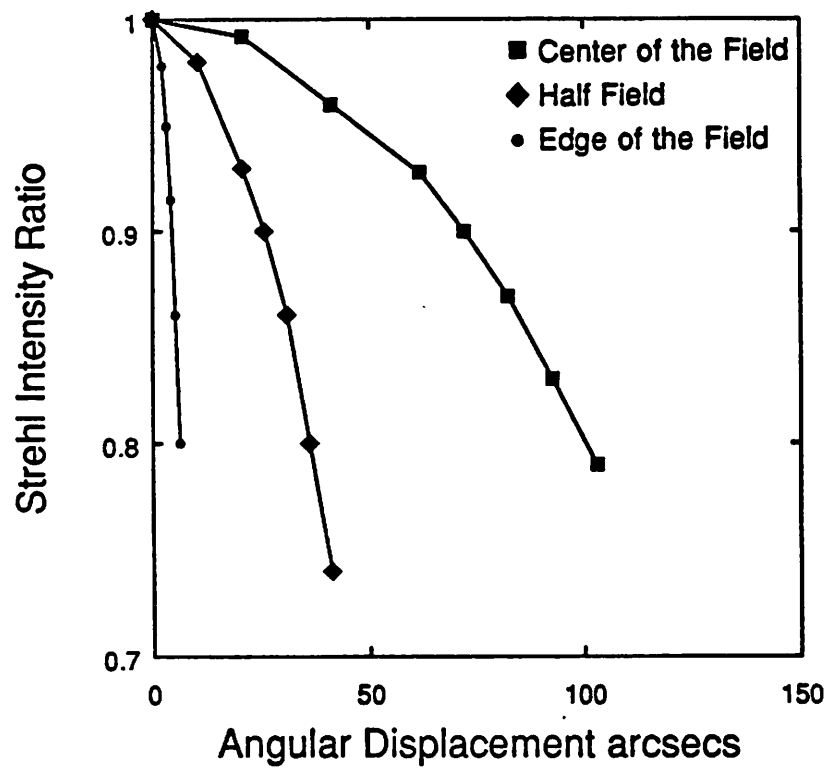

Figure 5.51 Strehl Intensity Ratio for angular displacement of the illumination beam at the center, half height, and edge of the field for multi-element lens at NA of .2.

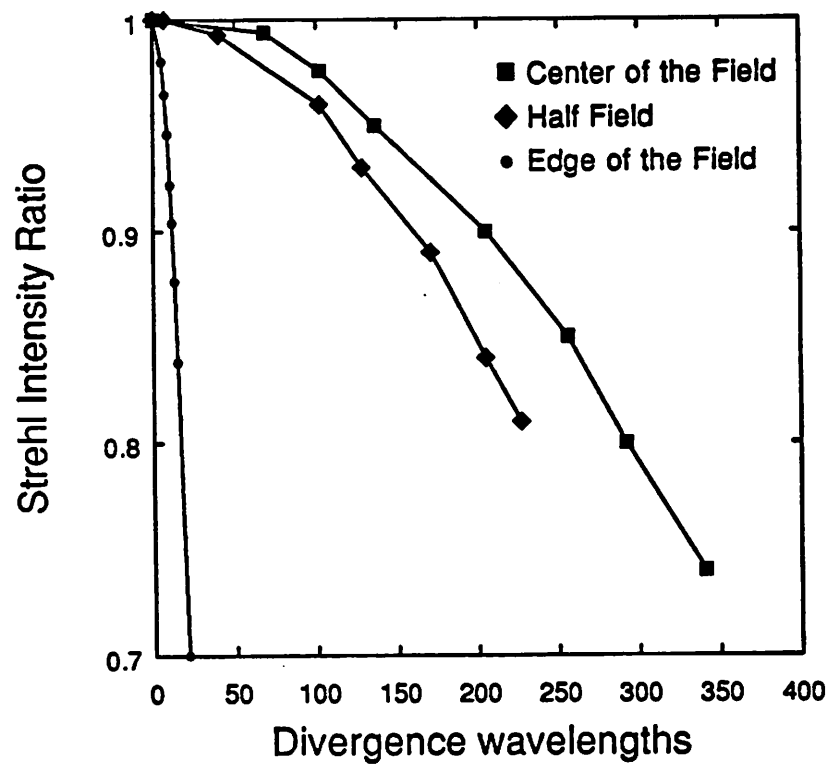# Strehl Intensity vs Divergence of Reconstruction Beam

Figure 5.52 Strehl Intensity Ratio for divergence of the illumination wave-front at the center, half height, and edge of the field for multi-element lens at NA of .2.
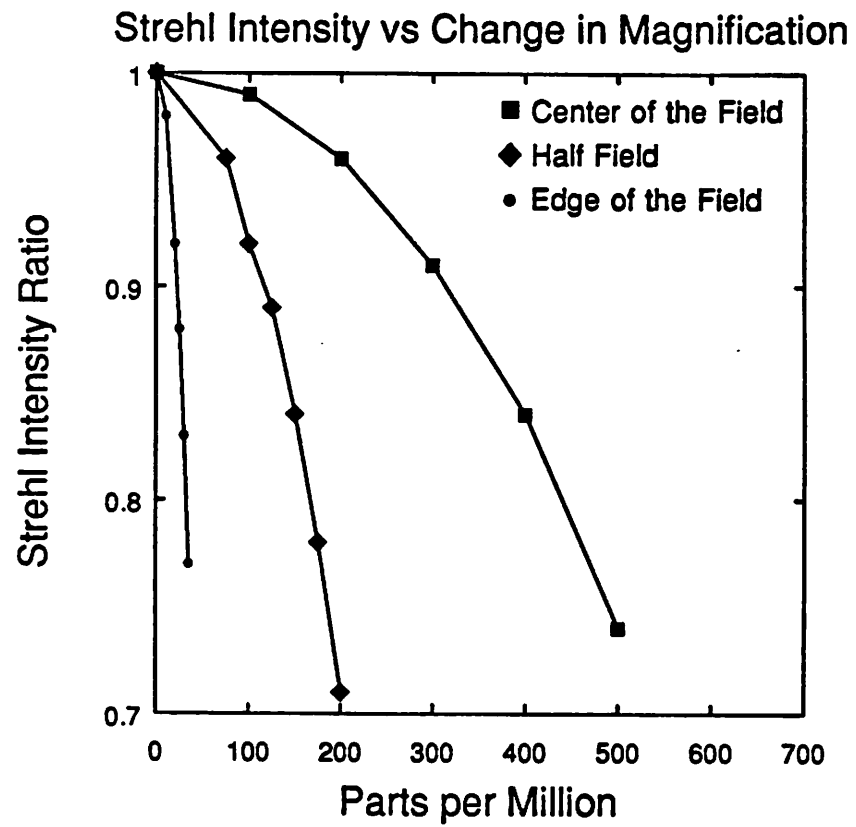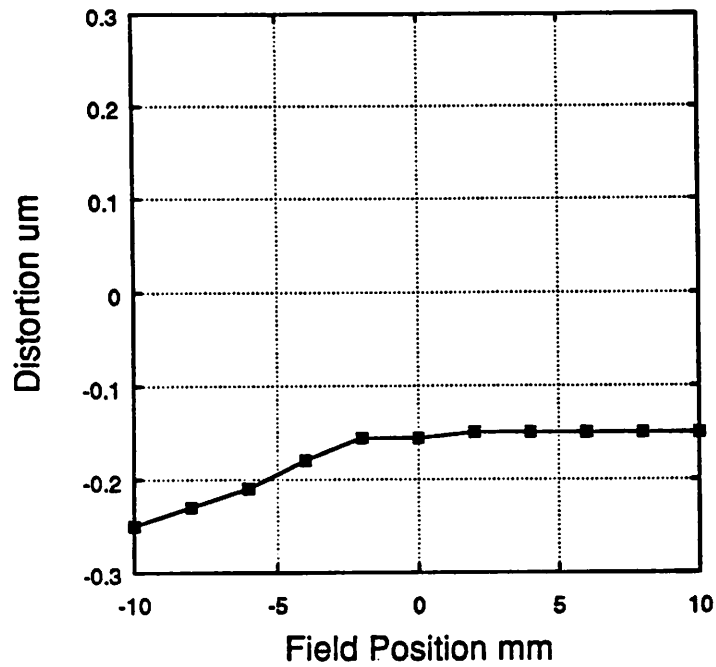
Strehl Intensity vs Change in Magnification

Figure 5.53 Strehl Intensity Ratio for changes magnification of the hologram at the center, half height and the edge of the field for the multi-element lens at NA of .2.

Distortion vs Field Position for Delta Lambda = .0075

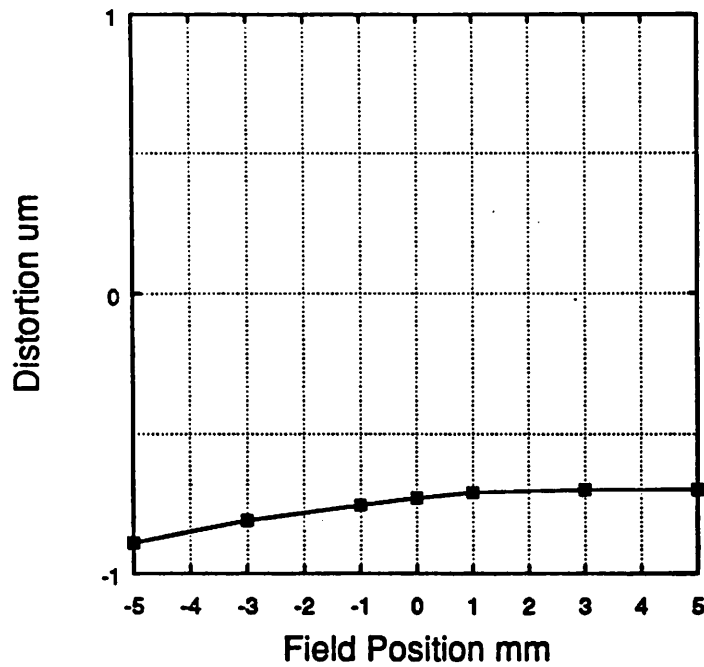## Distortion vs Field Position for Delta Lambda = .035

Figure 5.54 Distortion across the image field for change in the illumination wavelength of (a) .0075 and (b) .035 nm.
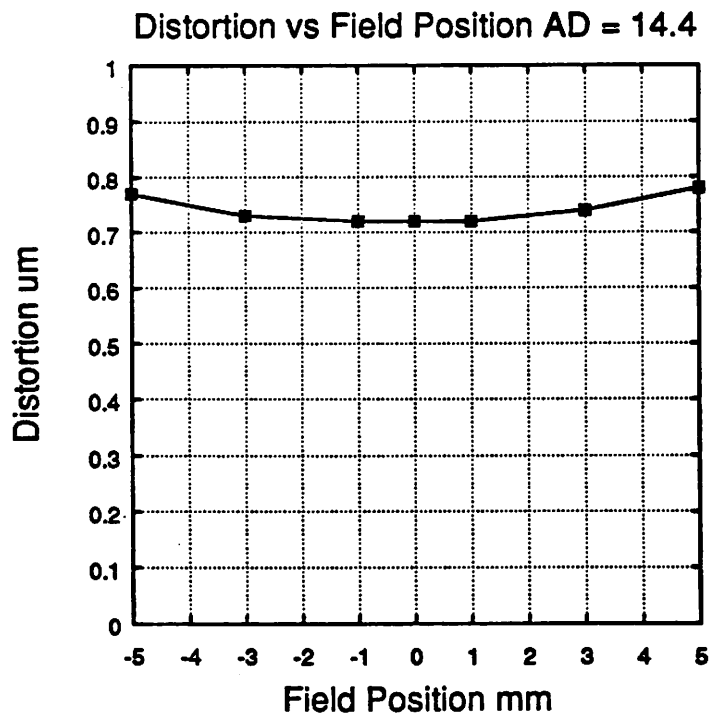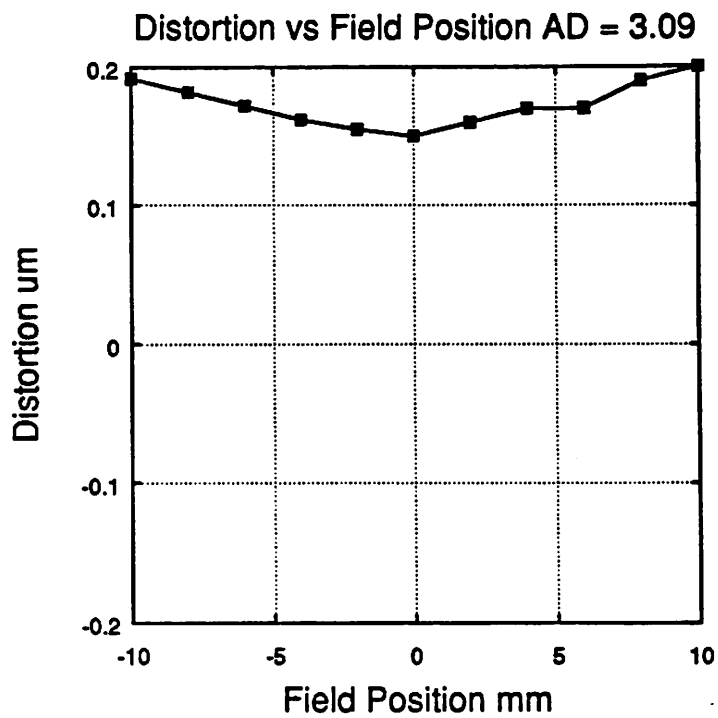
Figure 5.55 Distortion across the image field for angular displacement of the illumination beam of (a) 3.09 and (b) 14.4 arcsecs.
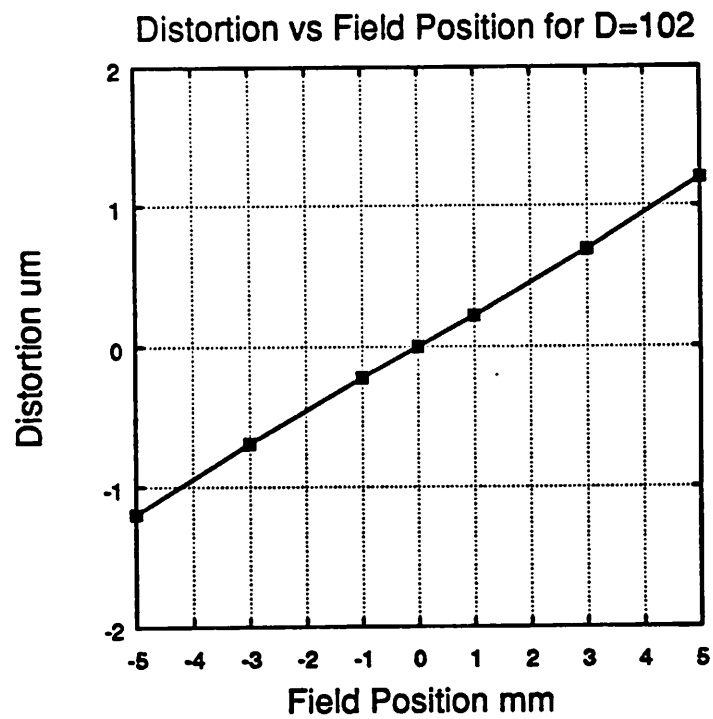
Distortion vs Field Position for D=6.8
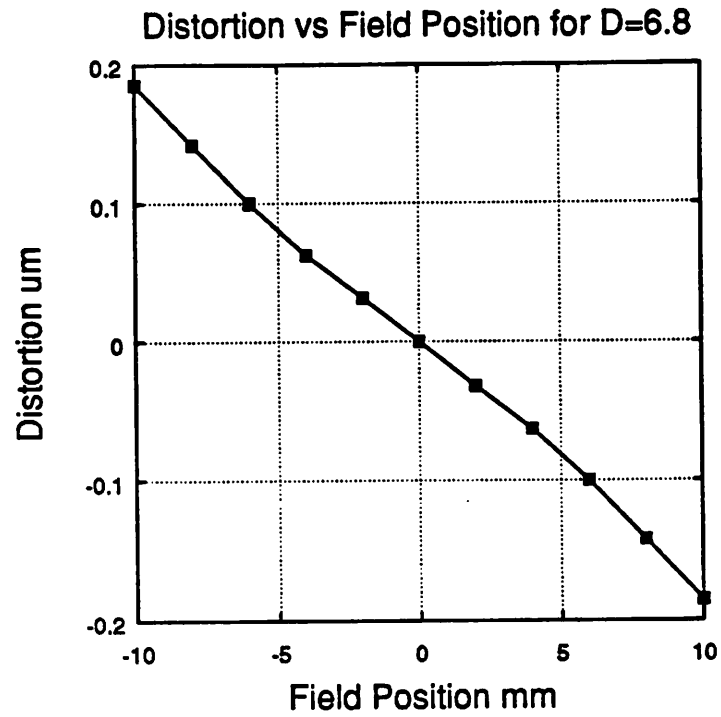

Distortion vs Field Position for D=102

Figure 5.56 Distortion across the image field for divergence in the illumination beam wave-front of (a) 6.8 and (b) 102 wavelengths.

CHAPTER 6

CONCLUSIONS

AND SUGGESTIONS FOR FUTURE WORK

6.1 SUMMARY

In this dissertation, a focused-image holographic projection system was investigated as an alternative method for microlithography to circumvent current lens design limitations. A prototype focused-image holographic projection system was constructed to investigate the resolution limits achievable from such a system. Two imaging lenses were explored: a simple single element symmetric bi-convex lens and a well-corrected photographic multi-element lens. In addition, three holographic recording materials were employed: optical photoresist, Polaroid DMP-128 photopolymer, and E.I. Dupont DeNemours proprietary photopolymer. Diffraction-limited-images were reconstructed from the systems utilizing the simple lens and the multi-element lens. The system incorporating the simple lens has a theoretical resolution limit of 0.62 μms and achieved a resolution of 0.7 μms. However, the reconstructed images of features less than a micrometer in size all showed signs of aberrations. These images were also extremely sensitive to any changes in the image

construction configuration. In fact, changes on the order of micrometers in the reconstruction system configuration completely annihilated the images. The system incorporating the multi-element lens has a theoretical resolution limit of 0.82 μms and achieved a resolution of 1.0 μm which was the smallest line-width on the object mask. The images were all well defined showing little or no aberrations. In addition, the images were much less sensitive to any changes in the reconstruction configuration than the simple lens.

The reconstructed images using photoresist as the holographic recording material were littered with optical noise. The major source of this noise was concluded to be derived from the hologram itself. Images reconstructed from the volume phase holograms based on photopolymers suffered from much less noise. The major source of optical noise in this specific system is generated from the imaging lens and the hologram itself. The imaging optics produced a similar amount of noise to that generated by the volume phase holograms. To help reduce the noise, a spatially and temporally filtered Hg arc lamp was employed as the reconstruction illumination source for a focused-image hologram recorded with the well-corrected lens. The optical noise in the reconstructed images was significantly reduced while achieving near diffraction-limited performance.

A key element of this imaging system is the imaging optics. Two unique approaches were developed to analyze the imaging sensitivity of various reconstruction parameters to the quality of the imaging optics. The first method utilizes a simple analytic model of the imaging lens combined with an ideal model of the hologram to ascertain the wave-front aberrations. Several registration errors in the reconstruction configuration were modelled including axial and lateral displacement of the hologram as well as the angular displacement of the reconstruction beam. A numerical "ray-trace" simulator was also developed and employed to analyze a

specific lens-holographic system. A sensitivity analysis of several system variables such as construction beam angle, wavefront, and wavelength as well as hologram repositioning and magnification errors was completed for two lenses, a simple single element symmetrical bi-convex lens and a well-corrected multi-element lens. The image quality sensitivity for the simple lens was found to be very large and attributed to the poor correction of the lens. The multi-element lens is fairly insensitive to changes in the image construction system compared to the simple lens.

6.2 CONCLUSIONS

Experimentally, near diffraction-limited images can be reconstructed from a focused-image lens-hologram projection system. The quality of the imaging optics has a large impact of the sensitivity of the reconstructed images to alterations in the reconstruction configuration parameters. The better the quality of the imaging lens, the less sensitive the reconstructed images are to registration errors. Spherical aberration in the imaging lens has the largest influence on the sensitivity followed by coma and astigmatism. Recording the hologram downstream from the lens' conjugate plane increases the image sensitivity for deviations in the reconstruction wavelength, angular displacement and divergence of the reconstruction beam, and magnification of the hologram. The sensitivity does not increase for an axial or lateral displacement of the hologram. Random optical noise is present in the reconstructed images which is due to illumination scattering from the imaging lens and the hologram itself. Using a broad-band source for the reconstruction illumination reduces the optical noise with little degradation to the image resolution.

6.3 SUGGESTIONS FOR FUTURE WORK

In this dissertation, we have demonstrated, in principle, that focused-image lens-hologram projection imaging is a simple method that can be used for high-resolution microlithography. In this research, several aspects of the technology have been investigated, but further work is necessary to completely evaluate the potential of this approach to microlithography.

The reconstructed image was recorded with the use of a microscope objective and an eye-piece with Polaroid type 35 instant film. A more realistic recording material to evaluate the the image fidelity and placement properties is photoresist. This requires the operating wavelength to be in the UV region of the spectrum because commercially available photoresists are only sensitive in that region.

The origins of the optical noise in the reconstructed image must be first identified, and then evaluate whether they are fundamental sources or not. Once the all sources are ascertained, effective methods can be undertaken to reduce the number of sources of optical noise. In addition, quantifying the impact of the noise on the reconstructed image is essential for establishing limits and specifications for optics, apparatus configuration geometry, and material properties for the hologram.

The numerical "ray-trace" simulator provides the path difference that each ray travels to that of the principle ray. This path difference also incorporates the effect of the refraction of the recording wave-fronts when they are incident upon the holographic recording material and the refraction of the reconstruction beam with the hologram. However, if we need to know more about not only the the direction of the wave-fronts but also their amplitude and phase distribution as well as any additional wave-fronts created due to any non-linearity effects at the output plane of the hologram, then considerably more complicated interaction models between the

reconstruction beam and the hologram must be introduced. For example, at reconstruction, we need to solve a set of differential equations governing the relationship between the amplitudes of the various diffracted modes and the reconstruction beam. The simulator also does not include the effects of the reference and object beam polarizations. Their effects can be included in the by introducing a polarization dependent intensity model for the interference of the object and reference beam recording of the hologram.

APPENDIX A

This appendix lists the major equipment employed in the experimental apparatus described in Chapter 4. Other components such as pin-holes, hologram mounting plate, and mask holder were built in either the student shop or the ERL machine shop. A granite slab 4'x8'x1' on a brick and plywood base served as the optical table. The optical components were affixed to the table with a non-permanent glue.

APPARATUS COMPONENTS
Spectra Physics 165-09 Argon Ion Laser with Intra-Cavity Etalon
Newport Corporation BSD-1 Beam Steering Unit
Newport Corporation 930-51 Variable Attenuator/Beamsplitter
Oriel Corporation 15280 Laser Beam Expanders with Spatial Filters
Janos Technology A2010-562 Plano Mirrors
Newport Corporation 610 Ultra-Resolution Mirror Mount
Newport Corporation MM-2 Mirror Mounts
Newport Corporation LP-2B Five-Axis Gimbal Optic Mount
Newport Corporation 705 Lens Positioner
Newport Corporation 400 Dual Axis Translation Stage
Newport Corporation KBX139 Bi-Convex Optical Glass Lenses
Nikkor 50mm f/1.2 Optical Lens

APPENDIX B

This appendix computes the new wave-front aberration coefficients for a lateral shift in the exit pupil. Let the wave-front aberration function be represented by[B.1]

$$W(x_p, y_p, h) = F\ (x_p^2 + y_p^2) +$$ B.1

$$\frac{1}{8}\ S\ (x_p^2 + y_p^2)^2 +$$

$$\frac{1}{2}\ C\ y_p(x_p^2 + y_p^2)\ \frac{h}{h_o} +$$

$$\frac{1}{4}\ A\ (x_p^2 + 3y_p^2)\ \frac{h^2}{h_o^2} +$$

$$\frac{1}{4}\ P\ (x_p^2 + y_p^2)\ \frac{h^2}{h_o^2} +$$

$$\frac{1}{2}\ D\ y_p\ \frac{h^3}{h_o^3}$$

where $W(x_p, y_p, h)$ is the wave-front deviation from a perfect sphere, x_p and y_p are the normalized exit pupil coordinates, h is the specific field point of interest in the image field, and $F\dagger$ is the coefficient for a constant focus error over the entire field, S is the coefficient for spherical aberration, C is the coefficient for coma, A is the coefficient for astigmatism, P is the coefficient for Petzval curvature, and D is the coefficient for distortion. A exit-pupil shift is equivalent to a change in origin of (0,-

---

A shift of amount $\frac{2F}{NA^2}$[B.2] occurs along the principle ray.

y_o) where y_o is the normalized shift. Thus, for every y_p in the above equation, $y_p + y_o$ is substituted. The resultant expression after extensive algebraic manipulation is

$$W(x_p, y_p, h) = F(x_p^2 + y_p^2) +$$

$$\frac{1}{8} S(x_p^2 + y_p^2)^2 +$$

$$\frac{1}{2}\left[C\frac{h}{h_o} + QS\right]y_p(x_p^2 + y_p^2)$$

$$\frac{1}{4}\left[A\frac{h^2}{h_o^2} + 2QC\frac{h}{h_o} + Q^2S\right](x_p^2 + 3y_p^2)$$

$$\frac{1}{4} P(x_p^2 + y_p^2)\frac{h^2}{h_o^2} +$$

$$\frac{1}{2}\left[D\frac{h^3}{h_o^3} + Q(P + 3A)\frac{h^2}{h_o^2} + 3Q^2C\frac{h}{h^o} + QF + Q^3S\right]y_p$$

B.2

[B.1] Karl A. Stetson and Karl A. Stetson, and T. Suzuki and J. Tsujiuchi, and M. J. Beesley, H. Foster, and K.G. Hambleton, "A Holographic Image Printing Technique with High Resolution.," *Optics Communication*, vol. 9, no. 4, pp. 360-363, December 1973.

[B.2] M. Born and E. Wolf, in *Principles of Optics*, Pergamon Press, New York, 1984.

APPENDIX C

This appendix describes the conversion of the traverse-ray aberrations relations from being functions of the exit-pupil coordinates to being functions of the normalized exit pupil coordinates.

The wave-front aberration function can be expressed as a summation of polynomial functions of the exit pupil coordinates[C.1].

$$W(x,y) = \sum_{i=1}^{k} \sum_{j=1}^{k} A_{ij}X^iY^j .$$
C.1

The traverse-ray aberrations relationships are expressed as functions of the wave-front aberration function and they have the following form

$$\Delta X = \frac{R}{n} \frac{\partial W(x,y)}{\partial X}$$
C.2

$$\Delta Y = \frac{R}{n} \frac{\partial W(x,y)}{\partial Y}$$
C.3

where n is the index for refraction of the media, R is the radius of the reference sphere, and W(x,y) is the wave-front aberration function.

The wave-front aberration function can be reformulated to be a function of the normalize exit pupil coordinates and is written as

$$W(x,y) = \sum_{i=1}^{k} \sum_{j=1}^{l} A_{ij}X_{xmax}^i \left[\frac{X}{X_{xmax}}\right]^i Y_{ymax}^j \left[\frac{Y}{Y_{ymax}}\right]^j Y^j .$$
C.4

A new constant term A_{ij}' can be defined as

$$A_{ij}'=A_{ij}X_{xmax}^i Y_{ymax}^j .$$
C.5

The partial derivatives with respect to X and Y of the wave-front aberration function are

$$\frac{\partial W(x,y)}{\partial X} = \sum_{i=1}^{k} \sum_{j=1}^{l} \frac{i}{X_{xmax}} A_{ij}' \left[\frac{X}{X_{xmax}}\right]^{i-1} \left[\frac{Y}{Y_{ymax}}\right]^j$$
C.6

$$\frac{\partial W(x,y)}{\partial Y} = \sum_{i=1}^{k} \sum_{j=1}^{l} \frac{j}{Y_{ymax}} A_{ij}' \left[\frac{X}{X_{xmax}}\right]^i \left[\frac{Y}{Y_{ymax}}\right]^{j-1}$$
C.7

Reorganizing the terms, the following is attained

$$\frac{\partial W(x,y)}{\partial y} = \frac{1}{X_{xmax}} \sum_{i=1}^{k} \sum_{j=1}^{l} i A_{ij}' \left[\frac{X}{X_{xmax}}\right]^{i-1} \left[\frac{Y}{Y_{ymax}}\right]^j$$
C.8

$$\frac{\partial W(x,y)}{\partial Y} = \frac{1}{Y_{ymax}} \sum_{i=1}^{k} \sum_{j=1}^{l} j\, A'_{ij} \left[\frac{X}{X_{xmax}}\right]^{i} \left[\frac{Y}{Y_{ymax}}\right]^{j-1} \qquad \text{C.9}$$

The traverse-ray aberrations relationships can now be written as

$$\Delta X = \frac{R}{nX_{xmax}} \sum_{i=1}^{k} \sum_{j=1}^{l} i\, A'_{ij} \left[\frac{X}{X_{xmax}}\right]^{i-1} \left[\frac{Y}{Y_{ymax}}\right]^{j} \qquad \text{C.10}$$

$$\Delta X = \frac{R}{nY_{ymax}} \sum_{i=1}^{k} \sum_{j=1}^{l} j\, A'_{ij} \left[\frac{X}{X_{xmax}}\right]^{i} \left[\frac{Y}{Y_{ymax}}\right]^{j-1} \qquad \text{C.11}$$

Defining $\frac{R}{X_{xmax}}$ and $\frac{R}{Y_{ymax}}$ as $\frac{1}{NA_{xmax}}$ and $\frac{1}{NA_{ymax}}$ respectively, the relationships are written as

$$\Delta X = \frac{1}{nNA_{xmax}} \sum_{i=1}^{k} \sum_{j=1}^{l} i\, A'_{ij} \left[\frac{X}{X_{xmax}}\right]^{i-1} \left[\frac{Y}{Y_{ymax}}\right]^{j} \qquad \text{C.12}$$

$$\Delta X = \frac{1}{nNA_{ymax}} \sum_{i=1}^{k} \sum_{j=1}^{l} j\, A'_{ij} \left[\frac{X}{X_{xmax}}\right]^{i} \left[\frac{Y}{Y_{ymax}}\right]^{j-1} \qquad \text{C.13}$$

Thus, the traverse-ray aberration relationships are

$$\Delta X = \frac{1}{nNA_{xmax}} \frac{\partial W'(x,y)}{\partial X} \qquad \text{C.14}$$

$$\Delta Y = \frac{1}{nNA_{ymax}} \frac{\partial W'(x,y)}{\partial Y} \qquad \text{C.15}$$

where NA_{xmax} is the maximum numerical aperture in the x-direction and NA_{ymax} is the maximum numerical aperture in the y-direction and $W'(x,y)$ is the wave-front aberration function defined as a function of the normalized exit pupil coordinates.

[C.1] H.H. Hopkins, in *Wave Theory of Aberrations*, Clarendon Press, London, 1950.